Tracing the chemistry of high-energy processes in planetary atmospheres

Patrick Barth

A thesis submitted for the degree of PhD
at the
University of St Andrews

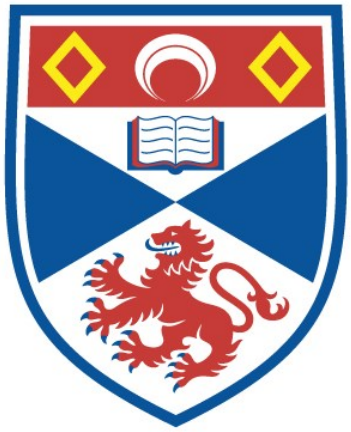

2024

“Light particles are written notes. Lightning can be an entire sonata. Thousand lightning balls are a concert. For this concert, I created a ball of lightning that can be heard on the frozen peaks of the Himalayas."

- Nikola Tesla, 1899

Declaration

Candidate's declaration

I, Patrick Barth, do hereby certify that this thesis, submitted for the degree of PhD, which is approximately 32,000 words in length, has been written by me, and that it is the record of work carried out by me, or principally by myself in collaboration with others as acknowledged, and that it has not been submitted in any previous application for any degree. I confirm that any appendices included in my thesis contain only material permitted by the 'Assessment of Postgraduate Research Students' policy.

I was admitted as a research student at the University of St Andrews in September 2019.

I received funding from an organisation or institution and have acknowledged the funder(s) in the full text of my thesis.

Date 1 Dec 2023 Signature of candidate

Supervisor's declaration

I hereby certify that the candidate has fulfilled the conditions of the Resolution and Regulations appropriate for the degree of PhD in the University of St Andrews and that the candidate is qualified to submit this thesis in application for that degree. I confirm that any appendices included in the thesis contain only material permitted by the 'Assessment of Postgraduate Research Students' policy.

Date 1 Dec 2023 Signature of supervisor

Permission for publication

In submitting this thesis to the University of St Andrews we understand that we are giving permission for it to be made available for use in accordance with the regulations of the University Library for the time being in force, subject to any copyright vested in the work not being affected thereby. We also understand, unless exempt by an award of an embargo as requested below, that the title and the abstract will be published, and that a copy of the work may be made and supplied to any bona fide library or research worker, that this thesis will be electronically accessible for personal or research use and that the library has the right to migrate this thesis into new electronic forms as required to ensure continued access to the thesis.

I, Patrick Barth, confirm that my thesis does not contain any third-party material that requires copyright clearance.

The following is an agreed request by candidate and supervisor regarding the publication of this thesis:

Printed copy

No embargo on print copy.

Electronic copy

Embargo on part (Chapter 3.4: The Effect of Lightning on the Chemistry of Exoplanet Atmospheres, and Appendix A.1) of electronic copy for a period of 1 year on the following ground(s):

- Publication would preclude future publication

Supporting statement for electronic embargo request

This chapter contains material that has just been submitted to a refereed journal but has not yet been published.

Title and Abstract

- I agree to the title and abstract being published.

Date 1 Dec 2023 Signature of candidate

Date 1 Dec 2023 Signature of supervisor

Underpinning Research Data or Digital Outputs

Candidate's declaration

I, Patrick Barth, understand that by declaring that I have original research data or digital outputs, I should make every effort in meeting the University's and research funders' requirements on the deposit and sharing of research data or research digital outputs.

Date 1 Dec 2023 Signature of candidate

Permission for publication of underpinning research data or digital outputs

We understand that for any original research data or digital outputs which are deposited, we are giving permission for them to be made available for use in accordance with the requirements of the University and research funders, for the time being in force.

We also understand that the title and the description will be published, and that the underpinning research data or digital outputs will be electronically accessible for use in accordance with the license specified at the point of deposit, unless exempt by award of an embargo as requested below.

The following is an agreed request by candidate and supervisor regarding the publication of underpinning research data or digital outputs:

Embargo on part (Spark experiments and photochemical simulations to identify lightning signatures in planetary atmospheres (dataset, coined DOI: 10.17630/8b72510f-62a8-43dc-94f1-af9b7766f817)) of electronic files for a period of 1 year on the following ground(s):

- Publication would preclude future publication

Supporting statement for electronic embargo request

This material is underpinning work that has just been submitted to a refereed journal but has not yet been published.

Title and Description

- I require an embargo on the title and description

Date 1 Dec 2023 Signature of candidate

Date 1 Dec 2023 Signature of supervisor

Collaboration Statement

This thesis is the result of my work carried out principally by myself in collaboration with others as acknowledged below at the University of St Andrews between September 2019 and June 2023. Parts of the work presented in this thesis have been published, or are submitted for publication in refereed scientific journals. In all cases, the text in the thesis has been written by me and the figures presented in the chapters have been produced by me, unless explicitly stated in the figure's caption.

1. Chapter 2 is based on (Barth et al., 2021b): 'MOVES – IV. Modelling the influence of stellar XUV-flux, cosmic rays, and stellar energetic particles on the atmospheric composition of the hot Jupiter HD 189733b', Barth. P., Helling, Ch., Stüeken, E. E., Bourrier, V., Mayne, N., Rimmer, P. B., Jardine, M., Vidotto, A. A., Wheatley, P. J., Fares, R., Monthly Notices of the Royal Astronomical Society, 2021, 502:4, 6201–6215, DOI: 10.1093/mnras/staa3989. All co-authors provided comments on the final manuscript.

2. Chapter 3 (Sections 3.1, 3.2, and 3.3) contains material from (Barth et al., 2023a): 'Isotopic constraints on lightning as a source of fixed nitrogen in Earth's early biosphere', Barth, P., Stüeken, E. E., Helling, Ch., Rossmanith, L., Peng, Y., Walters, W., Claire, M. 2023, Nature Geoscience, 16, 478–484, DOI: 10.1038/s41561-023-01187-2. Reproduced with permission from Springer Nature. Lukas Rossmanith conducted some of the experiments presented in this work, as part of his time as a summer student in our group. A set of samples was analysed for nitrite and nitrate concentration, nitrogen and oxygen isotopes by Wendell Walters at Brown University, Rhode Island. All co-authors provided comments on the final manuscript.

3. Chapter 3 (Sections 3.1, 3.2, and 3.4) and Appendix A contain material from 'The effect of lightning on the atmospheric chemistry of exoplanets and potential biosignatures',

Barth, P., Stüeken, E. E., Helling, Ch., Schwieterman, E. W., Telling, J., submitted to Astronomy and Astrophysics. A set of samples was analysed for CO concentration by Jon Telling at Newcastle University. The photochemical simulations and calculated spectra presented in Section 3.4.3 and Appendix A were provided by Edward W. Schwieterman at the University of California, Riverside, in close collaboration with myself. The figures have been produced by me. All co-authors provided comments on the final manuscript of the paper.

Abstract

Lightning, X-ray & UV radiation, stellar energetic particles, and galactic cosmic rays provide important sources of disequilibrium chemistry in planetary atmospheres and might be responsible for the production of important precursors for the origin of life. A growing number of known exoplanets with a large, diverse range of atmospheres provides new opportunities to explore the effects of these high-energy processes on the chemistry of planetary atmospheres.

By combining X-ray & UV observations of the host star with 3D climate simulations, we study the effect of different types of high-energy radiation on the production of organic and prebiotic molecules in the atmosphere of the hot Jupiter HD 189733 b. We identify 'fingerprint' ions for the ionization of the atmosphere by both galactic cosmic rays and stellar energetic particles and find an enhancing effect on the abundance of key organic molecules that are potentially detectable by *JWST*.

In addition to these types of external high-energy radiation, lightning provides another energy source from within a cloudy atmosphere when charged particles are separated to build up an electric field strong enough for a discharge to develop. Lightning has been suggested to play a role in triggering the occurrence of bio-ready chemical species and nutrients for Earth's earliest biosphere. We present results from spark discharge experiments in gas mixtures resembling the atmospheres of modern and early Earth. They suggest that lightning-driven nitrogen fixation may have been efficient on early Earth, but measurements of the isotopic composition of the discharge products do not agree with isotope ratios from the sedimentary rock record, which supports the early development of biological nitrogen fixation.

By combining our experimental results with photochemical simulations, we can investigate the effect of lightning on the atmospheric chemistry of terrestrial exoplanets. We find that lightning may be able to mask the ozone features of an oxygen-rich, biotic atmosphere, making it harder to detect the biosphere of such a planet. Similarly, lightning can reduce the concentration of ozone in the anoxic, abiotic atmosphere of a planet orbiting a late M dwarf, thereby reducing the potential for a false-positive life-detection. In summary, the work presented in this thesis provides new constraints for the full characterisation of atmospheric and surface processes on exoplanets and for the interpretation of observations of their atmospheres.

Acknowledgements

General acknowledgements

During the last nearly four years that I've worked on this project (during which I moved a few times across Europe and lived through a global pandemic), I could count on the support of a wonderful group of people without whom this thesis would not have been possible. I want to use this opportunity to look back and thank a few people:

First, I want to thank my supervisors Christiane Helling and Eva Stüeken, who continually supported me during my time in the lab, when writing papers, in the search for career opportunities, and much more, and Martin Dominik for his support on the final stretch. I also want to thank Ludmila Carone who, ever since she supervised me during my Master's at the Max Plank Institute for Astronomy in Heidelberg, has been a close collaborator, mentor and friend, and Rory Barnes for his support and guidance during my time at the University of Washington and beyond. During this project, I worked with great collaborators whom I want to thank for their support along the way: Paul Rimmer, who helped me during many zoom calls to understand and use his chemical model; Wendell Walters, who helped me with analysing and interpreting our nitrogen samples; and Eddie Schwieterman, who in seemingly infinite iterations deployed his photochemical model to investigate lightning chemistry on exoplanets with me. Finally, I want to thank "our" students Lukas Rossmanith and Yuqian Peng who have worked with us in the lab and provided important contributions to the project.

A really exciting part of my time in Graz was our participation in the Mobile Pavilion of the Steiermark Schau 2023. I want to thank Astrid Kury and Birgit Prack for giving us the opportunity to be part of this endeavour, Christiane Helling for entrusting me with the coordination of this project at the Space Research Institute (IWF), and Alexandra Scherr for her support during this time. Further, I'm very grateful that Markus Jeschaunig, one of the artists who participated in the Mobile Pavilion, allowed me to include excerpts of his work 'Electric Atmospheres' in this thesis.

I wouldn't have made it through those nearly four years without a great group of friends, both in St Andrews and later in Graz. First, I want to thank Dom and Oliver — the three of us were known as the 'holy trinity'. You made me feel very welcome from my first minute in

Scotland and we spent many long evenings together at the pub, at tastings, or playing skat, as well as going hillwalking in the highlands, and celebrating eurovision together. A special thanks also goes to Her Majesty, Cake Queen Kat, to Clara, Sandra, Till, and Johannes. Thank you for the baking sessions, pride marches, dinners, socially distant drinks in the cold, whisky tastings and so much more. From the Astro Suite, I want to thank Anna, Camilo, Elliot, Emma, Hin, James, Juan, Katy, Lewis, Sam, Steph, Suinan, Tatiana, Tom, and Yirui for a great time at the office, at the pub, and at bonfires on the beach, and for unforgettable football matches. I want to thank the Graz crew, Beatriz, David, Elena, Greta, Helena, Irene, J.P., Jayatee, Kundan, Nanna, Nidhi, Ruth, Sven, and Thorsten for the warm welcome to Graz, the advice on the best Backhendl places, snowy hikes through the mountains, post-colloquium drinks, and many more unforgettable moments.

For the time of my PhD, and my path before, I could always rely on the support of my family, in particular my parents Angelika and Rainer, my brother Christian, and my grandpa Lothar, for which I'm extremely grateful. Their support allowed me to pursue my passions, study abroad during my Master's, and when it came to starting my PhD, my parents moved me and my belongings multiple times across Europe.

Finally, I want to thank my partner Marc. When we met in late 2020 in Scotland, we were only allowed to meet each other on a cold beach on the North Sea. And less than two years later, I moved across the continent to Austria. But we made it! Throughout this time, you were always there for me: when I had something to celebrate, when I needed to release steam after setbacks in the lab, and everything in between. Thank you very much for always supporting me!

Funding

This work was supported by a St Leonard's Interdisciplinary Doctoral Scholarship at the University of St Andrews, with shared funding by St Leonard's College, the School of Physics & Astronomy, and the School of Earth & Environmental Sciences.

During the last ten months of the PhD, I have been a visiting PhD student at the Space Research Institute of the Austian Academy of Sciences, which provided further support during this period.

This work was further supported by a Royal Society research grant [RGS\R1\211184] and a NERC Frontiers grant [NE/V010824/1], both awarded to Eva E. Stüeken.

Research Data/Digital Outputs access statement

Research data underpinning this thesis are available at https://doi.org/10.17630/3ec84770-07ab-4611-bba7-e0f2cd1eb4bb, https://doi.org/10.1093/mnras/staa3989, https://doi.org/10.5285/81dfa4de-5a47-479f-8de8-15e5ef398072, and https://doi.org/10.17630/8b72510f-62a8-43dc-94f1-af9b7766f817.

Contents

List of Figures

List of Tables

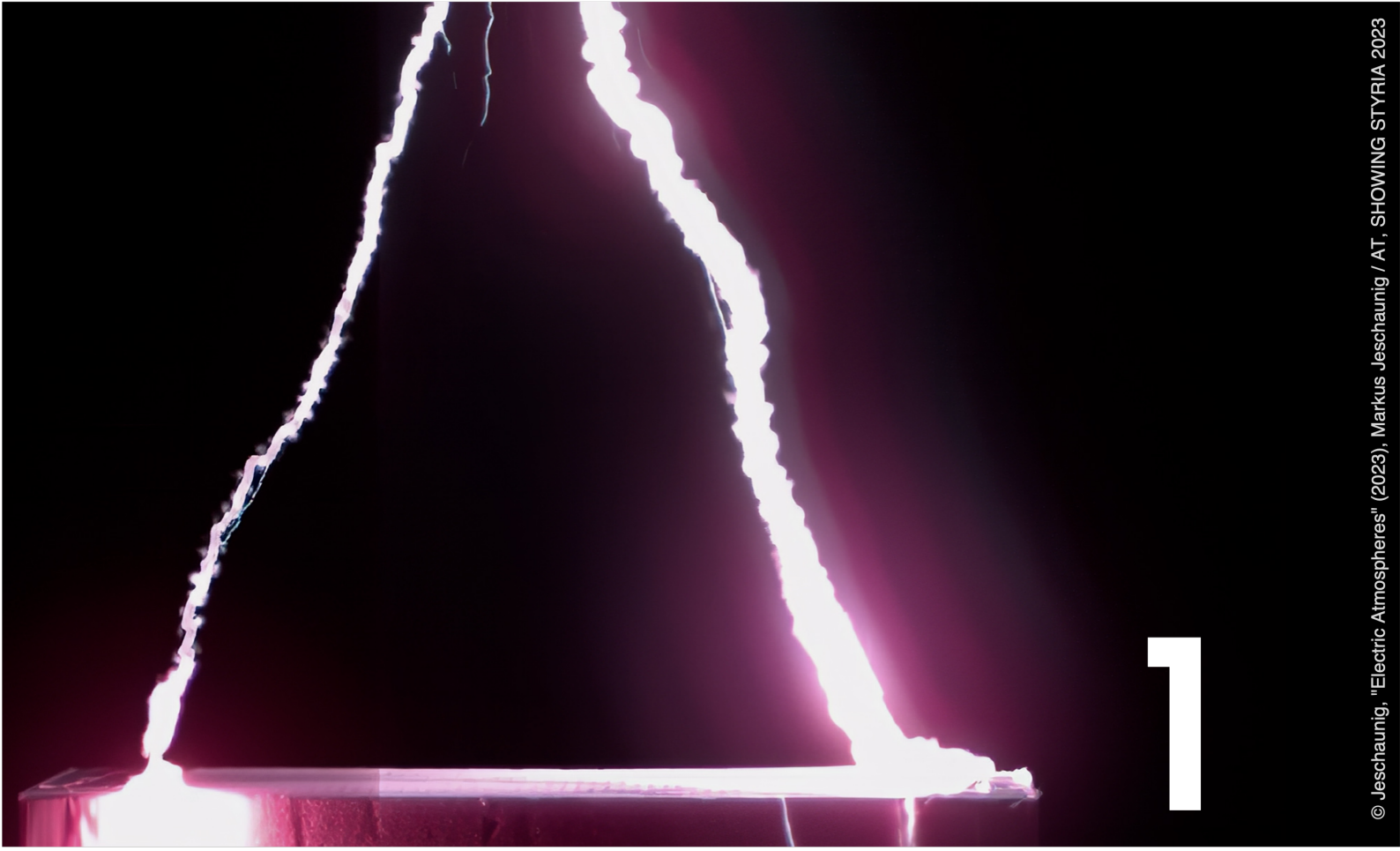

Introduction

Lightning is a fascinating and powerful phenomenon. It has the potential to significantly influence the chemistry in the surrounding atmosphere, and it has been hypothesised to have played an important role in the origin of life on Earth and the subsequent delivery of nutrients to the earliest forms of life. Lightning has also been observed on most of the planets in our Solar System, and thus it is critical to determine if lightning occurs on planets outside our Solar System as well, the consequences it has for the chemistry on those planets, and how we can detect this activity.

This thesis sets out to examine those questions, and the following sections will provide an introduction into the topics and methods relevant for the work presented here. First, the diversity of exoplanets and their atmospheres will be discussed, including how we can observe these atmospheres and what their composition can tell us about the presence of life on these exoplanets (Section 1.1). We then turn our focus to Earth and its atmosphere, including how

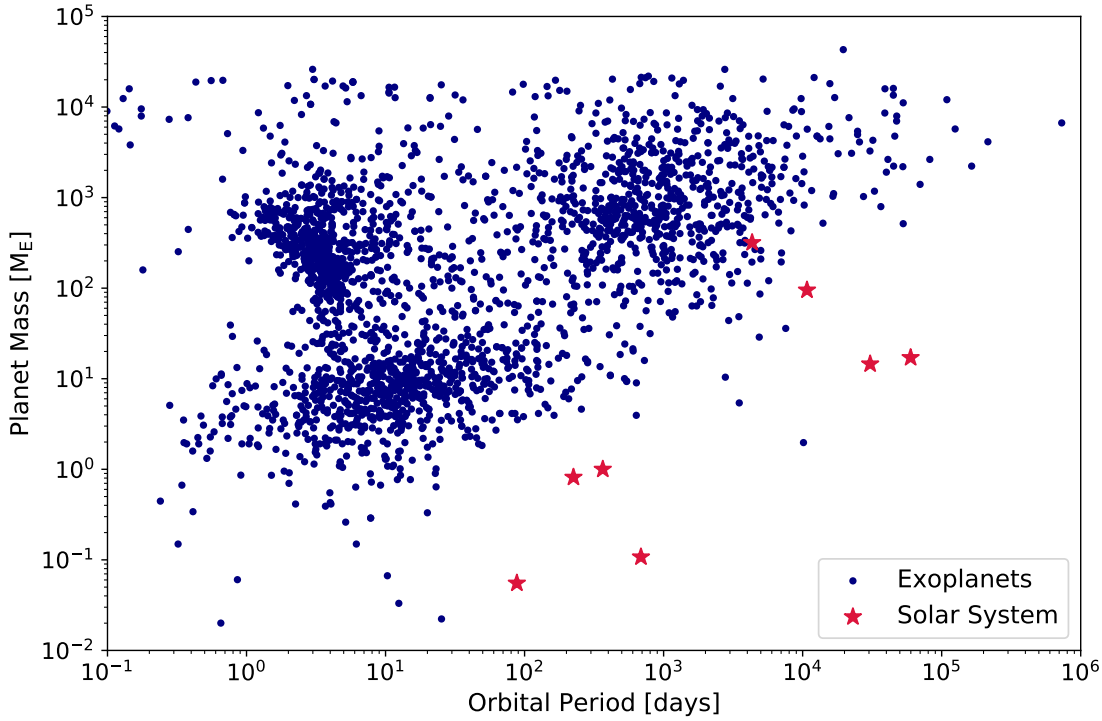

Figure 1.1: Mass (in Earth masses) vs. orbital period (in days) for detected exoplanets (*blue*) and Solar System planets (*red stars*). Some masses are only lower limits ($M \sin i$, i: inclination of orbital plain compared to line of sight). Data from exoplanet.eu, accessed 21.2.23.

it has changed over time, what we know about the origin of life, and how we can use nitrogen isotopes to track the nitrogen cycle through time (Section 1.2). This is followed by an introduction into the physics of lightning and what we know about lightning activity on Earth, in the Solar System, and beyond (Section 1.3). The chapter is concluded by an overview of the thesis (Section 1.4).

1.1 Atmospheres of Exoplanets

1.1.1 Diversity of Exoplanets

Nearly 28 years ago, Pegasi 51 b, the first exoplanet — a planet outside of our Solar System — around a Sun-like star was discovered (Mayor & Queloz, 1995). In the nearly three decades since, more than 5400 exoplanets have been detected[†] using a wide range of detection methods and observatories. About 50% of these planets were detected by the Kepler telescope alone (Borucki et al., 2010) and in recent years, the *Transiting Exoplanet Survey Satellite* (*TESS*; Ricker et al., 2014) has detected large numbers of exoplanets. These planets show a huge va-

[†]http://exoplanet.eu, accessed 15.06.23

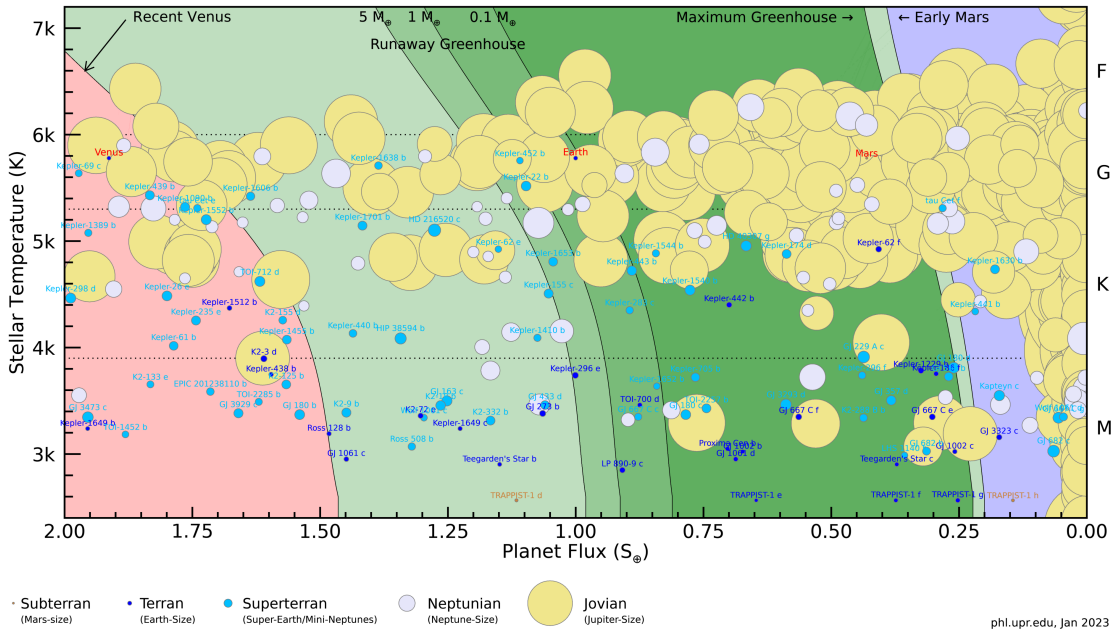

Figure 1.2: Stellar effective temperature against stellar flux at the planet's orbit for exoplanets orbiting in their host star's habitable zone. The location of the habitable zone is shown in green, the conservative habitable zone (inner edge 'runaway greenhouse') in dark green is dependent on the planet's mass. Different sized planets are shown with different symbols. From PHL @ UPR Arecibo, accessed 24.5.23.

riety in mass, radius, density, and the environment they experience in the radiation field of their host star (Fig. 1.1). Some are very similar to the planets in our Solar System: cold gas giants like Jupiter and Saturn, ice giants like Uranus and Neptune, and also Earth-sized planets. But many exoplanets are very different than what we can find in our own system: Hot and ultra-hot Jupiters, gas giants that orbit extremely close to their host star such that they can have atmospheric temperatures of more than 2200 K (Parmentier et al., 2018); Lava worlds like 55 Cancri e, Earth-sized planets with molten surfaces because they orbit in close proximity to their host stars (Demory et al., 2016); and super-Earths or mini-Neptunes like GJ 1214 b (Charbonneau et al., 2009), planets with masses between those of Earth and Neptune which we cannot find in our own Solar System and which might contain oceans thousands of kilometres thick or dense hydrogen-helium atmospheres. These exoplanets orbit around various kinds of host stars with different temperatures, spectral energy distributions, and activity. In particular, many exoplanets have been found orbiting cool M dwarfs. This type of star is the most common in our neighbourhood, and the low luminosity and smaller size make it easier to detect their planets.

From our perspective, in the context of habitability and extraterrestrial life, we are especially interested in Earth-sized planets that orbit their host star in the so-called 'habitable

zone': the range of orbital distances to the star, where the stellar radiation can heat the surface of the planet in such a way that liquid water is stable. However, this requires the presence of the right kind of atmosphere. The inner edge of the habitable zone can be defined as the 'moist-greenhouse' limit, where the effective stellar flux is $S_{\text{eff}} = F_{\text{OLR}}/F_{\text{ASR}} = 1.015$[†] and the surface temperature of an Earth-like planet reaches 340 K (in the Solar System this limit is at a distance of 0.99 au from the Sun) and the water vapour content of the atmosphere increases dramatically, allowing for efficient diffusion-limited escape (Kopparapu et al., 2013). A less conservative definition of the inner edge of the habitable zone is the 'runaway greenhouse' limit at $S_{\text{eff}} = 1.06$ where the entire ocean evaporates. In the Solar System this limit is at 0.97 au. The location of the inner edge depends on the mass of the planet, assuming that the atmospheric density scales with the planetary radius. For more massive planets the inner edge of the habitable zone is closer to the star than for lower mass planets as the higher gravity reduces the scale height and thus the escape rate at the top of the atmosphere (Kopparapu et al., 2014). A planet in the outer regions of the habitable zone needs an increased concentration of CO_2 to keep the surface temperate, but at too high CO_2 partial pressures, increased Rayleigh scattering cools the planet. The 'maximum greenhouse' limit is where a planet with approximately 8 bar of atmospheric CO_2 receives 32.5% of stellar radiation (compared to Earth), which for our Solar System is at 1.70 au (Kopparapu et al., 2013).

Figure 1.2 shows the location of the habitable zone for a range of stellar temperatures and the exoplanets that have been detected in this region. There are currently 16 exoplanets falling within the 'runaway greenhouse' limit habitable zone that are very likely to have a rocky composition and could support liquid surface water, with masses between 0.1 and 3 Earth masses and radii between 0.5 and 1.6 Earth radii. Most of these potentially habitable planets are orbiting M dwarfs. This comes with additional challenges (e.g., Childs et al., 2022): As the star is cooler and less luminous, the habitable zone is located much closer to the star than it is in the Solar System. This leads to much stronger tidal interactions between the star and the planet, i.e. the star slows the rotation of the planet until the rotation period matches the orbital period, a state that is called "tidally locked" (Kasting et al., 1993; Barnes, 2017). Just as the Moon shows the same side to Earth at all times, such a planet shows the same side to its host star. Unless a thick atmosphere with strong equatorial jets or strong ocean currents efficiently distributes the heat throughout the atmosphere, the planet will experience a heated day side

[†]OLR = Outgoing Longwave Radiation, ASR = Absorbed Stellar Radiation

and a significantly cooler, potentially frozen night side, which will complicate the prospects of life on such a planet (e.g., Kite et al., 2011; Hu & Yang, 2014; Checlair et al., 2019; Boutle et al., 2020; Sergeev et al., 2020). Further, M dwarfs are very active stars, in particular during their pre main sequence phase which is significantly longer than for a high-mass star (Reid & Hawley, 2006; Pass et al., 2023). During this time, the stellar X-ray and far UV radiation (XUV) is much higher than at a later stage of the planets evolution (Ribas et al., 2005). This XUV radiation slowly erodes any atmosphere that a planet in the star's habitable zone might have (Hilton et al., 2010; Lammer et al., 2011; Davenport et al., 2012), potentially removing all its water content from the planet (Luger & Barnes, 2015; Bolmont et al., 2016). Furthermore, even after the star enters the main sequence, M dwarfs produce more stellar flares that are accompanied by bursts of charged particles that will erode the planet's atmosphere (e.g., Segura et al., 2010; Fraschetti et al., 2019; Scheucher et al., 2020). A planetary magnetic field can protect the atmosphere from erosion by charged particles (Segura et al., 2010; Kay et al., 2016) and a magma ocean on the surface of the planet during its early evolution can help protect volatiles from erosion during the star's pre-main sequence phase (e.g., Barth et al., 2021a; Dorn & Lichtenberg, 2021; Bower et al., 2022).

1.1.2 Diversity of Atmospheres

The atmospheres of the exoplanets we have found are as varied as the exoplanets themselves. All planets initially form a hydrogen-helium envelope during formation in the protoplanetary disk. Whether they can keep this envelope after the gas disk dissipates depends on the mass of the planet, its distance to the host star, and the activity of the star. Figure 1.3, taken from Lichtenberg et al. (2022), is showing an overview of the atmospheric composition of exoplanets. If a planet is massive enough or far enough away from the host star, it can keep its primordial H/He atmosphere and become a gas or ice giant like the planets in the outer Solar System. These planets will occupy the upper, light blue region of Fig. 1.3. Earth-sized planets can usually not retain their primordial atmosphere. The surface gravity of these planets is too low to resist the forces of the stellar radiation and winds as well as impacts eroding their atmospheres. In their later evolution, terrestrial planets can outgas volatiles from their interior to form a secondary atmosphere which will be composed of gases with a higher molar mass than hydrogen or helium, such as H_2O, CO_2, or N_2. The exact composition of the outgassed volatiles will depend on the composition and redox state of the mantle (Deng et al., 2020; Ortenzi et al., 2020;

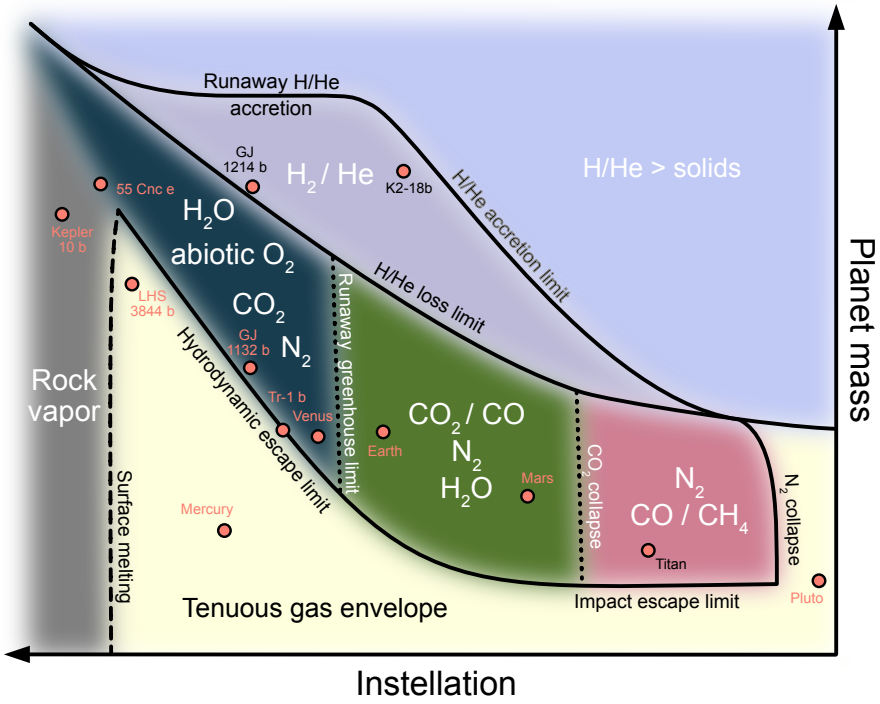

Figure 1.3: Atmospheric regimes for exoplanets with different mass and instellation. The dominating atmospheric constituents for each regime are given, the individual composition of an atmosphere depends on more factors than planet mass and instellation (see text). Black lines show the limits of specific regimes and the processes responsible for this limit. The range of planetary masses represented in this plot covers planets smaller than Earth to super Earths and mini Neptunes. Gas giants would populate the light blue region if the axis was extended upwards. Individual exoplanets shown for reference. Taken from Lichtenberg et al. (2022).

Lichtenberg, 2021). The composition and stability of these secondary atmospheres depends again on the mass of the planet and the distance from the star. Planets within in the 'runaway greenhouse' limit will find all their oceans evaporating (Kopparapu et al., 2013) while ongoing photodissociation of H_2O and subsequent escape of hydrogen can build up large amounts of abiotically produced O_2 in these atmospheres (Luger & Barnes, 2015). Further out, more temperate or even colder climates exist, with liquid water or water ice on the surface and an atmosphere of CO_2 and N_2. The composition will eventually depend on geological processes, which determine the efficiency of the carbon cycle (volcanism, plate tectonics, etc.), and the presence of life, which will determine the concentration of O_2, CH_4, and other biologically produced gases as well as N_2 (Sproß et al., 2021). Even further away from the star, temperatures will be low enough for CO_2 to condense, leaving N_2 as the only stable abundant species like in the atmosphere of Saturn's moon Titan (Forget & Leconte, 2014). Terrestrial planets extremely close to their host star might experience melting of the surface and can have an atmosphere of vaporised rock as suggested for K2-141 b (Nguyen et al., 2020).

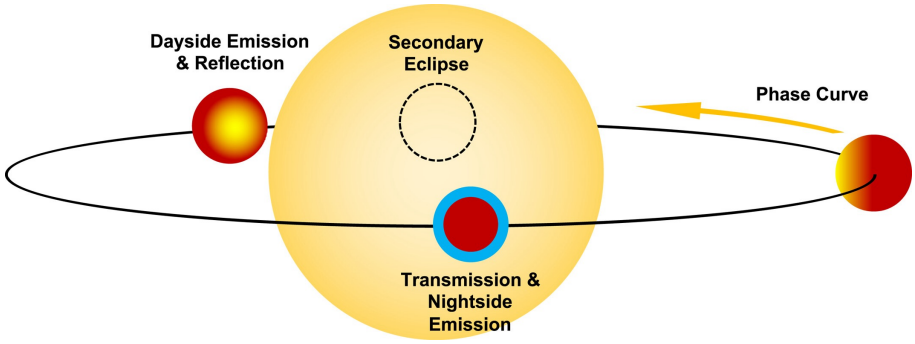

Figure 1.4: Position of an exoplanet in the orbit around the host star for the different observational methods. Transmission spectroscopy is performed when the planet is in transit, covering parts of the stellar light. Emitted and reflected light from the planet are observed just before or after the planet passes behind the star during the secondary eclipse. Taken from Gao et al. (2021), licensed under CC BY-NC 4.0.

Even within a specific region in the parameter space in Fig. 1.3, the composition of an individual atmosphere depends on many different parameters, such as the metallicity of the host star. The position where the planet formed in the protoplanetary disk determines the C/O ratio, for example whether it formed inside or outside the water snowline (Madhusudhan, 2012; Helling et al., 2014; Cridland et al., 2016; Mordasini et al., 2016). Varying the C/O ratio can change the abundance of important, potentially observable carbon molecules such as HCN, CH_4, and C_2H_2 (e.g., Madhusudhan, 2012). The presence of clouds will remove certain elements and molecules from the gas phase, like H_2O in Earth's atmosphere or sulphur in the atmosphere of Uranus (Hueso & Sánchez-Lavega, 2019; Fletcher, 2022). Eventually, the gas temperature and pressure determine which molecules are stable at a certain level in the atmosphere. On top of that, internal processes, like transport of molecules (by diffusion or winds) or lightning, and external energetic processes, such as stellar UV radiation, charged particles, or impacts, can change the composition of an atmosphere locally or globally. Some of these processes will be discussed in more detail in Chapter 2.

1.1.3 Observing Exoplanet Atmospheres

The nature and composition of exoplanetary atmospheres as well as the presence of clouds can be analysed with spectroscopic methods by splitting up the light we receive from the star and the planet into its wavelengths. Different methods can probe different regions of the atmosphere, at different points during the planet's orbit, and for different wavelength ranges, as shown in Fig. 1.4:

- **Transmission Spectroscopy:**

  This method can be used if the planet passes in front of its host star through the observer's line of sight. The planet blocks part of the light from the star causing a reduction in brightness which can then be used to detect that a planet does indeed exist there. Depending on the composition of the atmosphere, light at certain wavelengths can pass deeper through the atmosphere without being absorbed, but light at other wavelengths will be absorbed at much higher levels of the atmosphere. This will make the planet look smaller or larger, respectively, at those wavelengths. The transit depth at a certain wavelength λ is given by the ratio of the flux during and out of transit (Brown, 2001; Seager, 2010):

  $$\frac{F_{\text{in}}(\lambda)}{F_{\text{out}}(\lambda)} = 1 - \left(\frac{R_{\text{p}}(\lambda)}{R_*}\right)^2. \tag{1.1}$$

  Since the light detected with this method is probing the edge of the planet's disk, this method provides information about the planet's morning and evening terminators. Further, many of the planets that are being observed are tidally locked to their host star in which case the terminators are fixed places rather than changing like on Earth (Lacy & Burrows, 2020).

- **Emission and Reflected Light:**

  Emitted and scattered light from the planet are observed when the planet is close to its secondary eclipse, where it will disappear behind the star. By comparing the observed flux from the system during the secondary eclipse and just before or after the planet moves behind the star, it is possible to calculate the contribution of flux from the planet. With this method, the emission from the planet's dayside is observed with most contribution from the region around the substellar point, the point at the equator closest to the star. The ratio of the planetary to stellar flux is given by

  $$\frac{F_{\text{p}}(\lambda)}{F_*(\lambda)} = \left(\frac{R_{\text{p}}(\lambda)}{R_*}\right)^2 \frac{B(\lambda, T_{\text{p,eff}})}{B(\lambda, T_{*,\text{eff}})}, \tag{1.2}$$

  where $B(\lambda, T_{i,\text{eff}})$ is the black body radiation of a body i with an effective temperature $T_{i,\text{eff}}$ (Alonso, 2018). The flux emitted by the planet at a specific wavelength is given by the effective temperature of the atmosphere at the depth where it becomes optically thick at that wavelength. At wavelengths where abundant constituents in the atmosphere absorb light, the observer can only probe higher levels in the atmosphere which are

usually cooler than deeper layers (if no temperature inversion is present). The reflected light flux ratio for a planet with orbital distance a to its host star is given by

$$\frac{F_\mathrm{p}(\lambda)}{F_*(\lambda)} = \left(\frac{R_\mathrm{p}(\lambda)}{a}\right)^2 A_g(\lambda), \tag{1.3}$$

where $A_g(\lambda)$ is the geometric albedo which measures the reflected light at wavelength λ in comparison to a 'Lambertian disk' observed face on (Charbonneau et al., 1999; Seager, 2010). Reflected stellar light dominates at shorter wavelengths (UV and visible) where the emitted light from the planet is low while emitted light from the planet is strongest in the infrared. The exact contributions of reflected and emitted light depend on the effective temperatures of both the planet and the host star (Krenn et al., 2023).

With retrieval techniques and complex forward models, it is possible to infer the composition and properties of the atmosphere from these spectra (e.g., Madhusudhan & Seager, 2009; Lee et al., 2012; Hu, 2019; Lee et al., 2019; Taylor et al., 2020; Saxena et al., 2021; Ardévol Martínez et al., 2022). In Chapter 3.4.3, we simulate spectra for these three methods to investigate if lightning has an observable impact on the atmospheric chemistry of terrestrial exoplanets.

1.1.4 Looking for Biosignatures

In December 2021, *JWST* was launched which, for the first time, provides opportunities to perform detailed observations of the atmospheric composition of potentially habitable exoplanets. In order to interpret these observations, so-called 'biosignatures' have been postulated. Biosignatures are gases or other planetary features that — singly or in combination — are potentially indicative of life. In this section, we will take a look at potential biosignatures and antibiosignatures that we will later discuss in the context of lightning in exoplanet atmospheres (Chapter 3.4).

The most abundant biologically produced gas on modern Earth and therefore prime candidate for a biosignature is O_2 and its byproduct ozone O_3 which is more easily detectable with a prominent absorption feature at 9.6 µm while O_2 only has weak absorption features in the MIR within the 6.3 µm water band (Segura et al., 2003; Meadows et al., 2018). However, the relationship between the abundances of oxygen and ozone is not linear, and thus the ozone concentration depends strongly on the UV radiation from the host star (Kozakis et al., 2022;

Shapiro et al., 2023). On modern Earth, O_2 is produced by photosynthesis, but in other circumstances, large amounts of O_2 can be produced abiotically, for example when a rocky planet around an M dwarf loses a large part of its water inventory during the early, active phase of its host star. Since hydrogen is lighter and therefore lost more easily via hydrodynamic escape than oxygen, hundreds of bars of O_2 can build up on these planets (Luger et al., 2015; Meadows, 2017; Johnstone, 2020; Barth et al., 2021a). Planets with a significant overabundance of O_2 due to massive H escape could be identified by a lack of water features (in the case of complete desiccation) or O_2-O_2 collisionally-induced absorption features indicative of O_2 abundances too large to be biologically produced (Misra et al., 2014; Harman et al., 2015; Schwieterman et al., 2016). Nevertheless, there are further abiotic sources of O_2 that could imitate a biosignature, particularly on planets orbiting M dwarfs with a large atmospheric CO_2 concentration. The increased intensity of the XUV radiation can dissociate the CO_2 to produce CO and O, as we will discuss in Chapter 3.4. The recombination of CO and O is restricted by deficient NUV radiation from the M dwarf host star, which is key to generating photochemical catalysts that facilitate this reaction (the direct CO + O reaction is spin-forbidden), potentially producing a false positive O_2 biosignature (Segura et al., 2007; Harman et al., 2015). This scenario is particularly acute for atmospheres that lack radical precursors such as H_2O (Gao et al., 2015), though it has also been predicted for habitable, prebiotic planets with surface water oceans (Tian et al., 2014; Domagal-Goldman et al., 2014; Hu et al., 2020). The latter scenario is more destructive than the first, due to the co-occurrence of water vapor. Harman et al. (2018) suggest that lightning-produced NO might act as a catalyst to prevent the buildup of O_2 in such an atmosphere. We will discuss this possibility in Chapter 3.4. In any case, using just one gas like O_2 might not be a reliable biosignature. It is therefore necessary to look at the combination of several gases rather than just individual signatures, for example O_2 in combination with CH_4 (Lovelock et al., 1975; Sagan et al., 1993), which in equilibrium would react to CO_2 and H_2O (Segura et al., 2005).

Wogan & Catling (2020) discuss the potential of chemical disequilibria as biosignatures: only an 'inedible' disequilibrium, where a high activation energy is needed to move the system to equilibrium, can be considered a biosignature. This means, life forms on the planet cannot easily access the energy stored in this disequilibrium. If the required activation energy is very low, the presence of such an 'edible' disequilibrium cannot be considered as a biosignature, as life forms would have likely moved the system into equilibrium. Krissansen-Totton et al.

(2018b; 2019) suggest the combination of CO_2 and CH_4, which was present in the Archean atmosphere, as such an 'inedible' disequilibrium biosignature. This biosignature would be strengthened by the absence of CO (see below). However, Woitke et al. (2021) have shown that under certain conditions, CO_2 and CH_4 can both be present in chemical equilibrium. In their so-called 'Type C atmospheres', a temperate planet with a surface temperature of $T \sim 350\,\mathrm{K}$ can have an atmosphere containing a few percent of CO_2, with large amounts of CH_4, H_2O, and N_2, but no H_2, O_2, or CO. While stellar XUV radiation and outgassing processes will affect the stability of such an atmosphere, the possibility of this equilibrium at least for a short time period can lead to a false-positive biosignature detection. Similarly, impacts of reduced material from the remnants of the protoplanetary disk can generate a transient, reduced atmosphere during the planet's early evolution where abiotic CH_4 and CO_2 could exist simultaneously (Zahnle et al., 2020). Another disequilibrium that has been suggested as a biosignature is the combination of N_2 and O_2, i.e. modern Earth's atmosphere, as this gas mixture would not be stable on geological timescales without the constant production of both O_2 and N_2 by life (Stüeken et al., 2016a; Krissansen-Totton et al., 2018b; Lammer et al., 2019; Sproß et al., 2021). Without the presence of life, nitrogen would be removed from the atmosphere as abiotic fixation could not be matched by volcanic outgassing rates without the presence of anaerobic ammonium oxidation ('anammox') or 'denitrification' (Section 1.2.3; Lammer et al., 2019).

Nitrous oxide (N_2O) has been stipulated as another potential biosignature (Rauer et al., 2011; Grenfell, 2017; Schwieterman et al., 2022). In Earth's spectral energy distribution, N_2O produces detectable peaks in the near and mid infrared (Sagan et al., 1993; Gordon et al., 2022). Further, N_2O in Earth's atmosphere is mainly from biological origin and there are only few abiotic sources. Mainly, stellar radiation or lightning can photochemically produce NO, which in an anoxic and weakly reducing atmosphere can undergo further reactions to produce N_2O. To distinguish biotically from abiotically produced N_2O, spectral discriminants can be used, such as HCN and NO_2, which are abiotically produced together with the N_2O (Airapetian et al., 2016, 2020; Schwieterman et al., 2022). N_2O is an intermediate step of the biological nitrogen cycle and is produced during partial denitrification of nitrate (NO_3^-) in the ocean. If the availability of copper catalysts in the ocean is limited, the final step of denitrification to N_2 is inhibited, and larger concentrations of N_2O can build up, as was suggested for the Protero-

zoic Eon ($\sim 2.5 - 0.54$ Ga, Buick, 2007)[†]. Schwieterman et al. (2022) used photochemical simulations to study the lifetime and concentration of N_2O in the atmospheres of different Earth-like planets orbiting different stars in their habitable zone. The major sink of N_2O in the atmosphere is photolysis ($N_2O + h\nu(\lambda < 240\,\text{nm}) \longrightarrow N_2 + O(^1D)$) which is particularly efficient for UV-radiation with $\lambda < 200$ nm. If present in the atmosphere, O_2 via the Schumann-Runge bands ($175-195$ nm) — and, to a lesser extent, O_3 via the Hartley band ($200-310$ nm) — provide a shielding effect and protect the N_2O from photolysis. Oxygen-rich atmospheres will therefore have a higher N_2O concentration (at the same N_2O production) than anoxic atmospheres. A secondary photochemical sink for N_2O is the reaction with the $O(^1D)$ radical: $N_2O + O(^1D) \longrightarrow N_2 + O_2$ or $N_2O + O(^1D) \longrightarrow NO + NO$. The source of $O(^1D)$ is either photolysis of N_2O (as described above) or ozone ($O_3 + h\nu(\lambda < 330\,\text{nm}) \longrightarrow O_2 + O(^1D)$). However, the production of $O(^1D)$ from ozone is dependent on a very narrow band of NUV photons, strongly limiting the efficiency of this pathway for planets around late-type stars. Photolysis is the main N_2O destruction pathway for all types of stars, but especially important for solar-like stars, as well as M dwarfs due to increased magnetic activity enhancing the star's FUV radiation beyond its pre-main sequence phase. In addition, N_2O loss via $O(^1D)$ is most efficient for solar-like stars while less important for K dwarfs and even smaller for M dwarfs. Combined, this puts planets around K dwarfs into a sweet spot for N_2O lifetime (Schwieterman et al., 2022). In combination with NH_3, N_2O has also been proposed as a technosignature, confirming the presence of agriculture on the planet's surface (given an oxic atmosphere, Haqq-Misra et al., 2022).

In contrast to a false-positive biosignature, where life can still be present on a planet, an antibiosignature suggests the planet is not inhabited. However, the surface conditions might still be habitable. An antibiosignature is usually defined as the evidence for free energy not being exploited by life (Schwieterman et al., 2019). CO provides a source of chemical free energy and reduced carbon to life in metabolisms such as the Wood-Ljungdahl pathway (Ragsdale, 2004) and has been suggested as an antibiosignature for exoplanets (Wang et al., 2016) and its absence in combination with the presence of CO_2 and CH_4 as a biosignature (Krissansen-Totton et al., 2018b; Krissansen-totton et al., 2019). During the early Archean several metabolisms governed the concentration of CO in early Earth's atmosphere (Kharecha et al., 2005): 'Methanogenesis', net reaction $CO_2 + 4\,H_2 \longrightarrow CH_4 + 2\,H_2O$, is a source of CO,

[†]Ga = giga years ago

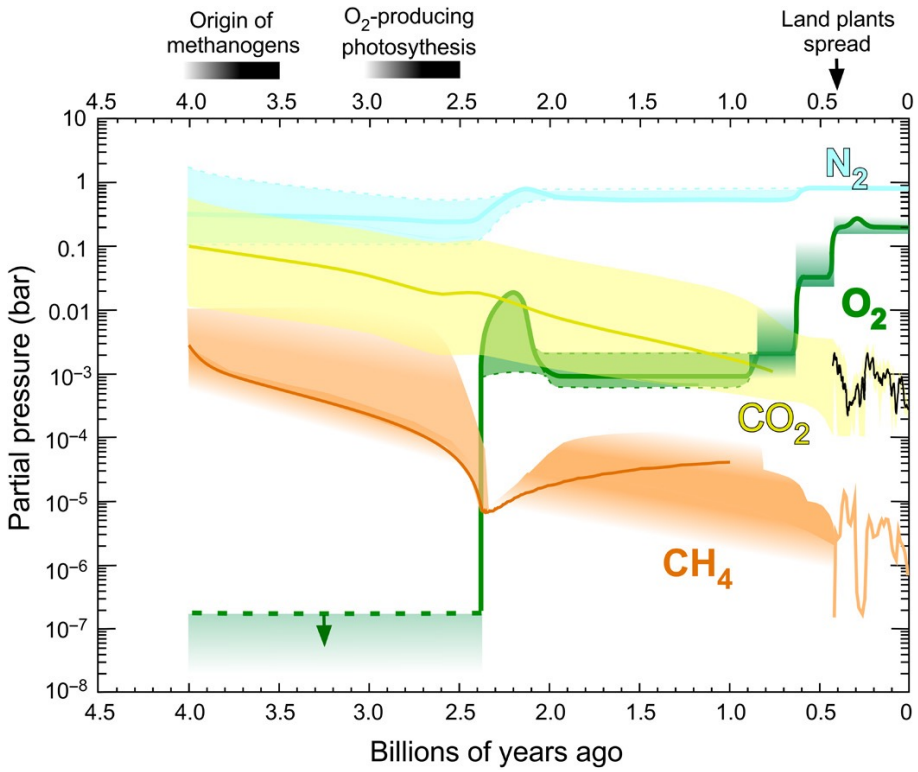

Figure 1.5: Possible evolution of the partial pressures of the main constituents of Earth's atmosphere over geologic time, with uncertainties. The total atmospheric pressure and N_2 partial pressure were probably lower during the Archean than today, the CO_2 partial pressure significantly higher. The CO_2 concentration decreased due to the geological carbon cycle, the CH_4 concentration first decreased due to rise of oxygen but was later protected under the ozone layer. Detailed geological records for CO_2 and CH_4 exist for the last ~ 0.4 Gyr. Taken from Catling & Zahnle (2020), licensed under CC BY 4.0.

as the produced CH_4 will be photochemically oxidised to CO if irradiated by FUV radiation. 'Acetogenesis', net reaction $4\,CO + 2\,H_2O \longrightarrow 2\,CO_2 + CH_3COOH$, is a biological sink of CO that is limited by the rate at which CO is deposited in the ocean (= deposition velocity, assuming immediate consumption of CO by acetogens). 'H_2-based photosynthesis', net reaction $CO_2 + 2\,H_2 + h\nu \longrightarrow CH_2O + H_2O$, removes H_2 from the atmosphere. An additional CO source is the photolysis of atmospheric CO_2 ($CO_2 + h\nu \longrightarrow CO + O$), an additional sink is the oxidation of CO by hydroxyl radicals ($CO + OH \longrightarrow CO_2 + H$) which are mainly produced by the photolysis of water ($H_2O + h\nu(\lambda < 200\,\text{nm}) \longrightarrow OH + H$, for anoxic atmospheres) and other photochemical processes (Schwieterman et al., 2019).

1.2 Atmosphere of Earth

1.2.1 Early Earth's Atmosphere

The atmosphere of Earth has undergone several changes throughout its evolution. Most notably, the abundance of oxygen increased from basically nothing to about 21% today. Like other planets inside and outside our Solar System, Earth likely has started with an atmosphere of hydrogen and helium, accreted from the gas of the protoplanetary disk (Hayashi et al., 1979), but lost most of this atmosphere under the strong XUV radiation of the young Sun (Wood et al., 2002) and the impacts of large bodies, in particular the Moon-forming impact (Canup, 2004). This impact likely has left Earth with a molten mantle and an atmosphere of vaporized rock. Once silicate condensates had rained out, the atmosphere was dominated by volatiles outgassed from the magma ocean: H_2O, CO_2, CO, and H_2 (Zahnle, 2006). Eventually, Earth cooled down sufficiently for the silicate crust to solidify and the water vapour to condense and form the oceans. Detailed information on the atmospheric composition of Earth during the Hadean, the first eon of Earth's evolution ($4.567 - 4\,\mathrm{Ga}$), is limited by the absence of rocks from that period. The Hadean rock record is mainly limited to zircons, very stable crytals of zirconium silicate $ZrSiO_4$, found in the Jacks Hills of Western Australia. Oxygen isotope and lithium abundance analyses of $4.3 - 4.4\,\mathrm{Gyr}$ old zircons suggest that continents and oceans existed already very early in the Hadean (Mojzsis et al., 2001; Wilde et al., 2001; Ushikubo et al., 2008). A $4.1\,\mathrm{Gyr}$ old zircon contains graphite inclusions with an isotopic signature consistent with a biogenic origin ($\delta^{13}\mathrm{C} = -24‰$), providing potential evidence for the origin of life on Earth at least $4.1\,\mathrm{Ga}$ (Bell et al., 2015).

After the Hadean eon, the Archean eon describes the period of Earth's evolution before the rise of oxygen during the Great Oxidation Event $\sim 2.5\,\mathrm{Ga}$. It is assumed that during this period, the atmosphere of Earth was weakly reducing with low levels of H_2, CH_4, and CO in a background gas mixture of CO_2 and N_2 (Kasting, 1993). Constraints on the atmospheric composition, temperature, and pressure are given by so-called proxies: seafloor minerals, soil samples, isotopic signatures in sediments, or fluid inclusions (Catling & Zahnle, 2020). The atmospheric pressure during the late Archean can be constrained by $2.7\,\mathrm{Gyr}$ old raindrop imprints, suggesting a maximum pressure of $2.1\,\mathrm{bar}$, with a more probable upper limit between 0.52 and $1.2\,\mathrm{bar}$ (Som et al., 2012). This is further constrained by vesicle volumes in lava flows of the same age, suggesting an atmospheric pressure of $0.23 \pm 0.23\,\mathrm{bar}$ (Som et al.,

2016). Fluid inclusions in 3.5 to 3 Gyr old hydrothermal quartz suggest that the N_2 partial pressure at that time was below 1.1 bar, possibly even as low as 0.5 bar (Marty et al., 2013). Goldblatt et al. (2009) on the other hand argue that a nitrogen pressure in the Archean higher than today's was necessary to prevent Earth from freezing over, as the Sun's total luminosity was at about 75-82% of today's (the faint young Sun problem, Gough, 1981). They argue that a higher N_2 pressure would enhance the warming efficiency of greenhouse gases by pressure broadening of their spectral absorption lines. The CO_2 fraction in the Archean atmosphere can be constrained by simulating the stability of the atmosphere under the XUV radiation from the young, active Sun: The increased XUV radiation Earth received from the Sun during the Archean will have led to the heating and expansion of Earth's atmosphere (Tian et al., 2008, 2009; Kuramoto et al., 2013), increasing the escape rate to space (Lammer et al., 2008; Lichtenegger et al., 2010; Lammer et al., 2018). High abundances of CO_2 in the upper atmosphere can cool down the atmosphere instead, limiting the escape rate (Kulikov et al., 2007; Lichtenegger et al., 2010). Johnstone et al. (2021b) found that 3.8 Ga a CO_2 mixing ratio of at least 40% is necessary to prevent rapid escape of Earth's atmosphere. This amount of CO_2 would also be enough to prevent Earth from freezing over during the Archean without the need for a high N_2 background pressure.

1.2.2 The Origin of Life

This atmospheric setting builds the backdrop for the origin of life on Earth which happened during the early Archean. Graphite grains found in sedimentary rock in the Isua Supracrustal Belt in Western Greenland, which are at least 3.7 Gyr old, show morphologies that are consistent with an organic origin and are the oldest evidence of life on Earth (Rosing, 1999; Ohtomo et al., 2014). The aforementioned 4.1 Gyr old zircon found in the Jack Hills in Australia might be evidence for even older life on Earth (Bell et al., 2015). If this is indeed an evidence for the emergence of life, the origin of life on Earth happened only a few hundred Myr after the formation of the Solar System. However, this topic is still not fully understood, and several competing theories exist to try and explain the origin of life.

One of these theories is Charles Darwin's postulation of the 'Warm Little Pond' (Darwin, 1871): It is believed that early Earth was nearly completely covered by oceans. Only some volcanic islands extend above the ocean surface. At the shore of these islands one would find small ponds and tide pools. Lightning in the volcanic clouds above provide the energy

necessary to break the bonds of the molecular nitrogen. Simple prebiotic compounds like hydrogen cyanide (HCN) form and dissolve into the water of the pond. During dry and wet cycles, these molecules can concentrate and polymerize to longer, prebiotic molecules, such as amino acids and finally RNA (Bada & Korenaga, 2018).

Haldane (1929) and Oparin (1938) postulated that a strongly reducing atmosphere was necessary for the origin of life on Earth. A famous experiment supporting this theory is the Miller-Urey experiment, first conducted by Stanley Miller and Harold Urey in 1952 (Miller, 1953). One small flask of the setup was filled with water heated from below, the other larger (5 L) flask contained two electrodes, inserting sparks into the gas mixture. The gases were chosen to resemble early Earth's atmosphere, which was thought to be reducing, containing CH_4, NH_3, and H_2. The experiment ran for one week and produced several amino acids: glycine, α-alanine, and β-alanine. The identification of aspartic acid and α-amino-n-butric acid were less certain (Miller, 1953). Archived samples from a similar and previously unreported experiment, conducted by Stanley Miller in 1958, were discovered just before Miller's death in 2007 and reanalysed with modern high-performance liquid chromatography and time-of-flight mass spectrometry. Parker et al. (2011) were able to detect 23 amino acids and four amines in these samples.

As discussed earlier, however, early Earth's atmosphere was most likely not reducing as assumed by Miller and Urey but rather neutral or only weakly reducing. Miller-Urey experiments with less reducing gas mixtures have been conducted (e.g., Schlesinger & Miller, 1983; Miyakawa et al., 2002; Cleaves et al., 2008), but these experiments led to drastically reduced yields of organic compounds with glycine being the only amino acid produced (Folsome et al., 1981). A main problem is the limited formation of hydrogen cyanide (HCN) which is an important precursor for the synthesis of nucleobases (Ferris et al., 1978; Patel et al., 2015). This could suggest that synthesis of prebiotic molecules from the Archean atmosphere might have only been a minor contributor to the inventory of prebiotic organic compounds with alternative sources of organic compounds coming into focus, such as hydrothermal vents and the panspermia theory which states that the seeds of life were delivered to Earth (Arrhenius, 1908; Chyba & Sagan, 1992; Hoyle & Wickramasinghe, 2000; Cleaves et al., 2008). However, further experiments with non-reducing gas mixtures showed that buffering the solution with calcium carbonate ($CaCO_3$) to increase the pH of the solution and adding oxidation inhibitors such as ascorbic acid ($C_6H_8O_6$) or Fe^{2+} can increase the yields of amino acids by more than

100 times (Cleaves et al., 2008). This suggests that the composition of the Archean ocean might have been very important for the origin of life on Earth. The ocean during the Archean probably had a pH close to neutral and a higher concentration of carbonate than today (Morse & Mackenzie, 1998), as well as a significant concentration of Fe^{2+} (Summers & Chang, 1993; Summers, 1999).

Even though the atmosphere during the Archean was dominated by CO_2 and N_2 with only minor amounts of reducing gases, more reducing atmospheres might have existed locally or for short periods of time. For example impacts, which were much more common during the Hadean and early Archean than today, can produce short-lived, reducing atmospheres, providing the ingredients for the origin of life (Zahnle et al., 2020). A further possibility are locally limited atmospheres: Bada & Korenaga (2018) suggest that most or all land areas on the Hadean Earth were volcanic hotspot islands, harbouring lakes and tide pools which can serve as the little ponds from Darwin's theory. Since Earth's deep mantle is strongly reducing (Smith et al., 2016), it is likely that volcanic outgassing on early Earth was equally reducing. As we will discuss later, volcanic ash plumes are rich in lightning activity, making them ideal places for the production of prebiotic ingredients. Miller-Urey experiments performed with a combination of reduced gases and volcanic ash particles have indeed led to the formation of glycine (Scheu et al., 2017).

1.2.3 The Role of Nitrogen

Nitrogen is a key ingredient for life on Earth, likely for several reasons: it is, and was, abundantly available, it forms versatile bonds with carbon (in single, double, or triple bonds), and it is redox-active in the stability field of water and thus providing a source of electrochemical energy for biological metabolisms (Stüeken et al., 2016b). To understand the origin and evolution of life, it is therefore necessary to understand the evolution of nitrogen in Earth's atmosphere and the nitrogen cycle. The most abundant form of nitrogen at Earth's surface is atmospheric N_2 gas; however, this molecule is relatively inert, requiring dedicated nitrogenase enzymes or high energy to be converted into more bioavailable forms (nitrogen fixation). On modern Earth, more than 97% of pre-industrial N_2 fixation is carried out by microorganisms; only a few percent of fixed nitrogen are produced by abiotic sources, the main source being lightning (Postgate, 1998; Fowler et al., 2013). On early Earth, before the origin of life and the onset of biological N_2 fixation, these abiotic sources such as lightning

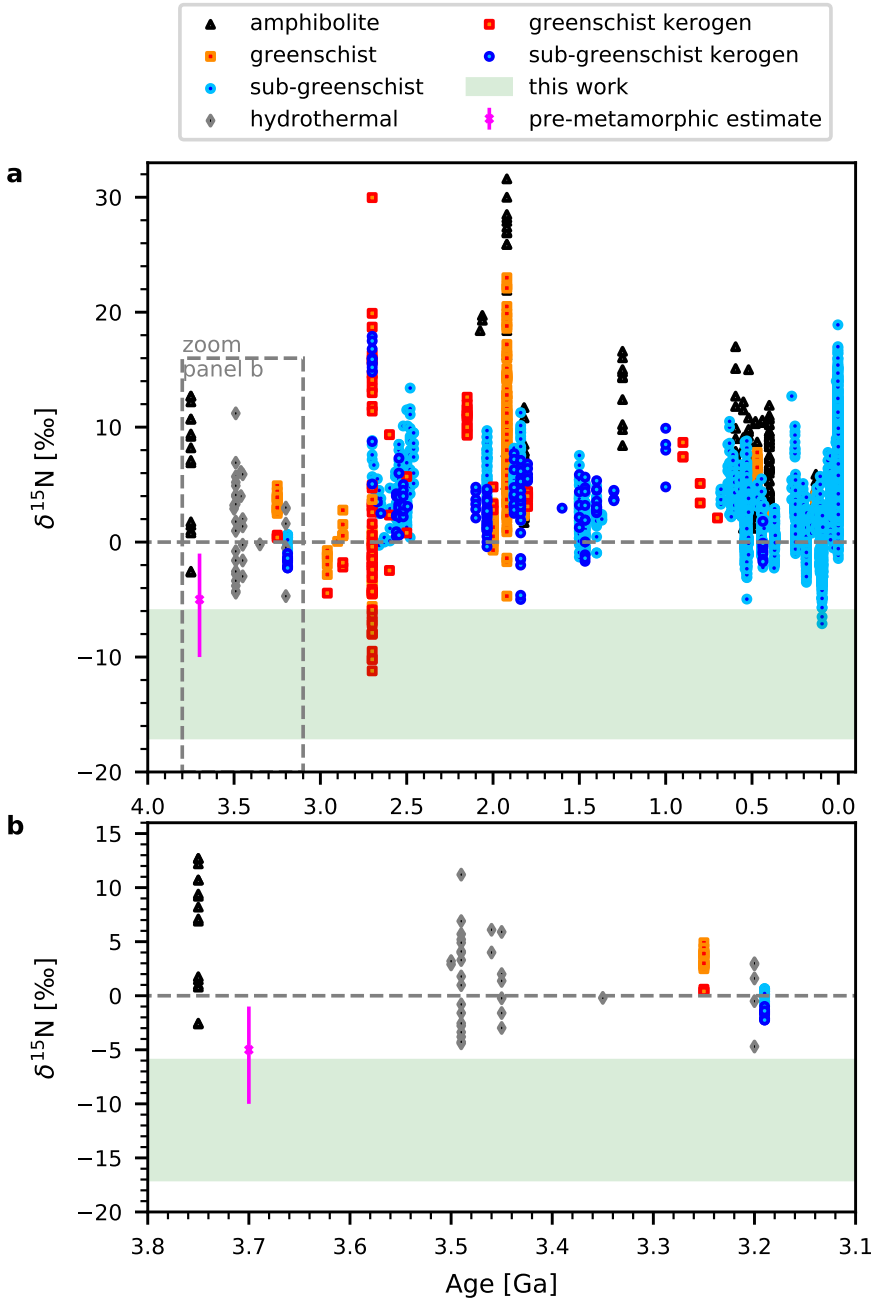

Figure 1.6: Measurements of δ^{15}N in sedimentary rocks over geologic time, separated by metamorphic grade. **a:** Data from Stüeken et al. (2016b, 2021) and Yang et al. (2019). Errors smaller than symbols. *Pink x:* pre-metamorphic estimate of 3.7 Ga old sample set (−5‰, values between −1 and −10‰ possible). Stüeken et al. (2021). Our results for the isotopic composition of nitrogen products in our spark experiments are indicated by green shading (see Chapter 3.3). **b:** Zoom into area indicated in panel a by grey box. First published in Barth et al. (2023a).

must have been the dominant producer of bioavailable nitrogen. Eventually, biological nitrogen fixation developed where microorganisms can reduce N_2 to NH_3. After cell death, the nitrogen is mineralized to NH_4^+ (e.g., Stüeken et al., 2016b; Zerkle & Mikhail, 2017). In the absence of chemical recycling pathways, which are still debated, the only way to return ni-

trogen to the atmosphere is by metamorphic and volcanic outgassing. If the outgassing rates were not higher than today, the partial pressure of N_2 may have decreased over time during the Archean (Stüeken et al., 2016a; Sproß et al., 2021). After the development of oxygenic photosynthesis and the rise of the oxygen abundance in Earth's atmosphere during the Great Oxidation Event (GOE, $\sim 2.5\,\mathrm{Ga}$) microorganisms used ammonium (NH_4^+) as a source of energy by oxidising it to nitrite (NO_2^-) and nitrate (NO_3^-), so-called 'nitrification' (net reaction: $NH_4^+ + 3H_2O \longrightarrow NO_3^- + 8e^- + 10H^+$, Stüeken et al., 2016b; Zerkle & Mikhail, 2017; Zerkle et al., 2017). New pathways to return nitrogen to the atmosphere developed: 'Denitrification', where nitrate is reduced to N_2 (net reaction: $2\,NO_3^- + 10e^- + 12H^+ \longrightarrow N_2 + 6\,H_2O$, Stüeken et al., 2016b), and anaerobic ammonium oxidation ('anammox'), where ammonium is oxidised with nitrite and converted to N_2 and water (net reaction: $NO_2^- + NH_4^+ \longrightarrow N_2 + 2H_2O$, Stüeken et al., 2016b). In both cases, the produced N_2 will be outgassed into the atmosphere, balancing biological and abiotic nitrogen fixation (Devol, 2003; Lammer et al., 2019).

It is possible to track the nitrogen cycle on Earth through time by studying the isotopic composition of nitrogen samples in sedimentary rocks. Nitrogen has two stable isotopes, ^{15}N and ^{14}N, with ^{14}N being far more abundant than ^{15}N. The standard, N_2 in modern Earth's atmosphere, shows a ratio of the two isotopes of $(^{15}N/^{14}N)_{\mathrm{standard}} = 3.676 \times 10^{-3}$ which is very close to the bulk ratio of nitrogen isotopes in chondrites that likely delivered Earth's volatile inventory (Füri & Marty, 2015). Isotope ratios of samples are measured in relation to this standard, using

$$\delta^{15}N = \left(\frac{(^{15}N/^{14}N)_{\mathrm{sample}}}{(^{15}N/^{14}N)_{\mathrm{standard}}} - 1 \right) \times 1000\,‰. \tag{1.4}$$

We know from measurements of fluid inclusions in hydrothermal quartz from $3.5 - 3\,\mathrm{Ga}$ that the isotopic composition of N_2 in early Earth's atmosphere was very similar to today's (within $\sim 2-3‰$, Marty et al., 2013), enabling us to compare nitrogen isotope samples from different ages.

Reactions involving nitrogen will change the isotopic composition of this nitrogen in a unique way, a process called isotope fractionation, mainly due to different physical and chemical properties of the isotopes because of their mass (Kendall & Caldwell, 1998). Depending on the nature of the individual reaction and the circumstances the reaction is taking place in, equilibrium or kinetic fractionation will take place. Equilibrium fractionation takes place in

closed, well-mixed systems and equilibrium reactions where the forward and backward reaction rates are identical for each isotope. As the mass of the isotope influences the strength of the individual bonds, equilibrium fractionation depends on the isotope mass. Kinetic isotope fractionation takes place in irreversible reactions and also depends on the ratios of the isotope masses as the mass of a molecule determines the velocity at which it travels at a given temperature. Rayleigh fractionation describes the process of partial fractionation, where ongoing reaction from the educt to the product changes the isotopic composition of both reservoirs (Kendall & Caldwell, 1998). An example for this is the relationship between water vapour and condensates in a cloud, where rain preferentially removes the heavier water molecules containing the oxygen isotope ^{18}O, rendering the isotopic composition of the vapour remaining in the cloud lighter with time, reducing the ratio of the oxygen isotopes ^{18}O to ^{16}O. Rayleigh fractionation can happen both in open and closed systems: In open systems, the product is removed from the system, like the rain water in the example of a cloud. In a closed system, the initial reservoir and the product remain in contact with each other. A system can only be described by Rayleigh fractionation if the individual fractionation between the educt and the product can be described by a constant factor that does not change during the fractionation process. In Chapter 3.3, we use Rayleigh fractionation to describe the isotope fractionation process in our spark experiments.

Figure 1.6 shows a compilation of nitrogen isotope measurements from sedimentary rocks from 3.8 Ga until today (Stüeken et al., 2016b, 2021; Yang et al., 2019). The different colours and symbols represent different metamorphic grades: rocks and minerals that have experienced similar pressure and temperature ranges. Rocks of greenschist facies, for example, have experienced relatively low pressures ($2-10$ kbar) and temperatures ($300-450^{\circ}$C) (Selverstone & Fyfe, 2023). These isotope ratios are likely to be within $1-2$‰ of the primary isotopic composition of the sample when it was deposited. Values around 0‰ and higher are generally associated with biological nitrogen fixation (Busigny et al., 2013; Zhang et al., 2014; Stüeken et al., 2016b; Zerkle & Mikhail, 2017; Zerkle et al., 2017; Stüeken et al., 2021). Rocks with higher metamorphic grades are not considered, because metamorphic alteration tends to volatilize N with a preference for ^{14}N over ^{15}N, leading to a significant deviation of the preserved sample from the original isotopic composition (Bebout & Fogel, 1992; Thomazo & Papineau, 2013). δ^{15}N values significantly below -5‰ have been documented from one site in the Neoarchean (Yang et al., 2019), interpreted as evidence of high ammonium availability.

In Chapter 3.3, we will compare the nitrogen isotope fractionation in our spark experiments to the values presented in the sedimentary rock record.

1.3 Atmospheric Discharges

1.3.1 Physics of Lightning

Lightning and other atmospheric discharge processes require an electrostatic potential difference and charged particles as seeds in order to develop (Rakov & Uman, 2003; Helling et al., 2016a; Hodosán, 2017). These electrons and ions will be produced by different ionization processes, depending on the energy sources available in the atmosphere. On Earth, these ionization sources are mainly cosmic rays and natural radioactivity (Stozhkov, 2003; Nicoll, 2014). In addition, lightning has been observed in volcanic plumes, where triboelectrification — frictional charging of colliding dust particles — is responsible for the generation of charges (Gilbert et al., 1991; Zheng, 2013). A similar process has been hypothesized to generate charges in the dust clouds in the atmospheres of exoplanets and brown dwarfs (Helling et al., 2011a). Cosmic ray ionization is also an important source of charges in extrasolar atmospheres as will be discussed in more detail in Chapter 2 (Rimmer & Helling, 2013). Rodríguez-Barrera et al. (2015) suggest that thermal ionization in the atmospheres of brown dwarfs produces sufficient amounts of charges to seed lightning processes.

Once enough charges are produced, they need to be separated to produce a potential difference that builds up a high electric field. To separate charges, transport mechanisms must be present in the atmosphere (Dwyer & Uman, 2014). One process, responsible for charge separation in thunderstorm clouds on Earth, is convection in water clouds. Because of the polar nature of the water molecule, when ice and graupel (soft hail) particles grow, they build layers of different charges, with an inner positive and an outer negative layer. If a larger graupel particle collides with a smaller ice grain, the graupel particle is removing the outer, negative layer of the ice grain which will now stick to the graupel particle. The lighter ice grain remains now net positively charged and is transported upwards by the convective draft. The heavier graupel particle is now net negatively charged and will remain stationary or even settle downward. This separates the charges in a thunderstorm cloud into a net negatively charged layer at the bottom of the cloud and a net positively charged layer above (Saunders, 1993). The other process leading to the separation of charges, is gravitational settling which is likely

to be happening in volcanic plumes where large, negatively charged ash particles are settling towards the bottom of the plume as negative charges accumulate in solid silicate particles while positive charges are found on volcanic gases and aerosols in the upper part of the plume (Lane & Gilbert, 1992). Similarly, models simulating cloud formation in the atmospheres of gas giant exoplanets and brown dwarfs show that gravitational settling can produce clouds with layers of differently sized particles (Woitke & Helling, 2003; Helling et al., 2008b), leading to large-scale charge separation Helling et al. (2013a,b).

In the established electric field, electrons are accelerated and collide with gas molecules, potentially ionizing these, producing more free electrons Helling et al. (2013b); Dwyer & Uman (2014). If the strength of the field is above a certain threshold, the rate at which free electrons are being produced is higher than the rate of recombination, producing an avalanche of electrons (Roussel-Dupré et al., 2008). This threshold is called the breakdown field and it depends on the atmospheric pressure, the composition of the gas, and on the presence of water droplets or ice grains (Dwyer & Uman, 2014; Köhn et al., 2019). Köhn et al. (2019) found that the breakdown field in an N_2-O_2 gas mixture is approximately twice as high as in an N_2-CH_4 gas mixture and varies slightly with the N_2 fraction in the gas. For air (modern Earth atmosphere) the breakdown field at 1 bar is $E_k \sim 3.5\,\mathrm{MV\,m^{-1}}$. However, there are a few processes that can lower the breakdown field strength on Earth, such as the presence of water or ice particles, or initiation of streamers by energetic runaway electrons, which allow lightning to be generated in thunderstorm clouds that have electric field strengths below the breakdown field (Dwyer & Uman, 2014).

The first step of a lightning discharge is the development of a streamer. Streamers are thin, only a few cm long channels of cold, ionized plasma, meaning the gas within the channel is at ambient temperature while the electrons are very energetic (Köhn et al., 2019; Nijdam et al., 2020). Streamers build the precursors of heat-dominated spark channels as we see them in our experiments. They are also responsible for the inception and propagation of lightning leaders and are observable in Earth's atmospheres as so-called 'sprite discharges' above thunderclouds (Ebert & Sentman, 2008; Dubrovin et al., 2010; Köhn et al., 2019; Nijdam et al., 2020). For most cloud-to-ground discharges, a downward negative leader develops, creating a conducting path between the cloud and the ground and depositing negative charge on the way. Before the leader reaches the ground, an upward positive leader develops from the ground, connecting to one of the branches of the downward leader, and triggering an

upward return stroke that neutralises the negative charges along the channel (Baba & Rakov, 2009). The return stroke channel has a diameter of about 3 cm, carries a peak current of about 30 kA and reaches a temperature of more than 30 000 K (Rakov & Uman, 2003). The peak temperature and subsequent decay can be measured by monitoring the emission of the 648.20 and 661.05 nm N II ion lines (An et al., 2019; Kieu et al., 2020).

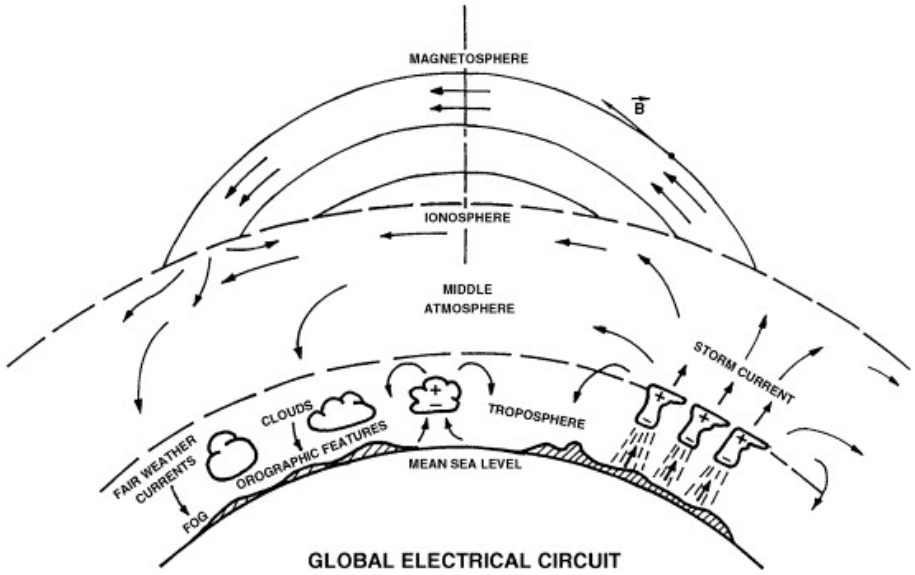

Figure 1.7: Schematic of the global electrical circuit in the atmosphere of Earth. From (Roble & Tzur, 1986) (license).

The 'Global Electrical Circuit' is a concept that describes all electrical phenomena in the Earth system. It has first been postulated by CTR Wilson one century ago (Wilson, 1921, 1929). Two conducting layers, Earth's surface and the ionosphere, are separated by the lower and middle atmosphere (Fig. 1.7). Thunderstorm clouds, where reservoirs of positive and negative charges build up at the top and bottom of the cloud, respectively, act like giant 'batteries' that drive an upward current. In other regions with fair weather, currents are flowing downward towards the surface (Aplin et al., 2008). Stellar energetic particles, cosmic rays, and natural radioactivity facilitate the flow of these currents by ionizing gas molecules in the atmosphere, creating seed charges for the development of lightning discharges (Stozhkov, 2003; Nicoll, 2014; Helling et al., 2016a), as we will discuss in more detail in Chapter 3.4.

1.3.2 Lightning Activity on Earth and Other Planets

In Earth's atmosphere, lightning activity can mainly be observed in the vicinity of convective thunderstorm clouds. Thus, about 77% of lightning occurs in the tropics, between 30° North

Table 1.1: Overview of lightning flash rates for Earth's atmosphere (see Schumann & Huntrieser, 2007, Table 8)

Source	**Flash rate** [s^{-1}]
Brooks (1925); Mackerras et al. (1998)	100
Chameides et al. (1977); Chameides (1979a)	400 (CG: 100)
Orville & Spencer (1979)	123 ± 60
Kowalczyk & Bauer (1981)	300 (CG: 60)
Kotaki & Katoh (1983)	63 ± 30
Mackerras et al. (1998)	65 (GC: 10-14)
Christian et al. (2003)	44 ± 5
Cecil et al. (2014)	46
Hodosán et al. (2016a)	33

CG: Cloud-to-ground flashes

and South, where most of the Sun's energy is deposited and the strongest convection occurs (Schumann & Huntrieser, 2007). Lightning produces optical and radio emission that can be observed both from the ground and from space with different parts of the flash producing different types of emission (MacGorman & Rust, 1998). The lightning channel acts as a giant antenna, emitting pulses of low-frequency radio emission (below 100 kHz, Price et al., 2007). Ground-based surveys are mostly detecting radio emissions from cloud-to-ground lightning flashes (Schumann & Huntrieser, 2007). The Optical Transient Detector (OTD, Christian et al., 2003) and the Lightning Imaging Sensor (LIS, Thomas et al., 2000) are space-based observatories, detecting lightning flashes (ground-to-cloud, intra-cloud, and cloud-to-cloud flashes) by their optical emission in the oxygen triplet line (777.4 nm). In Chapter 3, we use an estimate for the global lightning flash rate on modern Earth of $44 \pm 5\,s^{-1}$ which is based on combined observations with OTD and LIS (Christian et al., 2003). A comparison of flash rates estimates is shown in Table 1.1. The energy delivered by a lightning flash depends on the type of the discharge. Schumann & Huntrieser (2007) present values from different sources, ranging from 0.4 to 6.7 GJ per flash (see Table 1.2). Following their example we are using the estimate by Price et al. (1997a) of 6.7 GJ per flash to extrapolate the energy yields of lightning products from our experiments to global production rates.

Romps et al. (2014) showed that the lightning flash rate is directly proportional to the convective available potential energy (CAPE) by comparing measurements of CAPE, the precipitation rate, and the lightning flash rate over the contiguous United States. The lightning

Table 1.2: Overview of lightning flash energies for Earth's atmosphere (see Schumann & Huntrieser, 2007, Section 3.1.1)

Source	Flash energy per length [$\mathrm{kJ\,m^{-1}}$]	Energy per flash [GJ]
Uman (1987); Orville et al. (2002)	-	0.1
Vonnegut (1963)	-	10
Krider et al. (1968)	230	1.15^a
Hill (1979)	10	0.05^a
Uman (1987)	100 - 1000	0.5 - 5^a
Cooray (1997)	70	0.35^a
Borucki & Chameides (1984)	-	$0.4^{+0.8}_{-0.3}$
Price et al. (1997a,b)	-	6.7
Wong et al. (2017)	-	5

[a] For a flash length of 5 km

flash rate F in $\mathrm{m^{-2}\,s^{-1}}$ is given by

$$F = \frac{\eta}{E} \times P \times \mathrm{CAPE}, \tag{1.5}$$

with the precipitation rate $P(\mathrm{kg\,m^{-2}\,s^{-1}})$, the energy per flash $E(\mathrm{J})$, and the conversion efficiency η (the ratio of power dissipated by lightning to the available CAPE). CAPE, measured in $\mathrm{J\,kg^{-1}}$, is given by the difference between the buoyant and the potential energy of an air parcel and thus a measure of how unstable the atmosphere is. A higher CAPE leads to a stronger updraft (Moncrieff & Miller, 1976). While the amount of CAPE is similar over land area and oceans, the lightning rates above continents are $6-10$ times higher than over sea (Schumann & Huntrieser, 2007). This is usually explained by more intense convection over land area due to a lower water load of the air (Williams, 2005). With ongoing global warming, the concentration of water vapour and thus the amount of CAPE in Earth's atmosphere continues to increase (Ye et al., 1998). Romps et al. (2014) predict that with every degree of temperature increase, the lightning activity in the United States will increase by 12%, with a similar increase expected globally. Similarly, with increasing temperatures in the polar regions, convection and lightning activity in the Arctic is increasing (Zhang et al., 2023).

The relationship between CAPE and lightning flash rate can also be used to estimate lightning rates in different atmospheres, like on early Earth or exoplanets. Wong et al. (2017) used climate simulations and CAPE to estimate the lightning flash rate in potential Archean atmospheres with varying CO_2 partial pressure. Whilst the conversion efficiency η in Eq. (1.5) can be adjusted to take into account variations of the breakdown field with changing gas com-

position, Wong et al. (2017) assumed η to be the same as for modern Earth (Romps et al., 2014, suggest $\eta = 1\%$ for $E = 1\,\mathrm{GJ}$ for modern Earth). Processes that can initiate lightning at electric field strengths below the breakdown field (Section 1.3.1) make it difficult to estimate a value for η for different atmospheres. Wong et al. (2017) found the lightning flash rate on the Archean Earth to peak at $151\,\mathrm{s}^{-1}$ at 1 bar of CO_2, with flash rates of $6.6\,\mathrm{s}^{-1}$ and $50\,\mathrm{s}^{-1}$ for CO_2 partial pressures of 0.1 and 10 bar, respectively (with $1-2$ bar of N_2). Braam et al. (2022) suggest that the lightning flash rate on tidally locked exoplanets such as Proxima Centauri b is less than 10% of modern Earth's ($2.6\,\mathrm{s}^{-1}$) because clouds only form around the substellar point. As mentioned in the previous section, an additional factor that can influence the occurrence of lightning are cosmic rays. Planets orbiting M dwarfs will experience more frequent and intense stellar flares that are associated with flares of charged particles. TRAPPIST-1 e is bombarded by a proton flux of up to six orders of magnitude higher than what modern Earth is experiencing. Energetic particles like these solar protons or galactic cosmic rays are known to enhance the ionization in the planet's atmosphere (Stozhkov, 2003; Rimmer & Helling, 2013; Scheucher et al., 2020; Barth et al., 2021b). Comparison between lightning flash rates and cosmic ray ionization rates in Earth's atmosphere have shown a strong correlation between these two quantities (Stozhkov, 2003). However, the increased influx of charged particles into the atmospheres of planets orbiting M dwarfs is only likely to stimulate more efficient discharges of lightning if those atmospheres already have electric fields in their clouds. We might therefore only find a slightly enhanced lightning activity on these planets, but more detailed studies on the connection between cosmic ray ionization and lightning are necessary to fully understand these processes.

Observations of lightning outside of Earth are more difficult. So far, lightning activity has been recorded on Jupiter (Vasavada & Showman, 2005; Yair et al., 2008; Brown et al., 2018; Kolmašová et al., 2023), Saturn (Dyudina et al., 2010, 2013), Uranus (Zarka & Pedersen, 1986; Yair et al., 2008), and Neptune (Gurnett et al., 1990; Gibbard et al., 1999). Lightning detections on Venus are still controversial (Russell et al., 2007; Cardesín Moinelo et al., 2016; Lorenz et al., 2022), as they are on Mars (Melnik & Parrot, 1998; Renno et al., 2003; Gurnett et al., 2010; Wang et al., 2023). Lightning flash rates observed on the planets of the Solar System allow an estimate of the lightning activity in the atmospheres of exoplanets. Hodosán et al. (2016a) find lightning rates per area on Jupiter and Saturn to be slightly lower than on Earth, but instrument limitations only allow for the most powerful flashes to be detected,

and the energies of these flashes are likely to exceed the energies of the most powerful lightning flashes on Earth. Hodosán et al. (2021) estimate that average lightning energies on hot Jupiters and brown dwarfs are two to eight orders of magnitude higher than on Earth, and up to five orders of magnitude higher than on Jupiter or Saturn, with strong dependencies on the surface gravity and metallicity of these objects. Direct observation of radio emission from lightning on exoplanets is possible but would require extremely high flash densities (Hodosán et al., 2016b). Instead, or in addition, it might be possible to detect lightning due to the effect is has on the chemical composition of exoplanetary atmospheres. Species that have been suggested as lightning tracers are HCN, NO_2, and C_2N (Ardaseva et al., 2017) as well as HNO_3 and N_2O_5 (Braam et al., 2022). We will discuss the prospect of these and other potential signatures in Chapter 3.4.

1.4 Outline of Thesis

The work presented in this thesis seeks to understand the role of lightning in the production of prebiotic molecules on early Earth and exoplanets and to investigate observable signatures for lightning. In Chapter 2, X-Ray and UV radiation, stellar energetic particles, and galactic cosmic rays are investigated as a source of prebiotic chemistry in exoplanetary atmospheres using the example of the hot Jupiter HD 189733 b. Potential observable signatures are discussed, as well as the role of these processes in providing the necessary conditions for lightning. Chapter 3 focuses on the role of lightning in different atmospheres: First, the setup of the spark discharge experiments and the analytical and computational methods are presented. In Chapter 3.3, the experimental results on the role of lightning as a source of nutrients on early Earth are discussed. The isotopic signature of lightning in nitrogen products has been determined for comparison to the sedimentary rock record. This is followed by the investigation of lightning's potential to produce false-positive or false-negative biosignatures, as well as possible lightning signatures in exoplanetary atmospheres in Chapter 3.4. The thesis concludes in Chapter 4 with a conclusion and outlook.

Tracing the Chemistry of High-energy Radiation on the Hot Jupiter HD 189733 b

2.1 The Chemistry of Hot Jupiter Atmospheres

The hot Jupiter HD 189733 b (Bouchy et al., 2005) orbits an active K dwarf (HD 189733 A, hereafter HD 189733) at a distance of 0.031 au and is the closest transiting hot Jupiter to Earth and particularly well studied (e.g. Helling et al., 2016b; Lines et al., 2018; Drummond et al., 2020; Odert et al., 2020, and references therein). Various molecules have been detected in the planet's atmosphere so far, including H_2O (Grillmair et al., 2008; Birkby et al., 2013; Crouzet et al., 2014; Todorov et al., 2014; McCullough et al., 2014), CH_4 (Swain et al., 2014), and CO (Désert et al., 2009; de Kok et al., 2013; Rodler et al., 2013). However, thick clouds and photochemical hazes obscure the deeper layers of the atmosphere where other molecules are expected to be present (Gibson et al., 2012; Deming et al., 2013; Pont et al.,

2013; Helling et al., 2016b; Iyer et al., 2016; Zahnle et al., 2016; Kirk et al., 2017). Characterization of these deeper atmospheric layers therefore requires computational models that take into account various types of radiation and gas transport mechanisms. Such simulations are particularly important for unravelling the role of atmospheric processes in prebiotic reactions that may potentially lead to the establishment of a living biosphere. Although life is not expected to originate on hot Jupiters, the wealth of observational data collected from these objects over recent years make them ideal natural laboratories for improving our understanding of fundamental gas phase reactions on extrasolar worlds.

In previous work, Moses et al. (2011) carried out photo- and thermochemical kinetics simulations of the atmosphere of HD 189733 b with a neutral H/C/N/O network, showing an enhancement of NH_3 and CH_4 due to transport-induced quenching in the middle layers of the atmosphere. In the upper atmosphere, photochemistry enhances the abundances of atomic species, unsaturated hydrocarbons, nitriles, and radicals. More recent studies by Venot et al. (2012, 2020) with a chemical kinetics network that is validated by experimental data showed differences in the abundance of NH_3, HCN, and CH_4 due to different quenching pressures. Some work has also been done to investigate the effect of high-energy radiation. For example, Venot et al. (2016) studied the influence of stellar flares on the chemical composition of exoplanets at the example of a sub-Neptune/super-Earth-like planet orbiting an active M star. They found that individual and recurring flares can irreversibly alter the abundances of key molecules such as H or OH. However, in their simulations they only considered flares in the stellar radiation and not the effect of charged particles which could be associated with a stellar flare. In contrast, Segura et al. (2010) included the effect of stellar particles into their simulations to study the effect of flares on the oxygen-rich atmosphere of an Earth-like planet orbiting an active M star in its habitable zone. They found that such flares can severely deplete the ozone layer over several decades, which illustrates the importance of including energetic particles in realistic atmospheric chemistry models. Chadney et al. (2017) studied the effect of stellar flares on the upper atmosphere ($p < 10^{-6}$bar) of HD 189733 b and HD 209458 b where they found an enhancement in the electron densities of a factor of 2.2 – 3.5. However, while this study provided an estimate on the mass loss rate due to a stellar proton event, and also took into account photoionization and electron-impact ionization of H and He, the effect of stellar energetic protons on atmospheric chemistry were not explored.

The work presented in this chapter is part of the MOVES collaboration (*Multiwavelength*

Observations of an eVaporating Exoplanet and its Star, PI V. Bourrier) which aims to characterize the complex and variable environment of the HD 189733 system. In MOVES I, Fares et al. (2017) studied the evolving magnetic field of the host star HD 189733, an active K dwarf. They used spectropolarimetric data to reconstruct the magnetic field of the star and study its evolution over nine years. Kavanagh et al. (2019) (MOVES II) used these results to perform 3D MHD simulations of the stellar wind of HD 189733 and to predict the radio emission from both the planet and the star. The models predict that the planet experiences a non-uniform wind with the wind velocity and particle number density varying by up to 37 % and 32 %, respectively. Bourrier et al. (2020) (MOVES III) confirmed the variable HI escape from HD 189733 b (Lecavelier des Etangs et al., 2012; Bourrier et al., 2013), and used *HST*, *XMM-Newton*, and *Swift* data to derive semi-synthetic XUV spectra of the host star that we use for our simulations (Section 2.3.2).

In this study, we use these semi-synthetic XUV spectra to investigate the effect of stellar X-ray and UV (XUV) radiation, as well as the effect of stellar energetic particles (SEP) and cosmic rays (CR) on the atmospheric chemistry of HD 189733 b. First, the chemical kinetics network STAND2019 (Rimmer & Helling, 2016, 2019; Rimmer & Rugheimer, 2019) which we use for our simulations will be introduced in Section 2.2. In Section 2.3 we discuss the atmospheric pressure-temperature profiles and the parameterization of the different sources of high-energy radiation before we present the resulting abundances of neutral and charged molecules at the substellar and antistellar point (Section 2.4). We put particular emphasis on the effect of high-energy radiation sources on the ionization of the atmospheric gas as precursor for the formation of a magnetosphere. Furthermore, we explore the possible production of prebiotic organic molecules in giant gas planets as the atmosphere of HD 189733 b provides a potentially observable laboratory for the onset of prebiotic synthesis.

2.2 Photochemical and Kinetic Chemistry Simulations

We use the chemical kinetics network STAND2019 (Rimmer & Helling, 2016, 2019; Rimmer & Rugheimer, 2019) to simulate the influence of XUV radiation and cosmic rays on the atmospheric chemistry. STAND2019 is an H/C/N/O network with reactions involving He, Na, Mg, Si, Cl, Ar, K, Ti, and Fe. It contains all reactions for species of up to six H, two C, two N, and three O atoms and is valid for temperatures between 100 and 30 000 K. The network has been benchmarked against modern Earth and Jupiter (Rimmer & Helling, 2016), as well as

Table 2.1: New reactions added to STAND2019. The full network is available in the supplementary materials of Barth et al. (2021b). Note that reverse reactions are not included in the network file.

Number	Reaction	Class[c]	α	β	γ	Source
627[l]	$Cl^+ + e^- \longrightarrow Cl$	T	3.43×10^{-14}	-3.77	0	Reaction no. 623[a]
628[h]	$Cl^+ + e^- \longrightarrow Cl$	T	10^{-7}	0	0	Reaction no. 624[a]
1406	$C_2N + H \longrightarrow HCN + C$	A	2×10^{-10}	0	0	Loison et al. (2014)
1407	$CNC + H \longrightarrow HCN + C$	A	2×10^{-10}	0	0	Reaction no. 1406
3072	$C_3^+ + e^- \longrightarrow C_2 + C$	U	3×10^{-7}	-0.5	0	OSU[b], Loison et al. (2017)
3085	$Cl^+ + e^- \longrightarrow Cl$	RA	1.13×10^{-10}	-0.7	0	OSU[b]

[c] reaction classes: T – Three-body recombination reactions, A – Neutral bimolecular reactions, U – Dissociative recombination reactions, RA – Radiative association reaction, [l] low pressure regime, [h] high pressure regime, [a] rates adopted from corresponding reaction with Na^+, [b] Ohio State University chemical network (Harada et al., 2010).

hot-Jupiter models (Tsai et al., 2017; Hobbs et al., 2019). The full network is available in the supplementary materials of Barth et al. (2021b).

STAND2019 uses the 1D photochemistry and diffusion code ARGO which requires the following inputs:

1. $p_{\mathrm{gas}} - T_{\mathrm{gas}}$ profile of the atmosphere
2. Vertical eddy diffusion coefficient profile K_{zz}
3. Atmospheric element abundances
4. Boundary conditions at the top and bottom of the atmosphere
5. Actinic flux at the top of the atmosphere
6. Chemical network (STAND2019)
7. Initial chemical composition

ARGO follows a single gas parcel while it moves up- and downwards through the atmosphere due to eddy diffusion. The kinetic gas-phase chemistry has no feedback onto the initial (T_{gas}, p_{gas})-profiles.

The model consists of two parts: a chemical transport model that considers ion-neutral and neutral-neutral reactions and a model calculating the chemical rate constants for photochemistry and cosmic rays. The gas-phase number densities, n_{i}, are determined by 1D continuity

equations (Rimmer & Helling, 2016, 2019),

$$\frac{\partial n_i}{\partial t} = P_i - L_i - \frac{\partial \Phi_i}{\partial z}, \tag{2.1}$$

where n_i is the number density of species i, P_i is the rate of production and L_i the rate of loss of species i (both in $\mathrm{cm^{-3}\,s^{-1}}$). $\frac{\partial \Phi_i}{\partial z}$ is the vertical change in the flux $\Phi_i[\mathrm{cm^{-2}\,s^{-1}}]$ due to Eddy and molecular diffusion. Ambipolar diffusion is not included in the model. In the presence of a magnetic field, this type of diffusion might slow down vertical mixing but as long as the degree of ionization remains low the effect on the chemistry is not expected to be large. For strongly ionized atmospheres, ambipolar diffusion can be parameterized to represent the electron-induced electric field that is acting on the ions.

The source and sink term P_i and L_i in Eq. (2.1) describe two-body neutral-neutral and ion-neutral reactions, three-body neutral reactions, dissociation reactions, radiative association reactions, as well as thermal ionization and recombination reactions. In total, the version of STAND2019 used in this study includes 3085 forward reactions with 197 neutral and 224 ion species and is available in the supplementary material of Barth et al. (2021b) (note that the reverse reactions are not included in the available network file). The network is a modified version of STAND2019 (Rimmer & Helling, 2019; Rimmer & Rugheimer, 2019) which itself is a new version of the original STAND2015 network (Rimmer & Helling, 2016). In the following, we will describe the changes made to the network for this work which are summarised in Table 2.1.

Additions to the network

One of the cosmic ray ionization reactions in STAND2019 leads to the production of Cl^+, but until now the network has not included any destruction reactions for Cl^+, leading to an over-estimation of the abundance of this ion. We therefore have included additional production and destruction reactions for Cl^+:

$$\mathrm{Cl + M} \longrightarrow \mathrm{Cl^+ + e^- + M}, \tag{2.2}$$

$$\mathrm{Cl^+ + e^- + M} \longrightarrow \mathrm{Cl + M}, \tag{2.3}$$

where M represents a not defined third body. As there are no published rate coefficients for these reactions, we used the rates for the corresponding Na reactions. Even though Na and

Cl have different electron affinities, that should not strongly affect the reaction rates. We will make sure to update these coefficients as soon as there are new data available.

The rates of these thermal ionization (Eq. 2.2) and three-body recombination reactions (Eq. 2.3) follow the Lindemann form (Lindemann et al., 1922), which provides pressure dependent reaction rates with limits for the low (k_0[cm^6/s]) and the high-pressure regimes (k_∞[cm^3/s]):

$$k_0 = \alpha_0 \left(\frac{T}{300\,\mathrm{K}}\right)^{\beta_0} e^{-\gamma_0/T}, \tag{2.4}$$

$$k_\infty = \alpha_\infty \left(\frac{T}{300\,\mathrm{K}}\right)^{\beta_\infty} e^{-\gamma_\infty/T}. \tag{2.5}$$

The coefficients α_i, β_i, and γ_i for above rates can be found in Table 2.1 (reactions 1193 and 1351 for the low-pressure and reactions 1194 and 1352 for the high-pressure regime). The pressure-dependent rate can now be calculated with the reduced pressure $p_\mathrm{r} = k_0 n_\mathrm{M}/k_\infty$, where n_M[cm^{-3}] is the number density of the neutral third body (Rimmer & Helling, 2016):

$$k = \frac{k_\infty p_\mathrm{r}}{1 + p_\mathrm{r}}. \tag{2.6}$$

In addition, a radiative association reaction for the destruction of Cl^+ (Reaction 5742) was added:

$$Cl^+ + e^- \longrightarrow Cl + h\nu, \tag{2.7}$$

where the excess energy of the recombination is emitted as a photon with energy $h\nu$. The reaction rate follows the Kooji equation (Kooij, 1893):

$$k_\mathrm{RA} = \alpha \left(\frac{T}{300\,\mathrm{K}}\right)^{\beta} e^{-\gamma/T}. \tag{2.8}$$

The coefficients (Table 2.1) are taken from the KIDA database (Wakelam et al., 2012) and originally from the Ohio State University (OSU) chemical network (Harada et al., 2010). This rate is then combined with the rate for the three-body recombination reaction presented above (Eq. 2.3) to

$$k = \frac{(k_0 n_\mathrm{M} F + k_\mathrm{RA}) k_\infty}{k_0 n_\mathrm{M} + k_\infty}, \tag{2.9}$$

where F is a dimensionless function to more accurately approximate the transition from high

to low pressure which gives the Troe form (Troe, 1983; Rimmer & Helling, 2016).

When running ARGO for HD 189733 b, HCCN was overproduced due to the absence of the destruction reactions for CNC. This was resolved via the addition of two neutral bimolecular reactions to the network:

$$C_2N + H \longrightarrow HCN + C \tag{2.10}$$

$$CNC + H \longrightarrow HCN + C \tag{2.11}$$

The coefficients for the first reaction (Eq. 2.10) were taken again from the KIDA database and were presented previously by Loison et al. (2014). For the destruction reaction of CNC we assume the same rate constant. Since β and γ are zero (Table 2.1), the reaction rate is given by

$$k = \alpha \left(\frac{T}{300\,\mathrm{K}} \right). \tag{2.12}$$

Similar to the above described case of Cl^+, destruction reactions for $C_3{}^+$ were missing in STAND2019. Therefore, a dissociative recombination reaction has been added to the network (Reaction 5729):

$$C_3{}^+ + e^- \longrightarrow C_2 + C \tag{2.13}$$

The reaction rate follows the Kooji form (Eq. 2.8). The coefficients presented in Table 2.1 are again from the KIDA database and originally from the OSU network and Loison et al. (2017). Further, the NASA coefficients for K^+ were updated to those from Burcat et al. (2005)[†].

2.3 The Atmosphere and Energetic Environment

2.3.1 Atmospheric Profiles

We extract 1D profiles from the 3D Met Office Unified Model (UM) simulations of the atmosphere of HD 189733 b by Lines et al. (2018) which consistently solve a kinetic cloud formation model (Helling et al., 2001; Woitke & Helling, 2003, 2004; Helling & Woitke, 2006; Helling et al., 2008a). Some of the input parameters for the UM are given in Table 2.2. Cloud properties like particles sizes or their number density are consistent with the thermodynamic profile of the atmosphere within this model. Lines et al. (2018) show that clouds form throughout

[†]http://garfield.chem.elte.hu/Burcat/burcat.html

Table 2.2: Model parameters for HD 189733 b, adapted from Southworth (2010) (for more details see Lines et al., 2018, Table 1)

Parameter	**Initial value**
Specific gas constant[a], R ($\mathrm{J\,kg^{-1}\,K^{-1}}$)	3556.8
Specific heat capacity, c_p ($\mathrm{J\,kg^{-1}\,K^{-1}}$)	1.3×10^4
Radius, R_p (m)	8.05×10^7
Surface gravity, g_p ($\mathrm{m\,s^{-1}}$)	22.49
Semi-major axis, a_p (au)	3.14×10^{-2}

[a] Unlike noted in Lines et al. (2018, Tab. 1) the specific gas constant is not $R = 4593\,\mathrm{J\,kg^{-1}\,K^{-1}}$ but $3556.8\,\mathrm{J\,kg^{-1}\,K^{-1}}$ which was also used in the simulations in this work and used by (Drummond et al., 2018a).

most parts of HD 189733 b's atmosphere, i.e. the local atmospheric temperature is below the condensation temperature of the Mg/Si/Fe/O/Ti cloud species considered.

In this work, we utilize the vertical 1D ($T_\mathrm{gas}, p_\mathrm{gas}, K_\mathrm{zz}$)-profiles for the antistellar and the substellar points on the equator. Figure 2.1a (left) shows that the 1D profiles appear remarkably similar throughout the whole pressure range covered by our computational domain, $p_\mathrm{gas} = 10^2 - 10^{-5.5}$bar. Temperature differences of some 100 K occur in the uppermost region near the upper boundary of the 3D GCM model. The eddy diffusion coefficient, K_zz, varies between $10^6\mathrm{cm^2\,s^{-1}}$ at $p_\mathrm{gas} = 10^2$bar and $10^8\mathrm{cm^2\,s^{-1}}$ where $p_\mathrm{gas} < 10^{-2}$bar (Fig. 2.1a, right). Figure 2.1b shows the cloud particle number density (left) and the mean cloud particles sizes (right). Based on the 3D UM GCM, the cloud particle number density is rather homogeneous while all profiles show a strong accumulation of cloud particles due to gravitation settling at the inner boundary near 100 bar. Within the 3D UM GCM, the cloud particles are of size 0.1 µm throughout the atmosphere.

2.3.2 XUV Spectra

This work exploits XUV spectra of HD 189733 obtained within the framework of the MOVES collaboration (Bourrier et al., 2020). UV (*HST*) and X-ray (*XMM-Newton/Swift*) observations were obtained in four contemporaneous epochs between July 2011 and November 2013. After excluding flares, these observations provided measurements of the quiescent stellar emission in the soft X-ray (from the coronal region) and in a sample of FUV emission lines (from the chromosphere and transition region). Most of the stellar EUV spectrum is not observable from Earth because of interstellar medium absorption. The quiescent measurements were thus used to constrain a model of HD189733's atmosphere and to reconstruct its entire XUV

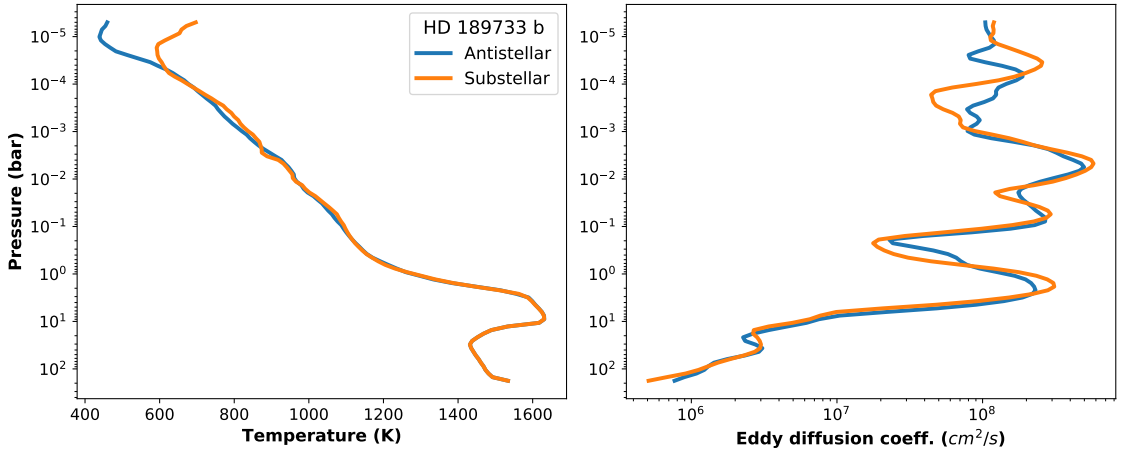

(a) Left: Atmospheric $(T_{\mathrm{gas}}, p_{\mathrm{gas}})$-profiles. **Right:** Profiles of the eddy diffusion coefficient K_{zz} derived from the standard deviation of the vertical velocity.

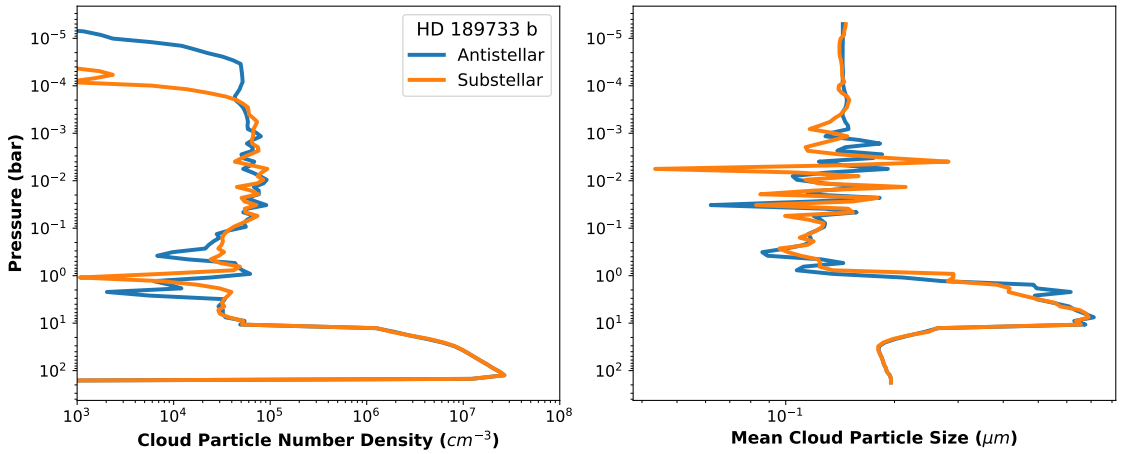

(b) Left: Cloud particle number density. **Right:** Mean cloud particle size

Figure 2.1: Atmospheric profiles for HD 189733 b from simulations with the 3D Met Office UM (Lines et al., 2018) at the antistellar ($\phi = 0^\circ, \theta = 0^\circ$) & substellar point ($180^\circ, 0^\circ$). First published in Barth et al. (2021b).

spectrum in each epoch, using the Differential Emission Measure retrieval technique described in Louden et al. (2017). The Ly α line of HD 189733 (reconstructed independently following the procedure described in Bourrier et al., 2017) which represents by itself half of the flux emitted in the entire EUV domain, has also been included in the synthetic spectra. The final semi-synthetic spectra cover a wavelength range from 0.016 to 1600 Å and therefore include not only the EUV but also the FUV flux (these XUV spectra are available online as machine readable tables, see Bourrier et al., 2020). The spread of the spectra is shown in Fig. 2.2, along with their binned version (with a width of $\Delta\lambda = 1$ Å) used as input into ARGO. The long-term monitoring of HD 189733 revealed variations in the spectral energy distribution of HD 189733 over these four epochs, with an increase in X-ray emission and a decrease in EUV

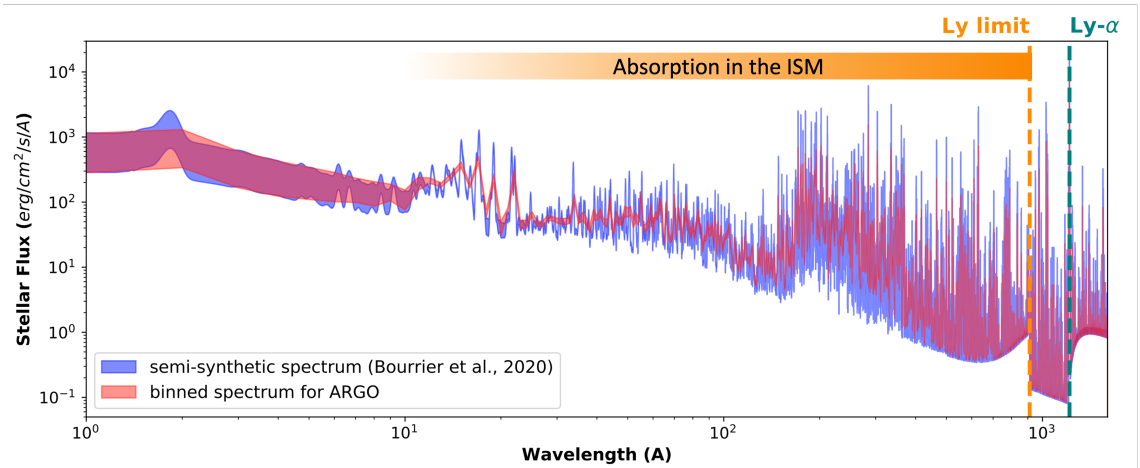

Figure 2.2: Semi-synthetic (*blue*) and binned (*red*) XUV spectra of HD 189733 at the orbit of HD 189733 b. Shown is the range in flux covered by the spectra from four different visits. The semi-synthetic spectra are reconstructed based on observations with *HST*, *XMM-Newton*, and *Swift* (Bourrier et al., 2020). The location of the Ly-α line (1215.67 Å) is shown in *teal*. Photons at the wavelengths of the Ly series and with wavelengths shorter than the Lyman limit (911.75 Å) are strongly absorbed by atomic hydrogen in the Interstellar Medium (ISM, *orange*). Adapted from Barth et al. (2021b).

emission, which could possibly trace a decrease in the chromospheric activity of the star while its corona became more active.

Figure 2.3 shows the XUV flux in comparison to the stellar energetic particles and the cosmic ray flux discussed in the following sections.

2.3.3 Cosmic Rays

The effect of cosmic rays and their ionization rates of the atmosphere is implemented into ARGO. In our simulations, we include the effect of low energy cosmic rays (LECR) based on Rimmer & Helling (2013). The flux of cosmic-ray particles $j(E)$ is given by

$$j(E) = \begin{cases} j(E_1)\left(\frac{p(E)}{p(E_1)}\right)^{\gamma} & \text{if } E > E_2 \\ j(E_1)\left(\frac{p(E_2)}{p(E_1)}\right)^{\gamma}\left(\frac{p(E)}{p(E_2)}\right)^{\alpha} & \text{if } E_{\text{cut}} < E < E_2 \\ 0 & \text{if } E < E_{\text{cut}} \end{cases}, \tag{2.14}$$

with $p(E) = 1/c\sqrt{E^2 + 2EE_0}$ and the proton rest energy $E_0 = 9.38 \times 10^8$eV, the constants $E_1 = 10^9$eV and $E_2 = 2 \times 10^8$eV, and the flux $j(E_1) = 0.22\text{cm}^{-2}\,\text{s}^{-1}\,\text{sr}^{-1}$. $E_{\text{cut}} = 10^6$eV is a low-energy cut-off. Cosmic rays with energies lower than E_{cut} are unlikely to travel further from their source than ~ 1 pc (Rimmer et al., 2012; Rimmer & Helling, 2013).

The effect of these cosmic rays on the atmosphere is parameterized by the ionization rate

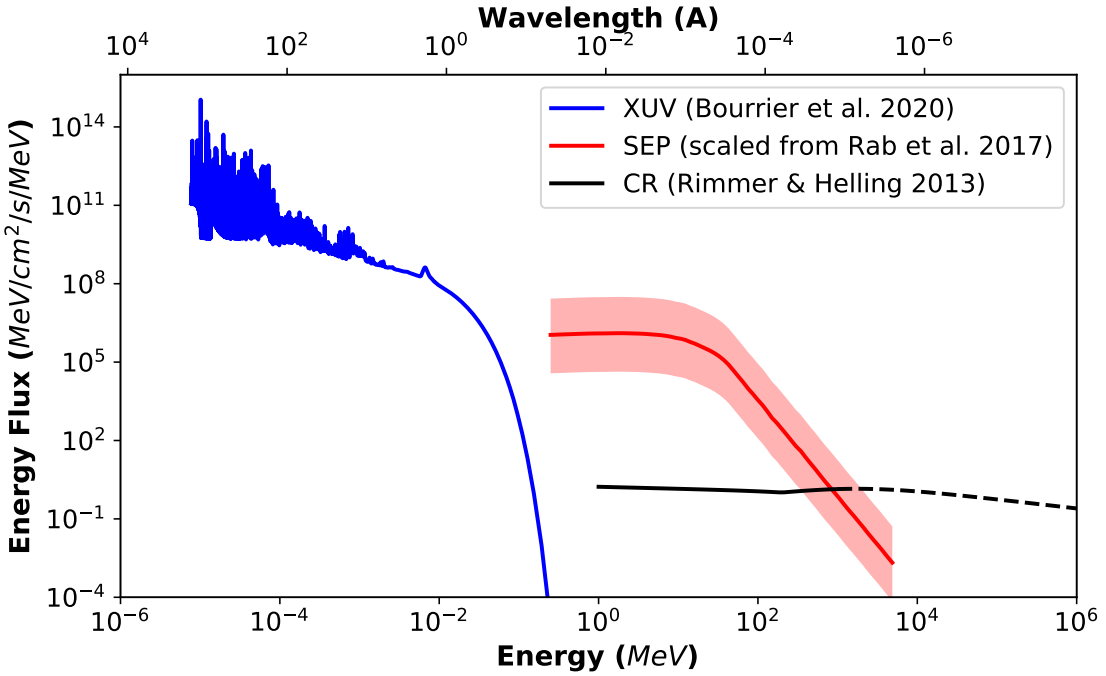

Figure 2.3: Comparison of high-energy spectra: XUV flux from HD 189733 (Bourrier et al., 2020, *blue line*), stellar energetic particle spectrum from HD 189733 at the planet's orbit (scaled from Rab et al., 2017, *red line*), and low energy cosmic ray spectrum (Rimmer & Helling, 2013, *solid black line*). Cosmic rays with energies above 1 GeV are not included in the model (*dashed black line*). All values are scaled to the orbit of HD 189733 b. Please note that these fluxes will most likely not occur at the same time and not on every part of the planet's surface. The SEP spectrum is only valid for a particle event associated with an X-ray flare while the XUV flux and the galactic cosmic rays are continuous energy sources. First published in Barth et al. (2021b).

ζ which depends on the column density $N_{\mathrm{col}}[\mathrm{cm}^{-2}]$ of the gas in the atmosphere. ζ is well fitted by:

$$\zeta(N_{\mathrm{col}}) = \zeta_0 \times \begin{cases} 480 & \text{if } N_{\mathrm{col}} < N_1 \\ 1 + (N_0/N_{\mathrm{col}})^{1.2} & \text{if } N_1 < N_{\mathrm{col}} < N_2 \\ \exp\left(-kN_{\mathrm{col}}\right) & \text{if } N_{\mathrm{col}} < N_2 \end{cases}, \tag{2.15}$$

with the standard ionization rate in the dense interstellar medium $\zeta_0 = 10^{-17}\mathrm{s}^{-1}$, the column densities $N_0 = 7.85 \times 10^{21}\mathrm{cm}^{-2}$, $N_1 = 4.6 \times 10^{19}\mathrm{cm}^{-2}$, $N_2 = 5.0 \times 10^{23}\mathrm{cm}^{-2}$, and $k = 1.7 \times 10^{-26}\mathrm{cm}^2$. The ionization rate is shown in Fig. 2.4 (lower panel, dotted black line).

2.3.4 Stellar Energetic Particles

Stellar energetic particle (SEP) events are caused by solar flares and coronal mass ejections. These events are accompanied by flares in the X-ray and UV emission and the peak size distribution of these flares follows a power law (Hudson, 1978; Belov et al., 2005). Herbst et al.

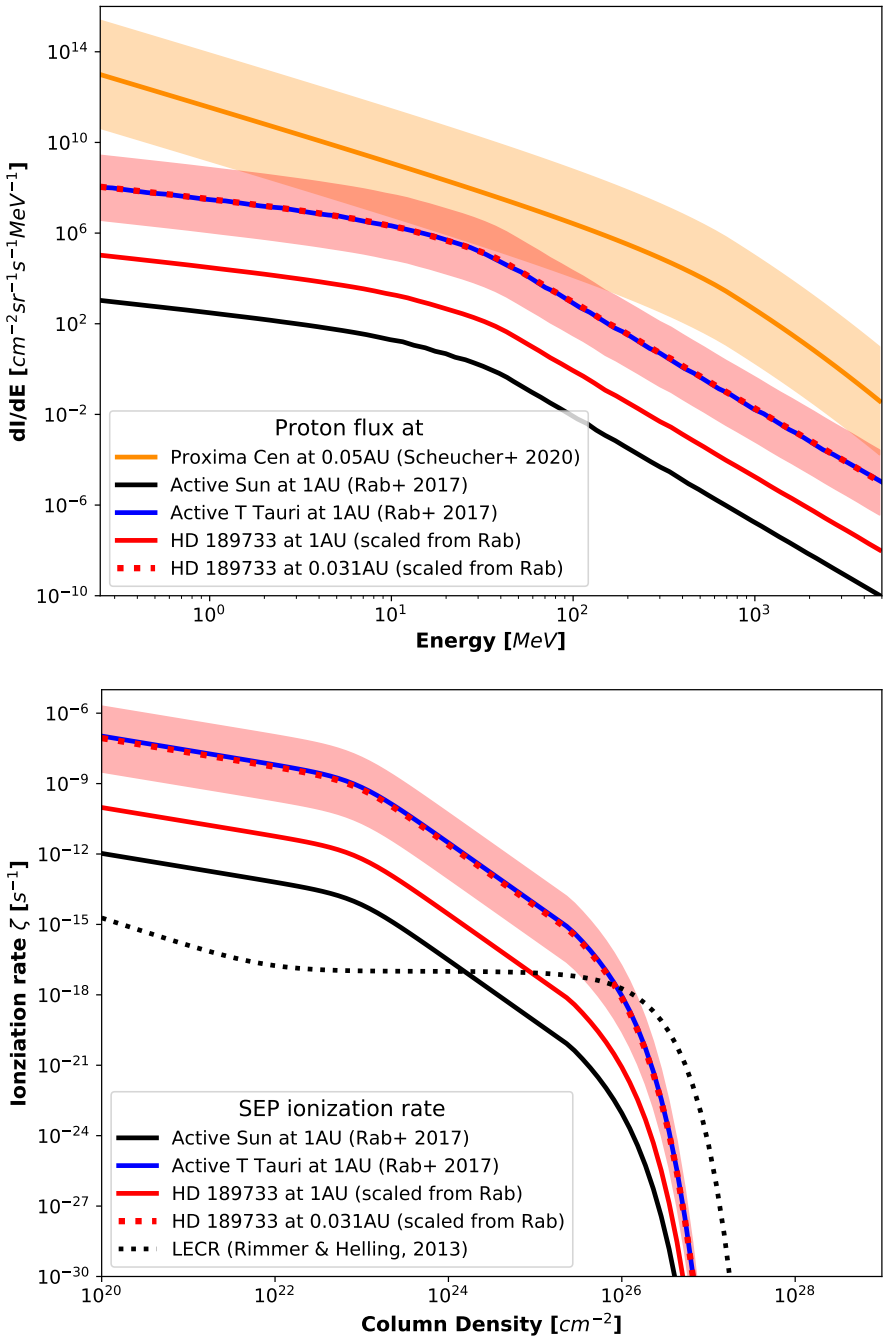

Figure 2.4: Top: Stellar energetic particle (SEP) spectrum from HD 189733 at 1 au (*red solid line*) and at the planet's orbit (0.031 au, *red dashed line*) are shown alongside the spectrum for an active Sun (*black line*) and an active T Tauri star (*blue line*, both at 1 au) from Rab et al. (2017). These were used to estimate the spectrum for HD 189733. For comparison the SEP spectrum at Proxima Centauri b's orbit is shown (Scheucher et al., 2020). The shaded areas indicate the error range based on the peak size distribution function in Herbst et al. (2019b). **Bottom:** The resulting ionization rates against the atmospheric column density are shown for the different spectra. For comparison the low energy cosmic rays (LECR) ionization rate from Rimmer & Helling (2013) is shown (*black dotted line*). First published in Barth et al. (2021b).

(2019b) present a new peak size distribution that allows an estimate of the proton flux associated with flares on G, K, and M dwarfs:

$$I_{\rm p}(E > 10\,{\rm MeV}) = (aI_{\rm x} + b\exp(-0.001I_{\rm x}))^{\gamma}, \tag{2.16}$$

with $a = 1.22 \times 10^5 (\pm 7.17 \times 10^4)$, $b = 3.05 \pm 1.79$, and $\gamma = 1.72 \pm 0.397$.

Pillitteri et al. (2010) provide *XMM-Newton* observations of an X-ray flare on HD 189733. In 2009, they measured an increase in the $0.3 - 8\,{\rm keV}$ band caused by a flare of 1.3×10^{-13} erg s^{-1} cm^{-2}. This corresponds to an X-ray flare intensity of $I_{\rm x} = 2.52\,{\rm W\,m^{-2}}$ at the planet's orbit. Using Eq. (2.16) this returns a proton flux[†] of $I_{\rm p} = 1.55(+36.4-1.50) \times 10^7 {\rm cm^{-2}\,sr^{-1}\,s^{-1}}$.

We derive the spectrum of the SEP event from the integrated proton flux by using the fitted spectrum of a solar SEP event from 2003 (Mewaldt et al., 2005). Rab et al. (2017) used this spectrum to estimate the SEP spectrum of an active T Tauri star by scaling the solar spectrum by a factor of 10^5. The integrated proton flux of the solar event spectrum is $I_{\rm p}(E > 10\,{\rm MeV}) = 151 {\rm cm^{-2}\,sr^{-1}\,s^{-1}}$. Scaling the solar SEP spectrum such that the integrated flux corresponds to the value we calculated for HD 189733 above results in the spectrum shown in Fig. 2.4 (top panel). The dotted red line represents the SEP event at the orbit of HD 189733 b and coincides with the spectrum for the active T Tauri star at a distance from the star of 1 au. This allows us to use both the spectrum and the parametrized ionization rate (below) for the active T Tauri star from Rab et al. (2017). Please note, that this is only the case because HD 189733 b is much closer to its host star than 1 au. At 1 au, the proton flux from HD 189733 is much smaller than the flux from the active T Tauri star (solid red line). Bourrier et al. (2020) also observed an X-ray flare of HD 189733 which has a slightly higher luminosity than the one observed by (Pillitteri et al., 2010), with an X-ray flare intensity at the planet's orbit of $I_{\rm x} = 7.4\,{\rm W\,m^{-2}}$.

Once we have an SEP spectrum for HD 189733 we can calculate the ionization rate $\zeta_{\rm SEP}$ as a function of the total hydrogen column density $N_{<{\rm H}>} = N_{\rm H} + 2N_{\rm H_2} + 2N_{\rm H_2O} + N_{\rm H^+}$ (Rab et al., 2017, their Eq. 1 & 2):

$$\zeta_{\rm SEP}(N_{<{\rm H}>}) = \zeta_{\rm SEP,0}(N_{<{\rm H}>}) \times \begin{cases} 1 & \text{if } N_{<{\rm H}>} \leqslant N_{\rm E} \\ \exp\left[-\left(\frac{N_{<{\rm H}>}}{N_{\rm E}} - 1\right)\right] & \text{if } N_{<{\rm H}>} > N_{\rm E} \end{cases}, \tag{2.17}$$

[†]Please note that Eq. (2.16) is only valid for fluxes at a distance of 1 au to the star. For HD 189733 b, $I_{\rm x}$ has to be scaled with r^2 to 1 au and then the resulting $I_{\rm p}$ back to the planet's distance to its host star.

Table 2.3: Fitting parameters for the stellar energetic particle (SEP) ionization rates.

Name	l	h
Active Sun at 1 au [a]	-12	-7
Active T Tauri at 1 au [a]	-7	-2
HD 189733 at 1 au	-10.0	-5.0
HD 189733 at 0.031 au	-7.1	-2.1

[a] Rab et al. (2017)

with

$$\zeta_{\mathrm{SEP},0}(N_{<\mathrm{H}>}) = \left[\frac{1}{\zeta_{\mathrm{L}} \left(\frac{N_{<\mathrm{H}>}}{10^{20}\mathrm{cm}^{-2}} \right)^{a}} + \frac{1}{\zeta_{\mathrm{H}} \left(\frac{N_{<\mathrm{H}>}}{10^{20}\mathrm{cm}^{-2}} \right)^{b}} \right]^{-1}, \tag{2.18}$$

$N_{\mathrm{E}} = 2.5 \times 10^{25}\mathrm{cm}^{-2}$, $a = -0.61$, $b = -2.61$, $\zeta_{\mathrm{L}} = 1.06 \times 10^{l}\mathrm{s}^{-1}$, and $\zeta_{\mathrm{H}} = 8.34 \times 10^{h}\mathrm{s}^{-1}$. The exponents l and h depend on the peak proton flux at the top of the atmosphere and are listed in Table 2.3. The resulting ionization rates are shown in Fig. 2.4 (lower panel) together with the ionization rate by the low energy cosmic rays as presented in Section 2.3.3.

2.4 Atmospheric H/C/N/O Composition Under the Effect of XUV, SEP, and CR on HD 189733 b

In this section, we present the atmospheric H/C/N/O gas-phase abundances of HD 189733 b for two different profiles: the substellar and antistellar point, i.e. the day- and nightside, respectively. We will examine the effect of the XUV flux, stellar energetic particles, and cosmic rays on the abundance of neutral molecules and ions.

First, we investigate the effect that the observed changing XUV and FUV radiation (in the following we assume XUV to include FUV radiation) of the host star HD 189733 (Bourrier et al., 2020) has on its planet HD 189733 b. For this, we study the influence of the four different XUV spectra (see Sec. 2.3.2) on the chemical composition of the planetary atmosphere. We concentrate our study on H/C/N/O binding species, metal atoms and their singly ionized states. The variations in the quiescent XUV flux of the host star HD 189733 are too small to significantly change the planet's gas composition. Hence, any variation of the gas-phase abundances must originate from other processes such as flares leading to SEP events. In the following, we will therefore present results for one XUV spectrum only, which is from an observation in September 2011 (Visit B in Bourrier et al., 2020).

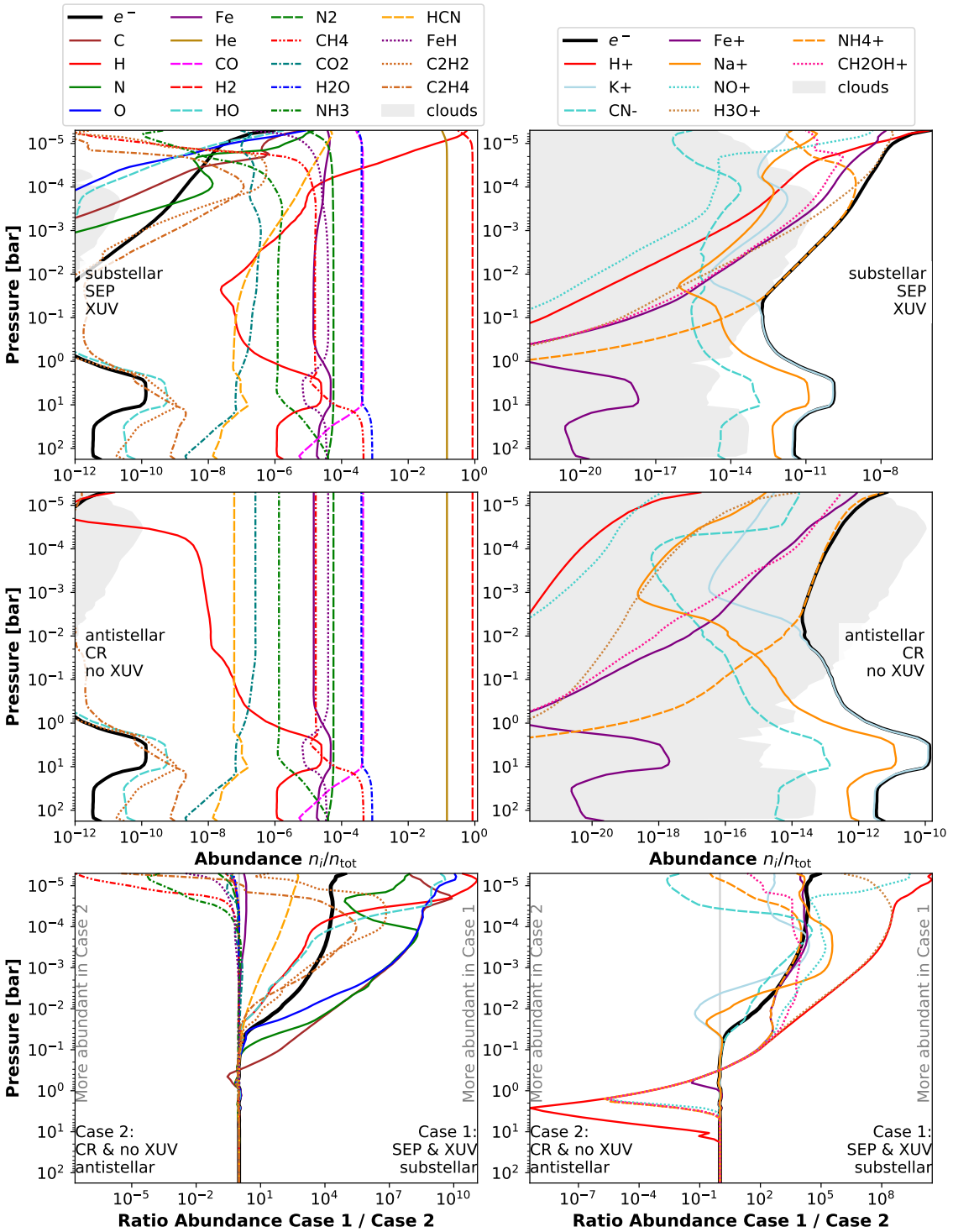

Figure 2.5: Atmospheric composition of HD 189733 b at the day- and nightside profiles: **Top:** substellar point with SEP and XUV radiation (case 1). **Middle:** antistellar point with cosmic rays but no XUV radiation (case 2). Relative abundances (n_i/n_{tot}) of most abundant neutral molecules (**left**) and most abundant ions (**right**) are shown. Thick, black line is the abundance of electrons and gives an estimate on the degree of ionization. Grey area indicates the abundance of cloud particles. **Bottom:** Ratio of abundances of most abundant neutral molecules and ions comparing the two cases shown in the panels above. Please note that the abundances (x axis) change from panel to panel. First published in Barth et al. (2021b).

For the initial element abundances in the atmosphere we assume solar element abundances (Asplund et al., 2009). As clouds form throughout the atmosphere, we account for the depletion of Mg, Si, and Ti due to consumption by cloud particle formation (TiO_2[s], SiO[s], SiO_2[s], $MgSiO_3$[s], and Mg_2SiO_4[s]).

2.4.1 Asymmetric Irradiation of Day- and Nightside

The dayside is irradiated by the stellar XUV radiation and the SEP flux. We do not take into account the galactic cosmic rays (CR) on the dayside since the particle flux is dominated by SEPs for most of the spectrum (Fig. 2.3). Furthermore, CRs are more likely to be shielded by the star's astrosphere on the dayside rather than on the nightside (Rimmer & Helling, 2016). The nightside in turn receives only the influx of CRs. We note that the influx of SEPs into the atmosphere is a function of time and will not be present at all times. Figure 2.5 shows the results of our simulations for both the substellar (top row, case 1) and the antistellar point (middle row, case 2) including the SEP and XUV flux on the dayside and the CR flux on the nightside. The bottom row shows the ratios of the abundances between the substellar and antistellar abundances. The abundances of the most important neutral elements are shown in the left column, the abundances of the most important ions in the right column.

The asymmetric irradiation of the planet's day- and nightside leads to strong differences between the chemical abundances of these profiles. While on the nightside the low energy input from cosmic rays leads to only marginal differences compared to the equilibrium case[†], the high SEP flux and XUV radiation on the dayside enhance atomic species (H, C, N, and O) and increase the abundance of HCN and several hydrocarbons such as C_2H_2 and C_2H_4.

We note that the atmospheres of close-in, tidally locked gas giants are characterised by strong equatorial jets (e.g. Cooper & Showman, 2006; Drummond et al., 2018a; Carone et al., 2020). Such jets lead to very similar day/night vertical temperature distributions (see Fig. 2.1a). Drummond et al. (2020) showed that a strong equatorial jet with zonal-mean velocities of $\sim 6\,\mathrm{km\,s^{-1}}$ may result in kinetic quenching of the methane abundances above $\sim 1\,\mathrm{bar}$ for all three wind components (zonal, meridional, and vertical). Unlike in their previous work (Drummond et al., 2018b) where they applied a simple chemical relaxation scheme by Cooper & Showman (2006), Drummond et al. (2020) used a more accurate coupled chemical kinetics

[†]This does not describe thermo-chemical equilibrium since vertical mixing is still present in these simulations. It rather describes the case without additional external, high-energy radiation sources.

scheme similar to what we use in this study. However, they used a reduced chemical network of Venot et al. (2019), containing only 30 species and 181 reactions.

Agúndez et al. (2014) used a 'pseudo-2D' model, moving a 1D column with vertical mixing along the equator to imitate a solid-body rotation of the atmosphere, including photochemistry. They used a chemical network with 105 species developed by Venot et al. (2012) and found that horizontal quenching enhances the abundance of HCN on the nightside by transporting photochemically produced HCN from the day- to the nightside. A first order comparison of the destruction time scale of HCN, CH_2O, and C_2H_4 to the transport time-scale from the sub- to the antistellar point indicates that the destruction time-scales are orders of magnitudes shorter than the transport time. At $6\,\mathrm{km\,s^{-1}}$, gas will be transported from the sub- to the antistellar point in approximately 12 h. In comparison to that, the destruction rates of HCN, CH_2O, and C_2H_4 are much faster, meaning it would take only 16, 0.3, and 5 min, respectively, to destroy the dayside abundances of these molecules. However, Moses et al. (2011) showed that changes in the abundance of NH_3 also impact the abundance of other nitrogen-bearing species even if they would otherwise not be quenched. Thus HCN remains in a 'pseudo equilibrium' with NH_3 and CH_4 and the potential horizontal quenching of these species has to be taken into account as well.

2.4.2 The Atmospheric Electron Production Rate and Fingerprint Ions

The ionization of the atmospheres of exoplanets and the electron production rates by XUV radiation and high-energy particles are linked to various high-energy processes. One example is the production of auroral emission that might be observable with future telescopes and help us understand the magnetic field of the planet (Burkhart & Loeb, 2017; Luger et al., 2017; Vedantham et al., 2020). Furthermore, ion production in the atmosphere will also ionize cloud particles which is necessary for the occurrence of lightning: the larger a cloud particle, the higher the charge it acquires and the faster it will gravitationally settle within its host cloud. Such particle settling leads to the buildup of a local electric field in the cloud, and if the field is large enough, a lightning strike will occur (Helling et al., 2011b,a; Helling & Rimmer, 2019). In an Earth-like atmosphere, a lightning strike produces an approximately 30 000 K hot plasma channel which only exists for a few seconds but has a strong influence on the chemistry in the surrounding atmosphere (An et al., 2019). The detailed effect of lightning on the atmospheric chemistry will be the focus of Chapter 3.

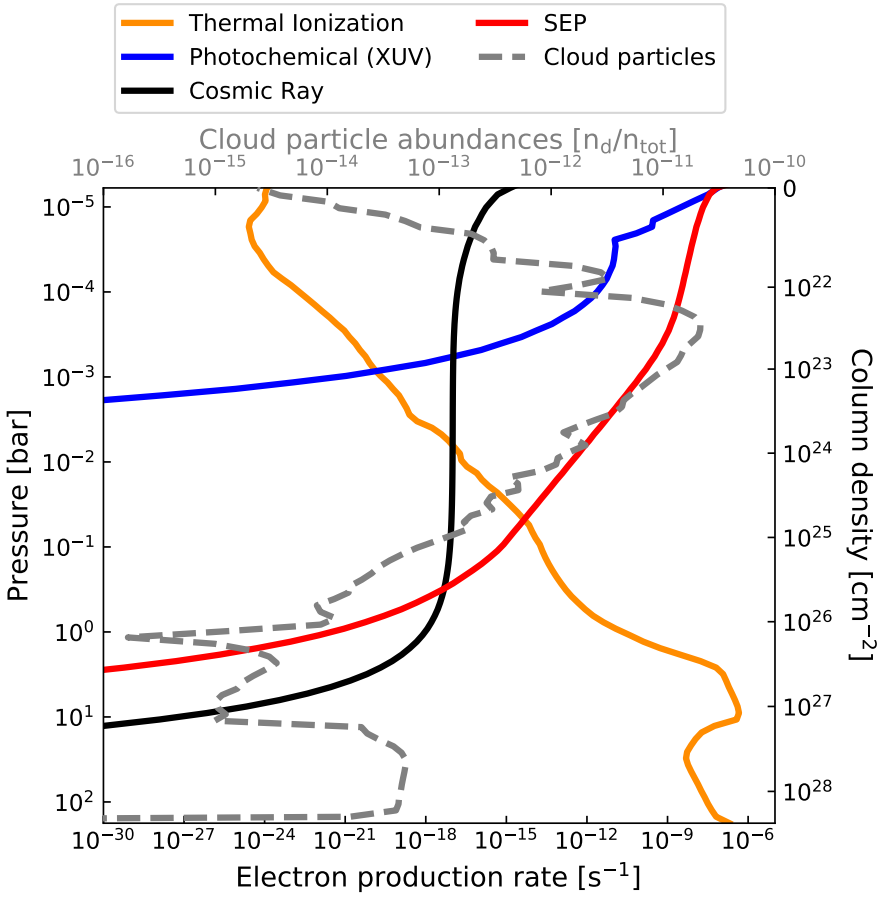

Figure 2.6: Overview of electron production rates as a proxy for the ionization rates of the individual ionization sources plotted against the atmospheric pressure and the atmospheric column density. Cloud particle abundances (*grey*) are added for comparison as the position of clouds and electrons are important for the presence of lightning. The temperature profile and cloud particles used for these simulations are for the substellar point. Note that the column density at the top of the atmosphere is by definition 0 since we do not have data on the layers further up. First published in Barth et al. (2021b).

To investigate the ionization environment of HD 189733 b's atmosphere, we calculate the electron production rates for all included ionization sources (XUV, SEP, and CR radiation as well as thermal ionization). Figure 2.6 shows a comparison of these ionization rates. In addition, the cloud particle density is shown to get an idea of the cloud position in comparison to the charge positions.

The lower atmosphere up to $10-100$ mbar is in all cases dominated by thermal ionization. Above $10-100$ mbar, ionization by external sources becomes more important. The electron production rates by XUV radiation, SEP, and CR can be explained by the shape of the individual spectra (Fig. 2.3): the XUV flux is very high but at the lower end of the energy spectrum. Most of the energy is deposited in the uppermost layers of the atmosphere, and comparatively few photons can ionize deeper layers. The SEP flux is slightly lower in magnitude but at much

higher energies and can therefore penetrate deeper into the atmosphere. The CR flux is much lower, leading to a correspondingly lower electron production rate compared to that of other radiation sources. Around 1 GeV, the CR flux is higher than the SEP flux, meaning that CRs can reach even deeper levels of the atmosphere. However, in these layers, the thermal ionization rate is much higher than that of the CRs. Expanding the parametrization of the CR ionization rate to high energy CR ($> 1\,\mathrm{GeV}$) would only shift the drop off of the CR electron production rate to higher pressures but would not increase the electron production rate itself.

The most important electron donors in the deep atmosphere ($p \gtrsim 10^{-2} - 10^{-1}\mathrm{bar}$) are potassium and sodium (Fig. 2.5, right top and centre panel). The most abundant ion produced by both CR and SEP is ammonium NH_4^+. In addition, the high ionization rates associated with the SEP flux and to a lesser extent with XUV radiation, produce a larger variety of ions: H_3O^+ and H^+, as well as smaller amounts of Fe^+ and CH_2OH^+. Therefore, we identify NH_4^+ and H_3O^+ as the fingerprint ions for ionization by SEP and NH_4^+ for ionization by CR.

2.4.3 The Effect of High-energy Radiation on the Production of Organic, Prebiotic Molecules

Ultimately, we are interested in the effect of the different types of high-energy radiation on the organic and prebiotic chemistry. The famous experiment by Stanley Miller and Harold Urey suggests that lightning is an important source of organic molecules, at least in a reducing (i.e. hydrogen rich) atmosphere (Miller, 1953). Cloud-forming exoplanets such as HD 189733 b are expected to produce lightning due to their very dynamic and cloudy atmosphere (Lee et al., 2016; Lines et al., 2018). Before we can study the effect of lightning on the atmospheric chemistry and identify observable signatures, we need to understand the effect of other types of high-energy radiation on potential lightning signatures in the chemical abundances.

The average oxidation state of the carbon and nitrogen atoms in the C and N bearing molecules provides an overview over the processes in the atmosphere and their effect on these molecules. The oxidation state of an atom in a compound indicates the charge it would have if all bonds in the compound were ionic. One example is the oxidation state of the carbon atom in different neutral carbon molecules: CH_4 is the most reduced form of carbon with an oxidation state of -4, i.e. the C atom is slightly more electronegative and attracts the electrons from each of the four H atoms. CO_2 in comparison is the most oxidized form of carbon with an oxidation state of $+4$ as the O atoms have a higher electronegativity than C. As oxygen and

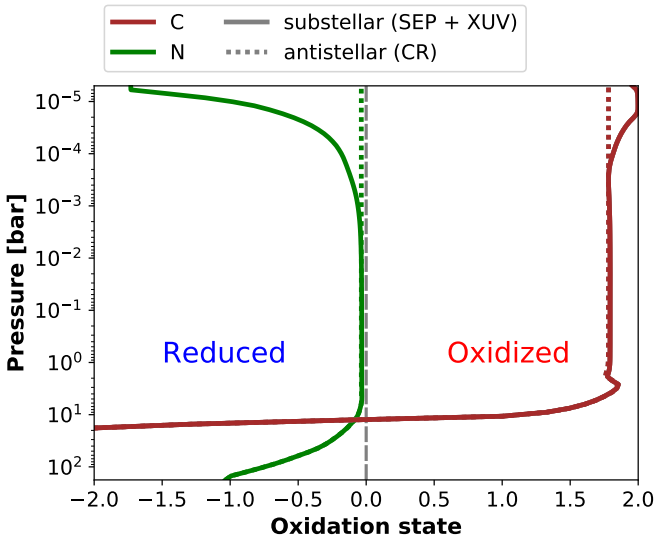

Figure 2.7: Average oxidation state of nitrogen (*green*) and carbon (*brown*) atoms in the atmosphere of HD 189733 b at the substellar (*solid*, SEP + XUV) and antistellar point (*dotted*, CR). Cosmic rays alone do not change the oxidation state of carbon and nitrogen, i.e. the antistellar profiles are the same as the equilibrium case. The dashed grey line indicates a neutral oxidation state. Negative values mean the nitrogen and carbon are reduced, positive values indicate a oxidized state. First published in Barth et al. (2021b).

hydrogen are, respectively, the most and least electronegative elements of the most abundant elements (the others being carbon and nitrogen, while helium is a noble gas and has therefore no defined electronegativity), the oxidation state of a gas can be approximated by the H/O ratio with H having an oxidation state of $+1$, i.e. reducing the C or N atom, and oxygen an oxidation state of -2.

Figure 2.7 shows the oxidation states of the C and N atoms at HD 189733 b's sub- and antistellar point. The most abundant nitrogen species is N_2 which is by definition neither oxidized nor reduced (oxidation state of 0). Therefore, the average oxidation state of the nitrogen atoms is close to zero. The second most abundant nitrogen molecule in most of the atmosphere is NH_3, where the nitrogen is reduced (-3). The SEP strongly enhance the abundance of HCN in the upper atmosphere (Fig. 2.5), further reducing the nitrogen. Importantly, life as we know it requires reduced N for the production of biomolecules such as amino acids and nucleobases. High-energy radiation may therefore make atmospheric N more bioavailable.

The effect on the average oxidation state of carbon is very different. Except for the very deep parts of the atmosphere of HD 189733 b ($p > 10\,\mathrm{bar}$), where methane is the most abundant carbon molecule and therefore reducing the atmospheric carbon, most of the carbon is bound in CO which has an oxidation state of $+2$. The enhanced abundance of HCN that further

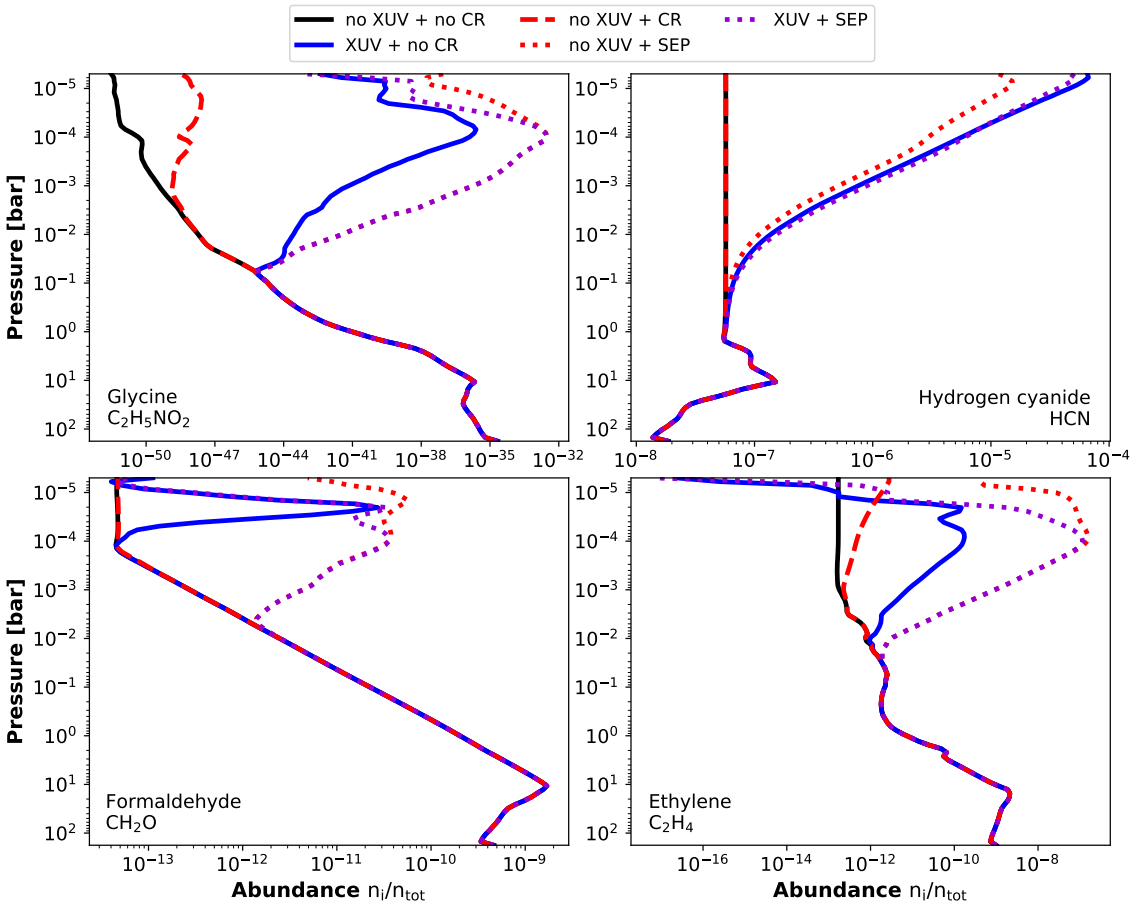

Figure 2.8: Abundance of glycine (**top left**), HCN (**top right**), formaldehyde (CH_2O, **bottom left**), and ethylene (C_2H_4, **bottom right**), in the atmosphere of HD 189733 b at the substellar point with different combinations of the ionization sources XUV radiation, SEP, and CR. We note that a lightning induced HCN increase would be best observable on the nightside as we do not see any enhancement by other ionization sources. Note the different ranges on the x axis. First published in Barth et al. (2021b).

reduces the atmospheric nitrogen when adding SEP radiation, leads to an additional oxidation of carbon in the upper atmosphere. In biomolecules, the oxidation state of organic carbon is variable with an average around 0. Both oxidized and reduced carbon can act as metabolites for autotrophic life and is therefore readily bioavailable.

The species that dominates the change in the oxidation state of carbon and nitrogen is HCN which contains a CN bond that is also found in the amino acid glycine and in other biomolecules. Figure 2.8 shows the abundance of glycine ($C_2H_5NO_2$, top left) and HCN (top right) with different combinations of external ionization sources XUV, CR, and SEP. The results in Fig. 2.8 are shown using the atmospheric profile at the substellar point. The same results using the atmospheric profile at the antistellar point are not shown because the pressure-temperature structure is very similar for both profiles (see Fig. 2.1a). The STAND2019 network includes the complete gas-phase production reactions for glycine which was one of the amino

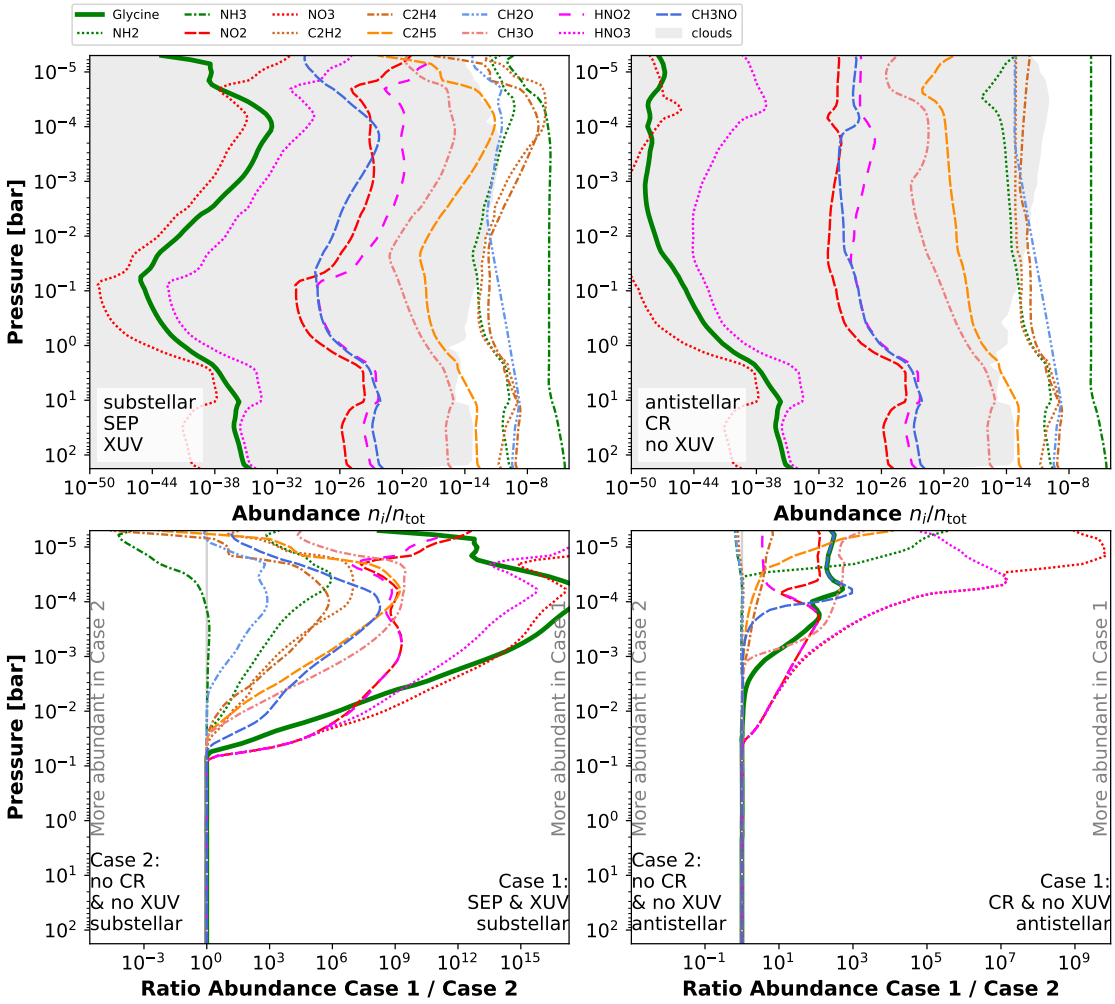

Figure 2.9: Abundances of molecules important for the formation of glycine (*solid green*) in the atmosphere of HD 189733 b. **Top left:** substellar point with SEP and XUV radiation (case 1). **Top right:** antistellar point with cosmic rays but no XUV radiation (case 2). Grey shaded areas indicate the presence of clouds. **Bottom:** Ratio of abundances shown in the panels above to the equilibrium case. First published in Barth et al. (2021b).

acids produced in the original Miller–Urey experiment (Miller, 1953).

We find that all external energy sources lead to an enhancement of the glycine abundance in the upper atmosphere with the much higher flux of SEP and XUV changing the abundance by up to 18 orders of magnitude. The lower CR flux only increases glycine by up to three orders of magnitude. Nevertheless, the overall abundance of glycine is very low (below 10^{-30}) such that the presence of glycine in the atmosphere of this planet will be challenging or impossiible to detect. HCN, however, is much more abundant (up to 10^{-4}) and similarly enhanced by SEP and XUV radiation. Therefore, HCN provides an example of an observable signature that suggests the presence of prebiotic molecules. CRs alone cannot significantly enhance the abundance of HCN in the atmosphere. This result presents an opportunity for the future

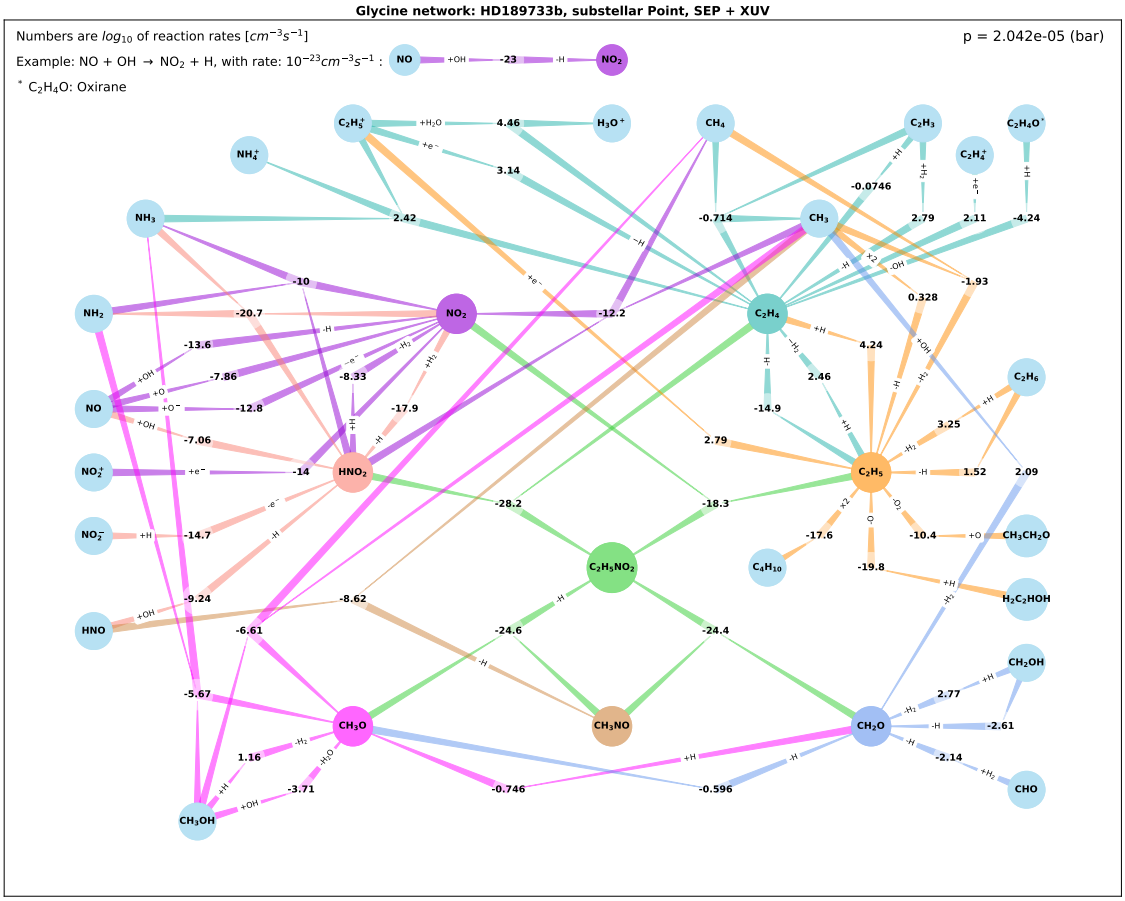

Figure 2.10: Production pathways of glycine ($C_2H_5NO_2$, *green*) and its precursors. Numbers are reaction rates ($cm^{-3}\,s^{-1}$, $\log_{10}$) for forward reactions (in the direction towards the sharp end of the lines, mainly from the outer regions towards the centre of the network) producing the molecule in the same colour as the arrows and potential side products. Reaction rates for reverse reactions are not shown. Small, abundant reactants and products (e.g. OH) are written along the reaction path to decrease number of paths; '+': molecule is added to reaction, '-': molecule is additional product of reaction, '×2': 2 CH_3 molecules needed for production of C_2H_5. Examples: NH_2 and HNO_2 (*pink*) produce NH_3 and NO_2 (*purple*) at a rate of $10^{-10}cm^{-3}\,s^{-1}$; NO and OH produce NO_2 (*purple*) and H at a rate of $10^{-13.6}cm^{-3}\,s^{-1}$. First published in Barth et al. (2021b).

study of the effect of lightning on the nightside of the planet: with SEPs and XUV unable to reach that side of the planet, lightning might be the only way to significantly enhance the HCN abundance at the antistellar point. We note, however, that this conclusion is only valid if horizontal transport between the day- and nightside can be neglected (Section 2.4.1).

Figure 2.9 shows the abundance of glycine and its precursors at the substellar (case 1) and antistellar (case 2) points with the same energy sources as in Fig. 2.5, and the ratio between both abundances. In addition, Fig. 2.10 shows the reaction rates for the production pathways of glycine at the substellar point (SEP + XUV) at a pressure of $p = 2 \times 10^{-5}$bar. The numbers between the reactants and products in Fig. 2.10 are the reaction rates ($cm^{-3}\,s^{-1}$, $\log_{10}$) in the

Table 2.4: Pathways of glycine production at $p = 2 \times 10^{-5}$bar in the atmosphere of HD 189733 b at the substellar and antistellar point, as well as for the equilibrium case. Colours correspond to path diagram (Fig. 2.10), bold numbers indicate most important pathways.

	$\log_{10}$(Rate [$cm^{-3}\,s^{-1}$])		
Reaction	**Equ.**	**CR**	**SEP + XUV**
$C_2H_5^+ + H_2O \longrightarrow C_2H_4 + H_3O^+$	-47.1	**-3.47**	**4.46**
$C_2H_5^+ + NH_3 \longrightarrow C_2H_4 + NH_4^+$	-48.1	-4.42	2.42
$C_2H_5^+ + e^- \longrightarrow C_2H_4 + H$	-55.1	-9.22	3.14
$C_2H_3 + H_2 \longrightarrow C_2H_4 + H$	**-8.32**	-6.73	2.79
$C_2H_4 + H \longrightarrow C_2H_5$	**-7.12**	**-9.29**	**4.24**
$NO + OH \longrightarrow HNO_2$	**-21.7**	**-20.7**	-7.06
$NO + O \longrightarrow NO_2$	-31.4	-21.6	**-7.86**
$HNO_2 + NH_2 \longrightarrow NO_2 + NH_3$	-24.3	**-24.0**	-10.0
$HNO_2 + H \longrightarrow NO_2 + H_2$	**-22.5**	-25.2	-8.33
$CHO + H_2 \longrightarrow CH_2O$	**-6.35**	-9.17	-2.14
$CH_2OH \longrightarrow CH_2O + H$	-11.8	**-8.14**	-2.61
$HNO + CH_3 \longrightarrow CH_3NO$	**-22.9**	**-21.3**	-8.62
$NO_2 + C_2H_5 \longrightarrow C_2H_5NO_2$	-36.0	-38.3	**-18.3**
$CH_3NO + CH_2O \longrightarrow C_2H_5NO_2$	**-35.2**	**-32.1**	-24.4

direction towards the sharp end of the lines. The rates of the reverse reactions are not shown. Table 2.4 shows the rates of the most important production pathways of glycine for three different cases: the equilibrium substellar point (no SEP or XUV), the antistellar point (CR), and the substellar point (SEP and XUV). The comparison of these different pathways shows that SEP and CR strongly enhance the production of C_2H_4 from $C_2H_5^+$ with the byproducts H_3O^+ and NH_4^+ which belong to the most abundant ions in these scenarios (Fig. 2.5). At the substellar point (SEP + XUV), this pathway is the most efficient pathway of glycine production:

$$C_2H_5^+ + H_2O \longrightarrow C_2H_4 + H_3O^+ \tag{2.19}$$

$$C_2H_4 + H \longrightarrow C_2H_5 \tag{2.20}$$

$$C_2H_5 + NO_2 \longrightarrow C_2H_5NO_2 \tag{2.21}$$

Formaldehyde (CH_2O) and ethylene (C_2H_4) belong to the most important and most abundant precursor molecules of glycine. Similarly to glycine and HCN, they are strongly enhanced by the influx of SEP and XUV radiation in the upper atmosphere. The bottom half of Fig. 2.8

shows the abundances of these organic molecules for different combinations of high-energy radiation.

2.5 Conclusion

In this work we studied the influence of different high-energy radiation sources on the atmospheric H/C/N/O chemistry of the hot Jupiter HD 189733 b. We combined recent simulations of the planetary atmosphere with the 3D Met Office Unified Model which self-consistently takes into account cloud formation (Lines et al., 2018) with three different sources of high-energy radiation:

1. multi-epoch observations of the stellar X-ray and UV spectrum (Bourrier et al., 2020),
2. low-energy cosmic rays (Rimmer & Helling, 2013), and
3. stellar energetic particles associated with an X-ray flare observed by Pillitteri et al. (2010) and based on a parametrization by Rab et al. (2017) and Herbst et al. (2019b).

We then simulate the effect of these processes on the atmospheric chemistry of HD 189733 b with the ion-neutral kinetics network STAND2019.

We identify ammonium (NH_4^+) and oxonium (H_3O^+) as important and potentially observable signatures of an ionization of the atmosphere by cosmic rays and stellar particles. Even though we note that glycine abundances remain low ($< 10^{-30}$) in all our simulations, the influx of XUV radiation and SEPs enhances glycine by nearly 20 orders of magnitude. In addition, we identify two important precursors for the production of glycine: formaldehyde (CH_2O) and ethylene (C_2H_4), which are strongly enhanced by incoming XUV radiation and more so by the influx of SEPs. Especially the abundance of ethylene gets enhanced to potentially observable values for *JWST* in the upper atmosphere (Gasman et al., 2022). Ethylene has a strong absorption feature around 10 µm (Mant et al., 2018) which could be detected by emission spectroscopy (Hu & Seager, 2014). We therefore propose ethylene and potentially formaldehyde to be important signatures for incipient prebiotic synthesis under the influence of stellar energetic particles and XUV radiation.

Ethylene and other hydrocarbons have also been predicted by simulations of Jupiter's atmosphere by Moses et al. (2005) and with STAND2015 by Rimmer & Helling (2016). In addition, these molecules have been detected by observations in the stratosphere of Jupiter (e.g.

Gladstone et al., 1996; Moses et al., 2005; Romani et al., 2008). Due to the very different temperature of Jupiter's atmosphere (in comparison to HD 189733 b's atmosphere), however, we do not expect much glycine to form as most of the nitrogen and oxygen will be bound in NH_3 and H_2O ice, respectively.

Even though hot Jupiters are not ideal places for the formation of complex, prebiotic molecules such as glycine, they provide a unique laboratory to study the first steps of prebiotic synthesis under the influence of different high-energy radiation sources. This is not least due to the better observability of giant gas planets in comparison to Earth-sized terrestrial planets. Stellar energetic particles and XUV and FUV radiation strongly enhance the abundance of hydrocarbons and other organic molecules. In particular, XUV radiation enhances the abundance of HCN to nearly 10^{-5} at the top of the atmosphere. HCN is a crucial molecule in prebiotic chemistry and the formation of amino acids (Airapetian et al., 2016, 2020). We note that the influx of cosmic rays on the nightside is not strong enough to produce additional HCN. It will be therefore of special interest to study the production rate of HCN by lightning on the nightside where it could potentially be observable.

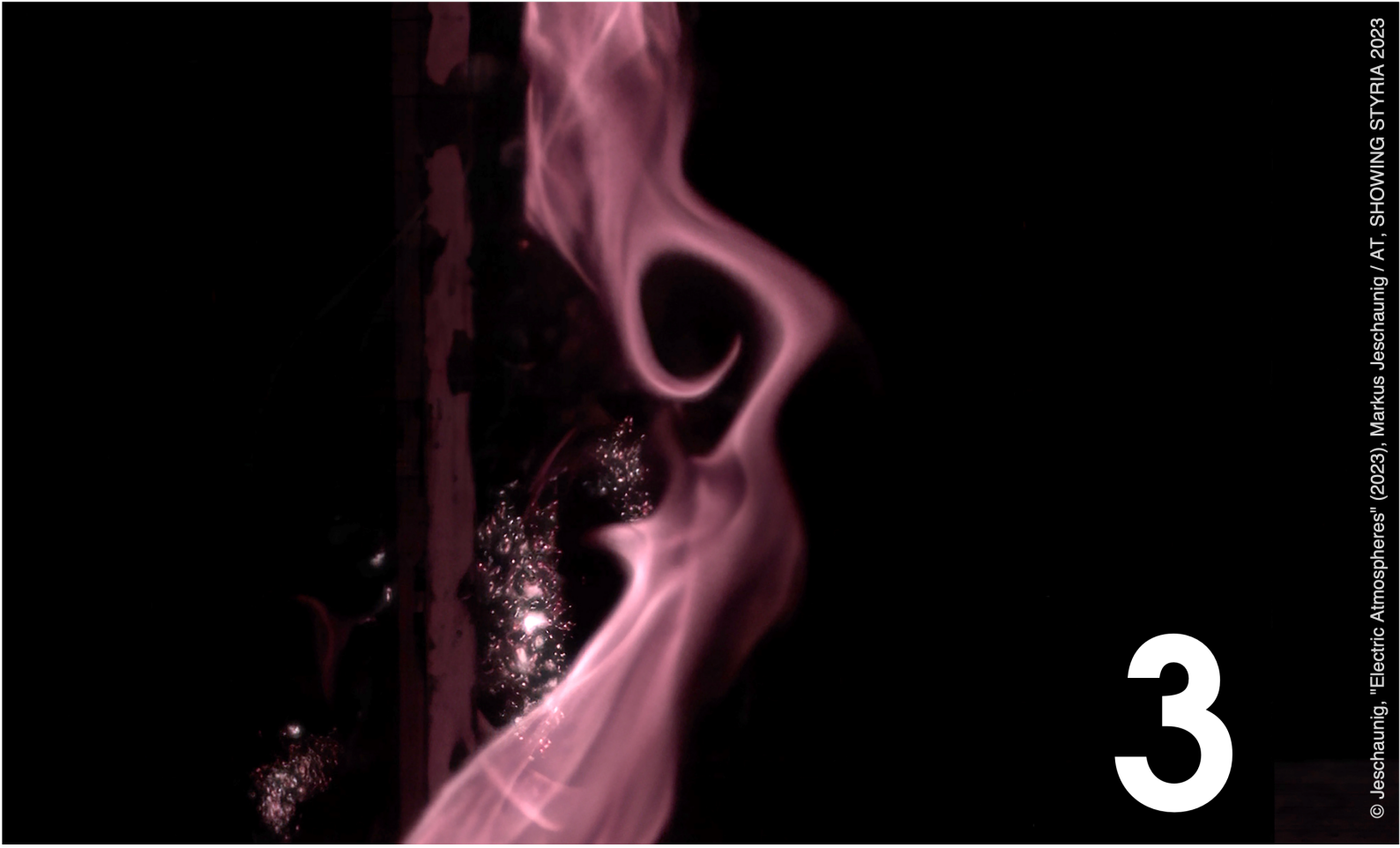

3

Tracing the Chemistry of Atmospheric Discharges on Early Earth and Exoplanets

Having discussed the effect of different types of high-energy radiation on the atmospheric chemistry of exoplanets in the previous chapter, this chapter focuses on the role of lightning in different kinds of atmospheres: To study lightning chemistry in the atmospheres of Earth and terrestrial exoplanets, we conducted a range of spark discharge experiments. The setup of the experiments and the analytical methods are discussed in Section 3.1. We also conducted chemical kinetics calculations and photochemical simulations, as well as simulations of atmospheric spectra. These computational methods are presented in Section 3.2. We continue, discussing the experimental results on the role of lightning as a source of nutrients on early Earth in Section 3.3, and the investigation of lightning's potential to produce false-positive or false-negative biosignatures, as well as possible lightning signatures in exoplanetary atmospheres in Section 3.4.

3.1 Spark Discharge Experiments

3.1.1 The Experimental Setup

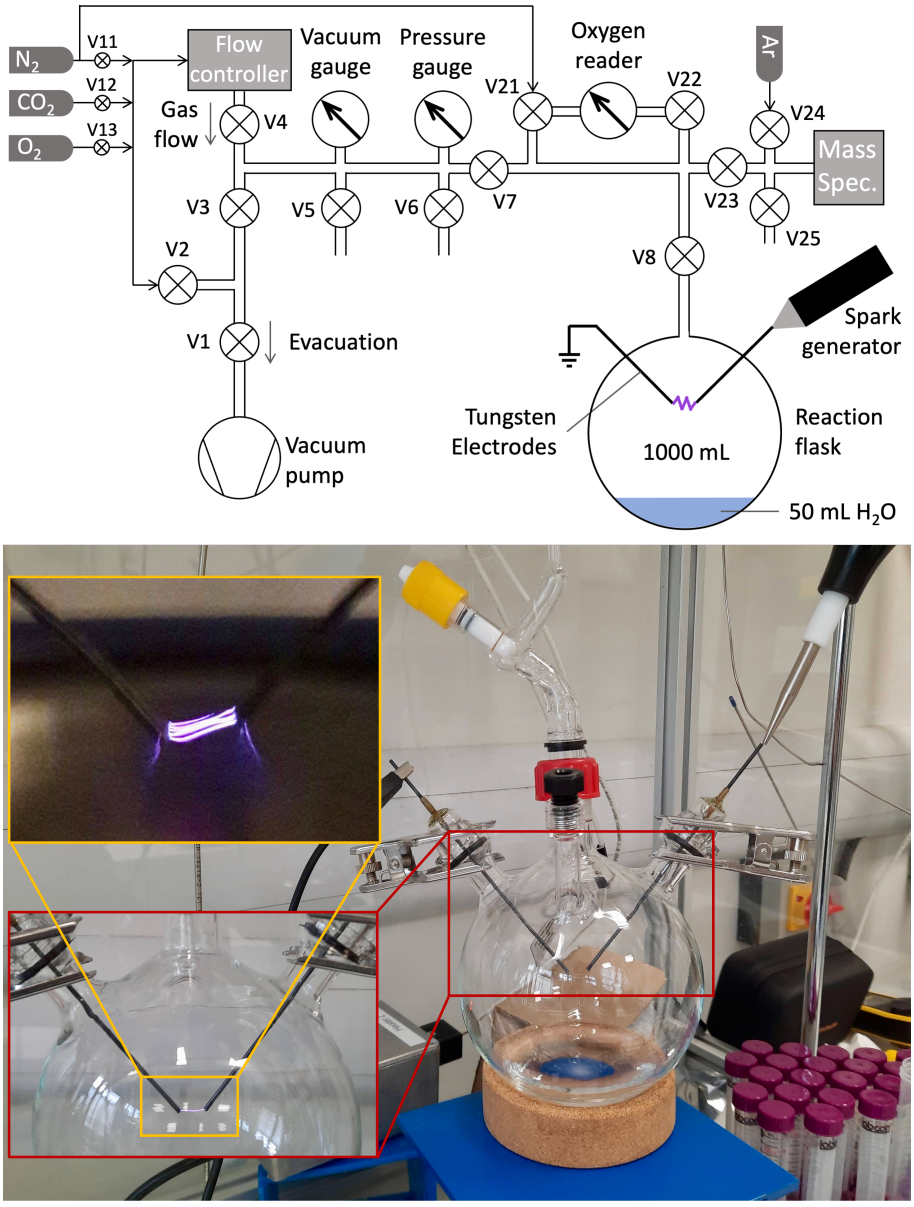

Figure 3.1: Schematic (first published in Barth et al., 2023a) and photo of experimental setup of the discharge experiment.

All experiments were carried out at the University of St Andrews in the St Andrews Isotope Geochemistry Lab (StAIG). We used an experimental setup similar to the one described by Parker et al. (2014) (Fig. 3.1). The spark discharge was contained in the 1-litre reaction flask (Pyrex glass), which contained 50 mL of water at the bottom and the spark electrodes (tungsten metal) secured in the headspace. This flask was connected to a vacuum line (stainless

steel) with an ultra-torr fitting and thus could be disconnected at the end of the experiment. The sparks were generated by a BD-50E heavy-duty spark generator with a maximum voltage of 49 kV which produces a continuous series of sparks with a frequency of 0.5 MHz. Before starting an experiment, the system was evacuated by opening V1 and V3 to the vacuum pump. The valve to the reaction flask (V8) was only opened once the rest of the line was evacuated to minimize evaporation of water from the experimental flask. Once the pressure within the flask had reached a few mbar, V3 and V1 were closed and the system was filled with N_2 gas via V2 up to 1 bar pressure. The N_2 was re-evacuated, and this process was repeated two times to completely purge the reaction flask. After that, the desired gas mixture was introduced. For small contributions of individual gases, we used a flow controller (Bronkhorst EL-FLOW Prestige). Before starting the spark discharge, valve V8 was closed to disconnect the reaction flask from the rest of the setup. An oxygen sensor was used to monitor the trace amount of oxygen present in anoxic experiments.

We performed to sets of experiments with different gas mixtures and analysed them for different compounds:

- **Set 1**: Experiments with N_2-O_2 (modern) and N_2-CO_2 (Archean-like) gas mixtures, performed between November 2020 and February 2022. These experiments were analysed for NO, NO_2, nitrite (NO_2^-), nitrate (NO_3^-), and ammonium (NH_4^+), as well as for the nitrogen isotope ratios of nitrite and nitrate. A subset of samples was shipped to Brown University for analysis of nitrite and nitrate as well as nitrogen and oxygen isotopes. The results and discussion of these experiments are presented in Section 3.3. A table with the detailed results can be found in Barth et al. (2023c).

- **Set 2**: Experiments with $N_2-CO_2-H_2$ gas mixtures, performed between May and August 2022. These experiments were analysed for NO, CO, N_2O, CH_4, nitrite (NO_2^-), nitrate (NO_3^-), ammonium (NH_4^+), cyanide (CN^-), and urea. The CO analysis was performed at Newcastle University for a subset of samples. The results and discussion of these experiments are presented in Section 3.4. A table with the detailed results can be found in Barth et al. (2023b).

In order to investigate the effect of water vapor in the gas phase on the final results, a set of dry experiments was run for Set 2. For these, we added the water with a syringe through the septum port on the flask only after the spark had been turned off. The water was previously

flushed with pure N_2 (10 min at $\sim$ 50 mL min^{-1}) to remove dissolved oxygen. We did then let the experiment with the water sit for 3 hours (with the spark still switched off) to allow for the gaseous and liquid phase to equilibrate. The water was continuously stirred with the magnetic stir bar to facilitate gas exchange between the headspace and the liquid phase.

Before and after each experiment, the gas from the flask was allowed to flow towards a quadrupole mass spectrometer gas analyser via V23 (see below for analytical method). We did not perform gas analyses during the experiment, because we found that a larger reservoir of NO and NO2 needed to be generated before reliable measurements could be made. When not connected to the experiment, argon gas was fed to the mass spectrometer via V24 and V25 to keep the system free from contaminants. After the experiment, a gas sample was extracted from the flask with a gas-tight, lockable syringe to determine the concentration of CH_4 and N_2O with a gas chromatograph. From a limited sample of experiments of Set 2, multiple gas samples were extracted for analyses of CO. The fluid phase was transferred into a 50ml Falcon centrifuge tube for subsequent analyses of dissolved nitrite, nitrate, ammonium, urea, and cyanide (see below). From these concentrations, the energy yield (molecules/J) can be calculated, using the energy of the spark $E = UIt/2$ with the applied voltage $U = 49$ kV, the current $I = 1$ mA, and the duration t of the spark. To extrapolate this yield to an annual, global production, we used an estimate for the global lightning flash rate on modern Earth of $44 \pm 5\,s^{-1}$ (Christian et al., 2003) with an energy of 6.7 GJ per flash (Price et al., 1997a).

3.1.2 Analysis of Gaseous Species

Nitrogen Oxides (NO_x)

Before and after the spark experiment, the gas composition in the flask was analysed with a quadrupole mass spectrometer (Hiden Analytical ExQ Quantitative Gas Analyser) to determine the abundance of all gases, including NO and NO_2. The instrument was run in 'multiple ions detection' mode to monitor the abundance of several mass/charge ratios (m/z) (12, 14, 15, 16, 17, 18, 20, 28, 30, 32, 40, 46, 48) and thus detect N_2, O_2, CO_2, NO, N_2O, NO_2, and O_3. When analysing the pure N_2-O_2 gas before running the spark experiment, a peak at m/z 30 was detected. This is likely due to the recombination of ^{14}N and ^{16}O fragments from the N_2 and O_2, respectively, to NO inside the mass spectrometer (Cardinal et al., 2003). By comparing measurements from before and after the spark experiment, this interference could be subtracted. We found these background measurements to be very stable with variations in the

background between 3% and 17% for the Archean-like and modern experiments, respectively. We also measured and subtracted the background for the other masses and used the standard deviation of these background measurements for the error of our gas measurements. However, after combining multiple measurements, the standard deviation of this average is substantially larger than the combined individual errors which scale with $1/\sqrt{N}$ for N data points.

To determine the molecular abundances from the measured intensities, we used the mass spectra provided in the database of the NIST Mass Spectrometry Data Center, which accounts for fragmentation of molecules in the ion source of the instrument. Unfortunately, N_2O produced signals at m/z 30 and 44, overlapping with peaks for NO and NO_2 at m/z 30, and CO_2 at m/z 44. However, calculations and experiments suggest that N_2O production in lightning and discharge experiments is approximately 4 magnitudes lower than NO production Levine et al. (1979); Hill et al. (1984), suggesting that the contribution of N_2O to the peak at m/z 30 can be neglected. The abundance of NO_2 could be determined by the signal intensity of the m/z 46 peak; the abundance of NO from m/z 30 after subtracting the contribution by the NO-fragment from NO_2. For experiments with a high CO_2 abundance, the CO_2 isotopologue $^{16}O^{12}C^{18}O$ also contributes to the m/z 46 peak. We tried to subtract this interference, but the uncertainty is relatively large. The data from the CO_2-rich experiments of Set 1 therefore only gave us an upper limit of the NO_2 concentration. As most experiments of Set 2 included CO_2, we could not measure the concentration of NO_2 for those experiments. We also found trace amounts of ozone (m/z 48) of $\sim 8\times10^{-7}$ bar in the N_2-CO_2 experiments and $\sim 4\times10^{-5}$ bar in the modern atmosphere experiments of Set 1, with the detection limit being $\sim 10^{-7}$ bar (100 ppb).

Carbon Monoxide (CO)

A limited number of samples of Set 2 was analysed for their concentration of CO at the School of Natural and Environmental Sciences, Newcastle University, with an SRI 8610C gas chromatograph with an Hg reduction gas detector (RGD). The following run parameters were used: 25 psi N_2 carrier gas at 20 mL min^{-1}; column oven at 80°C; 5 min run time with the RGD at 280°C and in low sensitivity setting. All samples were diluted by a factor of 100 by adding 120 µL of the sample to an exetainer vial filled with 12 mL of N_2. 3 mL of N_2 were then injected into the diluted samples in the exetainer, the gas was mixed using a 5 mL gas-tight syringe, and then 3 mL of the gas were injected into a 0.5 mL sample loop on the GC.

The sample loop then injected 0.5 mL of the gas into the column (molecular sieve 5A packed 60/80 mesh, 6 ft length). The centre of the CO peak leaves the column after approximately 3.0 to 3.1 minutes, depending on the concentration. No evidence of any interfering peaks in standards or samples was found. 1 ppm and 10 ppm standards were prepared by diluting a certified 100 ppm CO in N_2 standard (Calgaz Ltd). A four point calibration (0, 1 , 10, 100 ppm) was performed. Multiple 100 ppm standard runs were conducted to determine the precision of the measurement to 3.5%. The error of both dilution steps is estimated to be 8.3%, giving a combined error of the CO concentration measurements of 12.3%.

Methane (CH_4) and Nitrous Oxide (N_2O)

Concentrations of methane (CH_4) and nitrous oxide (N_2O) were measured for our experiments in Set 2 with a Thermo Fisher gas cromatograph (Trace Ultra) equipped with an electron capture detector (ECD) for N_2O and a flame-ionization detector (FID) for CH_4. The packed column was held at 60°C, the ECD at a base temperature of 180°C and a central temperature of 330°C, and the FID at 300°C throughout the run. 10 mL of sample gas were extracted from the experiment with a gas-tight, lockable syringe through the septum, and this volume was injected undiluted into the GC to fill and flush out the 2 mL sample loop. Helium was used as a carrier gas at a pressure of 450 kPa. Auxiliary gases for the detectors were N_2 (10 mL min^{-1}), H_2 (35 mL min^{-1}) and zero air (350 mL min^{-1}). Analysis of the measurements is limited by the availability of only one standard gas mixture (CH_4: 10 ppm, N_2O: 2.5 ppm). The lowest methane concentration that still produced a recognizable peak was about 0.2 ppm. However, this limit could not be tested with a low standard. Repeated measurements of the standard produced a standard deviation of 0.6 ppm, a relative error of 6%, which we assume for the error of each individual measurement.

3.1.3 Analysis of Aqueous Species

Nitrate (NO_3^-) and Nitrite (NO_2^-)

For the experiments of Set 1: To determine the concentrations of nitrate (NO_3^-) and nitrite (NO_2^-) in our solutions, we used a Metrohm 930 ion chromatograph (IC) with a Metrohm 919 autosampler, a 150 mm Metrosep A Supp 5 separation column (4 mm bore) with 3.2 mM Na_2CO_3 / 1 mM $NaHCO_3$ anion eluent at a flow rate of 0.7 mL min^{-1}. We ran it using a Metrohm suppressor module with a phosphoric and oxalic acid eluent suppressor solution.

The subset of samples shipped to Brown University was analysed for NO_2^- and NO_3^- using colorimetric and IC analytical techniques. The concentration of NO_2^- was determined using a standardized colorimetric technique (e.g., US EPA Method 353.2) involving the diazotization with sulfanilamide dihydrochloride followed by detection of absorbance at 520 nm that was automated using a discrete UV-Vis spectrophotometer (Westco SmartChem). The analysis of the NO_3^- concentration was conducted using a reagent-free Dionex Integrion HPIC System with a Dionex AS-HV Autosampler, Dionex AG19 guard and analytical columns, with 20 mM KOH anion eluent at a flow rate of 1 mL min^{-1}.

For the experiments of Set 2: To determine the concentrations of nitrate (NO_3^-) and nitrite (NO_2^-) in our solutions, we used a Thermo Scientific Dionex ICS-6000 ion chromatograph equipped with a Dionex AS-AP autosampler, a 25 mm Dionex IonPac AS17-C separation column (2 mm bore), a 25 mm Dionex IonPac AG17-G guard column (2 mm bore), and a Dionex ADRS-600 2 mm suppressor. The flow rate was held constant at 0.5 mL min^{-1} while the concentration of the KOH eluent solution was ramped up from 1 mM to 40 mM over 20 minutes.

Ammonium (NH_4^+) and Ammonia (NH_3)

We followed a colorimetric method (Solórzano, 1969; Cleaves et al., 2008) to measure the ammonium concentration in our samples. Three stocks of reagents were prepared in larger quantities and stored for several months: (1) sodium citrate buffer (7.6 g trisodium citrate ($Na_3C_6H_5O_7$) and 0.4 g sodium hydroxide (NaOH) in 500 mL of water), (2) phenol alcohol (1 mL liquefied phenol (C_6H_5OH) in 90 mL of 100% ethanol (C_2H_5OH), brought up to 100 mL with water), and (3) aqueous sodium nitroprusside (0.15 g of sodium nitroprusside ($C_5FeN_6Na_2O$) in 200 mL of water). Each day, an oxidizing solution of 10 mL of the sodium citrate buffer with 0.1 mL of aqueous sodium hypochlorite (ClNaO, with $10-15\%$ available chlorine) was prepared fresh (amount adjusted to number of samples). For our standards, we used a 1 mM stock of NH_4Cl, diluted to 1, 2, 5, 10, 20, 50, and 100 µM. For analyses, 1 mL of sample or standard were transferred into a 15 mL Falcon centrifuge tube, followed by 0.5 mL phenol alcohol, 0.5 mL aqueous sodium nitroprusside, and 1 mL of the oxidizing solution. The mixture is incubated for $60-80$ min at room temperature, allowing it to develop a blue colour. Absorption was measured at 640 nm with a Thermo Fisher Evolution 220 UV-Vis spectrophotometer. We found the detection limit of this method to be at 3 µM. According to Solórzano (1969), there is no interference between ammonium and other nitrogen compounds or sea

water, which contains nitrate. From the ammonium concentration in the water, we can estimate the ammonia concentration in the gas phase. The ratio between the concentration of ammonium in the liquid phase and the pressure of ammonia gas is given by Henry's law constant for NH_3 which is $H = (73 \pm 5)\,\mathrm{M\,bar^{-1}}$ for temperatures between 20 and 23°C (Edwards et al., 1978; Burkholder et al., 2019).

Urea ($CO(NH_2)_2$)

For the quantification of urea in solution (Set 2), we followed the colorimetric method described by Cleaves et al. (2008). The following stocks of reagents were prepared: (1) Acidic ferric chloride (AFC, 0.208 g $FeCl_3 \bullet 6H_2O$ + 20 mL concentrated H_2SO_4 + 2.5 mL 85% H_3PO_4 in 250 mL of DI-water), (2) diacetyl monoxime (DAM, 2.5 g in 100 mL DI-water), and (3) thiosemicarbazide (TSC, 0.25 g in 100 mL DI-water). Each day, 12 mL of DAM stock were combined with 5 mL of TSC stock and 33 mL DI-water. Then 8 mL of this combined DAM-TSC stock were added to 40 mL AFC to prepare the colour reagent. 2 mL of colour reagent are added to 200 µL of sample in a 15 mL centrifuge tubes. The closed tubes are then heated in boiling water for 15 minutes and then analysed at 520 nm with the UV-Vis spectrophotometer. We found the detection limit of this method to be 1 µM. Analyses were calibrated with a 1 mM stock solution of urea, diluted to 1, 2, 5, 10, 20, 50, and 100 µM.

Cyanide (CN^-) and HCN

For the quantification of aqueous cyanide (CN^-) in our experiments of Set 2, we followed the method described by Cacace et al. (2007), which requires three stock solutions of reagents: (1) Borax buffer: 4.767 g of sodium tetraborate decahydrate are dissolved in 500 mL DI-water. The solution is then brought to a pH of 10.8 by adding approximately 2 mL of 10 M NaOH. This buffer can be stored in the fridge for several months. (2) Combined reagents: 0.2996 g copper(II) nitrate trihydrate are dissolved in 20 mL DI-water. Then, 0.1861 g ethylenediaminetetraacetic acid (EDTA) are added and dissolved (stir). Finally, 0.1777 g of phenolphthalin are added and the solution is topped up to 50 mL with DI-water. (3) Stabilizing solution: 0.324 g triethanolamine hydrochloride and 1.25 g sodium sulfite are dissolved in 100 mL DI-water. Both the combined reagents and the stabilizing solution should be made fresh every few weeks as the absorption efficiency will deteriorate. For the analysis, 0.2 mL of sample are added to 9 mL of borax buffer, followed by 0.2 mL of the combined reagents. After three minutes, 0.2 mL

of stabilizing solution are added. The sample was then analysed at 553 nm with the UV-Vis spectrophotometer. Measurements were calibrated with a 1000 ppm stock solution of KCN, diluted to 5, 8, 10, and 20 ppm. The detection limit was 5 ppm. Similar to ammonia, from the cyanide concentration in the water, we can estimate the HCN concentration in the gas phase using the respective Henry's law constant. For HCN, this constant at 20 to 23°C is $H = (13 \pm 4)\mathrm{M\,bar^{-1}}$ (Ma et al., 2010).

3.1.4 Nitrogen Isotope Measurements

We measured the isotopic composition of nitrite and nitrate in our experiments of Set 1. For the 'evaporated residue' method, carried out at the University of St Andrews, 40 mL of each water sample were mixed with 250 mg of KOH to form KNO_3 and KNO_2. This solution was then evaporated with a freeze drier for about one week until the residue was completely dry. The dried residue was weighed into tin capsules and analysed by flash-combustion, using an EA IsoLink elemental analyser coupled to a MAT253 Thermo Finnigan isotope ratio mass spectrometer via a ConFlo IV. The analyses were calibrated with the international reference materials RM8568/USGS34 ($\delta^{15}\mathrm{N} = -1.8$‰; $\delta^{18}\mathrm{O} = -28$‰), RM8569/USGS35 ($\delta^{15}\mathrm{N} = 2.7$‰; $\delta^{18}\mathrm{O} = 57$‰), RM8549/IAEA-NO-3 ($\delta^{15}\mathrm{N} = 4.7$‰; $\delta^{18}\mathrm{O} = 25.6$‰) (Böhlke et al., 1993; Böhlke & Coplen, 1995; Böhlke et al., 2003). We note that adding KOH to the sample increases the pH of the solution, which includes small amounts of NH_4^+. Once the pH is increased above 9.25, most NH_4^+ will dissociate to NH_3 which can be lost by volatilisation with a fractionation of −45‰ (Li et al., 2012; Stüeken et al., 2016b). Tests to quantify this effect on the bulk measurement of the nitrogen isotope fractionation showed that the ammonium concentration was too small for any volatilisation to affect the measured bulk isotopic value. A subset of samples was also analysed for nitrogen and oxygen isotope composition at Brown University using the denitrifer method (Sigman et al., 2001; Casciotti et al., 2002). Briefly, samples were injected into vials containing P. aureofaciens that quantitatively convert nitrate and nitrite to nitrous oxide (N_2O). The generated N_2O was concentrated and purified using an automatic purge and trap system and introduced to a continuous flow isotope ratio mass spectrometer with a modified gas bench interface. Measurement of N_2O was conducted at an m/z of 44, 45, and 46 for $\delta^{15}\mathrm{N}$ and $\delta^{18}\mathrm{O}$ determination, and unknowns were corrected relative to internationally recognized nitrate salt reference materials that included: USGS34, USGS35, and IAEA-NO-3 (see above). Both methods return the combined isotopic compositions of

nitrate and nitrite.

3.2 Computational Methods

3.2.1 Kinetic Chemistry Calculations

To test how the production of NO_2 in our Set 1 experiments depends on atmospheric pressure, we performed calculations with the photochemistry and diffusion code ARGO and the chemical kinetics network STAND2019 (see Chapter 2.2, Rimmer & Helling, 2016; Rimmer & Rugheimer, 2019; Rimmer & Helling, 2019). For the starting conditions, we assumed that 1% of the gas mixture was cycled through the spark in our experiments. We further assumed that the composition of this portion of the gas corresponds to the chemical equilibrium composition of the initial gas mixture (84% N_2, 15% CO_2, 1% H_2O) at a freeze-out temperature of 3000 K. We calculated the chemical equilibrium composition at 3000 K with GGCHEM (Woitke et al., 2018), including 87 neutral and charged species containing the elements H, C, N, O, as well as electrons. We then added the calculated concentrations of H, N, O, H_2, N_2, O_2, OH, NO, CO, CO_2, H_2O (in total 1%) to the background gas (99%) and used this total gas mixture as input for ARGO/STAND2019.

We performed the kinetic chemistry simulations at a temperature of 300 K and pressures of 0.5, 1, and 3 bar and compared the resulting NO_2 concentrations when steady state was reached after 69, 23, and 3 min at 0.5, 1, and 3 bar, respectively. Increasing the fraction of gas cycled through the spark channel does not affect the ratio between the NO_2 concentrations for the different gas pressures, but decreases the time scale to reach steady state.

3.2.2 Photochemical Simulations

We conducted photochemical simulations to calculate the mixing ratios of CO, NO, and NO_2 in the atmosphere of different test planets for a range of NO and CO production rates, corresponding to a range of lightning flash rates (see Section 3.4.3). To conduct these tests, we use the photochemical model component of the Atmos coupled climate-photochemistry code (Arney et al., 2016; Lincowski et al., 2018)[†]. We conducted all simulations in uncoupled mode (no climate adjustment) to isolate the specific chemical impact of varying CO and NO fluxes from lightning. When simulating anoxic atmospheres, we adopt an Archean-Earth planet tem-

[†]`https://github.com/VirtualPlanetaryLaboratory/atmos`

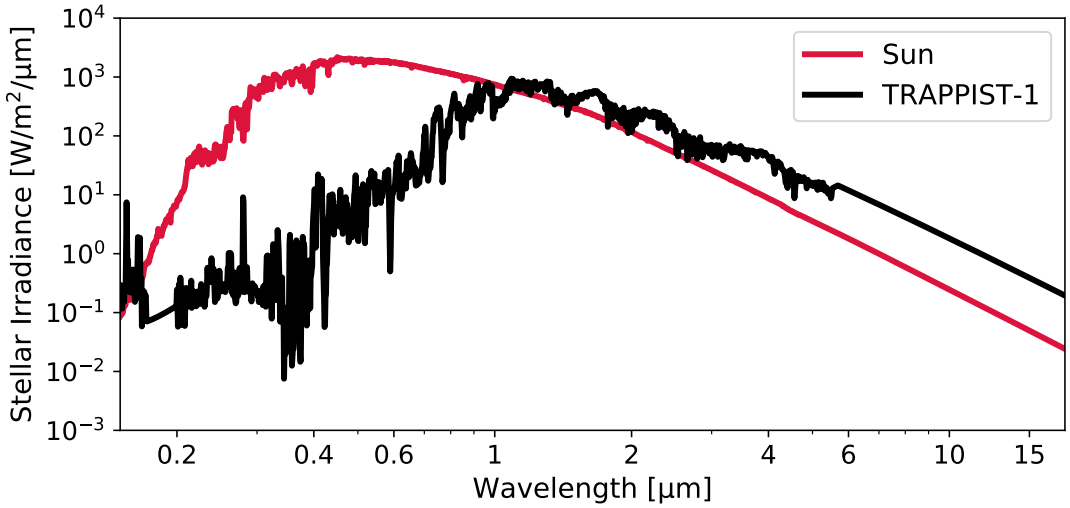

Figure 3.2: Spectral Energy Distributions at the top of the planets' atmospheres of the Sun (*red*) and TRAPPIST-1 (*black*) as used in the photochemical model and for the planetary spectra.

plate with 74 chemical species and 392 photochemical reactions. For O_2-rich atmospheres, we adopt a modern Earth-like template with 50 species and 239 reactions. We have incorporated the latest H_2O cross-sections and corrected sulphur reaction rate as recommended by Ranjan et al. 2020. The model normally includes the impact of Earth-like lightning by injecting NO into the troposphere (Harman et al., 2018); however, we have removed this feature and replaced it with a variable NO injection rate in order to assess the impact of varying NO production from lightning. The model includes diffusion-limited hydrogen escape (Harman et al., 2015).

We ran the simulations for an Earth-sized planet, orbiting the Sun at 1 au and the M dwarf TRAPPIST-1 at an instellation identical to that of TRAPPIST-1 e (Agol et al., 2021). The initial atmospheric composition was set to be similar to our high-CO_2 experiments (4.6% CO_2 with N_2 as filler gas). We also calculated the CO and NO_2 mixing ratios in a corresponding oxic atmosphere (21% O_2, 4.6% CO_2 with N_2 as filler gas). In both cases, the CO_2 concentration is fixed to the initial value of 4.6%. The tropospheric water vapour concentration is governed by the surface temperature of the planet: 0.5% H_2O for $T = 275\,\mathrm{K}$, 1.2% H_2O for $T = 288\,\mathrm{K}$, and 2.5% H_2O for $T = 300\,\mathrm{K}$. The pressure-temperature profiles for the anoxic simulations assume surface temperatures of $T_{\mathrm{surf}} = 275\,\mathrm{K}$ and $T_{\mathrm{surf}} = 300\,\mathrm{K}$, adiabatic cooling throughout the troposphere, and then an isothermal temperature of $T_{\mathrm{gas}} = 180\,\mathrm{K}$. For the oxic simulations, the pressure-temperature profile of modern Earth is used, with a surface temperature of $T_{\mathrm{surf}} = 288\,\mathrm{K}$. The spectra of the Sun and TRAPPIST-1 (Fig. 3.2) are used for the photochemistry

Table 3.1: Parameters for the photochemical model

Species	**Mixing ratio**	**Flux** [molecules/cm^2/s]	**Deposition velocity** [cm s^{-1}]
CO_2	4.6%	-	-
O_2	Anoxic: 0% Oxic: 21%	- -	-
H_2O[a]	rel. hum.	-	-
CH_4	-	Abiotic: 10^8 Biotic: 10^{11}	-
CO[b]	-	Anoxic: $10^7 - 3.2 \times 10^{12}$ Oxic: $2.1 \times 10^6 - 6.7 \times 10^{11}$	Abiotic: 10^{-8} Biotic: 1.2×10^{-4}
NO[b,c]	-	Anoxic: $5.4 \times 10^6 - 1.7 \times 10^{12}$ Oxic: $3.5 \times 10^7 - 1.1 \times 10^{13}$	3×10^{-4}
NO_2	-	-	3×10^{-3}
HNO	-	-	1
HNO_3[c]	-	-	0.2
H_2[b]	-	Anoxic: 10^{10} (anoxic) Oxic: 0	2.4×10^{-4}
H_2S[b]	-	Anoxic: 3.5×10^8 Oxic: 2×10^8	0.02
SO_2[b]	-	Anoxic: 3.5×10^9 Oxic: 9×10^9	1

[a] Depending on surface temperature, [b] Distributed over lower 10 km of atmosphere, [c] Only dry deposition

simulations and to simulate the planetary spectra. The spectrum of the Sun was sourced from Thuillier et al. (2004) while the TRAPPIST-1 spectrum represents an average of the three activity models presented in Peacock et al. (2019). Each spectrum is re-interpolated onto the standard Atmos base grid (Lgrid=0 setting).

We ran the model for different scenarios (see Table 3.1 for detailed parameters):

- *Abiotic scenarios:* Volcanic fluxes of CH_4, H_2, H_2S, and SO_2 are included and distributed over the bottom 10 km of the atmosphere profile (as is the variable CO flux). The CO deposition velocity is $v_{dep} = 10^{-8}$cm s^{-1} which is the limit for the abiotic formation of formate (Kharecha et al., 2005).

- *Biotic scenarios:* In addition to the volcanic sources of the abiotic scenario, a biological methane production of 10^{11}molecules/cm^2/s is included, which corresponds to Earth's

current biogenic methane flux (Jackson et al., 2020). The CO deposition velocity in the biotic case is $v_{\mathrm{dep}} = 1.2 \times 10^{-4} \mathrm{cm\,s^{-1}}$ which is the maximum deposition velocity for an ocean with a CO concentration of 0, i.e. where all CO is immediately consumed by acetogens (Kharecha et al., 2005).

- The volcanic fluxes for H_2, H_2S, and SO_2 are different for the *oxic* and *anoxic scenarios* as are the CO and NO production rates from lightning.

3.2.3 Spectral Simulations

To simulate reflectance, emission, and transmission spectra we used the Spectral Mapping Atmospheric Radiative Transfer code (SMART, Meadows & Crisp, 1996; Crisp, 1997) with transit updates as described in Robinson (2017). SMART is a versatile and well-validated line-by-line, multi-stream, multiple scattering and absorption model that can produce planetary spectra from the far-UV to far-IR. SMART relies on the DISORT Fortran code (Stamnes et al., 1988) to solve the radiative transfer equation via the discrete ordinate method. SMART includes opacity data from HITRAN (Gordon et al., 2017) that are preprocessed by their Line-By-Line Absorption Coefficients (LBLABC) companion model. SMART has been used to simulate spectra of planets inside and outside of the Solar System including the TRAPPIST-1 planets (Tinetti et al., 2005; Robinson et al., 2011; Arney et al., 2014; Lustig-Yaeger et al., 2019). For the spectra presented in Section 3.4.3, we show reflectance spectra degraded to a spectral resolving power of R=400, transmission spectra degraded to R=200, and emission spectra with a spectra resolution of 1 $\mathrm{cm^{-1}}$.

3.3 Isotopic Constraints on Lightning as a Source of Fixed Nitrogen in Earth's Early Biosphere

3.3.1 Nitrogen Fixation in Experiments and Theory

As discussed in Chapter 1.2.3, before the onset of biological nitrogen fixation on Earth, abiotic processes such as lightning must have provided the fixed nitrogen necessary to sustain the earliest forms of life. Cavendish (1788) first described that electric discharges can produce nitrogen oxides in Earth's atmosphere. Over the past five decades, studies tried to quantify the role of lightning in the production of fixed nitrogen in Earth's atmosphere, using theoretical and experimental methods as well as field data and different approaches to extrapolate their

Table 3.2: Nitrogen fixation rates from theoretical calculations and experiments (compiled from Schumann & Huntrieser, 2007; Heays et al., 2022, and individual sources). If not otherwise specified, gas mixture is that of modern Earth's atmosphere.

Source	NO production 10^{16}molec/J	Annual yield[a] TgN/yr	Method
Theoretical calculations			
Chameides et al. (1977)	$3-7$	$6-15$	chemical equilibrium
Hill et al. (1980)	0.9 [b]	1.9	at freeze-out temperature
Borucki & Chameides (1984)	9 ± 2	19 ± 4	
Goldenbaum & Dickerson (1993)	15	32	Fluid dynamics model coupled with chemistry
Experiments			
Chameides et al. (1977)	6 ± 1 [c]	13 ± 1	Spark discharge
Levine et al. (1981)	5 ± 2	11 ± 4	Spark discharge
Levine et al. (1982)	0.37 ± 0.07	0.8 ± 0.2	Spark discharge: N_2:CO_2 4:96
Hill et al. (1988)	1.4 ± 0.7	3 ± 1.5	Corona discharge
Stark et al. (1996)	$0.4-0.6$ [c]	$0.9-1.3$	Spark discharge
Wang et al. (1998)	1.8 [b]	3.9	Spark discharge and flash chemistry model
Cook et al. (2000)	1.1 ± 0.2 [c]	2.4 ± 0.4	Spark discharge
Navarro-González et al. (2001)	0.07 10	0.15 22	Laser-induced plasma: N_2:CO_2 85:15 modern air
Nna Mvondo et al. (2001)	1.3	2.8	Laser-induced plasma: N_2:CO_2 20:80
Nna Mvondo et al. (2001)	0.013	0.003	Corona discharge: N_2:CO_2 50:50
Rehbein & Cooray (2001)	3.0 ± 0.2 [c]	6.5 ± 0.4	Spark discharge
Rehbein & Cooray (2001)	$0.036-0.057$ [c]	$0.08-0.12$	Corona discharge
Rahman & Cooray (2003)	6.7 ± 0.5 [c]	14 ± 1	Laser-induced plasma
Cooray & Rahman (2005)	$1-2$ [c]	$2.2-4.3$	Spark discharge
Navarro-González et al. (2019)	4.1	8.9	Laser-induced plasma: N_2:CO_2:H_2 40:40:20
Heays et al. (2022)	0.008 ± 0.8	$0.02-2$	Laser-induced plasma: O_2-free gas mixtures

[a] with a global lightning flash rate on modern Earth of $44\,s^{-1}$ (Christian et al., 2003) and an energy of 6.7 GJ per flash Price et al. (1997a); [b] result in source presented in molec/flash; [c] including other NO_x species

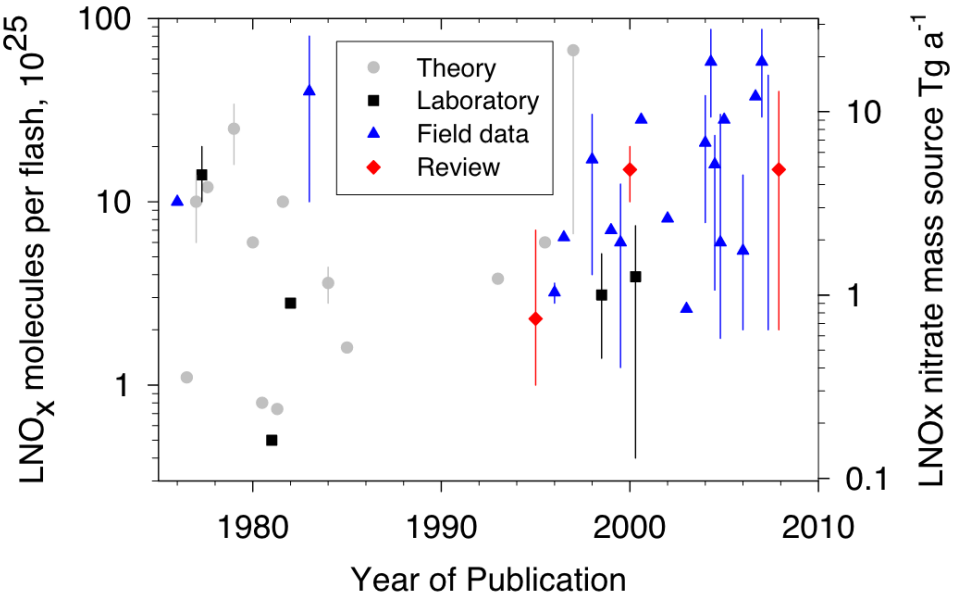

Figure 3.3: Review of production of fixed nitrogen by lightning in Earth's atmosphere. Nitrogen fixation rate is given per flash (**left**) and as annual production (using a flash rate of 44 s^{-1} (Christian et al., 2003), **right axis**) against year of publication of the study. Results from different methods are compared: theoretical calculations (*grey*), laboratory experiments (*black*), field data (*blue*), and reviews (*red*). Some data points correspond to entries in Table 3.2. For a complete overview, see Table 21 in Schumann & Huntrieser (2007). Taken from Schumann & Huntrieser (2007), licensed under CC BY-NC-SA 2.5.

results to a global nitrogen fixation rate (Fig. 3.3, Table 3.2, Schumann & Huntrieser, 2007). Theoretical calculations (e.g., Chameides et al., 1977; Borucki & Chameides, 1984) use the concentration of NO in chemical equilibrium at the freeze-out temperature of NO (see next section for a discussion of the chemistry in a spark discharge) and an estimate of the volume of gas heated to that temperature for a given amount of spark energy. With an average energy per flash and a global flash rate it is possible to estimate the global nitrogen fixation rate from lightning. The yield estimated with this method depends on assumptions on the cooling timescale of the lightning channel and subsequently the freeze-out temperature of NO, as well as on other parameters like the diameter of the lightning channel.

Experimental approaches to study the nitrogen fixation rate by lightning cover a wide range of deposited energies and include experiments with laser-induced dielectric breakdown (LIDB; e.g., Navarro-González et al., 2001; Nna Mvondo et al., 2001; Rahman & Cooray, 2003; Heays et al., 2022), spark discharges (e.g., Chameides et al., 1977; Levine et al., 1981; Stark et al., 1996), or coronal electric discharges (e.g., Hill et al., 1988; Nna Mvondo et al., 2001; Rehbein & Cooray, 2001). A detailed overview over the NO production rates in such experiments can be found in Table 3.2, Schumann & Huntrieser (2007), and Heays et al. (2022).

For modern Earth's atmospheric composition, the resulting NO or NO_x[†] yields cover a range of $(0.4-10)\times10^{16}$molecules/J. Using a global lightning flash rate on modern Earth of $44\,s^{-1}$ (Christian et al., 2003) and an energy of 6.7 GJ per flash Price et al. (1997a), this corresponds to an annual production of fixed nitrogen by lightning between 0.9 and 22 TgN/yr. Figure 3.3 (taken from Schumann & Huntrieser, 2007) compares the nitrogen fixation rates from theoretical calculations and experiments to field data where nitrogen oxides and nitrate abundances during or near thunderstorms were measured, showing general agreement between the results. Schumann & Huntrieser (2007) determine the average nitrogen fixation rate to be 2.3×10^{16}molecules/J or 5 TgN/yr.

Some studies have shown that spark discharges also produce nitrogen oxides in (N_2-CO_2)-dominated atmospheres (e.g., Levine et al., 1982; Nna Mvondo et al., 2001; Navarro-González et al., 2001; Summers & Khare, 2007; Heays et al., 2022) and models suggest that a significant flux of these lightning products to Earth's surface could potentially have fuelled prebiotic chemistry (Kasting & Walker, 1981; Wong et al., 2017; Adams et al., 2021). However, it has so far not been possible to verify these model predictions and the role of lightning in the evolution of life, because the isotopic fingerprint of this nitrogen source was unknown, i.e. the ratio of the nitrogen isotopes ^{15}N and ^{14}N expressed as $\delta^{15}N = [(^{15}N/^{14}N)_{sample}/(^{15}N/^{14}N)_{standard} - 1]\times1000$ ‰, where the standard is modern air. In one laboratory experiment, values near 0‰ were reported from the gas phase (Hoering, 1957). However, natural measurements of atmospheric nitrate from different sources suggested values of -5‰ to -15‰ (Moore, 1977) with extreme values between < -30‰ (nitrate and NO_x emission from the Antarctic snowpack) and $> +5$‰ (fossil fuel emissions, Shi et al., 2021), indicating the wide range of sources of nitrate emissions on modern Earth. Because experimental measurements of the aquatic phase have not yet been conducted, it has so far been impossible to detect evidence of lightning from the sedimentary rock record of nitrogen isotope ratios (Fig. 1.6, Stüeken et al., 2016b, 2021; Yang et al., 2019).

In this study we identified an isotopic fingerprint with spark discharge experiments in N_2-O_2 and N_2-CO_2 gas mixtures. We know from measurements of fluid inclusions that the isotopic composition of N_2 in early Earth's atmosphere was very similar to today's (within $\sim 2-3$‰) (Marty et al., 2013), enabling us to compare our fingerprint to sedimentary rock samples. The experimental setup resembled a Miller-Urey apparatus (Parker et al., 2014) with

[†]NO_x includes the combined NO and NO_2 production

a 1 L glass flask and two needle electrodes at a distance of ~ 1.5 cm (Section 3.1, Fig. 3.1). A current (I) of 1 mA at a voltage (U) of 49 kV was applied continuously for a time span (t) of $15-60$ min per experiment. The flask was filled with artificial gas mixtures to 1 bar, mimicking modern (85% N_2, 14% O_2), O_2- and CO_2-depleted (99.5% N_2, 0.06% O_2, <0.02% CO_2), and Archean-like (83% N_2, 16% CO_2) atmospheres. Originally, we aimed for O_2 concentrations of 21% and 1% for the modern and low-O_2 experiments, respectively, and a CO_2 concentration of 20% for the Archean-like experiments. However, slow mixing of the gases in our the setup led to slightly lower final concentrations of CO_2 and O_2: Archean-like: (0.16 ± 0.03) CO_2 and $< 5 \times 10^{-4}$ O_2; Low-O_2: $< 2 \times 10^{-4}$ CO_2 and $(6 \pm 1) \times 10^{-4}$ O_2; Modern: $< 6 \times 10^{-4}$ CO_2 and (0.14 ± 0.03) O_2. The small amounts of CO_2 present in the modern and low-O_2 experiments and of O_2 in the Archean-like experiments is probably due to these gases being dissolved in the water and not completely removed during evacuation, traces of air remaining in the setup, and recombination of atomic oxygen produced by dissociation of H_2O and CO_2 in the experiment and the ion source of the mass spectrometer. For the CO_2 fraction in the Archean-like experiments we followed estimates predicting a CO_2 mole fraction of 15 to 20% in the early Archean (Catling & Zahnle, 2020).

In each case, 50 mL of deionized water at the bottom of the flask were used to trap soluble nitrogen oxides. Electrode spacing, energy input, and experiment duration were varied and their effect on the results explored (Section 3.3.3). We measured the isotopic composition and abundances of these dissolved oxides by gas-source mass spectrometry, and the composition of the gas before and after the experiment using an on-line quadrupole gas analyser (Section 3.1). The molecular concentrations allowed us to determine energy yields (molecules/Joule), where energy input was calculated as $E = 1/2\ UIt$. The energy yield could in turn be used to estimate global fluxes to Earth's surface for each of the major products. The isotopic composition allows us to test if lightning might have been an important nutrient source for early life.

3.3.2 Chemical Pathways of Nitrogen Fixation

The production of NO in the channel of the spark discharge in our experiments follows the Zel'dovich mechanism (Zel'dovich & Raizer, 1966) with the following reactions in an N_2-O_2

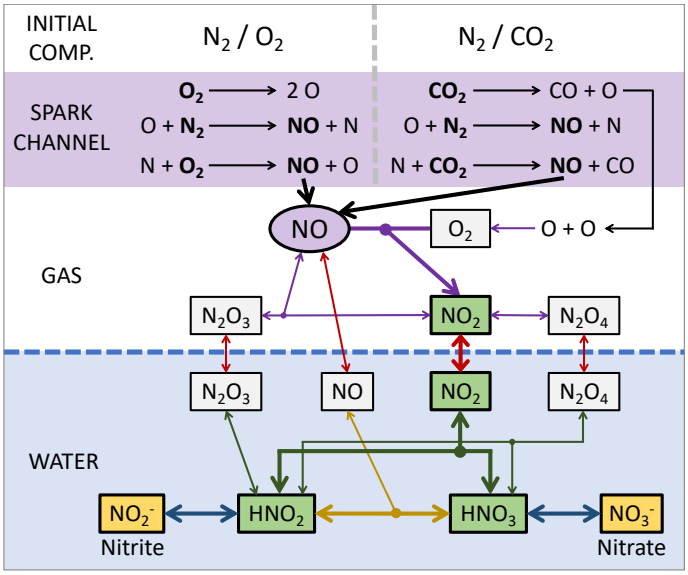

Figure 3.4: Chemical pathways during spark discharge in $N_2{-}O_2$ (left) and $N_2{-}CO_2$ (right) gas mixtures. Once NO is produced, further oxidation follows the same reactions in both cases: NO is oxidised to NO_2, some being converted to N_2O_3 and N_2O_4. In $N_2{-}CO_2$ experiments, O_2 is produced by the recombination of atomic oxygen. All gaseous nitrogen oxides equilibrate with water and convert to HNO_2 and HNO_3. HNO_2 is thermodynamically unstable and will oxidise to HNO_3. Both acids may dissociate to nitrite (NO_2^-) and nitrate (NO_3^-), respectively, depending on solution pH. In a low-pH environment, HNO_2 is more abundant than NO_2^-, allowing further oxidation to HNO_3 and nitrate. The dominant pathways are indicated with bold arrows and coloured molecule labels. First published in Barth et al. (2023a).

atmosphere (Yung & McElroy, 1979; Chameides, 1986):

$$O_2 \rightleftharpoons O + O \tag{3.1}$$

$$O + N_2 \rightleftharpoons NO + N \tag{3.2}$$

$$N + O_2 \rightleftharpoons NO + O. \tag{3.3}$$

Similar reactions lead to the production of NO in an $N_2{-}CO_2$ atmosphere (Nna Mvondo et al., 2001):

$$CO_2 \rightleftharpoons CO + O \tag{3.4}$$

$$O + N_2 \rightleftharpoons NO + N \tag{3.5}$$

$$N + CO_2 \rightleftharpoons NO + CO. \tag{3.6}$$

In addition, atomic oxygen will recombine to form O_2. A schematic showing the chemical reactions in our experiment is shown in Fig. 3.4. In both gas compositions, the NO will then oxidise further to NO_2, which will be in equilibrium with N_2O_3 and N_2O_4 (Joshi et al., 1985;

Miller, 1987):

$$2\,NO + O_2 \longrightarrow 2\,NO_2 \tag{3.7}$$

$$NO + NO_2 \rightleftharpoons N_2O_3 \tag{3.8}$$

$$2\,NO_2 \rightleftharpoons N_2O_4. \tag{3.9}$$

Another potential product of further reactions involving NO is N_2O. However, discharge experiments found that the yield of N_2O is about four magnitudes lower than that of NO (Levine et al., 1979, 1981), 4×10^{12}molecules/J and 5×10^{16}molecules/J, respectively. Theoretical calculations return an even slightly lower N_2O yield of 8×10^{11}molecules/J (Hill et al., 1984). We therefore neglected any N_2O production in our analysis. NO can also react to NO_2 in the presence of ozone. We did measure low ozone concentrations in some of our experiments but it is uncertain how important this pathway is here. The gas mixture in our experiments contains approximately 1% of water vapour due to evaporation of the liquid water in the flask at room temperature. This water vapour limits the abundance of ozone in the gas mixture (Stark et al., 1996). In anoxic conditions, Summers et al. (2012) have shown that the disproportionation reaction

$$3\,NO \longrightarrow N_2O + NO_2 \tag{3.10}$$

is an important source of NO_2. However, in their experiments, NO was introduced directly into a gas mixture of N_2 and CO_2, meaning no spark is present that could provide O_2 from CO_2 and H_2O dissociation for NO_2 production via Reaction (3.7).

NO_2, N_2O_3, and N_2O_4, will be absorbed into the water (in equilibrium with the partial pressure in the gas) where they will further react with the water to HNO_2 and HNO_3 (Joshi et al., 1985; Miller, 1987):

$$2\,NO_2 + H_2O \rightleftharpoons HNO_2 + HNO_3 \tag{3.11}$$

$$N_2O_4 + H_2O \rightleftharpoons HNO_2 + HNO_3 \tag{3.12}$$

$$N_2O_3 + H_2O \rightleftharpoons 2\,HNO_2, \tag{3.13}$$

HNO_2 is not stable and will further react to HNO_3,

$$3\,HNO_2 \rightleftharpoons HNO_3 + H_2O + 2\,NO. \tag{3.14}$$

HNO_2 and HNO_3 will further react with water to nitrite (NO_2^-) and nitrate (NO_3^-), respectively:

$$HNO_2 + H_2O \rightleftharpoons NO_2^- + H_3O^+ \tag{3.15}$$

$$HNO_3 + H_2O \rightleftharpoons NO_3^- + H_3O^+. \tag{3.16}$$

In a low pH environment like in our experiment, HNO_2 is more abundant than NO_2^-, allowing further oxidation to HNO_3 and nitrate. We found that the nitrite concentrations in our samples were systematically lower if the analyses were performed several days after the experiment rather than on the same day, suggesting that nitrite was continuously converted to nitrate in the aqueous phase. We speculate that this is due to the presence of another strong oxidizer produced in the spark experiment, such as H_2O_2, which is known to be produced by lightning (Zuo & Deng, 1999). Our oxygen isotope data ($\delta^{18}O$ has a consistent value of 20 ‰ throughout all experiments) further supports this pathway of nitrate formation via nitrite: In acidic conditions (our solutions have a pH < 4), nitrite exchanges oxygen with water, completely eradicating the isotopic signature of the initial nitrite (Bunton et al., 1959; McIlvin & Casciotti, 2006).

The dominant pathway for nitrate formation is indicated in Fig. 3.4 with bold arrows and goes via Reaction (3.11). Even for our experiments where the final NO_2 pressure is largest, both N_2O_3 and N_2O_4 pressures are approximately four orders of magnitude smaller than the overall NO_x pressure when using the equilibrium constants (Joshi et al., 1985). Since the final partial pressure of NO_2 is below 1 mbar in all our experiments, NO_2 absorption is the most important route of nitrate formation, as opposed to N_2O_4 absorption (Joshi et al., 1985; Newman & Carta, 1988).

3.3.3 The Energy Yield of Nitrogen Fixation

Figure 3.5a shows the energy yield for the major products in our experiments for the different gas compositions. Yields for dissolved ammonium were also measured but found to be very low ($< 0.5\%$ of total fixed N) and are therefore not considered further, though our ammonium detection is consistent with previous observations of ammonium production in anoxic N_2-CO_2 spark experiments (Cleaves et al., 2008). The modern and Archean-like scenarios both show a total energy yield for the sum of all fixed nitrogen species of $(3-5) \times 10^{15}$ molecules/J.

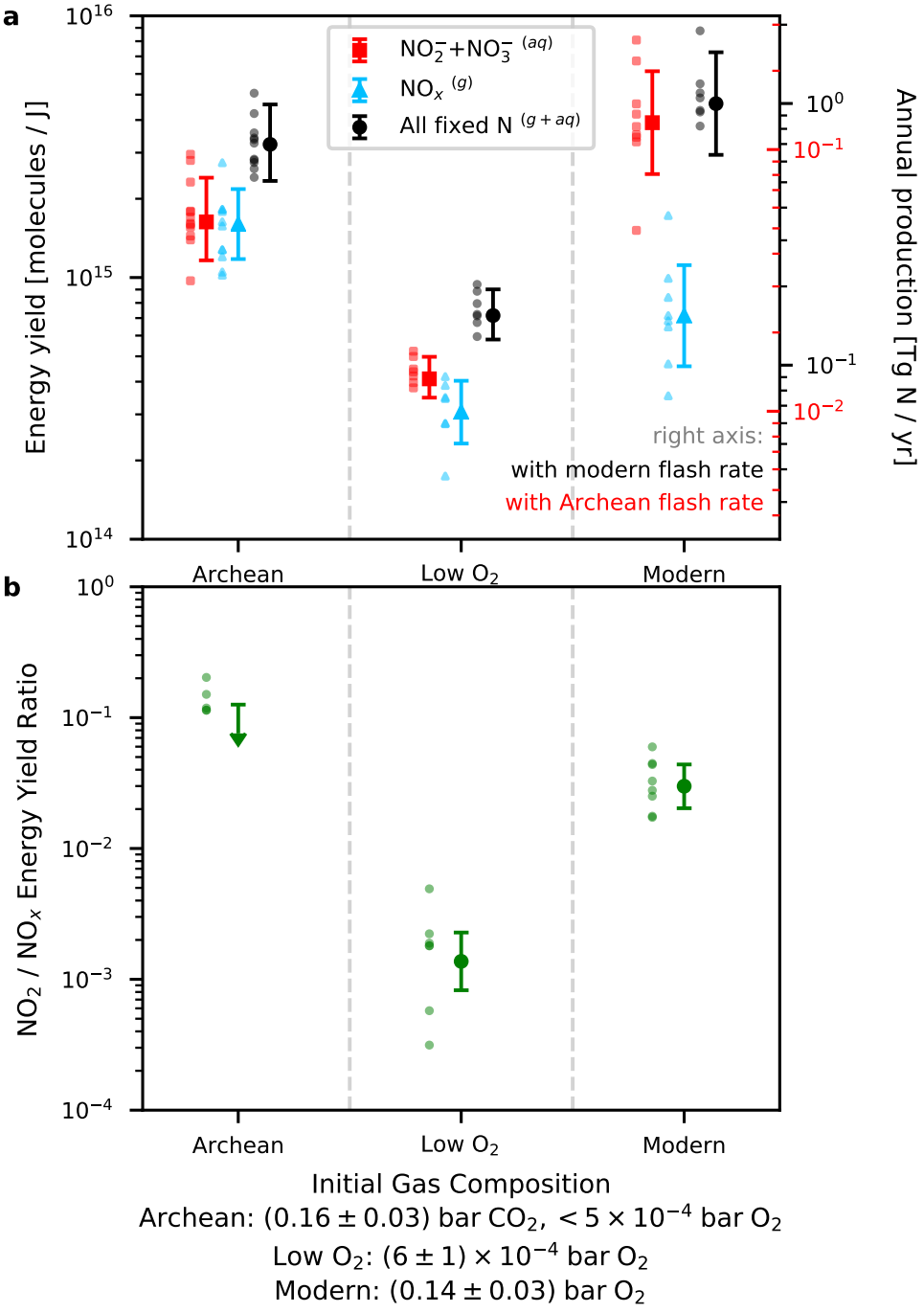

Figure 3.5: Energy yield of fixed nitrogen products. **a:** Combined gaseous products (NO_x, *blue*), combined aqueous nitrate and nitrite (*red*), and total fixed nitrogen yield (*black*) for different initial gas compositions (difference to 1 bar is N_2). Individual measurements shown as small symbols, the large symbols represent the mean values (with SD error). Nitrate and nitrite are not separated, because nitrite conversion to nitrate was found to continue after the experiments. Right axis shows corresponding annual production for modern (Christian et al., 2003) (*black*) and potential Archean (Wong et al., 2017) (*red*) lightning flash rates in Tg of fixed nitrogen per year. **b:** Ratio of the energy yields of NO_2 and NO_x for different initial gas compositions of the experiment (same as above). The data point for N_2–CO_2 gas represents only an upper limit due to interferences between NO_2 and CO_2 in the gas analyser. First published in Barth et al. (2023a).

Total yields are lower in the low-O_2 experiments, probably because NO formation was oxygen-limited. The speciation of the fixed nitrogen was found to vary with atmospheric composition: In the modern experiments (14% O_2), approximately 85% of the fixed nitrogen is stored in dissolved nitrate and nitrite. The Archean-like (16% CO_2) and low-O_2 experiments yielded a smaller fraction of aqueous nitrogen species, nearly half of the fixed nitrogen remained in the gas phase. This suggests that in the Archean-like experiments the CO_2 provided enough oxygen for equally efficient NO formation as in an oxygen-rich atmosphere. However, O_2 availability appears to limit the efficient conversion of NO to NO_2 and aqueous species. This interpretation is supported by the low NO_2/NO ratios measured in the low-O_2 experiment compared to the modern gas mixture (Figure 3.5b). Reliable NO_2 measurements for the Archean-like experiments could not be obtained due to interference between NO_2 and CO_2 isotopologues at mass 46, but the relatively low abundance of aqueous compared to gaseous products suggests that the Archean-like NO_2/NO ratio was also lower, due to oxygen limitation.

To estimate global fluxes of fixed nitrogen to Earth's surface, based on our results, we assumed a lightning flash rate in Earth's atmosphere of $44 \pm 5\ s^{-1}$ (Christian et al., 2003) and for the average energy dissipated by one lightning flash of 6.7 GJ (Price et al., 1997a). Based on these assumption, our Archean-like and modern experiments predict the production of $0.7-1$ Tg fixed nitrogen per year. A global lightning flash rate of only $6.6\,s^{-1}$, as proposed for the Archean, would lower the annual fixed nitrogen production by lightning accordingly (Wong et al., 2017). The results are lower for the low-O_2 case (Fig. 3.5). Overall, these estimates are comparable to those of previous studies, including experiments that more closely mimic natural lightning conditions in terms of total energy input and spark length (Wang et al., 1998; Cook et al., 2000; Schumann & Huntrieser, 2007), supporting our approach of simulating lightning chemistry with small spark experiments. Previous experiments with a laser-induced plasma to simulate lightning discharge (Nna Mvondo et al., 2001; Navarro-González et al., 2001) found a four-times-lower NO energy yield (compared to our total fixed N yield) of 7×10^{14} molecules/J in N_2-CO_2 gas mixtures and a 20-times-higher yield in modern air, compared to our measurements. However, it is uncertain how well a laser can mimic lightning chemistry. In a natural lightning channel, gas is heated within a few microseconds to a peak temperature of 30 000 K (Uman & Rakov, 2003; An et al., 2019). The gas cools to $\sim$ 3000 K over a few to tens of milliseconds (Uman & Voshall, 1968; Picone et al., 1981). While the gas is cooling NO forms. However, the time-scale for thermochemical equilibrium to establish

increases with further cooling from microseconds at 4000 K to 1000 yr at 1000 K (Chameides, 1986), causing the NO concentration to be fixed once the cooling time-scale drops below the equilibrium time-scale (Zel'dovich & Raizer, 1966). Hence, even though in our experiments the spark channel does not reach the temperature of a fully-developed lightning channel, NO was still observed to be the dominant product, which allows us to mimic natural atmospheric chemistry induced by lightning. To further verify the validity of our results for natural settings, a subset of experiments with artificial seawater and $CaCO_3$ as a pH buffer was conducted and found no effect on the nitrite concentrations, indicating that our results are valid for both fresh and saline water (see supplementary material of Barth et al., 2023a). Experiments with anoxic seawater and 0.8 mM ferrous iron, akin to the Archean ocean (Tosca et al., 2019), had similar yields, suggesting that potential reactions between nitrogen oxides and ferrous iron (Summers & Chang, 1993) are relatively minor and do not impact our conclusions.

Sensitivity Tests

We tested the influence of the electric field strength on the production of nitrite and nitrate. The field strength depends on the applied voltage and the size of the gap between the electrodes. We used an approximation of the electrodes by long and thin ellipsoids (Köhn & Ebert, 2015) but could not find a clear correlation to the nitrate production.

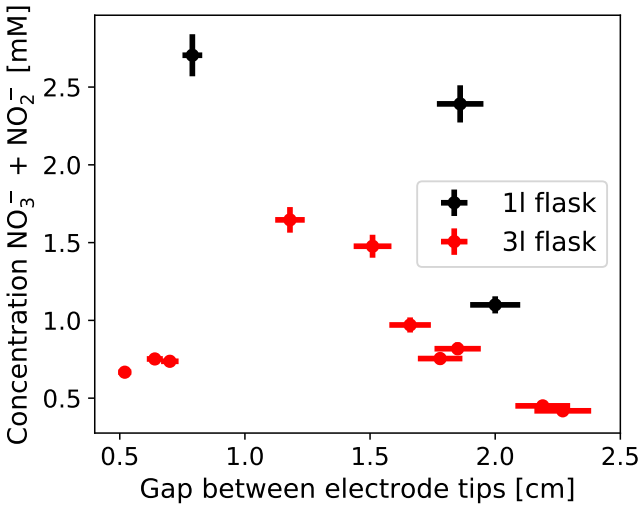

Figure 3.6: Final concentration of combined nitrate and nitrite for experiments with varying distance between the electrode tips. Only experiments with modern atmospheric composition. Experiments performed with a 1 L and 3 L flask are shown in black and red, respectively. Data points are individual measurements with uncertainties in concentration and distance. First published in Barth et al. (2023a).

However, experiments with differently sized spark gaps showed an interesting behaviour

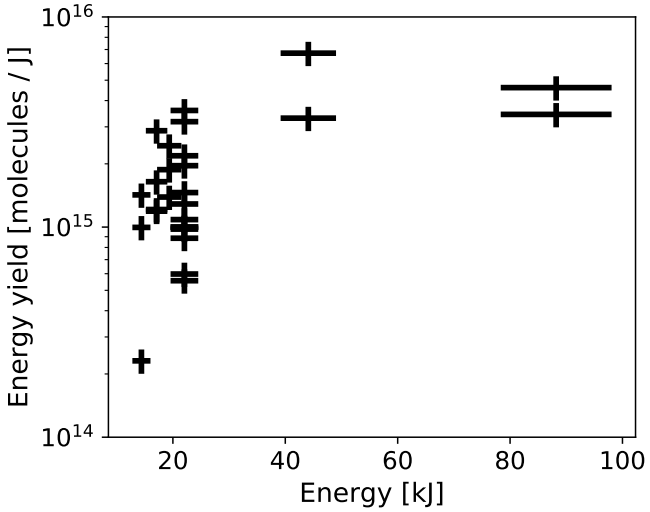

Figure 3.7: Energy yield (N atoms fixed per Joule) against input energy for production of nitrate and nitrite. Only experiments with modern atmospheric composition. Data points are individual measurements with uncertainties in energy and energy yield. First published in Barth et al. (2023a).

(Fig. 3.6). For large spark gaps, the production of nitrate and nitrite dropped as the electric field strength approached the breakdown field in dry air (Köhn et al., 2019) of 35 kV cm^{-1} and the continuity of the spark was disturbed. On the other hand, with a decreasing spark gap, the total volume of the spark channel decreased which in return limited the degree of nitrogen fixation, possibly because a larger portion of the energy was lost heating the electrodes. We identified a setting where the nitrate production peaked for spark gaps between 1 cm and 1.5 cm which we used for all further experiments. Note that some of the initial experiments were carried out with a 3 L flask, but we transitioned to a 1 L flask for the majority of the project, because this allowed for a more efficient absorption of the produced nitrogen oxides into the water as the partial pressures of NO and NO_2 were relatively higher in the smaller volume. Furthermore, the 1 L flask was faster to evacuate.

We found the rate of nitrogen fixation increases with increasing energy. The energy input into the experiment can be calculated with the voltage U and current I of the spark generator and the duration t of the spark: $E = 1/2\ UIt$. The voltage can be changed in increments with $U_{\max} = (49 \pm 2)$kV and the current is $I = (1 \pm 0.1)$mA. The duration of the spark ranged between 15 and 60 min. The energy yield (nitrate and nitrite) increases with increasing energy, levelling off above approximately 40 kJ (Fig. 3.7). Reasons for the less efficient production of nitrate and nitrite at lower energies are likely a combination of higher energy losses by heating of the electrodes and less time for further oxidation of NO_x to nitrate and nitrite as the low-energy experiments typically represent spark durations of 15 min.

3.3.4 Isotope Fractionation During Spark Experiment

We analysed the nitrogen isotopic composition in the dissolved oxides with two different techniques (Section 3.1.4). For most experiments, the solutions were mixed with KOH powder, freeze-dried, and then analysed as dried salt. For a subset of experiments, dissolved nitrate and nitrite were treated with the denitrifier method and analysed as N_2O gas (Sigman et al., 2001; Casciotti et al., 2002) which allowed separating out other nitrogen compounds such as ammonium. The two datasets combined define an overlapping trend of progressively more negative $\delta^{15}N$ values with higher combined nitrate and nitrite concentrations, with values as low as -15‰ (Fig. 3.8a). Neither of the two methods could separate nitrite from nitrate, which is why we report them together.

Combined with the gas data, we find that the isotopic composition decreases as the fraction of NO remaining in the gas phase $f = [NO]/([NO] + [NO_2] + [NO_2^-] + [NO_3^-])$ decreases (Fig. 3.8b). The extrapolated endmember composition with 0% NO remaining is $\delta^{15}N_0 = (-17 \pm 1)$‰, the initial $\delta^{15}N$ of the NO reservoir, with an ϵ factor (i.e. the fractionation between the NO reservoir and the first produced nitrate) of (47 ± 6)‰. We used a linear fit as our experiment can be described by a closed system Rayleigh fractionation where the initial reservoir and the accumulated products remain in contact as supported by further experiments where the flask was let sit idle for several hours after the end of the experiment, leading to even lower values for $\delta^{15}N$ (open squares in Fig. 3.8a) than in experiments with no additional rest time (circles). In natural thunderstorm clouds, we might find some open-system behaviour when large rain droplets escape from the system. However, the fractionation in an open system is very similar to that of our closed system experiments as we would start with the same $\delta^{15}N_0$ and ϵ (blue line in Fig. 3.8b).

Theoretical calculations of equilibrium isotope fractionation have shown that NO gas should be isotopically depleted relative to N_2 and NO_2 (Walters & Michalski, 2015). Very light $\delta^{15}N$ values (-15 to -25‰) have also been measured in organic particulates forming in spark discharge experiments, consistent with significant isotopic fractionation occurring in lightning chemistry (Kuga et al., 2014). Hence the following sequence of events is the most logical explanation for the trend in our data: First, isotopically light NO ($\delta^{15}N$ near -17‰) is produced in the gas phase. Our extrapolated endmember for NO ($\delta^{15}N_0 = (-17 \pm 1)$‰) falls close to the value predicted for the kinetic isotope fractionation in the reaction $N_2 + O \longrightarrow NO + N$,

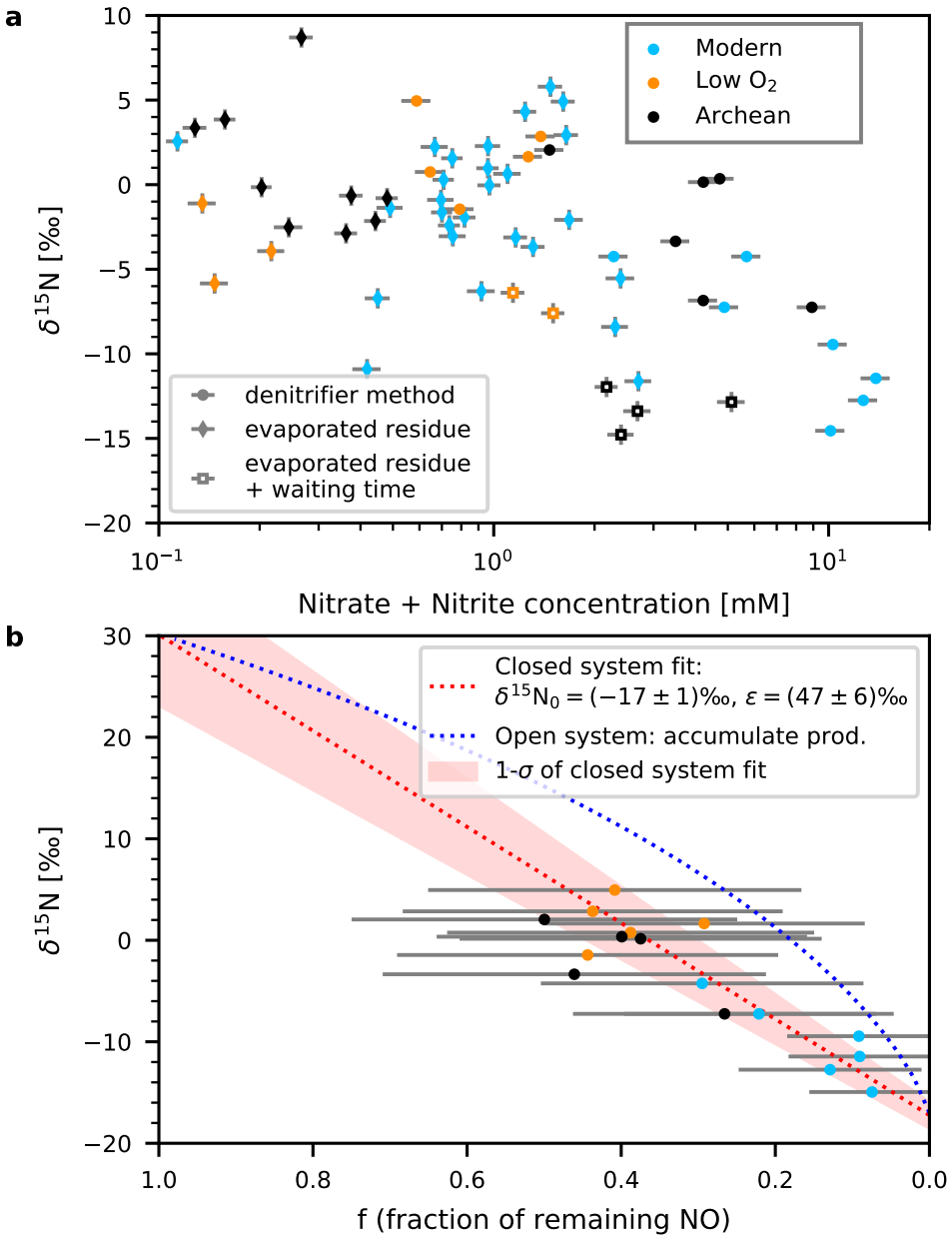

Figure 3.8: Nitrogen isotope ratios of aqueous nitrate and nitrite. **a:** δ^{15}N against combined concentration of nitrate and nitrite in mM (10^{-3}mol/L). Data from three sets of experiments (*symbol shape*) and three gas mixtures (*symbol colour*). Data points are individual measurements with uncertainties in concentration and δ^{15}N (errors in δ^{15}N for denitrifier method smaller than symbols). **b:** δ^{15}N against remaining fraction of NO f =[NO]/([NO]+[NO_2]+[NO_2^-]+[NO_3^-]). NO abundances to calculate f only available for experiments analysed with the denitrifier method (*circles*). Dashed red line is fit to a closed system Rayleigh fractionation ($\delta^{15}N(f) = \delta^{15}N_0 + \epsilon f$) with 1-$\sigma$ envelope, allowing to extrapolate to endmember where all NO oxidised to nitrate and nitrite. Blue line represents the δ^{15}N of the accumulated product in a Rayleigh fractionation assuming an open system with same $\delta^{15}N_0$ and ϵ as closed system. See text for discussion of open and closed system fractionation. Data points represent individual measurements with error in f propagated from uncertainties of the measurements of the individual concentrations (NO, NO_2, NO_2^-, NO_3^-). First published in Barth et al. (2023a).

$\epsilon = -17.4‰$, resulting from the higher velocity and increased reaction rate of $^{14}N^{14}N$ compared to the heavier $^{15}N^{14}N$ (Kuga et al., 2014). Second, some NO is converted to NO_2 with a positive fractionation, i.e. isotopically heavy NO is preferentially converted to NO_2. Previous studies have reported nitrogen enrichment factors of 29‰ (Li et al., 2020) to 36‰ (Walters et al., 2016) between these two species, with additional, minor fractionation possible between gaseous and aqueous NO_2. Since we find efficient conversion of NO_2 to nitrite and nitrate, the final isotopic composition of these products is very similar to the $\delta^{15}N$ of the NO_2. When only a small fraction of NO has been converted (high f-value in Fig. 3.8b), the isotopic composition of nitrate and nitrite falls near 20‰. Third, progressive conversion of isotopically heavy NO to aqueous species (via NO_2) renders the residual NO gas phase isotopically lighter. Hence, nitrite and nitrate forming at a larger conversion factor (a smaller f in Fig. 3.8b) become isotopically lighter as well.

This is supported by our experiments with additional wait time, allowing more NO to convert to aqueous species over time. The system trends over time towards an equilibrium with isotopically light aqueous species (-6 to $-15‰$ and possibly lighter, given more time). In our experiments, the equilibration time is likely to be affected by diffusion kinetics between the gas and the water reservoir. In a natural lightning storm in a water-saturated atmosphere, the equilibration between gaseous NO and aqueous nitrite and nitrate is likely to be reached faster, possibly leading to even lower $\delta^{15}N$ values trending towards the depleted lightning-generated $\delta^{15}N(NO)$.

3.3.5 Quantifying Lightning as a Source of Nitrogen for Early Life

It has long been postulated that lightning may have driven the origin and early evolution of life on Earth, based on estimates of fluxes and biological demands (Kasting & Walker, 1981; Nna Mvondo et al., 2001; Navarro-González et al., 2001; Wong et al., 2017). In this work we find that nitrogen fixation in an Archean-like (N_2-CO_2) atmosphere is similarly efficient to a modern (N_2-O_2) atmosphere, but further oxidation of NO to nitrite and nitrate is limited by the absence of O_2. The overall production of fixed nitrogen products depends on the Archean lightning flash rate which might have been lower than today's (Wong et al., 2017). There is still significant uncertainty relating to the CO_2 fraction in the early Archean atmosphere (Catling & Zahnle, 2020) which will influence the final nitrogen fixation rate (Nna Mvondo et al., 2001). An additional uncertainty is the total atmospheric pressure in the Archean, where estimates

vary between 0.5 (Marty et al., 2013) and 3 bar (Goldblatt et al., 2009). The velocities of the electrons inside the spark channel, responsible for the dissociation of N_2, O_2, and CO_2, are independent from the gas density, i.e. the pressure (Nijdam et al., 2020). However, the three-body reactions outside the spark channel depend on the gas number density. To check whether our results are still valid for different atmospheric pressures, we used simulations with the chemical kinetics network STAND2019 (Section 3.2.1; Rimmer & Helling, 2016; Rimmer & Rugheimer, 2019; Rimmer & Helling, 2019) to compare the NO_2 production outside the spark channel (at 300 K) for pressures of 0.5, 1, and 3 bar. The final NO_2 fraction varied between approximately 80% (for 0.5 bar) and 140% (for 3 bar) compared to 1 bar (our experiments) where we find an NO_2 mixing ratio of 2.8×10^{-5}. This uncertainty is much smaller than other factors that influence the NO_2 production rate such as the initial CO_2 fraction in the atmosphere or the lightning flash rate on early Earth. A further factor of uncertainty is the availability of O_2 for the production of NO_2 in the Archean atmosphere. When O_2 is formed by the recombination of atomic oxygen outside of the spark channel, it will be diluted in the background gas. While our experiments present a limited gas volume in which the chemistry takes place, in real lightning conditions, the O_2 could be transported away from the thunderstorm cloud, reducing the efficiency of NO_2 production. We expect the production of NO_2 to happen relatively quickly while the gases are still in the vicinity of the lightning channel, but kinetic rate modeling is necessary to answer this question definitively.

Our isotopic data allow us to place first empirical constraints on the role of lightning-derived bioavailable nitrogen in the early evolution of life. We find the dissolved lightning products significantly lighter ($\delta^{15}N = -6$ to -15‰ or less) than the vast majority of sedimentary rocks through geologic time (Fig. 1.6). This conclusion holds when corrected for metamorphic alteration, which is around $1-2$‰ at greenschist facies (Thomazo & Papineau, 2013), applicable to most samples in the compilation. $\delta^{15}N$ values significantly below -5‰ have been documented from one site in the Neoarchean (Yang et al., 2019), interpreted as evidence of high ammonium availability. No other settings display such light values, making it unlikely that lightning was a significant source of nitrogen to the biosphere for most of Earth's history. It is possible that atmospheric products would have undergone further fractionation after raining out into the ocean, such that the residuum became isotopically heavier and was subsequently trapped in biomass. However, such fractionating processes would deplete the nitrite and nitrate reservoir, making it unlikely that sufficient fixed nitrogen remains in so-

lution to support the ecosystem. Similarly, UV photolysis can reduce the nitrate and nitrite concentration in the ocean, limiting the contribution to the ecosystem (Ranjan et al., 2019).

Another source of fixed nitrogen on early Earth could have been photochemical production of HCN due to UV irradiation of the atmosphere (Tian et al., 2011). However, on Titan, where UV radiation and cosmic rays produce a significant amount of HCN, the nitrogen in the HCN is very heavily enriched in ^{15}N compared to the N_2 (δ^{15}N values of $\sim$ 4000‰ (for HCN, Vinatier et al., 2007) and $\sim$ 650‰ (for N_2, Niemann et al., 2010), respectively). If photochemical HCN production had been a significant source of nutrients on early Earth, we would expect to see a strong enrichment of ^{15}N in the rock samples, which we do not see.

3.3.6 Conclusion

Measurements of the isotopic composition of fixed nitrogen in spark-discharge experiments shows a strong depletion in ^{15}N compared to the sedimentary rock record from the early Archean. Our results are thus consistent with the notion that biological N_2 fixation evolved early (Weiss et al., 2016), making the biosphere independent from lightning as a nutrient source. There is, however, potentially one exception, that we know of, of rocks from the Paleoarchean, where reconstructed pre-metamorphic δ^{15}N values may have been as low as -10‰ (Stüeken et al., 2021, pink line in Fig. 1.6). If correct, those numbers could represent a lightning contribution, meaning that Earth's earliest ecosystems and by extension prebiotic networks may have benefitted from lightning reactions.

To conclude, our results suggest that lightning was not the main source of bioavailable nitrogen for the established biosphere, but it could have been significant for Earth's earliest ecosystems and possibly for the origin of life. In addition, our results allow the community to investigate the source of fixed nitrogen on other bodies in the Solar System such as Mars where the Mars Science Laboratory and subsequent measurements have detected deposits of nitrate in several locations (Stern et al., 2015; Sutter et al., 2017).

3.4 The Effect of Lightning on the Atmospheric Chemistry of Exoplanets

3.4.1 Introduction

In the Introduction (Chapter 1.1.4) we have discussed several potential biosignatures that may be indicative of life on exoplanets. *JWST* may be able to detect some of those gases, for example NH_3 and CH_4, in an early-Earth like atmosphere of TRAPPIST-1 e over a few transits if the concentration is high enough (Claringbold et al., 2023). To avoid misinterpreting such signatures, other processes, such as lightning, that may lead to an observable abundance of these gases need to be quantified. Lightning is a significant though small source of fixed nitrogen on modern Earth (Schumann & Huntrieser, 2007, and references therin). In the previous section we have shown that lightning can also produce fixed nitrogen in an N_2-CO_2 atmosphere similar to the early Archean. Lightning has also been postulated to have played an important role in the origin of life itself (Miller, 1953). In this section, we therefore aim to study the effect of lightning on the atmospheric chemistry, how it affects false-positive and false-negative biosignatures, and if its effect would be observable on an exo-Earth and on TRAPPIST-1 planets.

Past studies demonstrated that many exoplanets will be covered in clouds for an extended period during their evolution such that it is reasonable to expect lightning to occur also in extrasolar planets (Woitke & Helling, 2003; Helling et al., 2008b, 2013a,b; Hodosán et al., 2021). Moreover, lightning will contribute to the formation of a global electric circuit (Helling, 2019) and produce chemical tracers of a convectively active atmosphere of any planet (Hodosán et al., 2016b). However, the only planets where in-situ measurements can be conducted are those within the Solar System and the only planet for which lightning can be studied to a reasonable degree of completeness with respect of flash density and energy range, is modern Earth (Chapter 1.3.2, Hodosán et al., 2016a). This work therefore adopts a different approach, namely a combination of laboratory experiments and modelling in order to investigate the impact of lightning on the atmospheric chemistry of exoplanets. In Section 3.4.2 we present the results of our spark discharge experiments with different gas mixtures initially containing N_2, CO_2, and H_2 and their implications. We apply our experimental results to two different hypothetical exoplanets and use photochemical simulations and calculated spectra to determine

potentially observable signatures from lightning and the prospect for false-positive or false-negative biosignatures (Section 3.4.3). We discuss our assumptions on lightning flash rates and atmospheric composition in Section 3.4.4 and present our conclusions in Section 3.4.5.

3.4.2 Results and Implications of Experimental Measurements

Table 3.3: Initial gas compositions in spark discharge experiments in bar[a]

Gas	Pure N_2	N_2–H_2	+ low CO_2	+ high CO_2
120-min experiments (wet)				
N_2	0.99 ± 0.00	0.98 ± 0.00	0.98 ± 0.00	0.93 ± 0.01
H_2	0.00 ± 0.00	$(9.98 \pm 0.02) \times 10^{-3}$	$(9.98 \pm 0.02) \times 10^{-3}$	$(9.3 \pm 0.1) \times 10^{-3}$
CO_2	$(2.6 \pm 1.8) \times 10^{-5}$	$(1.1 \pm 0.2) \times 10^{-4}$	$(2.5 \pm 0.2) \times 10^{-3}$	$(4.6 \pm 1.3) \times 10^{-2}$
O_2	$(1.3 \pm 0.8) \times 10^{-4}$	$(8 \pm 2) \times 10^{-5}$	$(1.2 \pm 0.4) \times 10^{-4}$	$(1.3 \pm 0.7) \times 10^{-4}$
H_2O	$(1.1 \pm 0.2) \times 10^{-2}$	$(1.4 \pm 0.2) \times 10^{-2}$	$(1.0 \pm 0.1) \times 10^{-2}$	$(1.2 \pm 0.1) \times 10^{-2}$
120-min experiments (dry)				
N_2	0.99 ± 0.00	0.99 ± 0.00	0.98 ± 0.01	0.94 ± 0.01
H_2	0.00 ± 0.00	$(9.9 \pm 0.1) \times 10^{-3}$	$(9.8 \pm 0.1) \times 10^{-3}$	$(9.4 \pm 0.1) \times 10^{-3}$
CO_2	$(2 \pm 2) \times 10^{-6}$	$(2 \pm 5) \times 10^{-5}$	$(6 \pm 7) \times 10^{-3}$	$(4.7 \pm 1.0) \times 10^{-2}$
O_2	$(6 \pm 2) \times 10^{-5}$	$(1.4 \pm 0.8) \times 10^{-4}$	$(5 \pm 7) \times 10^{-4}$	$(2.6 \pm 0.2) \times 10^{-4}$
H_2O	$(6 \pm 5) \times 10^{-3}$	$(4 \pm 5) \times 10^{-3}$	$(6 \pm 5) \times 10^{-3}$	$(6 \pm 3) \times 10^{-3}$
Overnight experiments (wet)				
N_2	0.99 ± 0.00	0.97 ± 0.00	0.97 ± 0.00	0.94 ± 0.01
H_2	0.00 ± 0.00	$(9.74 \pm 0.01) \times 10^{-3}$	$(9.71 \pm 0.03) \times 10^{-3}$	$(9.4 \pm 0.1) \times 10^{-3}$
CO_2	$(1.1 \pm 0.1) \times 10^{-5}$	$(4 \pm 4) \times 10^{-5}$	$(4 \pm 2) \times 10^{-3}$	$(3.8 \pm 1.3) \times 10^{-2}$
O_2	$(9 \pm 5) \times 10^{-5}$	$(5 \pm 2) \times 10^{-5}$	$(2.5 \pm 2.1) \times 10^{-4}$	$(1.4 \pm 1.0) \times 10^{-4}$
H_2O	$(1.0 \pm 0.8) \times 10^{-2}$	$(1.6 \pm 0.1) \times 10^{-2}$	$(1.5 \pm 0.3) \times 10^{-2}$	$(1.8 \pm 0.3) \times 10^{-2}$

[a] values are averaged from multiple sets of experiments, errors are standard deviations of these averages

We performed spark discharge experiments (Section 3.1) in gas mixtures with different combinations of N_2, CO_2, and H_2 to investigate the effect of lightning on the chemistry of lightly reducing gas mixture with varying fraction of CO_2. Our goal is to give a complete picture of the most abundant gaseous and aqueous compounds produced in spark discharge experiments in such gas mixtures. These compounds can be grouped into three categories: (1) CO and NO are, as we will see later, the most abundant products and directly produced in the spark channel. Thus, they might present signatures for lightning activity in exoplanetary atmospheres as we will discuss in Section 3.4.3. (2) N_2O, NH_3, and CH_4 are potential biosignatures (e.g., Seager et al., 2013b; Schwieterman et al., 2022; Thompson et al., 2022) and we want to investigate whether lightning might present a significant source of these gases. (3)

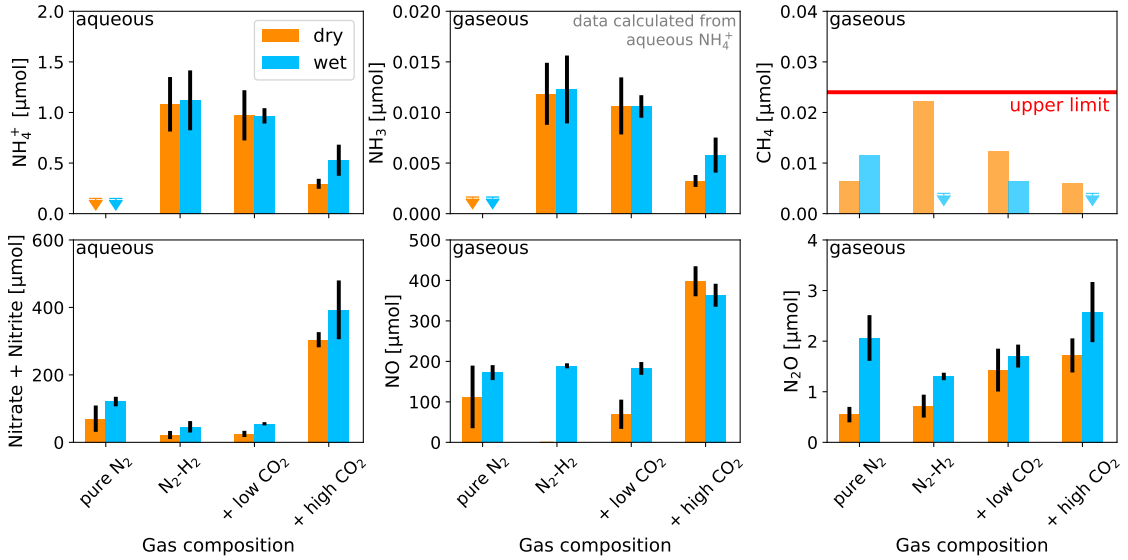

Figure 3.9: Final abundance of ammonium (NH_4^+), ammonia (NH_3), methane (CH_4), nitrate (NO_3^-) and nitrite (NO_2^-), nitrous Oxide (N_2O), and nitric Oxide (NO) in 120-min spark experiments with different gas compositions (see Tab. 3.3 for individual gas compositions). Results from experiments with (*blue*) and without (*orange*) water are shown separately. If no concentrations were measurable, the detection limit is indicated with an arrow. The data presented here are based on averages of multiple measurements with the error bars representing the individual standard error of the mean ($\sigma/\sqrt{N}$). Data for NH_3 is calculated from aqueous NH_4^+ and not measured directly. Measurements of methane abundance are within 1σ of 0 (*red line*) and are therefore shown without error bars and semi-transparent.

NH_4^+, NO_2^-, NO_3^-, HCN, and urea are important prebiotic compounds, either as precursors for the formation of biological macromolecules or as nutrients for early life forms (e.g., Miller, 1957; Schopf et al., 2007; Wong et al., 2017; Das et al., 2019). We investigated how the gas composition changes the yields of these products and what effect the presence of water vapour in the gas mixture has. We conducted a range of short, 120-min experiments as well as longer, over-night experiments to study the production of molecules with low yields that could not be detected in our short experiments. First, we present the results from our short experiments in individual sections for each compound and discuss their implications on the importance of lightning as a source of the specific molecule in the same section. We then present and discuss the results from our over-night experiments. The different gas compositions for all experiments are compiled in Table 3.3.

For our short, 120-min experiments, we performed experiments both with (wet) and without water (dry) in the flask during the spark. As described in Section 3.1, we added 50 mL of water to the dry experiments after turning off the spark. We then analysed the gas and water for the concentrations of NO, CO, N_2O, CH_4, NH_4^+, NO_2^-, and NO_3^-. Figure 3.9 shows the combined results from our short experiments. The individual measurements of each gas

composition are averaged over 3 to 7 replicates (see Barth et al., 2023b, for a detailed table with individual results), the results for wet and dry experiments are shown in different colours next to each other. As expected, one of the main results is that reduced nitrogen and carbon species (ammonium, ammonia, and methane) are more abundant in the pure N_2-H_2 and low-CO_2 experiments. Oxidised forms of nitrogen (nitrate, nitrite, nitric oxide, and nitrous oxide) are more abundant in the high CO_2 experiments where the dissociation of CO_2 provides the necessary oxygen source for NO and subsequent nitrogen oxides. We find increased efficiency of nitrogen oxides production in the experiments that contained water in the flask during the spark. The presence of liquid water resulted in approximately 1% of water vapour in the gas phase at room temperature (Table 3.3), which will also be dissociated in the spark, providing additional oxygen for the NO production. The individual products shown in Fig. 3.9 as well as CO are discussed in the following sections.

Ammonium (NH_4^+)

Ammonium is an important nutrient for microbial life on Earth and was the product of the first developed pathways of biological nitrogen fixation (Schopf et al., 2007; Dodd et al., 2017). Lightning-produced ammonium would therefore present a potential nutrient source for life before the onset of biological nitrogen fixation. We find that maximum ammonium production happens in experiments with no or $< 1\%$ of CO_2. A higher CO_2 concentration limits the efficiency of ammonium production. However, except for a few individual experiments, we find the final ammonium concentration to be lower than the concentration of nitrite and nitrate, in particular for the wet experiments. Our highest ammonium production rate (the wet, CO_2-free case) is $(3.8 \pm 1.7) \times 10^{12}$molecules/J which, using modern Earth's flash rate, corresponds to a yearly production of $(1.1 \pm 0.5) \times 10^{-3}\mathrm{Tg\,yr^{-1}}$. With a higher CO_2 concentration, more likely to resemble early Earth's atmosphere, this reduces to $(1.8 \pm 1.2) \times 10^{12}$molecules/J and $(0.5 \pm 0.3) \times 10^{-3}\mathrm{Tg\,yr^{-1}}$. This is much lower than the production of nitrite and nitrate (see below) which can subsequently be reduced to ammonium by iron in the ocean (Summers & Chang, 1993). Direct production of ammonium by lightning is therefore not significant on planets with a substantial concentration of CO_2 and/or water vapour in the atmosphere.

Ammonia (NH_3)

Ammonium is not directly produced by the spark. Instead, ammonia is the gaseous product of the spark discharge that then equilibrates with the water where it reacts to ammonium. Ammonia can be produced biologically and has been previously suggested as a biosignature for planets with a significant H_2 fraction in the atmosphere (Seager et al., 2013a,b; Huang et al., 2022). Ranjan et al. (2022) describe a scenario where NH_3 is produced in such high quantities that it saturates its photochemical sinks, such as O_2 in modern Earth's atmosphere, and goes into a runaway mode. The surface flux above which the NH_3 concentration enters into this runaway state, depends on the level of UV radiation. In their simulations of atmospheres with 10% H_2 and 90% N_2 (with 1% water vapour) on an Earth-sized planet orbiting an M dwarf, Ranjan et al. (2022) find this flux to be approximately $10^{11}\mathrm{cm}^{-2}\,\mathrm{s}^{-1}$, and as low as $10^{8}\mathrm{cm}^{-2}\,\mathrm{s}^{-1}$ for an elevated stratospheric temperature (from $T_{\mathrm{strat}} = 170\,\mathrm{K}$ to $210\,\mathrm{K}$). The modern Earth NH_3 flux is $1.1 - 1.8 \times 10^{10}\mathrm{cm}^{-2}\,\mathrm{s}^{-1}$ (Bouwman et al. 1997) and the pre-industrial flux $2 - 9 \times 10^{9}\mathrm{cm}^{-2}\,\mathrm{s}^{-1}$ (Zhu et al. 2015). The maximum lightning-induced NH_3 flux we can extrapolate from our experiments with an atmosphere of 1% H_2 and 1% H_2O (in N_2), including the aqueous NH_4^+, is approximately $(2.2 \pm 1.0) \times 10^{5}\mathrm{cm}^{-2}\,\mathrm{s}^{-1}$ (wet, pure $N_2{-}H_2$). This is many orders of magnitude below the flux necessary to enter into a runaway state, suggesting that lightning cannot be responsible for a false-positive biosignature detection of NH_3.

Methane (CH_4)

Methane is frequently discussed as a potential biosignatures, in particular for Archean Earth-like worlds (e.g., Thompson et al., 2022). If lightning could produce significant amounts of methane in an early-Earth-like atmosphere, this would present an important restriction on methane's role as a biosignature. However, in our experiments, only small amounts of methane are produced. Most of the measurements are below the error of an individual measurement (0.6 ppm) which means that they are within 1σ of 0. We therefore assume 0.6 ppm (or a total production of 0.024 µmol) to be the upper limit for methane production in our experiments, as indicated by the red line in Fig. 3.9. This limit corresponds to an annual methane production with modern lightning flash rate of less than $2\times10^{-5}\mathrm{Tg\,yr}^{-1}$ or $1.3\times10^{-6}\mathrm{Tmol/yr}$. The annual methane production on modern Earth is $37\,\mathrm{Tmol/yr}$ or $596\,\mathrm{Tg\,yr}^{-1}$, of which about 40% are natural, i.e. not anthropogenic, (Jackson et al., 2020) while the possible Archean biological

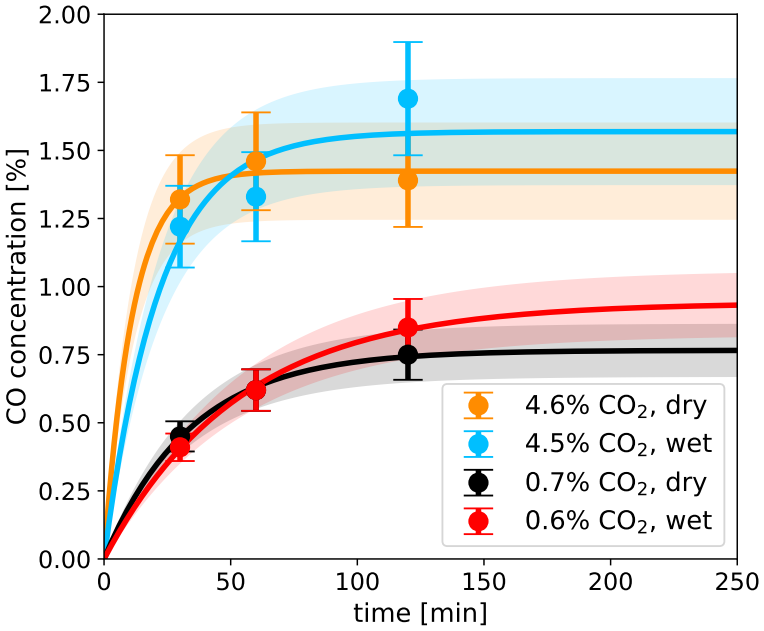

Figure 3.10: CO concentration in four different spark experiments (high and low-CO_2, wet and dry), measured at 3 different points in time during the experiment. Fitted lines give the CO concentration assuming CO is product of an equilibrium reaction, following $c_{CO_2} = (1-(k_1+k_2 \cdot \exp(-(k_1+k_2)t))/(k_1+k_2)) \cdot c_1$. Shaded areas represent errors of CO measurements.

methane production was between 20 and 40 Tmol/yr (Kharecha et al., 2005). The upper limit for abiotic methane production by serpentinizing systems (hydrothermal alteration of crustal mafic rocks) is between 0.02 and 10 Tmol/yr (Krissansen-Totton et al., 2018b). This suggests that in the atmospheric conditions explored in this study, methane production by lightning is negligible compared to other abiotic and biotic sources. The lightning flash rate in such an atmosphere would have to be five to six orders of magnitude higher than on modern Earth to produce a comparable amount of methane.

Carbon Monoxide (CO)

In contrast to methane, carbon monoxide has been suggested as a potential antibiosignature and if lightning were to produce detectable amounts of CO, this would provide again a limitation on the use of CO as an antibiosignature. We analysed the CO concentrations of four experiments, each at three different points in time during the experiment (after 30, 60, and 120 min). These results are shown in Fig. 3.10. The CO production rate decreases with time, probably because CO concentration reaches equilibrium. We extrapolated the CO concentration to estimate the equilibrium concentration (Fig. 3.10). Following the equilibrium reaction $A_1 \rightleftharpoons A_2$ (A_2 is CO in this case), starting with all molecules in A_1 ($c_1 = c_{tot}, c_2 = 0$), the

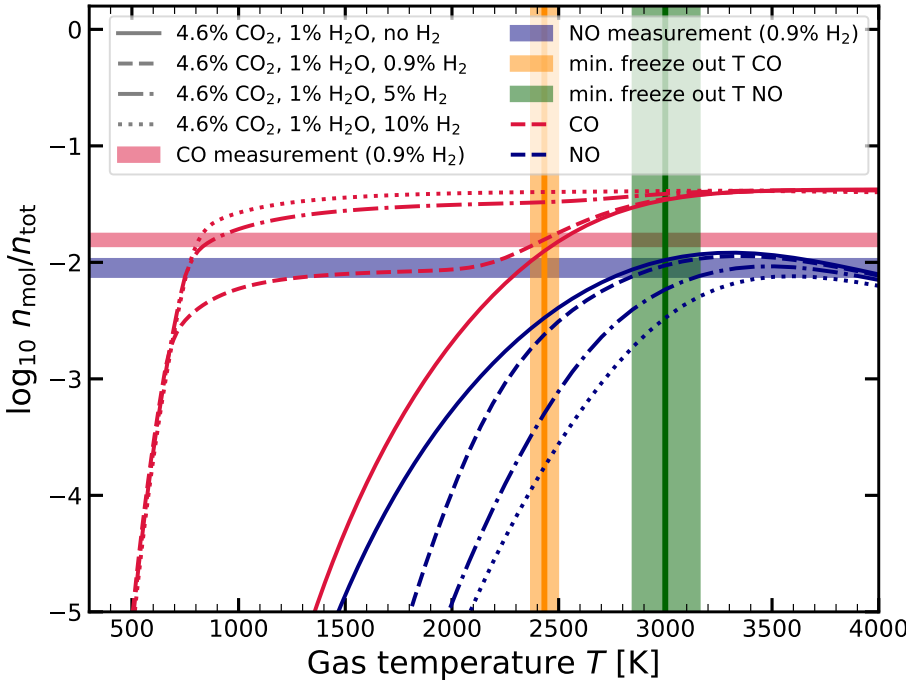

Figure 3.11: CO and NO concentrations in chemical equilibrium as function of gas temperature (with GGCHEM, Woitke et al., 2018) for high-CO_2 gas mixtures. The different cases considered are: 0% (*solid lines*), 0.9% (*dashed*), 5% (*dash dotted*), and 10% (*dotted*) of H_2. CO (*red*) and NO (*blue shaded area*) measurements with uncertainties from wet 120-min experiments. Minimum freeze-out temperature estimates for CO (*orange*) and NO (*green*) with uncertainties.

concentration of A_2 (c_2) increases with time, governed by the reaction coefficients k_1 and k_2:

$$c_2 = (1 - (k_1 + k_2 \cdot \exp(-(k_1 + k_2)t))/(k_1 + k_2)) \cdot c_1. \tag{3.17}$$

The resulting equilibrium concentrations of CO are 1.5% for the high-CO_2 experiments (4.5 – 4.6% CO_2) and 0.85% for the low-CO_2 experiments (0.6 – 0.7% CO_2).

Extrapolating CO Production for Different Atmospheres

In order to evaluate the effect of H_2 on the CO and NO production, we carried out equilibrium calculations with GGCHEM (Woitke et al., 2018) (Fig. 3.11). We used the subset of the species within GGCHEM with 87 charged and neutral species containing the elements H, C, N, and O, as well as electrons. We calculated the thermochemical equilibrium composition of gas mixtures with varying H_2 fraction resembling our wet, high-CO_2 experiments (4.6% CO_2, 1% H_2O, 0 – 10% H_2, with the rest to 100% N_2) for temperatures between 300 and 4000 K. By comparing our CO and NO measurements from the experiments with 0.9% H_2 (red and blue shaded areas, respectively) to the corresponding calculations (dashed lines), we can estimate a minimum freeze-out temperature for the respective gas. Here, the CO measurement is from

only one experiment, the NO concentration is the average of multiple experiments. The freeze-out temperature is the temperature at which the equilibrium time-scale is larger than the cooling time-scale of the gas mixture, freezing in the gas composition at that temperature. While the CO measurements with time allow us to estimate the equilibrium composition of CO in the flask (see Fig. 3.10), we only have one measurement of NO after the full 120 min run time of the experiment, which might increase slightly further. We therefore can only give a minimum estimate on the freeze-out temperature for NO. Our estimates are $T_{\mathrm{f}}(\mathrm{CO}) = 2430 \pm 65\,\mathrm{K}$ and $T_{\mathrm{f}}(\mathrm{NO}) = 3000 \pm 160\,\mathrm{K}$. The latter is similar to previous estimates of $T_{\mathrm{f}}(\mathrm{NO}) = 2300\,\mathrm{K}$ (Chameides et al., 1977), 2660 K (Borucki & Chameides, 1984), and 3500 K (Kasting & Walker, 1981). This estimate of the NO freeze-out temperature also allows us to determine a lower limit of the maximum temperature reached within the spark channel of approximately 3000 K.

The estimates for the freeze-out temperatures allow to extrapolate the CO and NO production to atmospheres with different H_2 fraction. Figure 3.11 shows additional equilibrium calculations for gas mixtures without H_2 (solid lines), with 5% (dash-dotted) and with 10% H_2 (dotted). The addition of H_2 increases the abundance of CO in the lower temperature regime where (in the absence of H_2) CO_2 would be more stable. The H_2 reacts with the atomic oxygen produced by the dissociation of the CO_2 to form H_2O, preventing the CO from recombining with the O to CO_2. Eventually, the abundance of CO is limited by the availability of C from the initial CO_2. Increasing the H_2 fraction from 0.9% to 10% (in a background of 4.6% CO_2 and in the context of the limited chemistry applied in these calculations) leads to an increase of the CO abundance by a factor of 2.5 at the freeze-out temperature of 2430 K. At the same time, the presence of H_2 (and subsequent production of H_2O) reduces the availability of oxygen for the production of NO. At 3000 K, we find that the NO concentration for 10% H_2 is only $1/3$ of the concentration expected in the 0.9%-H_2 case.

From the initial slope of our fit to the CO concentration with time (Fig. 3.10) a global, annual production of $6 - 18\,\mathrm{Tg\,yr^{-1}}$ and a surface flux of $7.6 - 24 \times 10^8\,\mathrm{cm^{-2}\,s^{-1}}$ can be estimated for the different H_2 concentrations (assuming modern Earth's lightning flash rate). Using those estimates for surface fluxes, a grid of photochemical simulations was performed, similar to those presented by Schwieterman et al. (2019). This allowed to test under which conditions a lightning contribution to the CO production could be observable (Section 3.4.3).

Previous experimental results and calculations for the CO production by lightning in mod-

ern Earth's atmosphere are $0.01\,\mathrm{Tg\,yr^{-1}}$ (Green et al., 1973), $0.04\,\mathrm{Tg\,yr^{-1}}$ (Levine et al., 1979), and $(0.004-0.2)\mathrm{Tg\,yr^{-1}}$ (Chameides, 1979b). If we use the approach outlined above, using the equilibrium concentration of CO at 2430 K in a gas mixture resembling modern Earth's atmosphere, our estimate for the global CO production by lightning is $(0.01\pm0.003)\mathrm{Tg\,yr^{-1}}$ which is in agreement with the values presented in the literature.

Nitrogen Oxide (NO) Production and Extrapolation to Different Atmospheres

In the previous section (3.3) we have shown that lightning can produce large amounts of nitrogen oxide in both N_2-O_2 and N_2-CO_2 atmospheres. This NO provides the precursor of other nitrogen oxides in the gas phase as well as nitrite and nitrate in the aqueous phase (see below). From our equilibrium calculations we find that the maximum possible NO concentration (at $\sim$ 3300 K) is only slightly higher than our measurement for the wet, high-CO_2 experiments (Fig. 3.11). This suggests, that at the time we took the NO measurement, the NO concentration in the flask had (nearly) reached equilibrium. We cannot fit the production law we used for CO (Reaction 3.17) to this single data point, but, assuming our data point represents the equilibrium NO concentration, we can find the slowest production that will reach equilibrium after 120 min (within 1%). The slope of this production curve at the origin provides a lower limit for the NO production rate. For the wet experiments with a high CO_2 concentration, this returns a lower limit of $(5.6\pm1.0)\times10^{15}$molecules/J or a yearly production of $(2.6\pm0.4)\mathrm{Tg\,yr^{-1}}$ with modern Earth's lightning flash rate.

For the other three sets of wet experiments (with N_2, N_2-H_2, and low CO_2 gas mixtures), the minimum NO production is independent from the CO_2 and H_2 fraction in the gas $(3\pm1)\times10^{15}$molecules/J or $(1.2\pm0.3)\times10^{-2}\mathrm{Tg\,yr^{-1}}$. In these experiments, water vapour in the gas mixture $(1-1.4\%)$ provides the necessary oxygen to oxidize nitrogen to NO. In the corresponding dry experiments, the NO production is lower than in the wet experiments, but not 0 due to traces of CO_2 (in particular in the low-CO_2 experiments), water vapour, and O_2 being present in the gas mixture. In our wet experiments presented in Section 3.3 with only trace amounts of O_2 (0.06%) we found that $\sim3\times10^{15}$molecules/J of NO are produced. This production rate is similar to our wet experiments presented here without any or with only small amounts of CO_2, suggesting that dissociation of water vapour is the main production pathway for NO in all of these experiments.

From the high-CO_2 experiments and subsequent equilibrium calculations (Fig. 3.11) we

find that the presence of H_2 in the gas mixture decreases the NO production. Instead, more H_2O is produced. We used these results for the NO production rate as input for photochemical simulations of the NO_2 concentration in the atmospheres of different potential exoplanets (Section 3.4.3). NO and NO_2 are spectrally active at 5.3 µm and 6 µm, respectively, and therefore potential signatures for lightning activity in exoplanet atmospheres (Gordon et al., 2022).

Nitrous Oxide (N_2O)

N_2O is another potential biosignature, making an investigation of the possibility for a false-positive signature from lightning important. The maximum N_2O production found in our experiments is 2.5 µmol which corresponds to an energy yield of 8.5×10^{12}molecules/J or 1.3×10^{-4}Tmol yr^{-1} with modern Earth's lightning flash rate. This value is similar to experimental results for modern Earth's atmosphere (Levine et al., 1979; Hill et al., 1984; Chameides, 1986). The total biological N_2O emissions on Earth is much larger with 0.45 Tmol yr^{-1} (Bouwman et al., 2002; Tian et al., 2020). This N_2O is produced by incomplete denitrification of Nitrate to N_2 (Schwieterman et al., 2022). In the Proterozoic, the N_2O flux might have been significantly higher due to the limited availability of copper catalysts, preventing the last step of denitrification from N_2O to N_2 (Buick, 2007).

In addition to the N_2O directly produced by lightning, other forms of fixed nitrogen (e.g. NO, NO_2, or HNO_3) can be deposited into the ocean, converted to N_2O by Fe^{2+} (Ranjan et al., 2019), and again outgassed into the atmosphere. If all lightning-produced NO (based on our experimental results) were to be converted to N_2O eventually, that would correspond to an annual production of 0.09 Tmol yr^{-1}. This would only be a factor of 5 lower than the modern Earth N_2O flux and potentially detectable in the emission spectrum of an Earth-like planet orbiting a K dwarf (Schwieterman et al., 2022). This would be particularly true if the lightning flash rate in the atmosphere of such a planet is larger than that on modern Earth. However, in the anoxic atmosphere of an Archean Earth-like planet, the N_2O abundance will be reduced by the missing O_2-shielding, decreasing the probability of a detectable signal and strengthening the case for the O_2/O_3 + N_2O biosignature. Moreover, an O_2-rich planet probably does not have Fe^{2+}-rich oceans. A detectable NO_2 signature from lightning might help to distinguish a lightning-produced N_2O signature from a biogenic source (Schwieterman et al., 2022). We use our results from the photochemical simulations to estimate the maximum potential N_2O production and compare it to the NO_2 concentration (Section 3.4.3).

Nitrate (NO_3^-) & Nitrite (NO_2^-)

Lightning-produced nitrite and nitrate have been hypothesised as potential nutrients for life on early Earth before the onset of biological nitrogen fixation (e.g., Wong et al., 2017). Even though we have shown that life probably became independent from lightning as a nutrient source very early, it might have still provided a contribution to support Earth's earliest biosphere. Further, this nitrate and nitrite could present a nutrient source for life on exoplanets.

We combined the concentrations of nitrate and nitrite (Fig. 3.9) because part of the nitrite will oxidise to nitrate in the solution during the experiment. The extent of this oxidation varies depending on the individual experiment setup. As was the case for NO, we find that in wet experiments, the production of nitrite and nitrate increases compared to the dry experiments. Also the experiments without CO_2 show some nitrite and nitrate production: in the wet experiments this is due to the presence of water, but also in the dry experiments some nitrite and nitrate are present. This small residue may reflect contamination of the initial gas mixture with small amounts of gaseous H_2O, CO_2, or O_2. Overall, in the high-CO_2 experiments the nitrite and nitrate yield is very similar to the NO yield, with a maximum production of $\sim 400\,\mu\text{mol}$. With modern Earth's lightning flash rate, that corresponds to $\sim 0.02\,\text{Tmol}\,\text{yr}^{-1}$ or $\sim 0.3\,\text{TgN/yr}$ of fixed nitrogen. This yield is very similar to the value we found for a potential Archean atmosphere (0.16% CO_2 in N_2, Section 3.3).

Overnight Experiments

In addition to the short 120-min experiments, we also conducted overnight experiments with an average total spark time of (925 ± 35)min to investigate the production of compounds that were not detectable in the short experiments or had only very small yields. Figure 3.12 shows the abundances of gaseous and aqueous products after the overnight experiments and linear fits to show the relation between CO_2 concentration and final abundance of the product. Again, the abundances of HCN and NH_3 are calculated from the measured aqueous abundances of CN^- and NH_4^+, respectively, with their respective Henry's law constants as described in Section 3.1.3. Similar to the short experiments, we see an increasing production of oxidised nitrogen (NO, nitrate and nitrite) and a decreasing production of reduced nitrogen (ammonium) with increasing CO_2 concentration. The maximum ammonium concentration (at 0% CO_2) is only about two to four times the corresponding ammonium concentration in the short experi-

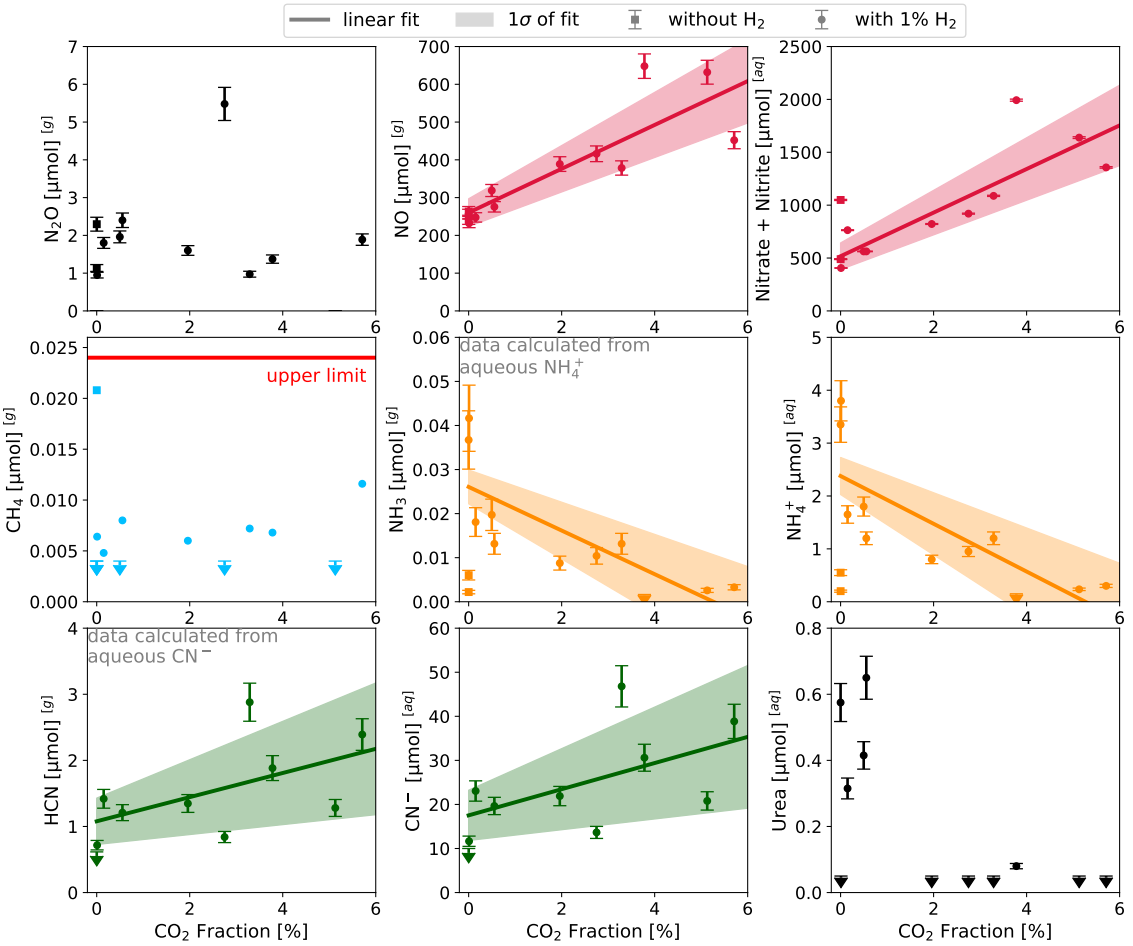

Figure 3.12: Final abundances of gaseous ($^{[g]}$; nitrous oxide (N_2O), methane (CH_4), hydrogen cyanide (HCN), nitric oxide (NO), and ammonia (NH_3)) and aqueous ($^{[aq]}$) products (CN^-, nitrite + nitrate, NH_4^+, and urea) in overnight experiments. Data points represent individual experiments with varying CO_2 fraction. Experiments without any H_2 and CO_2 are indicated by squares and not included in fits. Lines are best linear fits for dependency between CO_2 concentration and final abundance of products. Measurements below the detection limit (*arrows*) are included as (Detection Limit $/\sqrt{2}$) in the fitting process. Shaded areas give 1σ-range. No fit is shown for methane since all measured values are within 1σ of 0 (*red line*), for nitrous oxide since there is no trend visible in the data, and for urea as most measurements for $CO_2 > 1\%$ below detection limit. Abundances of HCN and NH_3 are calculated from measured aqueous abundances of CN^- and NH_4^+, respectively.

ments, even though the spark was running approximately eight times as long, suggesting that the ammonium concentration reached equilibrium during the experiment. For a CO_2 concentration of $\gtrsim 5\%$ basically no ammonium was produced. Instead the dissociated nitrogen was probably oxidized to NO and eventually nitrite and nitrate instead. A higher H_2 concentration might allow the production of ammonium at higher CO_2 concentrations, but eventually, if there is significantly more CO_2 (or a different oxygen source) than H_2 in the gas mixture, the ammonium production would probably still be suppressed. As discussed above, significant amounts of ammonium can still be produced by subsequent reduction of nitrite and nitrate by

iron in the ocean (Summers & Chang, 1993).

The concentration of nitrite and nitrate as well as NO in our discharge experiments shows a very clear trend with CO_2 concentration in the initial gas mixture. For CO_2 concentrations around 0, water vapour in the gas mixture is a significant source of oxygen for the production of nitrogen oxides. The slightly increased scatter of measurements at that point can be explained by the additional uncertainty of the concentration of water vapour and other trace gases like O_2. We also find the nitrite and nitrate concentration in the overnight experiments to be 5-10 times the concentration in the corresponding short experiments, suggesting that even though NO equilibrium in the gas phase is reached rather quickly (the final NO concentration in the overnight experiments is similar to the short experiments), the subsequent oxidation to NO_2 and equilibration with the aqueous phase takes more time, in particular in the experiments where relatively small amounts of nitrite and nitrate are produced. All of these experiments were run with 50 mL of water in the flask, so even when the CO_2 content is 0, there was sufficient oxygen available from the water to provide oxygen for the production of some NO and subsequently Nitrite and Nitrate. The presence of water as an oxygen source is probably also the reason that we again see only very small concentrations of methane, below the measurement error. Unlike for the other forms of oxidised nitrogen, we do not see a clear trend in the production of N_2O with CO_2 concentration. This follows the trend in our short, wet experiments where also no clear trend was visible, suggesting that if enough oxygen is available, nitrogen oxides with a higher oxidation state are prefered. N_2O has an oxidation state of $+1$ while NO, NO_2, nitrite and nitrate have oxidation states of $\geqslant 2$.

Urea ($CO(NH_2)_2$) is an important precursor for cyanamide (CH_2N_2) which itself is a precursor for RNA (Das et al., 2019). In our experiments, urea follows a similar trend as ammonium, with abundances of roughly one order of magnitude lower. However, because most measurements for CO_2 concentrations above 1% were below the detection limit, we did not try to fit a line to the urea data. It thus seems, that the production of (detectable levels of) urea is only possible under reducing conditions.

HCN is an important precursor molecule for the formation of RNA and has been hypothesized to be produced by lightning in reduced atmospheres (Miller, 1957; Miller & Schlesinger, 1983; Pearce et al., 2017, 2022). In our experiments, we can monitor the HCN production by its dissolved form, cyanide CN^-. The cyanide abundance increases with increasing CO_2

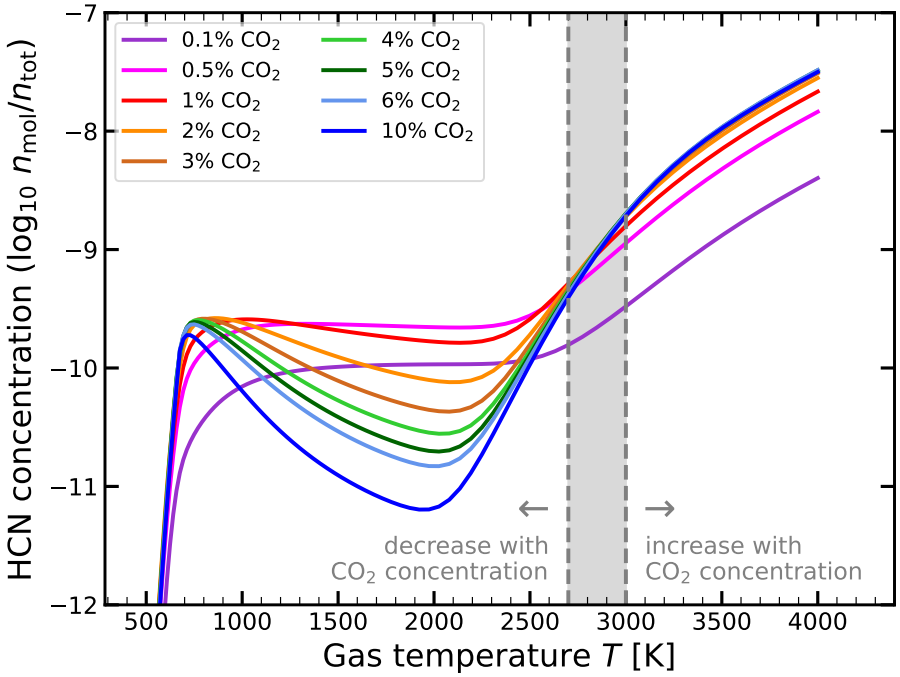

Figure 3.13: HCN concentration in chemical equilibrium (with GGCHEM, Woitke & Helling, 2003) as function of gas temperature for different CO_2 fractions in the gas mixture (other gases: 1% H_2, 1% H_2O, rest N_2). For $T \gtrsim 3000\,\mathrm{K}$ (*dashed grey line*), HCN concentration increases with increasing CO_2 concentration (until $\sim 3-5\%$ CO_2). For $T \lesssim 2700\,\mathrm{K}$ HCN concentrations decreases with increasing CO_2 concentration (except for 0.1% CO_2.

abundance, though much more slowly than the abundance of nitrite and nitrate. This follows the calculations performed by Chameides & Walker (1981), who predict an increase in HCN production when decreasing the C/O-ratio (at constant H_2 concentration), which is happening when increasing the CO_2 concentration (without adding other forms of carbon this limits the C/O ratio to 1/2). Chameides & Walker (1981) predict an HCN production rate of $\sim 3 \times 10^9$ to 4×10^{11}molecules/J for the range of C/O-ratios equivalent to our experiments (for a gas mixture with 0.9 bar N_2 and 0.05 bar H_2, C + O = 0.1 bar). We find our results for HCN production to be approximately two to three orders of magnitude larger than the values calculated by Chameides & Walker (1981). The reason for this might be that the water in our experiments acts as a buffer: produced HCN dissolves in the water, lowering the concentration in the gas-phase and allowing for more HCN to be produced. Chemical equilibrium calculations (Fig. 3.13) show that the concentration of HCN increases with CO_2 concentration for gas temperatures above approximately 3000 K, while for temperatures below 2700 K the HCN concentration decreases. This suggests that the freeze-out temperature for HCN in our experiment is $\gtrsim 3000\,\mathrm{K}$. Other experiments studied the effect of CH_4 concentration on the HCN production: an increase in CH_4 increases the C/O-ratio, leading to a strong increase in

HCN production (Chameides & Walker, 1981; Tian et al., 2011; Pearce et al., 2022).

3.4.3 Results and Implications of Photochemical Simulations

Now that we know the production rates for CO and NO, by far the most important direct products of lightning in N_2-CO_2 gas mixtures, we want to know how this influx of CO and NO changes the composition of different planetary atmospheres. We are particularly interested if lightning can produce observable signatures in transmission, emission, and reflected light spectroscopy. To answer those questions, we used the photochemical model of the Atmos coupled climate-photochemistry code (Section 3.2.2; Arney et al., 2016; Lincowski et al., 2018) to calculate the atmospheric mixing ratios of CO, NO, NO_2, and other gases for a large range of lightning flash rates. We modelled both oxygen-poor (anoxic) and oxygen-rich (oxic) atmospheres on Earth-sized planets orbiting the Sun (G-type star) and TRAPPIST-1 (M-type star) at the inner edge of their respective habitable zone.

Photochemistry in Anoxic Atmospheres

Figure 3.14 (a, b) shows the resulting CO mixing ratios for the anoxic atmosphere (4.6% CO_2 in N_2 filler gas) for abiotic and biotic scenarios with different CH_4 fluxes and CO deposition rates and for a range of lightning flash rates (Table 3.1). Using equilibrium chemistry calculations as described in Section 3.4.2, we can estimate the production of CO and NO with modern Earth's lightning flash rate to be 7.0×10^8 and 3.8×10^8molecules/cm^2/s, respectively, in this anoxic gas mixture. The results look very differently for the two different host stars with different spectra: On the planet orbiting the Sun the CO mixing ratio in the biotic scenario is up to three orders of magnitude larger than in the abiotic scenario. On the planet orbiting TRAPPIST-1, this trend is reversed. The CO ratio in the biotic scenario is 100 times smaller than in the abiotic scenario for most of the CO flux range. The high CO concentrations in the TRAPPIST-1 simulations are due to efficient CO_2 photolysis. The XUV flux is concentrated near the Lyα line and the FUV continuum and therefore absorbed by the abundant CO_2 molecules that are dissociated into CO and O. Thus, the CO_2 is shielding water molecules from the XUV radiation and the photolysis of water in the atmosphere of a planet orbiting an M dwarf is less efficient and the concentration of the OH radical is lower. Since the deposition velocity with which CO is deposited into the ocean is lower in the abiotic than in the biotic scenario, where acetogens in the ocean consume the CO, the abiotic CO concentration remains higher than in the biotic

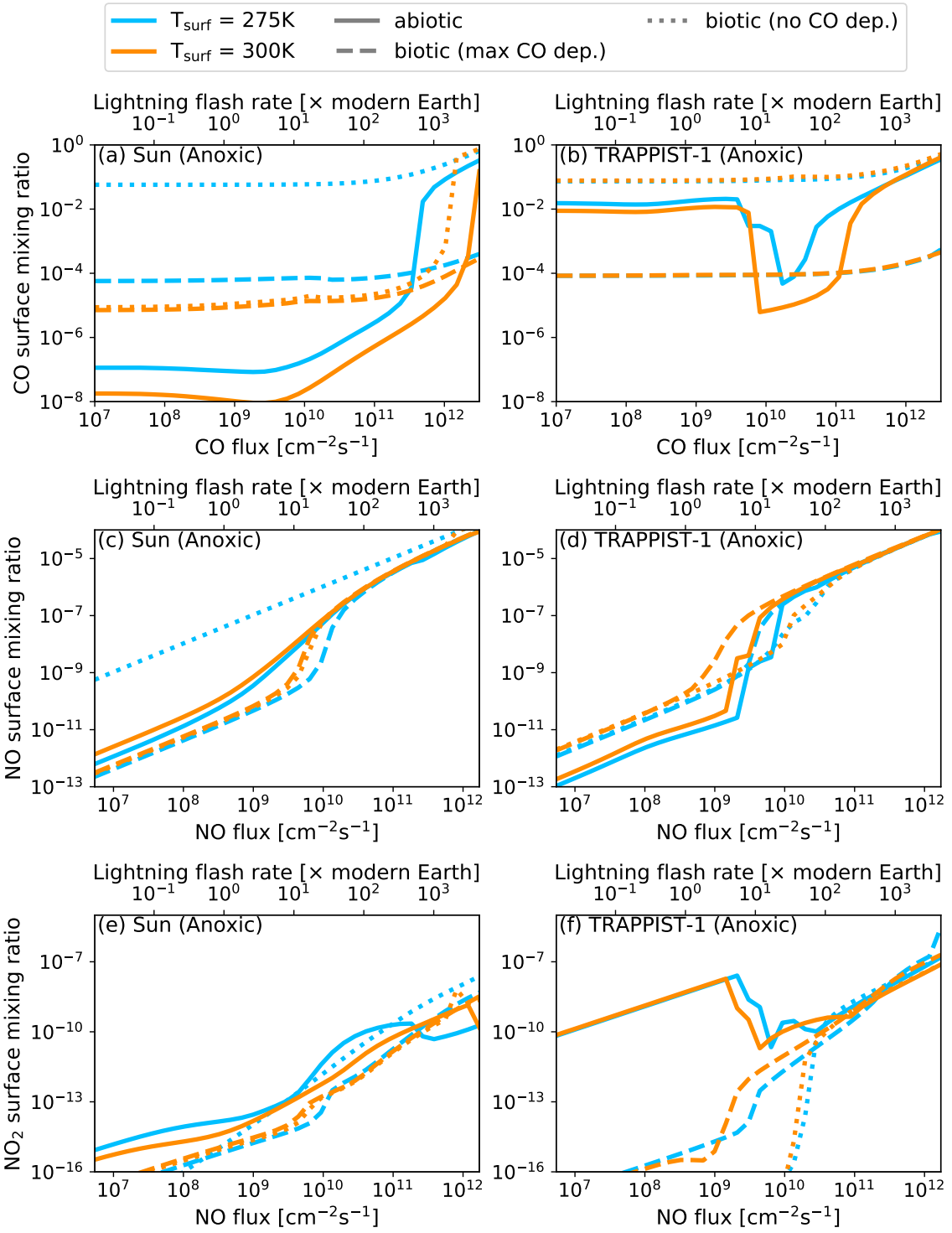

Figure 3.14: Photochemically simulated CO (**a** & **b**), NO (**c** & **d**), and NO_2 (**e** & **f**) mixing ratios in the anoxic atmosphere (4.6% CO_2) of an Earth-sized planet orbiting the Sun (**a, c, e**) and TRAPPIST-1 (**b, d, f**) for varying CO and NO production rates and different scenarios: abiotic (*solid*), biotic with CO deposition (*dashed*), and biotic without CO deposition (*dotted*). The surface temperature (*blue*: $T_{\mathrm{surf}} = 275\,\mathrm{K}$, *orange*: $T_{\mathrm{surf}} = 300\,\mathrm{K}$) controls the water vapour concentration. The second x-axis gives the corresponding lightning flash rate (in units of modern Earth's flash rate), as estimated for the respective atmospheric composition.

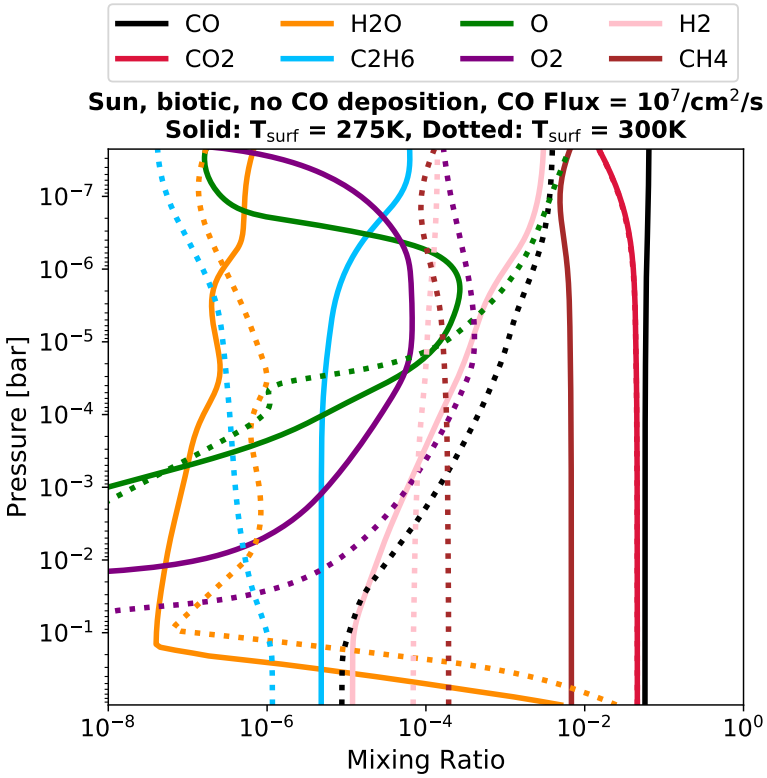

Figure 3.15: Atmospheric mixing ratios for biotic scenario (Sun) without CO deposition (CO flux $\sim 10^7$molecules/cm^2/s) for two different surface temperatures (*solid lines*: $T_{\rm surf} = 275\,$K, *dotted lines*: $T_{\rm surf} = 300\,$K) as result of a kinetic gas-phase calculation with photochemistry.

case.

In the simulations for the planet irradiated by the Sun, the OH concentration in the atmosphere is higher and the CO lifetime shorter. In the biotic scenario, the increased, biogenic flux of CH_4, which is photo-oxidised to CO, leads to a higher CO concentration than in the abiotic scenario. In a test case for the biotic scenario, where we assume no CO to be deposited into the ocean (dotted lines in Fig. 3.14), the final CO concentration is increased to well above 1% in all but one cases despite OH being present. An increase in surface temperature increases the concentration of water vapour in the atmosphere and subsequently the concentration of OH, decreasing the lifetime of CO and its final concentration. This is especially apparent for the biotic planet around the Sun when we assume no CO deposition: While for a surface temperature of $T_{\rm surf} = 275\,$K (blue dotted line) the CO concentration is enhanced to above 1%, for a slightly higher surface temperature of $T_{\rm surf} = 300\,$K (orange dotted line) the subsequently higher water and OH concentration allows for a more efficient removal of CO from the atmosphere (see Fig. 3.15 for comparison of mixing ratios of more species). This suggests that for the biotic scenario for the Sun-orbiting planet with $T_{\rm surf} = 300\,$K, recombination of CO with

OH is the major CO sink. Overall, the major sink for CO in both biotic scenarios for TRAPPIST-1 and the biotic scenario with $T_{\text{surf}} = 275\,\text{K}$ for the Sun is deposition in the ocean.

In nearly all anoxic simulations, the CO concentration is relatively high due to CO_2 dissociation and CH_4 photo-oxidation and additional contributions of CO by lightning cannot further increase the CO concentration. Only for lightning flash rates around 1000 times the modern-Earth lightning flash rate we can see the CO concentration increase slightly beyond the background level. The only scenario, where the background CO level is low enough to see an increase in CO concentration at lower flash rates, is the abiotic scenario for the planet orbiting the Sun. In fact, for CO production rates higher than $\sim 10^{11}$ or $\sim 10^{12}$molecules/cm^2/s for $T_{\text{surf}} = 275\,\text{K}$ an $T_{\text{surf}} = 300\,\text{K}$ respectively, the atmosphere enters into a CO runaway: the CO flux overwhelms the CO deposition and the CO concentration jumps up to several percent. This CO flux is similar to the total CO emission on modern Earth of $\sim 2\times10^{11}$molecules/cm^2/s which is mainly from anthropogenic sources (68%) and wildfire and deforestation (32%) (Zhong et al., 2017). However, on the uninhabited Archean Earth, the volcanic CO flux is estimated to be much lower at $\sim 1-2\times10^{8}$molecules/cm^2/s (Kasting & Walker, 1981). We also should note that for CO concentrations larger than the CO_2 concentration (4.6%), our assumption of constant CO_2 concentration might not be applicable anymore, as it would require very high volcanic fluxes of CO_2 to replenish the CO_2 dissociated by lightning and would greatly enhance the carbon budget in the atmosphere.

For the planet orbiting the Sun, we find a very similar trend for the NO_2 concentration for all scenarios (Fig. 3.14, e & f): Very low abundances ($< 10^{-8}$ for nearly all simulations), but a steady increase with increasing NO flux. For the planet orbiting TRAPPIST-1, this looks a bit different: In the biotic scenario with CO deposition, the NO_2 concentration follows a very similar trend to the same case for the Sun-planet, but with slightly higher mixing ratios of up to 1 ppm for the highest NO fluxes. In the abiotic case though, the NO_2 abundance is more than six orders of magnitude higher for low NO fluxes compared to the biotic case, before it rapidly decreases, parallel to the CO abundance, at an NO input flux of $\sim 3\times10^{9}$molecules/cm^2/s. At higher fluxes, the NO_2 abundance increases again, very similar to the biotic scenario.

We can also observe this behaviour in the CO concentration for the abiotic scenario on the TRAPPIST-1 planet (Fig. 3.14b, solid lines): here, the background CO concentration (for low CO lightning fluxes) is very high at approximately 1%. Once the CO and the corresponding

NO flux cross a certain threshold ($\sim 10^{10}$molecules/cm^2/s), the CO concentration drops by more than two orders of magnitude before rapidly climbing again in a CO runaway. This drop in the CO and NO_2 concentration is accompanied by a drop in O_2 concentration and a strongly increasing NO concentration (Fig. 3.14, c & d). In the anoxic gas mixture, where NO and CO are produced from dissociated CO_2 and N_2, free oxygen is produced if not the same amount of NO and CO is produced to match the stochiometric ratio of the split CO_2. In order to not change the balance of N, C, and O in our model atmosphere, we included an additional O flux to balance the ratio between these three elements. The background concentrations of O_2 and ozone as byproducts from CO photolysis are very high in this scenario and even slightly enhanced further by the addition of free oxygen from lightning, up to an O_2 surface mixing ratio of 1.4×10^{-3} and a peak ozone concentration of ~ 5 ppm at a height of 32 km. The high concentration of oxygen allows for efficient oxidation of NO to NO_2 ($NO + O_3 \longrightarrow NO_2 + O_2$ and $NO + HO_2 \longrightarrow NO_2 + OH$), resulting in a higher concentration of NO_2 than NO. However, eventually, enough OH is being produced as a side product of NO_2 oxidation, that this pathway becomes the most efficient for OH production. This in turn allows for increased recombination of $CO + OH \longrightarrow CO_2 + H$, leading to a sharp decrease in CO and O_2 concentration, a slower decrease in ozone concentration. Subsequently, due to the lack of oxidants, the NO_2 concentration decreases as well, while most of the lightning produced NO remains as such in the atmosphere.

This process was described by Harman et al. (2018) who suggested that lightning-produced NO can provide a catalyst for the recombination of CO and O to CO_2, preventing a false-positive O_2-biosignature. They assume an NO production of $\sim 6 \times 10^8$molecules/cm^2/s (for modern Earth's lightning flash rate) in an atmosphere with 5% CO_2 and find this to strongly reduce the CO and O_2 concentration (for an M dwarf host star). This NO production rate is about 50% higher than what we assume for modern Earth's lightning flash rate, but even if we correct for this difference, the additional production by lightning of CO and O in our model moves this behaviour to flash rates at least three times that of modern Earth. Using our assumption for the NO production per flash, a flash rate of more than six times modern Earth's is necessary to prevent the buildup of significant amounts of oxygen in the atmosphere. This discrepancy is probably because of differences in the UV spectrum used for the simulations. Larger stellar FUV/NUV flux ratios tend to drive higher abiotic O_2 production rates (Harman et al., 2015) and TRAPPIST-1 (M8V) has a larger FUV/NUV ratio than the latest host star

considered by Harman et al. (2018), an M4V dwarf. Importantly, this suggests that lightning may not eliminate all O_2 false-positive scenarios for CO_2-rich terrestrial planets orbiting ultra-cool dwarf hosts. Figure A.1 (top) in the appendix shows the atmospheric mixing ratio profiles for simulations before and after the drop in CO and O_2 concentration for the scenario with $T_{\mathrm{surf}} = 275\,\mathrm{K}$. The spectra for these two cases are discussed below (Fig. 3.18). Figures A.6 to A.11 show the column densities of the atmospheric constituents for the range of simulated CO and NO fluxes for all anoxic scenarios discussed in this section.

Photochemistry in Oxygen-rich Atmospheres

Earth's atmosphere was anoxic approximately for the first 2 Gyr of its evolution. After that, the oxygen concentration increased drastically, but it was only at about 0.5 Ga that the oxygen concentration reached today's level (e.g., Catling & Zahnle, 2020). Assuming that the evolution of oxygenic photosynthesis takes a similar amount of time on other worlds, if it happens at all, it is therefore most likely that if we find an inhabited planet, it will have an anoxic or low-oxygen atmosphere (Krissansen-Totton et al., 2018b). However, as we have discussed in Section 1.1.4, photochemistry and hydrogen escape can lead to the abiotic buildup of O_2 in an otherwise anoxic atmosphere. To fully investigate the impact of lightning on observable oxygen and ozone features, we therefore also conducted simulations for oxygen-rich atmospheres with a biosphere (4.6% CO_2, 21% O_2 in N_2 filler gas; biotic scenario with maximum CO deposition; Fig. 3.16). In addition, the O_2 and O_3 features of an N_2-O_2 atmosphere are probably not detectable with *JWST* (Krissansen-Totton et al., 2018a). Thus, the atmosphere of a modern-Earth like, inhabited planet might resemble the Archean Earth instead, with CH_4 and CO_2 features. In this case, it is important to understand the role of lightning in potentially producing a CO signature.

In such an oxic gas mixture, our estimate for the CO and NO production rates at modern Earth's lightning flash rate are 1.5×10^8 and $2.5 \times 10^9 \mathrm{molecules/cm^2/s}$, respectively, using the method described in Section 3.4.2. Our simulations find, for both host stars, a significantly lower CO mixing ratio than in the anoxic atmospheres, independent from the CO deposition velocity. The high abundance of O_2 in these atmospheres offers an additional sink for atmospheric CO: excited atomic oxygen from ozone photolysis increases the production of the OH radical: $O_3 + h\nu(\lambda < 320\,\mathrm{nm}) \longrightarrow O(^1D) + O_2$ and $H_2O + O(^1D) \longrightarrow 2\,OH$. Since the NUV radiation necessary for this pathway is lower for M dwarfs, the CO mixing ratio on the

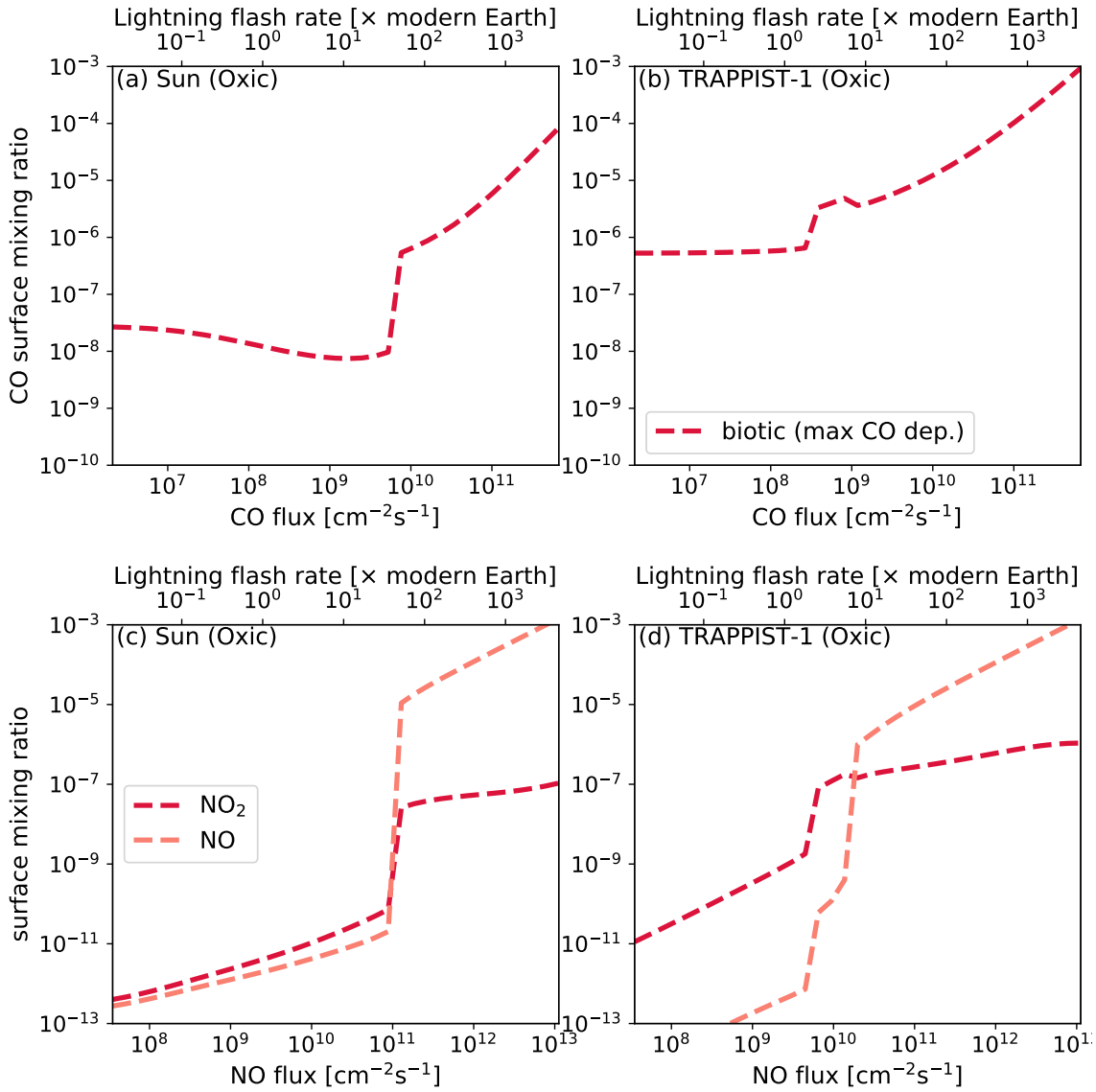

Figure 3.16: Photochemically simulated CO (**a** & **b**), NO and NO_2 (**c** & **d**) mixing ratios in the oxic atmosphere (4.6% CO_2, 21% O_2) of an Earth-sized planet orbiting the Sun (**a** & **c**) and TRAPPIST-1 (**b** & **d**) for varying CO and NO production rates and the biotic scenario with CO deposition ($T_{surf} = 288$ K). The second x-axis gives the corresponding lightning flash rate (in units of modern Earth's flash rate), as estimated for the respective atmospheric composition.

planet around TRAPPIST-1 is higher than on the planet around the Sun (Segura et al., 2005; Schwieterman et al., 2019). However, for CO fluxes $> 3 \times 10^9$molecules/cm^2/s for the planet orbiting the Sun and $> 10^8$molecules/cm^2/s for the planet orbiting TRAPPIST-1 we find an increase of the CO mixing ratio. This corresponds to lightning flash rates of ~ 10 and ~ 0.7 times modern Earth's flash rate, respectively. In the Sun case, the CO mixing ratio increases to $\sim 10^{-7}$ for a CO flux of 3×10^9molecules/cm^2/s and then steadily to $\sim 10^{-4}$ for a CO flux of 5×10^{11}molecules/cm^2/s. In the TRAPPIST-1 case, the CO mixing ratio increases to $\sim 10^{-6}$ for a CO flux of 10^8molecules/cm^2/s and then steadily to $\sim 10^{-4}$ for a CO flux of

10^{11}molecules/cm^2/s. We find that at modern Earth's lightning flash rate the CO concentration is approximately six and two orders of magnitude smaller than in the corresponding anoxic atmosphere for the Sun and TRAPPIST-1 planet, respectively (same concentration of CO_2: 4.6%), as the abundant O_2 increases the recombination of CO to CO_2. This means, lightning flash rates of 3000 and 500 times modern Earth's flash rate are needed to achieve CO concentrations similar to the corresponding anoxic scenarios (biotic with maximum CO deposition).

The NO_2 concentration follows a very similar trend to the concentration of CO, with a sharp increase at CO fluxes of $\sim 3 \times 10^9$molecules/cm^2/s and $\sim 10^8$molecules/cm^2/s, and corresponding NO fluxes of $\sim 6 \times 10^{10}$molecules/cm^2/s and $\sim 2 \times 10^9$molecules/cm^2/s, for the planet orbiting the Sun and TRAPPIST-1, respectively. This is again due to the influx of NO overwhelming photochemically sinks, leading to a runaway of the NO and NO_2 concentrations.

Similar to the anoxic case, in the oxic atmosphere, lightning will also produce free oxygen which we expect to mostly recombine to O_2. However, it is hard to determine how much atomic oxygen is produced. Stochimetrically, all NO and CO can be produced from dissociated N_2, O_2, and CO_2 without any remaining O. To test whether the addition of free O might change the chemistry significantly, we ran simulations with an O flux similar to the lightning NO flux. We only found small enhancements in the final NO_2 concentrations for the highest NO fluxes ($> 10^{12}$molecules/cm^2/s). Figure A.12 in the appendix shows the column densities of the atmospheric constituents for the range of simulated CO and NO fluxes for the oxic scenarios discussed in this section.

Nitrogen Deposition into an Ocean

To investigate the possibility of lightning-produced NO to be converted to N_2O in the ocean, which could in return be outgassed into the atmosphere where it might produce a false-positive biosignature, we calculate the nitrogen deposition flux into the surface of the planet. In addition to NO, also NO_2, HNO, and HNO_3 are deposited from the atmosphere. The combined nitrogen deposition flux is shown in Fig. 3.17 in comparison to the NO production from lightning for the anoxic and abiotic scenario for the planet orbiting the Sun ($T_{\text{surf}} = 275\,\text{K}$). A large part of the introduced NO is deposited into the surface, mainly in the form of HNO: up to $\sim$ 95% at NO fluxes of $\sim 10^{10}$molecules/cm^2/s, decreasing to $\sim$ 60% at NO fluxes of $\sim 10^{12}$molecules/cm^2/s. This behaviour is similar for the other anoxic-abiotic scenarios. Even

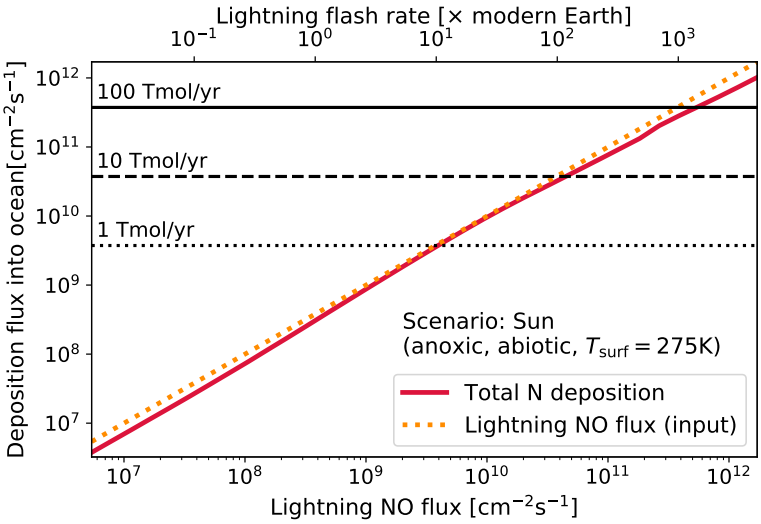

Figure 3.17: Deposition flux of fixed nitrogen into an ocean (*red*) for the anoxic, abiotic planet around the Sun ($T_{surf} = 275\,K$) for a range of lightning NO fluxes and corresponding lightning flash rates. For comparison, the total lightning produced NO flux is shown (*orange*). The corresponding deposition rates in $Tmol\,yr^{-1}$ are shown as black lines (converted into molecules/cm^2/s).

if all of this deposited nitrogen were to be converted to N_2O and outgassed into the atmosphere, a lightning flash rate of more than 100 times modern Earth's would be necessary to produce $10\,Tmol\,yr^{-1}$ of N_2O which would probably still not be enough to be detectable with *JWST* (Schwieterman et al., 2022). On an Earth-like planet orbiting a K dwarf, an N_2O flux of $1\,Tmol\,yr^{-1}$ or even less might be detectable though, potentially producing a false-positive biosignature. These calculations present an upper limit, assuming the whole surface is covered by an ocean. Such ocean worlds exist, for example Kepler-138 d (Piaulet et al., 2023), but on a planet with a lower ocean-to-land surface ratio, deposition of nitrogen oxides into the ocean will be less efficient. This and other uncertainties that are likely to decrease the N_2O flux significantly, such as the efficiency of the conversion of deposited nitrogen into N_2O, are the reason why we are not further investigating this potential signature.

Observational Signatures from Lightning in Transmission, Emission, and Reflected Light

To investigate whether lightning produces observable signatures, we calculated emission, transmission, and reflectance spectra for a selection of simulations. The calculated transmission spectra for two scenarios of the TRAPPIST-1 planet — the anoxic, abiotic scenario (T_{surf} = 275 K) and the oxic, biotic scenario — are shown in Fig. 3.18 and 3.19, respectively. The different shape of the CO_2 feature at around 15 µm in the emission spectra is due to the different atmospheric profiles we used: Since it is difficult to explore if and how the pressure-

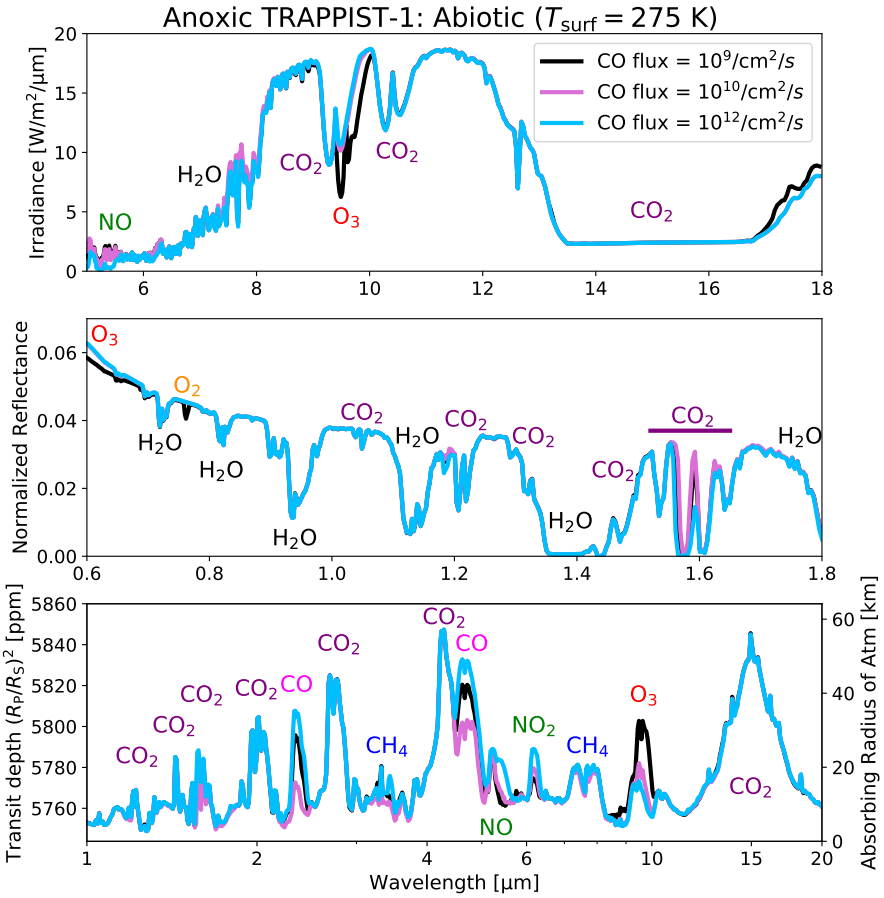

Figure 3.18: Simulated spectra for the TRAPPIST-1 planet: Emitted (**top**, MIR, $R = 400$), reflected (**middle**, NIR, $R = 400$), and transmitted light (**bottom**, NIR-MIR, $R = 200$). Anoxic, abiotic scenario ($T_{surf} = 275$ K): CO flux of 10^9 (*black*), 10^{10} (*magenta*), and 10^{12}molecules/cm^2/s (*blue*), corresponding to lightning flash rates of $\sim$ 2, $\sim$ 35 and $\sim$ 1500 times modern Earth's, respectively. Note that MIR features in emission are not just dependent on the abundance of spectrally active gases, but also the temperature structure of the atmosphere.

temperature profiles of these atmospheres differ from modern Earth's atmosphere, we used Earth's atmospheric profile with its stratospheric temperature inversion for the oxic atmosphere which is very similar to modern Earth's atmosphere. Since the emission is probing different heights in the atmosphere it registers different temperatures, with the centre of the line at 15 μm probing furthest up in the atmosphere, where the temperature is higher than deeper in the atmosphere. For the anoxic atmosphere, we assumed an isothermal atmosphere above the convective troposphere, such that the absorption feature appears flat. The spectra are shown for two different CO fluxes, representing scenarios at lightning flash rates below and above where the atmospheric composition changes drastically: For the anoxic/abiotic scenario, these are CO fluxes of 10^9 (*black*), 2×10^{10} (*magenta*), and 10^{12}molecules/cm^2/s (*blue*), corresponding to lightning flash rates of $\sim$ 2, $\sim$ 35, and $\sim$ 1500 times modern Earth's,

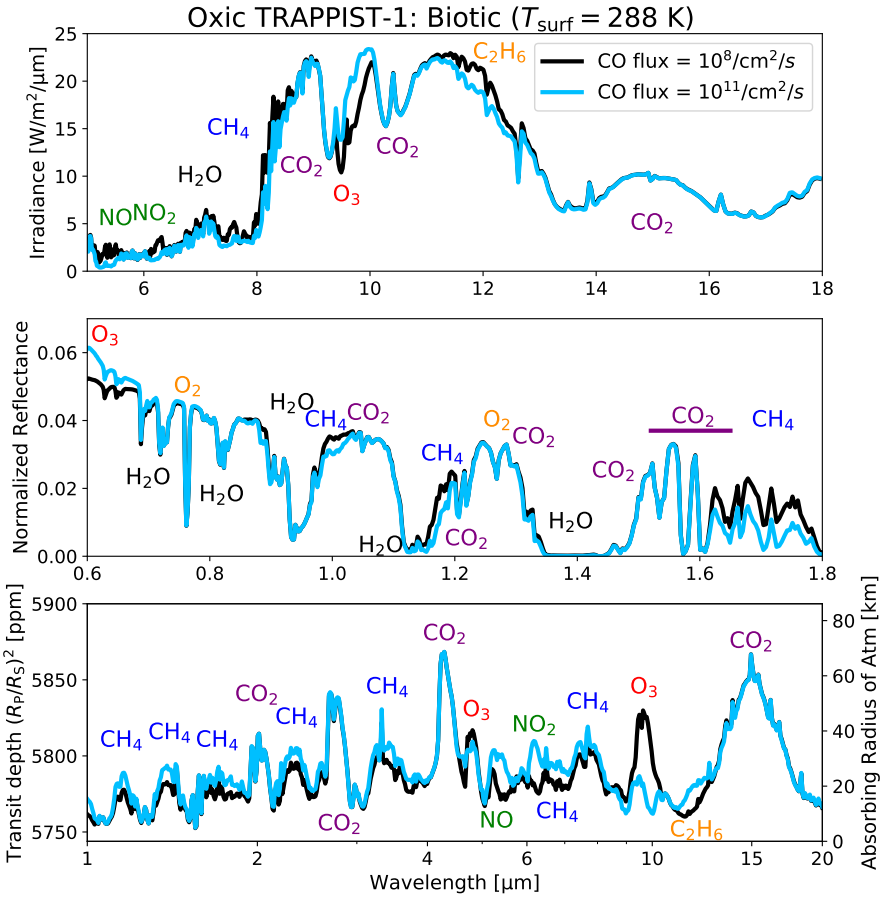

Figure 3.19: Simulated spectra for the TRAPPIST-1 planet: Emitted (**top**), reflected (**middle**), and transmitted light (**bottom**). Oxic, biotic scenario (T_{surf} = 288 K): CO flux of 10^8 (*black*) and 10^{11}molecules/cm^2/s (*blue*), corresponding to lightning flash rates of $\sim$ 0.9 and $\sim$ 680 times modern Earth's, respectively.

respectively. For the oxic/biotic scenario, CO fluxes of 10^8 (*black*) and 10^{11}molecules/cm^2/s (*blue*), corresponding to lightning flash rates of $\sim$ 0.9 and $\sim$ 680 times modern Earth's, respectively, are shown. Most notable is how the increased concentrations of NO and NO_2 reduce the ozone concentration and thus the ozone features at 9.6 µm (transmission and emission) and $<$ 0.65 µm (reflectance) in the scenario with the higher CO flux. The individual mixing ratio profiles for the two cases compared in Fig. 3.18 and 3.19 can be found in the appendix (Fig. A.1).

In the case of the anoxic planet, the removal of the ozone feature would prevent a possible false-positive detection of life. In contrast to the oxic scenario, the CO concentration is much higher here (for the low and high lightning flash rates), though, allowing for strong CO features in the transmission spectrum at 2.35 µm and 4.65 µm. This allows to identify a CO_2-rich atmosphere and for a correct interpretation of the ozone feature as potentially from

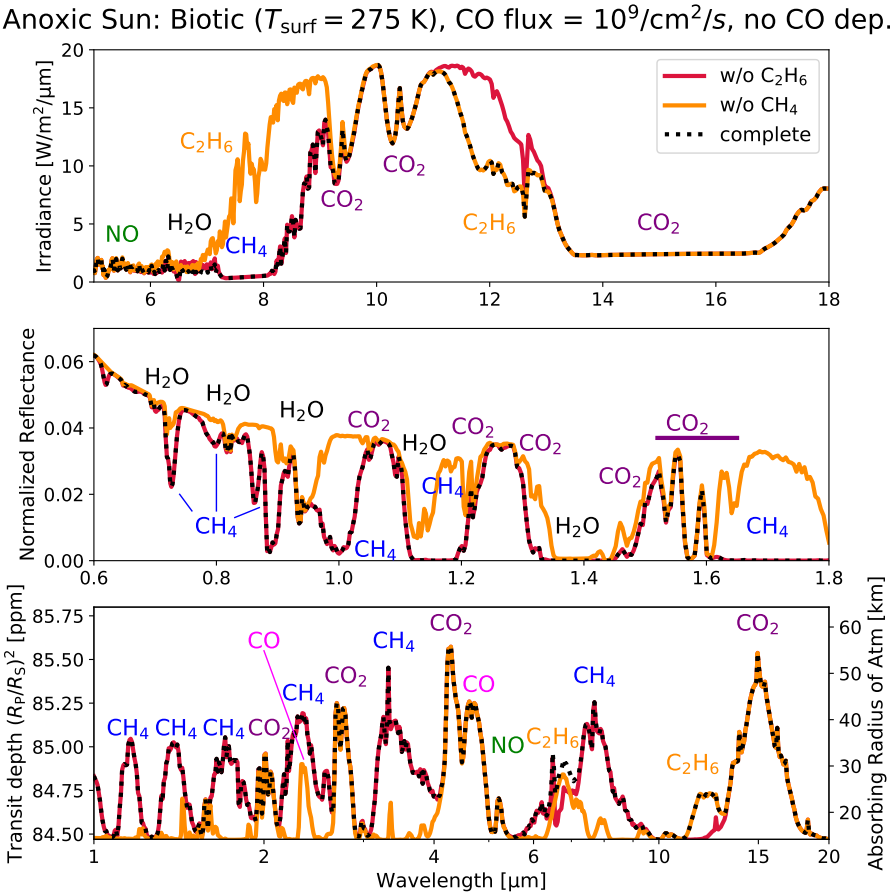

Figure 3.20: Simulated spectra for the planet orbiting the Sun: Anoxic, biotic scenario without CO deposition (CO flux $\sim 10^9$molecules/cm^2/s). Spectra with individual species removed are shown (without C_2H_6, *red*, and without CH_4, *orange*) in comparison to the full spectrum (*black dotted*).

an abiotic source. For the intermediate lightning flash rate ($\sim$ 35 times modern Earth's) we find both the CO and the ozone features to be removed or very weak. However, in the absence of strong methane features, the missing CO feature should not be interpreted as a sign for life. In the corresponding biotic scenario (Fig. A.5), where the CO concentration is similarly low, the biotic methane flux produces strong features that should allow to detect the present biosphere.

In the oxic/biotic scenario, lightning decreases the ozone concentration in the atmosphere, reducing the spectral ozone feature used to identify an oxygen-rich atmosphere. In that case, other biosignatures are necessary to identify that the planet is inhabited, for example the combination of CO_2 and CH_4 in the absence of CO, as suggested by Krissansen-Totton et al. (2018b). We actually find an increased concentration of CH_4 for the higher CO flux, most notably in the reflected spectrum (1.6 – 1.8 µm), probably because the increased CO flux is taking up most of the available sinks (e.g., OH). We also find an NO_2 feature at $\sim$ 6 µm and an C_2H_6

feature at $\sim 11\,\mu m$ (both in transmission and emission spectra) to appear for the higher CO flux scenario, indicating the presence of lightning activity and helping to explain the absence of an ozone feature. In the reflected light, we find molecular oxygen features at $0.76\,\mu m$ (O_2 A-band) and $1.27\,\mu m$ which are not affected by the lightning activity, potentially allowing for the identification of an oxygen-rich atmosphere if that wavelength range is observed. In any way, to enhance the CO concentration to a detectable level in the oxic scenario, significantly higher lightning flash rates are necessary.

Spectra for other scenarios and the corresponding atmospheric mixing ratio profiles are shown in in Appendix A. For the oxic, biotic Sun scenario (Fig. A.2), the behaviour is very similar to the TRAPPIST-1 planet: with higher CO and NO fluxes, the ozone features are reduced but we find enhanced methane features. The spectra for the anoxic, abiotic Sun planet (Fig. A.3), however, look very different compared to the TRAPPIST-1 planet: because of the lower XUV radiation of the Sun, there is no abiotic ozone buildup in the atmosphere. Also the CO concentration is much lower and the spectra mainly show CO_2 features. Only the NO feature at $5.3\,\mu m$ is stronger for when the CO flux is increased.

For the anoxic, biotic scenarios, we are comparing the spectra for simulations with and without CO deposition (Fig. A.4 & A.5): As expected, the main difference is that without CO deposition, we find a strong CO feature at $4.65\,\mu m$. For the anoxic, biotic planet around the Sun without CO deposition, we calculated the spectra with individual species removed (Fig. 3.20). In particular, we looked at the effect of removing methane (orange lines) and C_2H_6 (red). The complete spectra are shown in comparison (black dotted lines). As expected, we see many strong methane features in all three spectra, masking for example the $2.35\,\mu m$ CO feature. For C_2H_6 we find a strong feature between 11 and $13\,\mu m$ in the emitted (top) and transmitted spectra (bottom). Removing NO_2 and HNO_3 from the calculations did not change the spectra, suggesting features of these molecules are small and masked by other, more abundant molecules such as CH_4.

Whether these spectral features are eventually detectable or not depends on many factors such as the wavelength range and resolving power of the instrument, the duration of the observation, or the variability of the stellar radiation. For example the ozone feature at $9.6\,\mu m$ might not be detectable with *JWST* (Krissansen-Totton et al., 2018a). Future missions, dedicated to study the atmospheres of terrestrial exoplanets will be better suited to detect atmospheric con-

stituents of small planets, such as the *Habitable Worlds Observatory (HWO)* recommended by the US 2020 Astronomy & Astrophysics Decadal Survey (National Academies of Sciences & Medicine, 2021) with capabilities informed by the *Habitable Exoplanet Observatory* (*HabEx*, Gaudi et al., 2020) and *Large UltraViolet Optical and Infrared* (*LUVOIR*, The LUVOIR Team, 2019) mission concepts. This mission could detect O_3 and O_2 features in the UV and visible and CH_4 in the near-infrared. The proposed *Large Interferometer For Exoplanets* (*LIFE*, Alei et al., 2022; Quanz et al., 2022) could detect O_3 and CH_4 features in the MIR.

3.4.4 Discussion

Lightning flash rate

In this work, we estimated the production rates of several gaseous and aqueous species by lightning in different atmospheric and planetary environments. To do so, we used the global lightning flash rate on modern Earth of $44 \pm 5\,s^{-1}$ (Christian et al., 2003) with an energy of 6.7 GJ per flash Price et al. (1997a) to extrapolate from our laboratory experiments to an annual, global production. Lightning rates and energies have been well studied on modern Earth (Section 1.3.2; Schumann & Huntrieser, 2007; Hodosán et al., 2016a, and references therein). However, much uncertainty remains for the lightning flash rate on early Earth, terrestrial planets, and exoplanets in general (Hodosán et al., 2021). The atmospheric composition, temperature, cloud coverage, tidal interactions with the star, and the presence of cosmic rays all can influence the lightning flash rate in the atmospheres of terrestrial exoplanets (Section 1.3.2), with predicted values between less than 10% of modern Earth's flash rate for tidally locked ocean worlds (Braam et al., 2022) and more than three times modern Earth's flash rate for early Earth's atmosphere with 1 bar of CO_2 (Wong et al., 2017). The presence — or absence — and strength of certain spectral features as discussed above might allow us to constrain the lightning activity in the atmospheres of exoplanets.

Atmospheric stability

In our photochemical simulations, we studied the kinetic chemistry and photochemistry of terrestrial, habitable-zone planets around two different types of stars: the Sun and the M dwarf TRAPPIST-1. While we assumed a CO_2 concentration of 4.6% in the atmosphere (for both the anoxic and oxic atmospheres), the CO_2 partial pressure on early Earth probably was significantly higher. A lower CO_2 concentration would have allowed for a stronger heating

of the upper atmosphere under the young Sun's XUV radiation, leading to rapid escape of large parts of the atmosphere to space (Lichtenegger et al., 2010; Johnstone et al., 2021b). Further, for planets around M dwarfs such as TRAPPIST-1, it will be much harder to hold on to their atmosphere. Due to their proximity to the host star, the intense stellar wind and the enhanced and prolonged XUV activity of said star (Johnstone et al., 2021a), such planets are experiencing rapid non-thermal (e.g., Airapetian et al., 2017; Dong et al., 2020) and thermal escape (e.g., Lammer et al., 2011; Johnstone et al., 2019; Tian, 2009) of their atmospheres. In addition, many M dwarfs are very active, producing a high number of flares of XUV radiation and charged particles, leading to further escape of their planets' atmospheres (France et al., 2020).

Recent observations with *JWST* have shown that the innermost planet of the TRAPPIST-1 system, TRAPPIST-1 b, is likely to be a bare rock without any atmosphere (Greene et al., 2023), and that TRAPPIST-1 c probably does not contain a thick, CO_2-rich atmosphere (Zieba et al., 2023). While detailed observations of the outer planets have not been conducted yet, the studies mentioned above suggest that also the habitable-zone planets of the TRAPPIST-1 system, planets e, f, and g, probably have lost their atmosphere (Samara et al., 2021). Other studies instead suggest that the habitable zone planets of the TRAPPIST-1 may have been able to retain an atmosphere (Krissansen-Totton, 2023). Even if TRAPPIST-1 e has retained an atmosphere, ongoing escape of hydrogen and nitrogen will continue to modify the atmosphere, potentially enhancing the oxygen fraction in the remaining atmosphere (Tian, 2009; Johnstone et al., 2019). Connecting the upper atmosphere and the escape processes mentioned above to our photochemical model is beyond the scope of this study but should be investigated further in future studies. The here presented simulations are therefore not specific predictions for the atmospheric composition of TRAPPIST-1 e but rather an example to investigate the effect of lightning on different atmospheres around different types of host stars. TRAPPIST-1 and the Sun are good end-members for several of reasons, including the fact that TRAPPIST-1 is an immediate/near-term target, and terrestrial planets orbiting Sun-like stars are the targets for *HWO*. In case that TRAPPIST-1 e, or similar exoplanets in the habitable zones of M dwarfs, can indeed retain an atmosphere that is similar to our simulations, this study informs us about atmospheric signatures that one may expect to observe.

Adapting CO metabolisms

In this study we used biotic CO deposition and CH_4 production rates that were independent of temperature, following previous work (Kharecha et al., 2005; Schwieterman et al., 2019). However, the metabolisms responsible for CH_4 production and CO consumption might change depending on atmospheric composition, pressure, and temperature, and will probably vary substantially across a heterogeneous planetary surface. Taubner et al. (2023) show how the production of lipids and amino acids by methanogens can strongly depend on the temperature and nutrient supply. In addition, the productivity of a biosphere might be limited by the availability of other nutrients like phosphorus or fixed nitrogen, rather than CO or stellar irradiation, as is the case for modern Earth (Moore et al., 2013; Bristow et al., 2017). In particular, the availability of nickel can limit the CO consumption by acetogens (Dobbek et al., 2001). Over the course of Earth's history, the concentration of nickel in the oceans has varied, impacting the productivity of methanogens and acetogens (Konhauser et al., 2009, 2015). These uncertainties strongly suggest the behaviour of CO in realistic atmospheres will lie in between the end member scenarios we present here.

3.4.5 Conclusion

The search for key molecules that link astrophysical environments to the origin of life is ongoing. For example, the molecule urea ($CO(NH_2)_2$) was detected in the interstellar medium (Fourré et al., 2016), formamide (NH_2CHO), a precursor for more complex biomolecules, was detected in star forming regions (Codella et al., 2017), complex cyanides have been detected in a protoplanetary disk (Öberg et al., 2015), glycolaldehyde ($C_2(H_2O)_2$) has been found on comets (Zellner et al., 2020), and recently, the amino acid tryptophan has been detected in the interstellar gas of a young star cluster (Iglesias-Groth, 2023). This work provides another puzzle piece in the understanding of the prebiotic chemistry leading to the origin of life on Earth an beyond.

We conducted spark discharge experiments to study the production of different gaseous and aqueous products, including potential (anti-)biosignatures, by lightning in atmospheres of N_2, CO_2, and H_2. We then used the results from these experiments to estimate the concentration of CO, NO, and NO_2 in different types of atmospheres with varying lightning flash rates on planets around different host stars to investigate the atmospheric concentrations and

observability of these gases.

By comparing spark experiments with and without water in the flask, which subsequently determines the presence and concentration of water vapour in the gas mixture, we found that in the absence of other oxygen sources, such as CO_2, the oxygen provided by the dissociation of H_2O in the spark can efficiently oxidise nitrogen to NO. This suggests that in a slightly reducing atmosphere of a planet that has surface water and a habitable surface temperature, lightning will produce more oxidised than reduced nitrogen products. Also the production of methane will be inhibited. Thus, in a slightly reducing or oxidising atmosphere, lightning cannot produce a false-positive NH_3 or CH_4 biosignature and direct production of ammonium by lightning is not significant on such planets.

While only small amounts of N_2O are directly produced in our spark experiments, NO can be converted to N_2O in an iron-rich ocean, potentially enhancing the N_2O concentration in the atmosphere to detectable levels. However, photochemical sinks in the atmosphere and the simultaneous enhancement of NO_2 as a lightning signature make it unlikely that lightning can produce a false-positive N_2O biosignature. In our overnight experiments, we observed the production of HCN which is an important prebiotic precursor. As the HCN production was increasing slightly with CO_2 concentration, we could estimate a lower limit for the freeze-out temperature of HCN of approximately 3000 K.

The main gaseous products of lightning chemistry in an N_2-CO_2 atmosphere are CO and NO. NO can further oxidise to NO_2 which is spectrally active at 6 µm and therefore a potential signature for lightning activity in exoplanet atmospheres. By comparing our experimental results to chemical equilibrium calculations, we could estimate the freeze-out temperature of CO to be approximately 2400 K and of NO to be about 3000 K which allowed us to determine the minimum temperature of the spark to be 3000 K. We used these estimates for the freeze-out temperatures to calculate the production rate of CO and NO in an oxygen-rich atmosphere. This allowed us to calculate the CO and NO_2 mixing ratios over a range of different lightning flash rates with a photochemical model. We applied this model to anoxic ($CO_2 - N_2$) and oxic ($O_2 - CO_2 - N_2$) atmospheres on Earth-sized planets in the habitable zone of the Sun and TRAPPIST-1. In particular we ran simulations with and without an assumed biosphere on the planet, i.e. biological CH_4 surface flux and maximum CO deposition. We also calculated simulated spectra to identify signatures for the different scenarios.

CO is of special interest as a possible anti-biosignature, i.e. its presence suggests the absence of any lifeforms that would ultimately use the CO as an efficient source of carbon and energy. We find that in the biotic scenarios an unrealistically high flash rate (100 times modern Earth's flash rate or more) is necessary to increase the CO concentration to a detectable level, suggesting that lightning cannot produce a false-positive CO anti-biosignature. In an oxygen-rich atmosphere, however, lightning rates only a few times higher than modern Earth's can mask the O_3 biosignature. Enhanced NO, NO_2, and C_2H_6 features may help to identify these oxygen-rich atmospheres with increased lightning activity.

In an anoxic, abiotic atmosphere of a planet orbiting a late M dwarf, CO_2 photolysis is producing free oxygen and ozone, potentially producing a false-positive biosignature. For lightning flash rates ten times or more than modern Earth's, the additional NO input and subsequent oxidation to NO_2 enhance the recombination of CO and oxygen to CO_2, removing the abiotic ozone feature and preventing a false-positive biosignature detection. However, this also suggest that lightning may not be able to prevent all false-positive O_2 scenarios for CO_2-rich terrestrial planets orbiting ultracool M dwarfs. In summary, our work provides new constraints for the full characterization of atmospheric and surface processes on exoplanets.

Conclusion & Outlook

4.1 Summary & Conclusion

This thesis explores the effect of different high-energy processes on the atmospheric chemistry of Earth and exoplanets by combining experimental and computational methods.

Chapter 2 investigated the effect of stellar and galactic high-energy radiation on the atmospheric chemistry of the hot Jupiter HD 189733 b. While hot Jupiters are not expected to harbour life, they provide unique laboratories that allow us to explore and test our models on atmospheric chemistry, in particular as long as our capabilities to observe the atmospheres of terrestrial exoplanets are limited. Combining detailed climate models of the planet's atmosphere, multi-wavelength observations of the host star's radiation field, and a state-of-the-art kinetic and photochemistry model we investigated the effect, stellar X-ray and UV radiation, stellar energetic particles, and cosmic rays have on the ionization of HD 189733 b's atmosphere

and the production of important prebiotic molecules. We found ammonium and oxonium to be potential signatures for ionization by stellar energetic particles and cosmic rays. We also found that these high-energy radiation sources enhance the concentrations of ethylene and formaldehyde to potentially detectable levels (with *JWST*), which are important precursors in the production of the amino acid glycine. The concentration of the important prebiotic precursor HCN is strongly enhanced by stellar XUV radiation.

In Chapter 3, we focused on the effect of lightning on the atmospheric chemistry of early Earth and exoplanets. First, we conducted spark discharge experiments with gas mixtures resembling modern and early Earth's atmospheres to investigate the role of lightning as a source of nutrients to Earth's earliest biosphere (Chapter 3.3). We showed that nitrogen fixation by electric discharges is efficient in the CO_2-rich atmosphere of early Earth. We also analysed the isotopic composition of our fixed nitrogen products, determining for the first time the isotopic fingerprint of lightning in nitrogen compounds. When comparing our isotopic signature to the nitrogen isotopes in sedimentary rocks from the early Archean, we could not find an agreement. This suggests that biological nitrogen fixation developed early, making life on Earth independent from lightning as a nutrient source very quickly after the origin of life.

In a next set of spark experiments, we investigated the production of a range of molecules, including potential biosignature gases, in different $N_2-CO_2-H_2$ gas mixtures (Chapter 3.4). We found that, at the low H_2 concentrations of our experiments, even small amounts of CO_2 or water vapour in the gas mixture will prevent the efficient production of the reduced gases and potential biosignatures CH_4 and NH_3. We did find, however, large amounts of NO and CO to be produced. In order to investigate their effect on the chemistry of terrestrial exoplanets with different atmospheric compositions and different host stars, we conducted photochemical calculations and simulated transmission, emission, and reflected light spectra. We found lightning to enhance spectral features for NO and NO_2, and in some cases also CO, CH_4, and C_2H_6. Further, lightning may be able to mask the presence of ozone in a an oxygen-rich atmosphere of an inhabited planet, making it harder to detect the presence of life on such a planet. On the other hand, lightning can reduce the concentration of abiotically produced O_2 and ozone in CO_2-rich atmospheres of planets orbiting ultracool dwarfs, potentially preventing a false-positive life detection.

While high-energy processes can be detrimental to the origin and persistence of life —

for example when UV radiation is damaging biological molecules such as DNA — they can also provide ingredients necessary for the origin of life and the sustenance of the earliest biospheres. Understanding the effect of UV radiation, stellar energetic particles, or lightning on the chemistry of planetary atmospheres is therefore important to investigate the possibility of life on planets inside and outside our Solar System. In this thesis, we have shown that by combining experimental and computational methods it is possible to determine the effect of high-energy processes on the prebiotic chemistry in different kinds of atmospheres, and to find signatures for this activity. With current and upcoming space telescopes and observatories we can now look for these signatures to quantify the impact of such processes on the atmospheric chemistry of exoplanets.

4.2 Outlook

In a PhD project, like any scientific endeavour, for each question that is answered, at least one new question arises. This project is no different, and there are many open questions that — while beyond the scope of this thesis — would be very exciting to follow up in future projects. In this Section, we want to give a short overview of possible future opportunities.

In Chapter 2, we used an observed X-ray flare on HD 189733 (Pillitteri et al., 2010) and the energy spectrum of solar proton flares (Herbst et al., 2019b) to estimate the spectrum of stellar energetic particles at the top of HD 189733 b's atmosphere. We then used a parametrization of the propagation of these particles through a hydrogen-dominated atmosphere (Rab et al., 2017) to estimate the ionisation rate throughout the atmosphere. With this process, we were able to present predictions on potential signatures of ionisation by stellar energetic particles and their role in the production of prebiotic molecules. However, this process also involved many assumptions and approximations. When taking into account the huge diversity of stellar systems and planetary atmospheres present in our galactic neighbourhood, it becomes clear that these approximations can only be a first step. In recent years, much work has been done on the propagation of galactic and stellar cosmic rays through different stellar systems (Rodgers-Lee et al., 2021; Mesquita et al., 2021) and through different types of planetary atmosphere (Herbst et al., 2019a; Scheucher et al., 2020; Herbst et al., 2022; Rodgers-Lee et al., 2023). For example, Mesquita et al. (2021) simulate the transport of cosmic rays through the planetary system of the M dwarf GJ 436, taking into account different models for the stellar wind, and Rodgers-Lee et al. (2023) use these results to calculate the ionisation rates of galactic and

stellar cosmic rays in the atmosphere of the warm Neptune-like exoplanet GJ 436 b, a *JWST* and *Ariel* target (Edwards & Tinetti, 2022). By using system-specific simulations of cosmic ray propagation both through the inter-planetary medium and the planetary atmospheres as input for the chemical simulations described in this work, it will be possible to improve predictions of detectable signatures for upcoming observations, in particular as there are several proposals to study disequilibrium chemistry in exoplanet atmospheres in the current *JWST* Observation Cycle 2. Eventually, with an increasing number of diverse systems being investigated, it will be easier to apply our work to other planets with a variety of host stars, energetic environments, and atmospheric compositions.

In Section 2.4, we present our results for 1D simulations of the atmospheric chemistry at two points on the planet's surface. As we discuss there, this approach allows for first predictions for the atmospheric chemistry and potentially observable signatures while being computationally cheap. However, this approach is limited as exoplanets and their atmospheres are 3D objects, where lateral transport can influence the chemistry significantly (Drummond et al., 2020). While full 3D models are expensive to run and time consuming, a possible next step based on this work could be to construct a 'pseudo-2D' model, similar to Agúndez et al. (2014). The input atmospheric profiles by Lines et al. (2018) we used have a resolution of 144 cells in longitude and 90 cells in latitude. A 'pseudo-2D' model could now calculate the chemistry in a 1D column above the equator while moving the cell along the equator with the velocity of the equatorial jet, thus taking into account the transport of chemical species from the day- to the nightside and vice versa.

Our experimental setup described in Section 3.1 allows for a range of different further projects: a first step could be to widen the parameter space using the same input gases as in our experiments. By increasing the concentration of CO_2 in the gas mixture for example, the discharge chemistry in an atmospheric composition as suggested by Lammer et al. (2019) and Sproß et al. (2021) for early Earth can be investigated. Experiments at different pressures might require an adaptation of the setup, but would also be very interesting, as a pressure below 1 bar has been suggested for the Archean atmosphere (Som et al., 2016). Eventually, choosing different gases for the experiments would allow to investigate different types of planetary atmospheres. For example, by adding SO_2, potential lightning chemistry in the atmosphere of Venus can be studied.

Our photochemical simulations in Section 3.4 covered a range of different scenarios including surface temperature, atmospheric composition, and stellar type. Yet, there are more parameters that can have an important influence on the atmospheric chemistry of a terrestrial exoplanet. For example, we have shown that a lightning flash rate of at least ten times modern Earth's is necessary to remove the false-positive O_3 signature for CO_2-rich abiotic planets orbiting the late M dwarf TRAPPIST-1. The XUV activity of late M dwarfs is very variable (Johnstone et al., 2021a), though, and at a different activity level, the lightning flash rate necessary to remove the spectral O_3 feature could be very different from the case studied here. Expanding the range of stellar types and activity levels would allow for a more general picture of lightning chemistry in exoplanet atmospheres.

We have used the 1D photochemistry and diffusion code ARGO with the chemical kinetics network STAND2019 (Rimmer & Helling, 2016, 2019; Rimmer & Rugheimer, 2019) to investigate the effect of different types of high-energy radiation on the atmospheric chemistry of a hot Jupiter. Eventually, it would be possible to use this model to simulate lightning chemistry in exoplanet atmosphere, similar to Ardaseva et al. (2017) who coupled a 2D hydrodynamical simulation of lightning-produced shock waves to ARGO and STAND2015. A first step could be to replicate the experimental setup with ARGO by inferring the spark parameters from the simulations of streamers, the small, a few cm long channels that represent the first step of a lightning return stroke (Köhn et al., 2019). The results from our spark discharge experiments can be used to benchmark the photochemical model, before extrapolating the simulations to full-scale planetary atmospheres.

This is of course only an incomplete list of the many possible ways to continue our research on lightning chemistry on the early Earth and exoplanets. Of course, each of the ideas described above will open a whole new set of research questions worth multiple PhD theses. So, to any reader who made it this far and wants to continue any of the open threads: good luck and enjoy!

Appendix: Lightning in Exoplanet Atmospheres

A.1 Additional Results from Photochemical Simulations

This section contains the atmospheric mixing ratio profiles for the spectra shown in Fig. 3.18 and 3.19 (Fig. A.1) and further spectra for different scenarios with the corresponding atmospheric mixing ratio profiles (Fig. A.2 - A.5), as well as the column densities of the major atmospheric constituents for the whole range of CO fluxes and for all scenarios presented in Section 3.4 (Fig. A.6 - A.12).

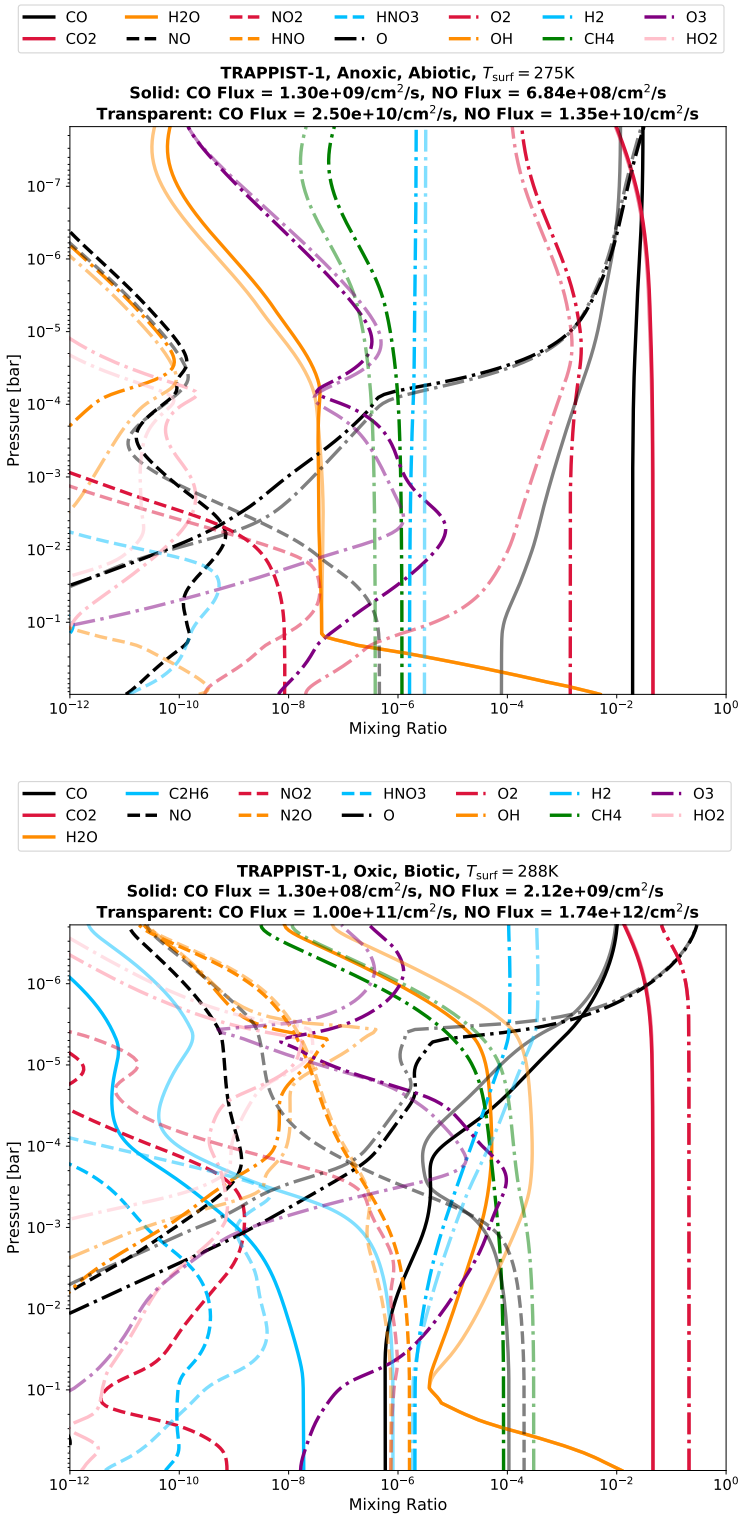

Figure A.1: Atmospheric mixing ratios of most abundant species for scenarios shown in spectra in Fig. 3.18 and 3.19. **Top**: TRAPPIST-1, Anoxic, abiotic scenario ($T_{\mathrm{surf}} = 275\,\mathrm{K}$): CO flux of 10^9 (*solid*) and 10^{11}molecules/cm^2/s (*transparent*), corresponding to lightning flash rates of ~ 2 and ~ 160 times modern Earth's, respectively. **Bottom**: TRAPPIST-1, Oxic, biotic scenario ($T_{\mathrm{surf}} = 288\,\mathrm{K}$): CO flux of 10^8 (*solid*) and 10^{11}molecules/cm^2/s (*transparent*), corresponding to lightning flash rates of ~ 0.9 and ~ 680 times modern Earth's, respectively.

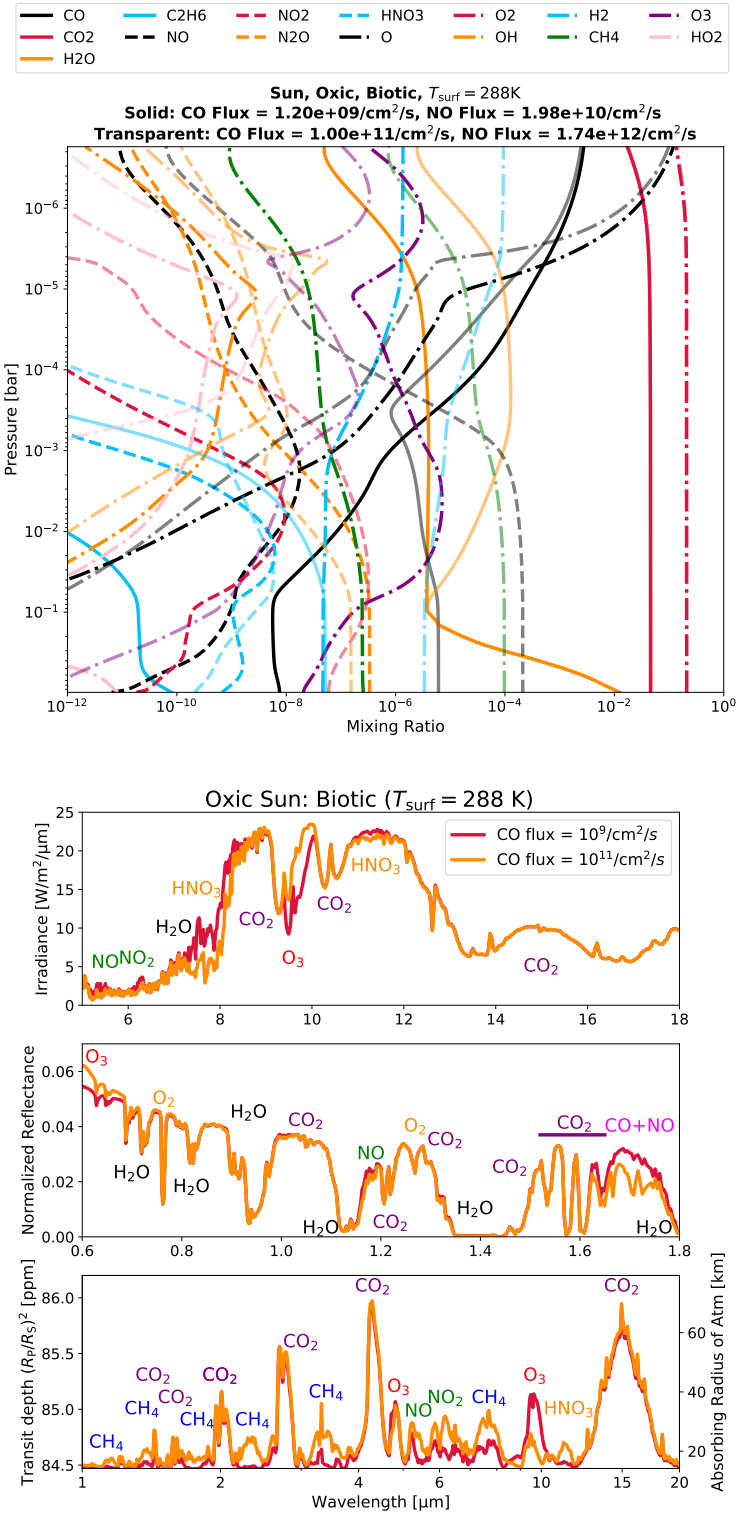

Figure A.2: Oxic, biotic Sun scenario ($T_{\text{surf}} = 288\,\text{K}$): CO flux of 10^9 and 10^{11}molecules/cm^2/s, corresponding to lightning flash rates of ~ 9 and ~ 680 times modern Earth's, respectively. **Top**: Atmospheric mixing ratios of most abundant species. **Bottom**: Simulated spectra: Emitted (*top*), reflected (*middle*), and transmitted light (*bottom*).

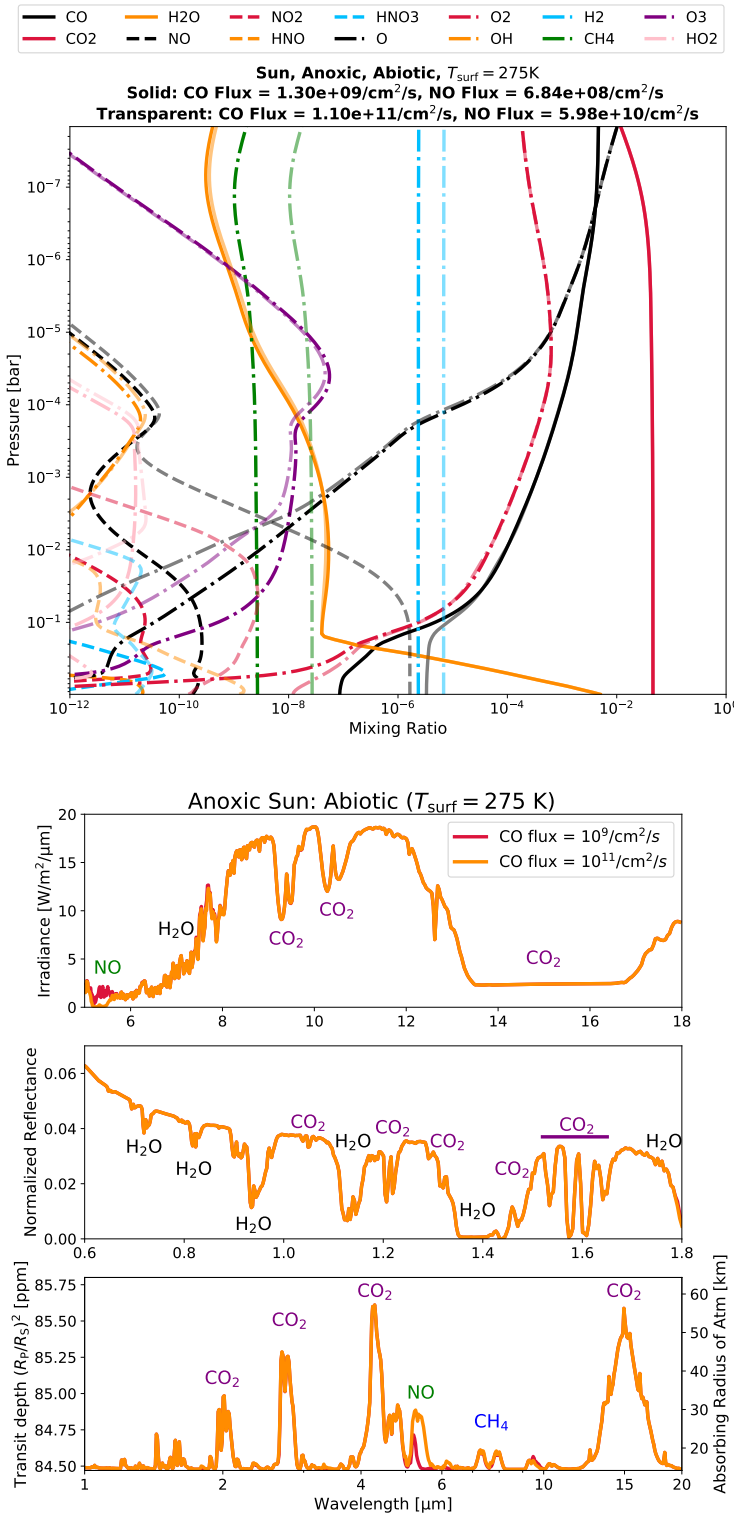

Figure A.3: Anoxic, abiotic Sun scenario ($T_{\text{surf}} = 275\,\text{K}$): CO flux of 10^9 (*black*) and 10^{11}molecules/cm^2/s (*blue*), corresponding to lightning flash rates of ~ 2 and ~ 160 times modern Earth's, respectively. **Top**: Atmospheric mixing ratios of most abundant species. **Bottom**: Simulated spectra: Emitted (*top*), reflected (*middle*), and transmitted light (*bottom*).

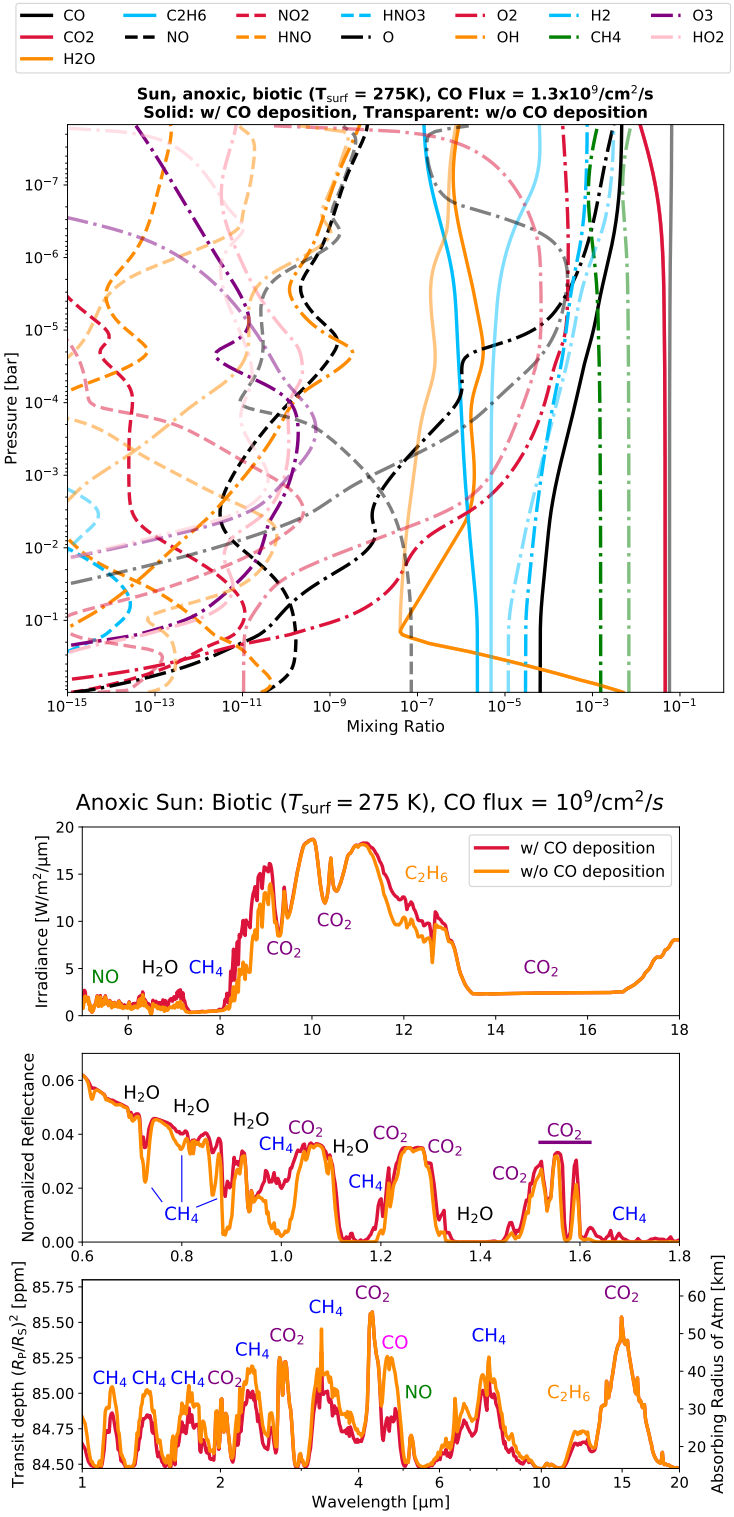

Figure A.4: Anoxic, biotic Sun scenario ($T_{\text{surf}} = 275\,\text{K}$) with CO flux of 10^9molecules/cm^2/s, corresponding to lightning flash rate of ~ 2 times modern Earth's. Comparison between scenarios with and without CO deposition. **Top**: Atmospheric mixing ratios of most abundant species. **Bottom**: Simulated spectra: Emitted (*top*), reflected (*middle*), and transmitted light (*bottom*).

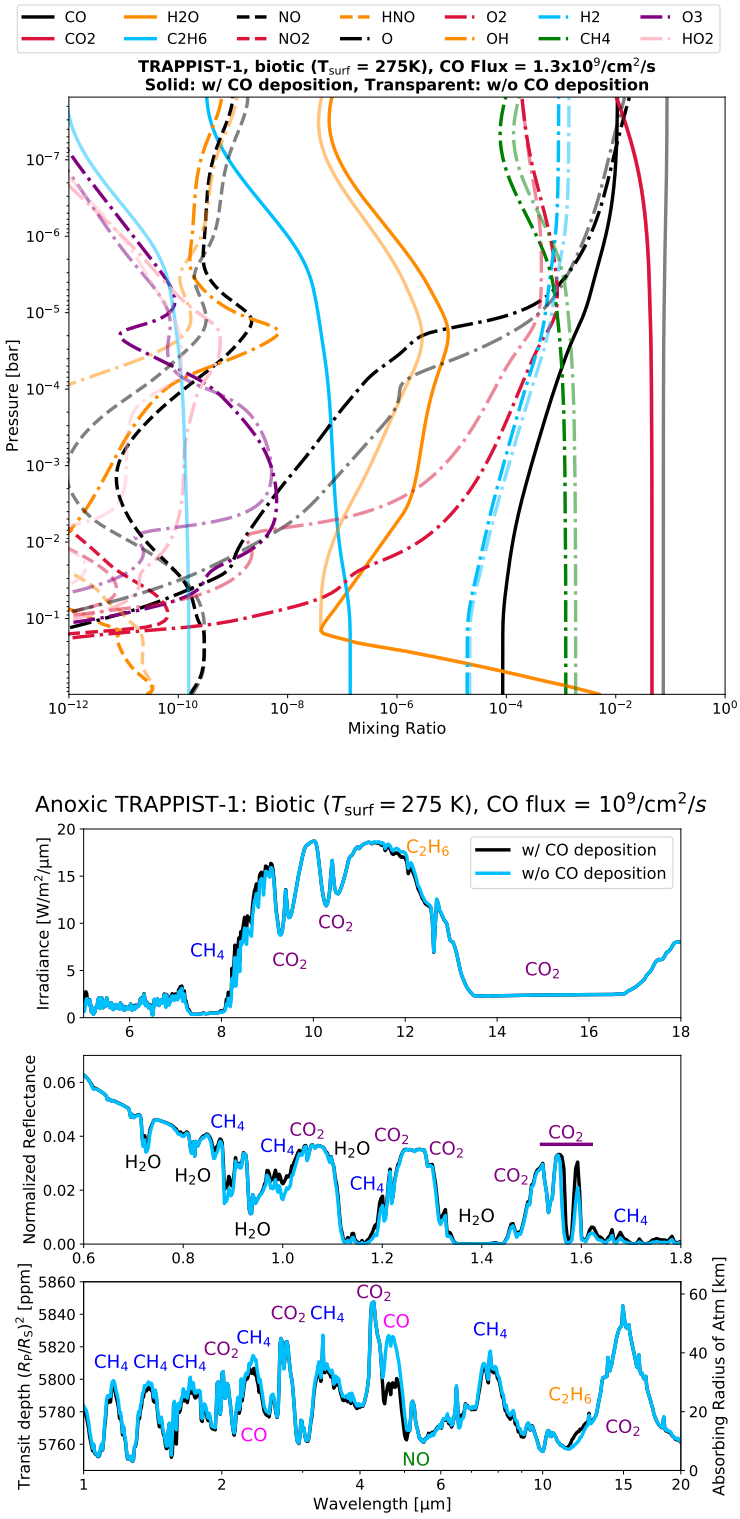

Figure A.5: Anoxic, biotic TRAPPIST-1 scenario ($T_{\text{surf}} = 275\,\text{K}$) with CO flux of 10^9molecules/cm^2/s, corresponding to lightning flash rate of $\sim$ 2 times modern Earth's. Comparison between scenarios with and without CO deposition. **Top**: Atmospheric mixing ratios of most abundant species. **Bottom**: Simulated spectra: Emitted (*top*), reflected (*middle*), and transmitted light (*bottom*).

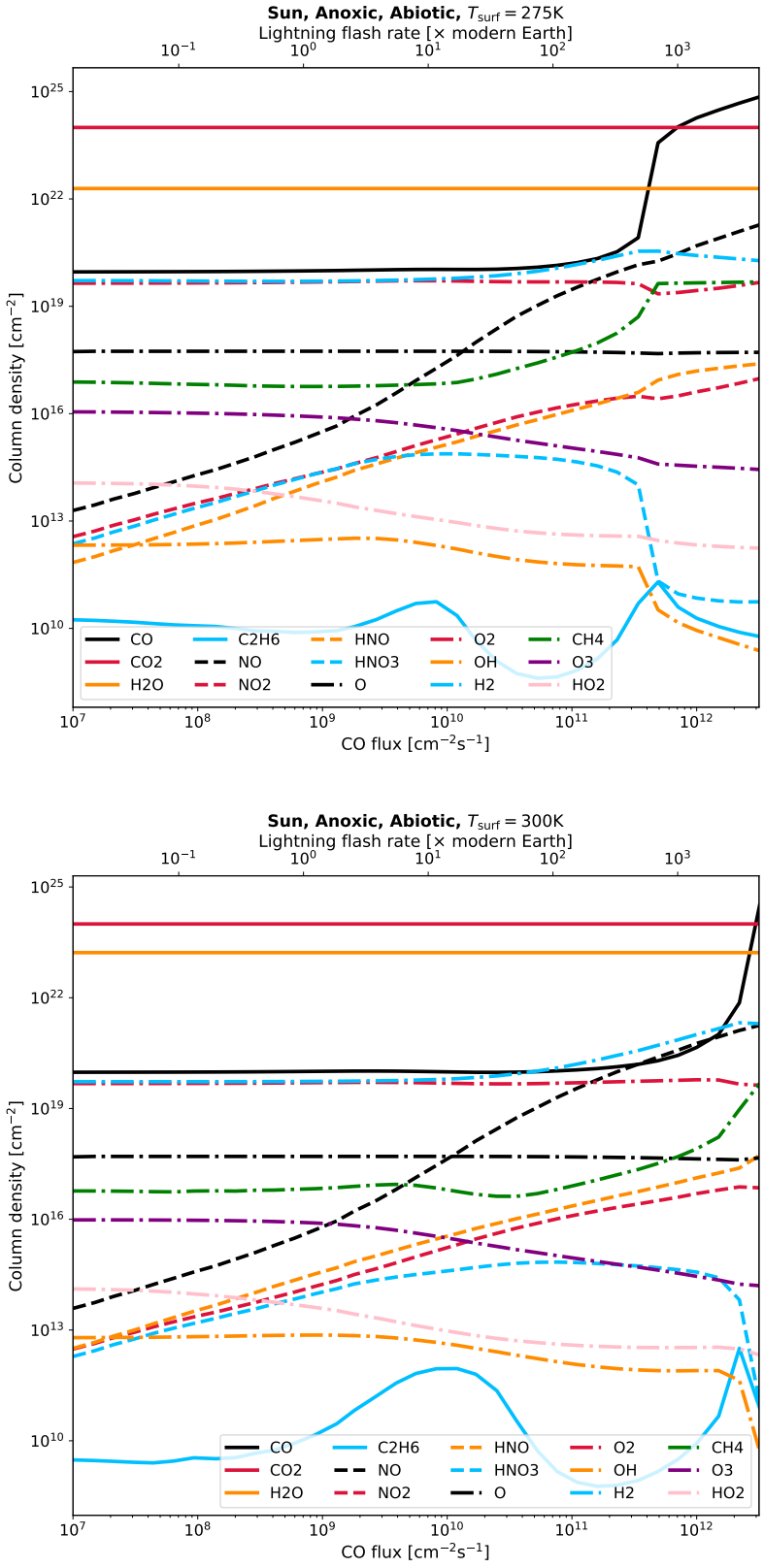

Figure A.6: Column densities for range of CO and NO fluxes. Anoxic abiotic cases.

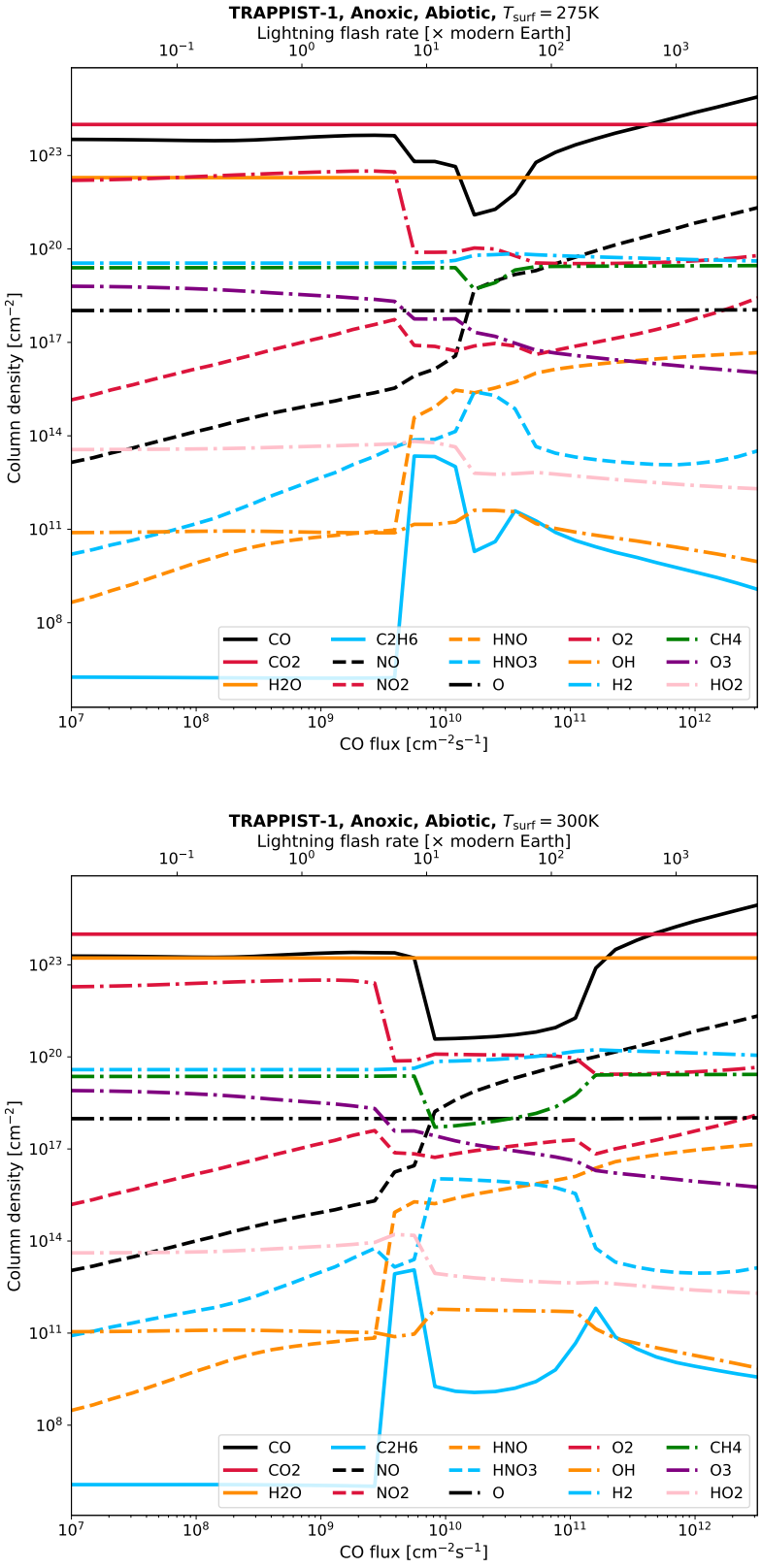

Figure A.7: Column densities for range of CO and NO fluxes. Anoxic abiotic cases. (*cont.*)

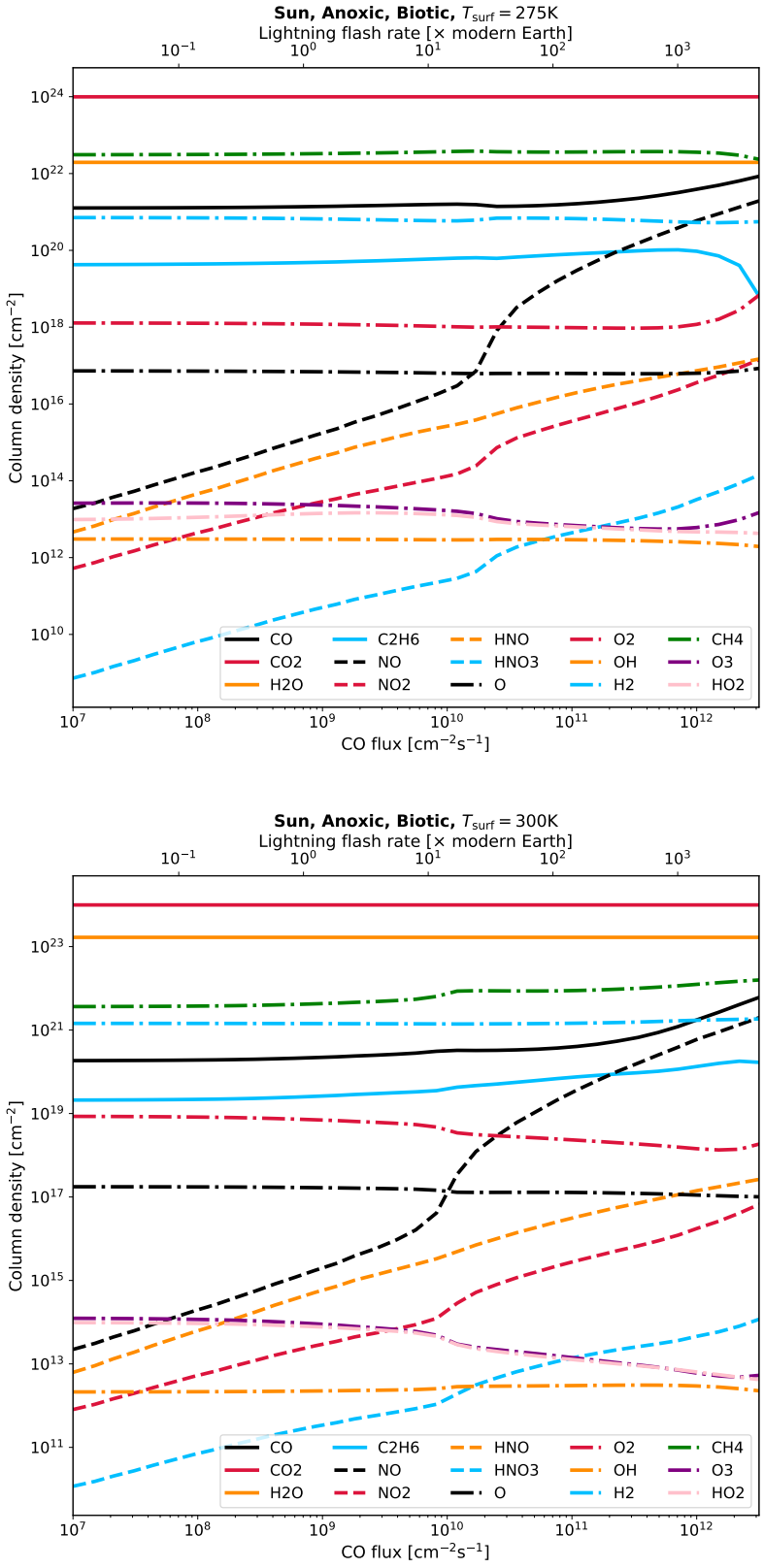

Figure A.8: Column densities for range of CO and NO fluxes. Anoxic biotic cases.

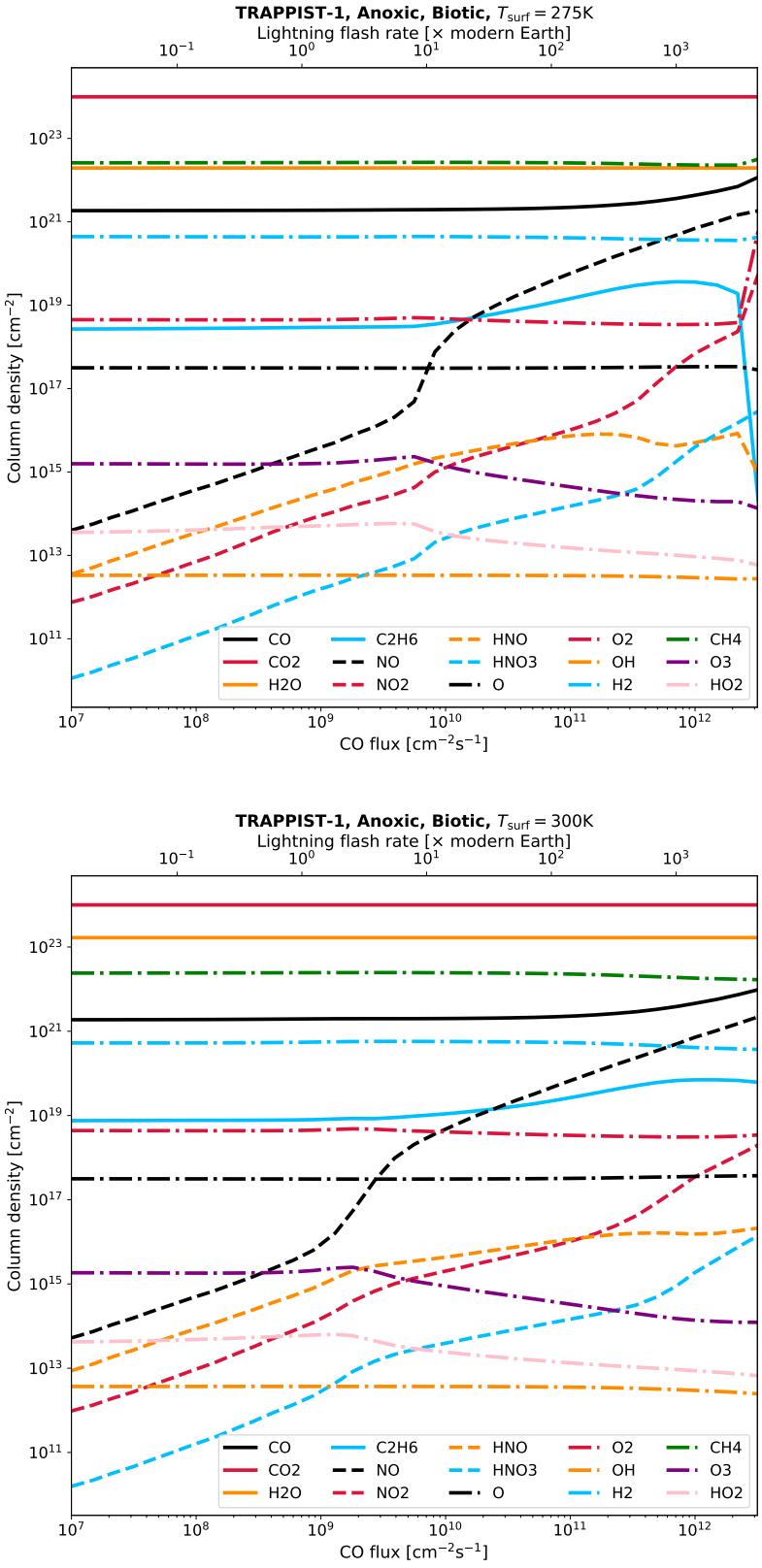

Figure A.9: Column densities for range of CO and NO fluxes. Anoxic biotic cases. (*cont.*)

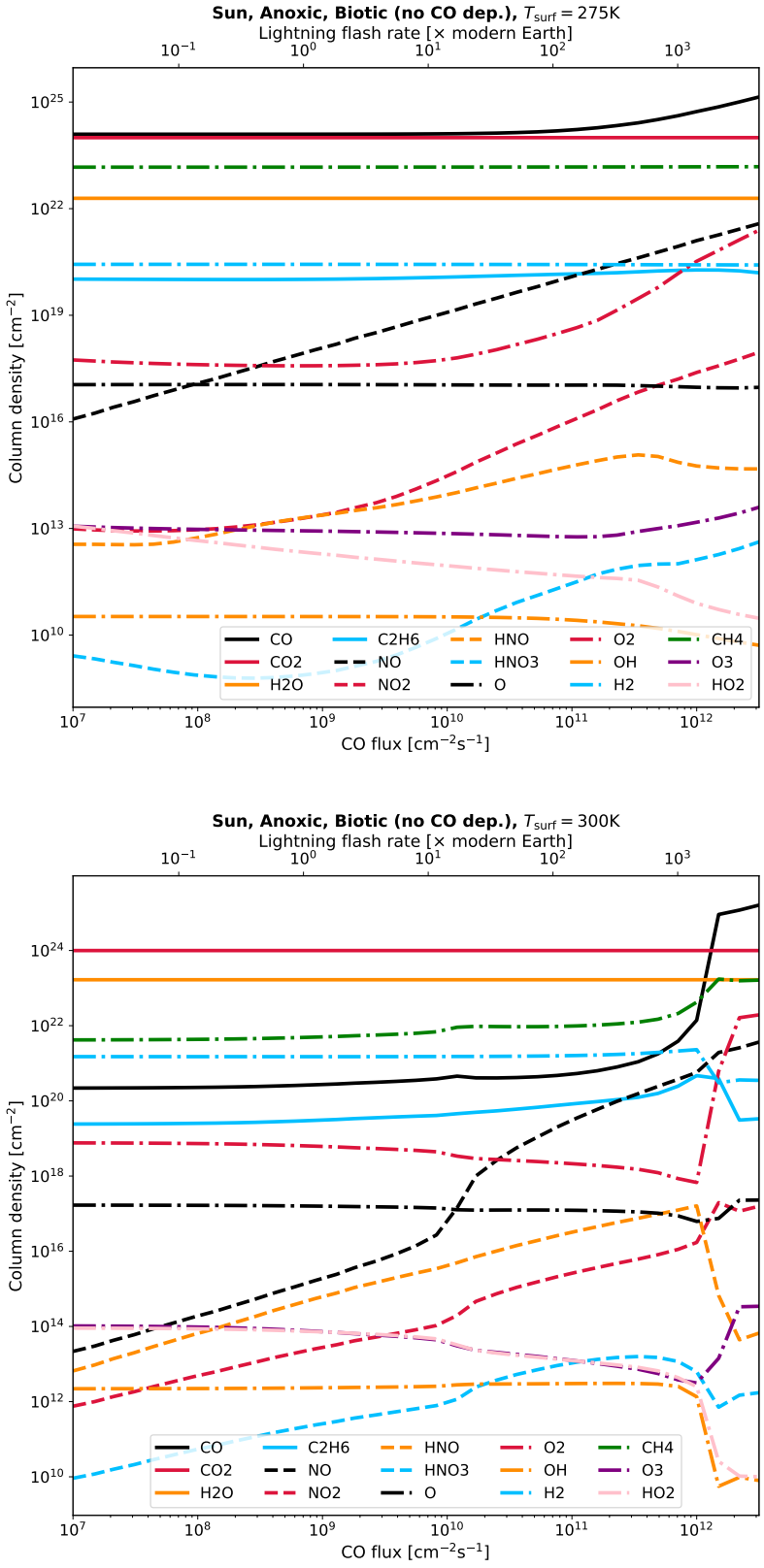

Figure A.10: Column densities for range of CO and NO fluxes. Anoxic biotic (no CO deposition) cases.

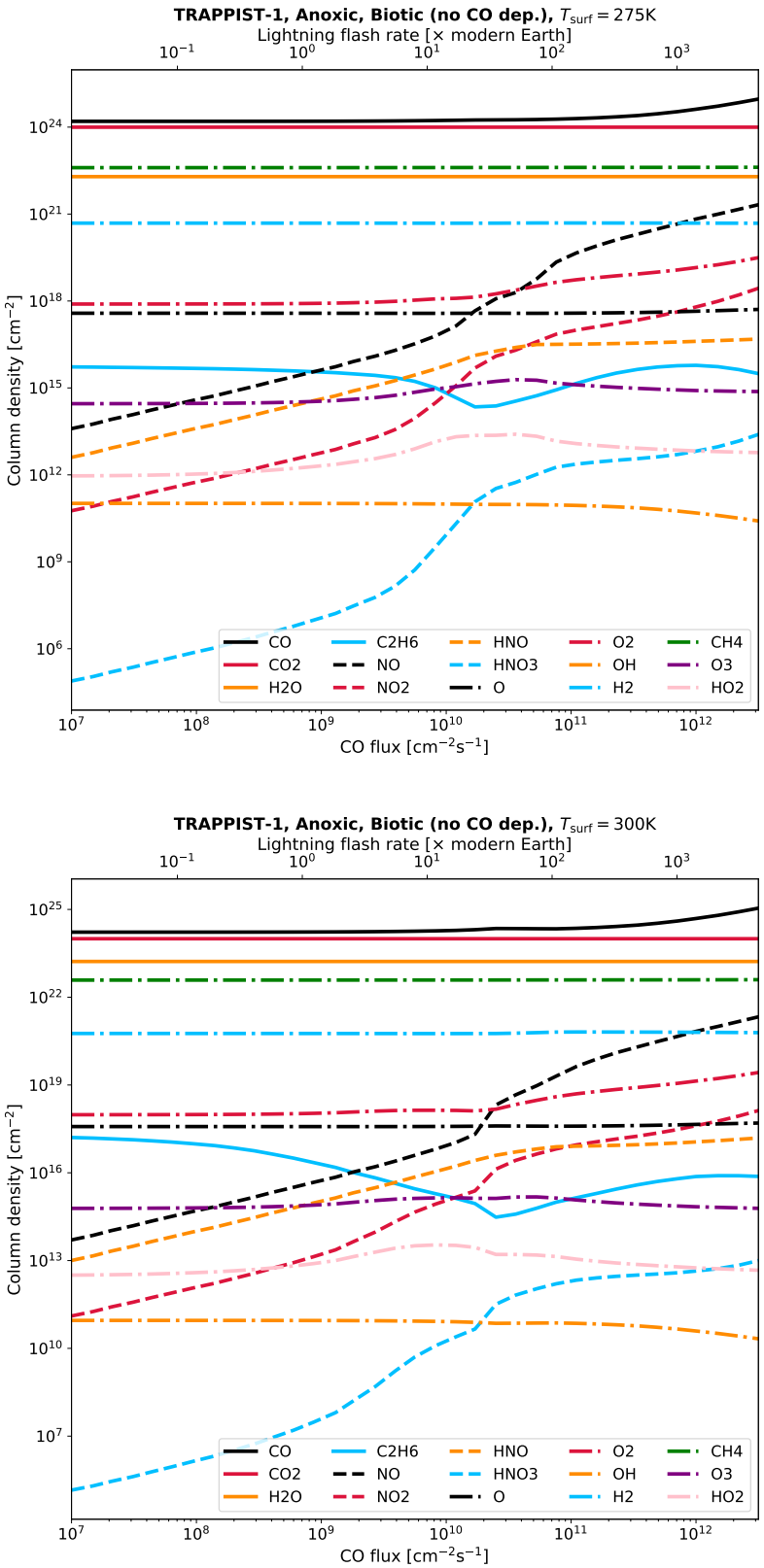

Figure A.11: Column densities for range of CO and NO fluxes. Anoxic biotic (no CO deposition) cases. (*cont.*)

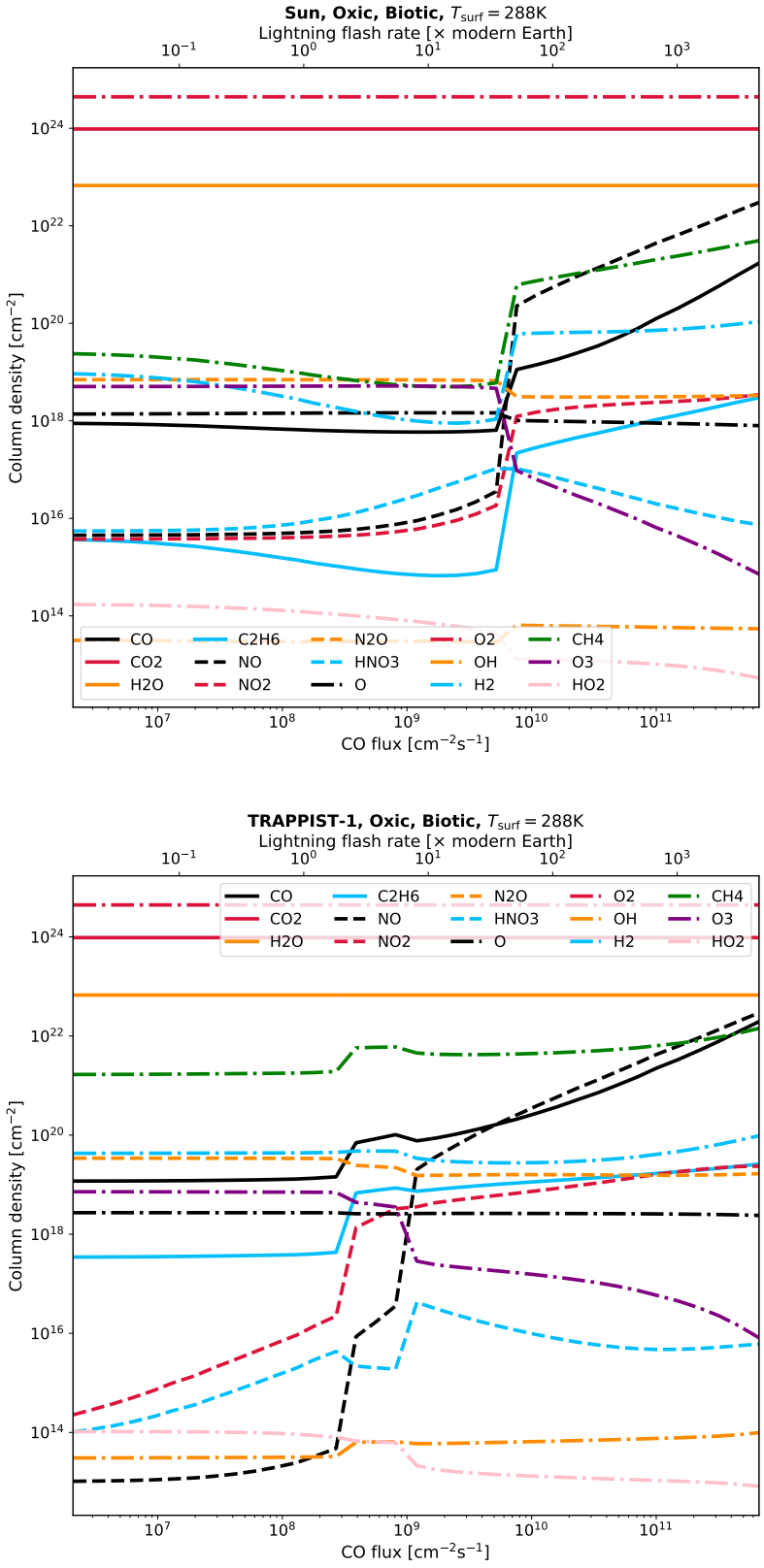

Figure A.12: Column densities for range of CO and NO fluxes. Oxic biotic cases.

Bibliography

Adams, D., Luo, Y., Wong, M. L., Dunn, P., Christensen, M., Dong, C., Hu, R., & Yung, Y. 2021, Astrobiology, 21, 968

Agol, E. et al. 2021, PSJ, 2, 1

Agúndez, M., Parmentier, V., Venot, O., Hersant, F., & Selsis, F. 2014, A&A, 564, 1

Airapetian, V. S. et al. 2020, Int. J. Astrobiol., 19, 136

Airapetian, V. S., Glocer, A., Gronoff, G., Hébrard, E., & Danchi, W. 2016, Nature Geoscience, 9, 452

Airapetian, V. S., Glocer, A., Khazanov, G. V., Loyd, R. O. P., France, K., Sojka, J., Danchi, W. C., & Liemohn, M. W. 2017, ApJL, 836, L3

Alei, E. et al. 2022, A&A, 665, A106

Alonso, R. 2018, in Handbook of Exoplanets, ed. H. J. Deeg & J. A. Belmonte (Cham: Springer International Publishing), 1–26

An, T., Yuan, P., Liu, G., Cen, J., Wang, X., Zhang, M., & An, Y. 2019, Physics of Plasmas, 26, 13506

Aplin, K. L., Harrison, R. G., & Rycroft, M. J. 2008, Space Sci. Rev., 137, 11

Ardaseva, A., Rimmer, P. B., Waldmann, I., Rocchetto, M., Yurchenko, S. N., Helling, C., & Tennyson, J. 2017, MNRAS, 470, 187

Ardévol Martínez, F., Min, M., Kamp, I., & Palmer, P. I. 2022, A&A, 662, A108

Arney, G. et al. 2016, Astrobiology, 16, 873

Arney, G., Meadows, V., Crisp, D., Schmidt, S. J., Bailey, J., & Robinson, T. 2014, J. Geophys. Res. Planets, 119, 1860

Arrhenius, S. A. 1908, Worlds in the Making: The Evolution of the Universe (New York and London: Harper & brothers)

Asplund, M., Grevesse, N., Sauval, A. J., & Scott, P. 2009, ARA&A, 47, 481

Baba, Y., & Rakov, V. A. 2009, in Lightning: Principles, Instruments and Applications: Review of Modern Lightning Research, ed. H. D. Betz, U. Schumann, & P. Laroche (Dordrecht: Springer Netherlands), 1–21

Bada, J., & Korenaga, J. 2018, Life, 8, 55

Barnes, R. 2017, Celest. Mech. Dyn. Astron., 129, 509

Barth, P., Carone, L., Barnes, R., Noack, L., Mollière, P., & Henning, T. 2021a, Astrobiology, 21, 1325

Barth, P. et al. 2021b, MNRAS, 502, 6201

Barth, P., Stüeken, E. E., Helling, C., Rossmanith, L., Peng, Y., Walters, W., & Claire, M. 2023a, Nature Geoscience, 16, 478

Barth, P., Stüeken, E. E., Helling, C., Schwieterman, E. W., & Telling, J. 2023b, Spark experiments and photochemical simulations to identify lightning signatures in planetary atmospheres. University of St Andrews. (Dataset). doi: 10.17630/8b72510f-62a8-43dc-94f1-af9b7766f817

Barth, P., Stüeken, E. E., Rossmanith, L., Peng, Y., & Walters, W. W. 2023c, Nitrogen fixation rates and isotopic measurements of aqueous nitrite and nitrate from spark discharge experiments. NERC EDS National Geoscience Data Centre. (Dataset). doi: 10.5285/81dfa4de-5a47-479f-8de8-15e5ef398072

Bebout, G. E., & Fogel, M. L. 1992, Geochim. Cosmochim. Acta, 56, 2839

Bell, E. A., Boehnke, P., Harrison, T. M., & Mao, W. L. 2015, Proc. Natl. Acad. Sci. U.S.A., 112, 14518

Belov, A., Garcia, H., Kurt, V., & Mavromichalaki, E. 2005, Cosmic Research, 43, 165

Birkby, J. L., de Kok, R. J., Brogi, M., de Mooij, E. J. W., Schwarz, H., Albrecht, S., & Snellen, I. A. G. 2013, MNRAS Letters, 436, L35

Bolmont, E., Raymond, S. N., Leconte, J., Owen, J. E., Gillon, M., Ribas, I., & Selsis, F. 2016, MNRAS, 464, 3728

Borucki, W. J., & Chameides, W. L. 1984, Reviews of Geophysics, 22, 363

Borucki, W. J. et al. 2010, Science, 327, 977

Bouchy, F. et al. 2005, A&A, 444, L15

Bourrier, V., Ehrenreich, D., King, G., Lecavelier des Etangs, A., Wheatley, P. J., Vidal-Madjar, A., Pepe, F., & Udry, S. 2017, A&A, 597, A26

Bourrier, V. et al. 2013, A&A, 551, A63

——. 2020, MNRAS, 493, 559

Boutle, I. A., Joshi, M., Lambert, F. H., Mayne, N. J., Lyster, D., Manners, J., Ridgway, R., & Kohary, K. 2020, Nature Communications, 11, 2731

Bouwman, A. F., Boumans, L. J. M., & Batjes, N. H. 2002, Global Biogeochemical Cycles, 16, 6

Bower, D. J., Hakim, K., Sossi, P. A., & Sanan, P. 2022, PSJ, 3, 93

Braam, M., Palmer, P. I., Decin, L., Ridgway, R. J., Zamyatina, M., Mayne, N. J., Sergeev, D. E., & Abraham, N. L. 2022, MNRAS, 517, 2383

Bristow, L. A., Mohr, W., Ahmerkamp, S., & Kuypers, M. M. 2017, Current Biology, 27, R474

Brooks, C. E. P. 1925, The distribution of thunderstorms over the globe, Geophysical memoirs (Great Britain. Meteorological Office) (London: H.M. Stationery Off.)

Brown, S. et al. 2018, Nature, 558, 87

Brown, T. M. 2001, ApJ, 553, 1006

Buick, R. 2007, Geobiology, 5, 97

Bunton, C. A., Llewellyn, D. R., & Stedman, G. 1959, J. Chem. Soc. (Resumed), 568

Burcat, A., Ruscic, B., Chemistry, & Tech., T. I. I. o. 2005, Third millenium ideal gas and condensed phase thermochemical database for combustion (with update from active thermochemical tables)., Tech. rep., United States

Burkhart, B., & Loeb, A. 2017, ApJL, 849, 6

Burkholder, J. et al. 2019, in PL Publication 19-5 (Pasadena: Jet Propulsion Laboratory)

Busigny, V., Lebeau, O., Ader, M., Krapež, B., & Bekker, A. 2013, Special Issue dedicated to H.D. Holland: Evolution of the atmosphere and ocean through time, 362, 115

Böhlke, J., Gwinn, C., & Coplen, T. 1993, Geostandards Newsletter, 17, 159

Böhlke, J. K., & Coplen, T. B. 1995, Interlaboratory comparison of reference materials for nitrogen-isotope-ratio measurements, Tech. rep., Vienna, Austria

Böhlke, J. K., Mroczkowski, S. J., & Coplen, T. B. 2003, Rapid communications in mass spectrometry : RCM, 17, 1835

Cacace, D., Ashbaugh, H., Kouri, N., Bledsoe, S., Lancaster, S., & Chalk, S. 2007, Analytica Chimica Acta, 589, 137

Canup, R. M. 2004, Icarus, 168, 433

Cardesín Moinelo, A., Abildgaard, S., García Muñoz, A., Piccioni, G., & Grassi, D. 2016, Icarus, 277, 395

Cardinal, D., Alleman, L. Y., de Jong, J., Ziegler, K., & André, L. 2003, J. Anal. At. Spectrom., 18, 213

Carone, L. et al. 2020, MNRAS, 496, 3582

Casciotti, K. L., Sigman, D. M., Hastings, M. G., Böhlke, J. K., & Hilkert, A. 2002, Analytical Chemistry, 74, 4905

Catling, D. C., & Zahnle, K. J. 2020, Science Advances, 6, 1420

Cavendish, H. 1788, Philos. Trans. R. Soc., 78, 261

Cecil, D. J., Buechler, D. E., & Blakeslee, R. J. 2014, Atmospheric Research, 135-136, 404

Chadney, J. M., Koskinen, T. T., Galand, M., Unruh, Y. C., & Sanz-Forcada, J. 2017, A&A, 608, A75

Chameides, W. L. 1979a, Nature, 277, 123

——. 1979b, Geophys. Res. Lett., 6, 287

——. 1986, in The Earth's Electrical Environment (Washington, DC: The National Academies Press), 70–77

Chameides, W. L. et al. 1977, J. Atmos. Sci., 34, 143

Chameides, W. L., & Walker, J. C. G. 1981, Origins of life, 11, 291

Charbonneau, D. et al. 2009, Nature, 462, 891

Charbonneau, D., Noyes, R. W., Korzennik, S. G., Nisenson, P., Jha, S., Vogt, S. S., & Kibrick, R. I. 1999, ApJ, 522, L145

Checlair, J. H., Olson, S. L., Jansen, M. F., & Abbot, D. S. 2019, ApJL, 884, L46

Childs, A. C., Martin, R. G., & Livio, M. 2022, ApJL, 937, L41

Christian, H. J. et al. 2003, J. Geophys. Res. Atmospheres, 108, ACL 4

Chyba, C., & Sagan, C. 1992, Nature, 355, 125

Claringbold, A., Rimmer, P., Rugheimer, S., & Shorttle, O. 2023, AJ, in press

Cleaves, H. J., Chalmers, J. H., Lazcano, A., Miller, S. L., & Bada, J. L. 2008, Orig. Life Evol. Biosph., 38, 105

Codella, C. et al. 2017, A&A, 605, L3

Cook, D. R., Liaw, Y. P., Sisterson, D. L., & Miller, N. L. 2000, J. Geophys. R. Atmospheres, 105, 7103

Cooper, C. S., & Showman, A. P. 2006, ApJ, 649, 1048

Cooray, V. 1997, J. Geophys. Res. Atmospheres, 102, 21401

Cooray, V., & Rahman, M. 2005, 10th International Conference on Electrostatics, 63, 977

Cridland, A. J., Pudritz, R. E., & Alessi, M. 2016, MNRAS, 461, 3274

Crisp, D. 1997, Geophys. Res. Lett., 24, 571

Crouzet, N., McCullough, P. R., Deming, D., & Madhusudhan, N. 2014, ApJ, 795, 166

Darwin, C. 1871, in The correspondence of Charles Darwin. Vol. 19, 1871, ed. F. Burkhardt (New York: Cambridge University Press), 0–26

Das, T., Ghule, S., & Vanka, K. 2019, ACS Central Science, 5, 1532

Davenport, J. R. A., Becker, A. C., Kowalski, A. F., Hawley, S. L., Schmidt, S. J., Hilton, E. J., Sesar, B., & Cutri, R. 2012, ApJ, 748, 58

de Kok, R., Brogi, M., Snellen, I., Birkby, J., Albrecht, S., & de Mooij, E. 2013, A&A, 554, A82

Deming, D. et al. 2013, ApJ, 774, 95

Demory, B.-O. et al. 2016, Nature, 532, 207

Deng, J., Du, Z., Karki, B. B., Ghosh, D. B., & Lee, K. K. M. 2020, Nature Communications, 11, 2007

Devol, A. H. 2003, Nature, 422, 575

Dobbek, H., Svetlitchnyi, V., Gremer, L., Huber, R., & Meyer, O. 2001, Science, 293, 1281

Dodd, M. S., Papineau, D., Grenne, T., Slack, J. F., Rittner, M., Pirajno, F., O'Neil, J., & Little, C. T. S. 2017, Nature, 543, 60

Domagal-Goldman, S. D., Segura, A., Claire, M. W., Robinson, T. D., & Meadows, V. S. 2014, ApJ, 792, 90

Dong, C., Jin, M., & Lingam, M. 2020, ApJL, 896, L24

Dorn, C., & Lichtenberg, T. 2021, ApJL, 922, L4

Drummond, B. et al. 2020, A&A, 636, A68

Drummond, B., Mayne, N. J., Manners, J., Baraffe, I., Goyal, J., Tremblin, P., Sing, D. K., & Kohary, K. 2018a, ApJ, 869, 28

Drummond, B. et al. 2018b, ApJ, 855, L31

Dubrovin, D., Nijdam, S., van Veldhuizen, E. M., Ebert, U., Yair, Y., & Price, C. 2010, J. Geophys. Res. Space Physics, 115, A00E34

Dwyer, J. R., & Uman, M. A. 2014, The Physics of Lightning, 534, 147

Dyudina, U. A., Ingersoll, A. P., Ewald, S. P., Porco, C. C., Fischer, G., Kurth, W. S., & West, R. A. 2010, Geophys. Res. Lett., 37, L09205

Dyudina, U. A., Ingersoll, A. P., Ewald, S. P., Porco, C. C., Fischer, G., & Yair, Y. 2013, Icarus, 226, 1020

Désert, J.-M., Lecavelier des Etangs, A., Hébrard, G., Sing, D. K., Ehrenreich, D., Ferlet, R., & Vidal-Madjar, A. 2009, ApJ, 699, 478

Ebert, U., & Sentman, D. D. 2008, Journal of Physics D: Applied Physics, 41, 230301

Edwards, B., & Tinetti, G. 2022, The Astronomical Journal, 164, 15

Edwards, T. J., Maurer, G., Newman, J., & Prausnitz, J. M. 1978, AIChE Journal, 24, 966

Fares, R. et al. 2017, MNRAS, 471, 1246

Ferris, J. P., Joshi, P. C., Edelson, E. H., & Lawless, J. G. 1978, Journal of Molecular Evolution, 11, 293

Fletcher, L. N. 2022, The Atmosphere of Uranus

Folsome, C. E., Brittain, A., Smith, A., & Chang, S. 1981, Nature, 294, 64

Forget, F., & Leconte, J. 2014, Philos. Trans. Royal Soc. A, 372, 20130084

Fourré, I., Rosset, L., Chevreau, H., & Ellinger, Y. 2016, A&A, 589, A18

Fowler, D. et al. 2013, Philos. Trans. R. Soc. B, 368, 20130164

France, K. et al. 2020, AJ, 160, 237

Fraschetti, F., Drake, J. J., Alvarado-Gómez, J. D., Moschou, S. P., Garraffo, C., & Cohen, O. 2019, ApJ, 874, 21

Füri, E., & Marty, B. 2015, Nature Geoscience, 8, 515

Gao, P., Hu, R., Robinson, T. D., Li, C., & Yung, Y. L. 2015, ApJ, 806, 249

Gao, P., Wakeford, H. R., Moran, S. E., & Parmentier, V. 2021, J. Geophys. Res. Planets, 126, e2020JE006655

Gasman, D., Min, M., & Chubb, K. L. 2022, A&A, 659, A114

Gaudi, B. S. et al. 2020, arXiv preprint 2001.06683

Gibbard, S., Levy, E., Lunine, J., & de Pater, I. 1999, Icarus, 139, 227

Gibson, N. P. et al. 2012, MNRAS, 422, 753

Gilbert, J. S., Lane, S. J., Sparks, R. S. J., & Koyaguchi, T. 1991, Nature, 349, 598

Gladstone, G., Allen, M., & Yung, Y. L. 1996, Icarus, 119, 1

Goldblatt, C., Claire, M. W., Lenton, T. M., Matthews, A. J., Watson, A. J., & Zahnle, K. J. 2009, Nature Geoscience, 2, 891

Goldenbaum, G. C., & Dickerson, R. R. 1993, J. Geophys. Res. Atmospheres, 98, 18333

Gordon, I. et al. 2022, Journal of Quantitative Spectroscopy and Radiative Transfer, 277, 107949

——. 2017, HITRAN2016 Special Issue, 203, 3

Gough, D. O. 1981, Solar Physics, 74, 21

Green, A. E. S., Sawada, T., Edgar, B. C., & Uman, M. A. 1973, J. Geophys. Res. (1896-1977), 78, 5284

Greene, T. P., Bell, T. J., Ducrot, E., Dyrek, A., Lagage, P.-O., & Fortney, J. J. 2023, Nature, 618, 39

Grenfell, J. L. 2017, Physics Reports, 713, 1

Grillmair, C. J. et al. 2008, Nature, 456, 767

Gurnett, D., Morgan, D., Granroth, L., Cantor, B., Farrell, W., & Espley, J. 2010, Geophys. Res. Lett., 37, L17802

Gurnett, D. A., Kurth, W. S., Cairns, I. H., & Granroth, L. J. 1990, J. Geophys. Res. Space Physics, 95, 20967

Haldane, J. B. S. 1929, The Rationalist Annual, 148, 3

Haqq-Misra, J., Fauchez, T. J., Schwieterman, E. W., & Kopparapu, R. 2022, ApJL, 929, L28

Harada, N., Herbst, E., & Wakelam, V. 2010, ApJ, 721, 1570

Harman, C. E., Felton, R., Hu, R., Domagal-Goldman, S. D., Segura, A., Tian, F., & Kasting, J. F. 2018, ApJ, 866, 56

Harman, C. E., Schwieterman, E. W., Schottelkotte, J. C., & Kasting, J. F. 2015, ApJ, 812, 137

Hayashi, C., Nakazawa, K., & Mizuno, H. 1979, EPSL, 43, 22

Heays, A. N. et al. 2022, J. Geophys. Res. Planets, 127, e2021JE006842

Helling, C. 2019, in Journal of Physics Conference Series, Vol. 1322, Journal of Physics Conference Series, 012028

Helling, C., Dehn, M., Woitke, P., & Hauschildt, P. H. 2008a, ApJ, 675, L105

Helling, C. et al. 2016a, Surveys in Geophysics, 37, 705

Helling, C., Jardine, M., Diver, D., & Witte, S. 2013a, Planet. Space Sci., 77, 152

Helling, C., Jardine, M., & Mokler, F. 2011a, ApJ, 737, 38

Helling, C., Jardine, M., Stark, C., & Diver, D. 2013b, ApJ, 767, 136

Helling, C., Jardine, M., Witte, S., & Diver, D. A. 2011b, ApJ, 727, 4

Helling, C. et al. 2016b, MNRAS, 460, 855

Helling, C., Oevermann, M., Lüttke, M. J. H., Klein, R., & Sedlmayr, E. 2001, A&A, 376, 194

Helling, C., & Rimmer, P. B. 2019, Philos. Trans. Royal Soc. A, 377

Helling, C., & Woitke, P. 2006, A&A, 455, 325

Helling, C., Woitke, P., Rimmer, P. B., Kamp, I., Thi, W.-F., & Meijerink, R. 2014, Life, 4, 142

Helling, C., Woitke, P., & Thi, W.-F. 2008b, A&A, 485, 547

Herbst, K. et al. 2019a, A&A, 631, A101

Herbst, K., Grenfell, J. L., Sinnhuber, M., & Wunderlich, F. 2022, Astronomische Nachrichten, 343, e210072

Herbst, K., Papaioannou, A., Banjac, S., & Heber, B. 2019b, A&A, 621, A67

Hill, R. D. 1979, Reviews of Geophysics, 17, 155

Hill, R. D., Rahmim, I., & Rinker, R. G. 1988, Industrial & Engineering Chemistry Research, 27, 1264

Hill, R. D., Rinker, R. G., & Coucouvinos, A. 1984, J. Geophys. Res. Atmospheres, 89, 1411

Hill, R. D., Rinker, R. G., & Wilson, H. D. 1980, J. Atmos. Sci., 37, 179

Hilton, E. J., West, A. A., Hawley, S. L., & Kowalski, A. F. 2010, The Astronomical Journal, 140, 1402

Hobbs, R., Shorttle, O., Madhusudhan, N., & Rimmer, P. 2019, MNRAS, 487, 2242

Hodosán, G. 2017, PhD thesis, University of St Andrews, St Andrews

Hodosán, G., Helling, C., Asensio-Torres, R., Vorgul, I., & Rimmer, P. B. 2016a, Monthly Notices of the Royal Astronomical Society, 461, 3927

Hodosán, G., Helling, C., & Vorgul, I. 2021, Planetary and Space Science, 204, 105247

Hodosán, G., Rimmer, P. B., & Helling, C. 2016b, MNRAS, 461, 1222

Hoering, T. 1957, Geochim. Cosmochim. Acta, 12, 97

Hoyle, F., & Wickramasinghe, N. C. 2000, Astronomical Origins of Life (Springer Dordrecht)

Hu, R. 2019, ApJ, 887, 166

Hu, R., Peterson, L., & Wolf, E. T. 2020, ApJ, 888, 122

Hu, R., & Seager, S. 2014, ApJ, 784, 63

Hu, Y., & Yang, J. 2014, Proc. Natl. Acad. Sci. U.S.A., 111, 629

Huang, J., Seager, S., Petkowski, J. J., Ranjan, S., & Zhan, Z. 2022, Astrobiology, 22, 171

Hudson, H. S. 1978, Solar Physics, 57, 237

Hueso, R., & Sánchez-Lavega, A. 2019, Space Sci. Rev., 215, 52

Iglesias-Groth, S. 2023, MNRAS, 523, 2876

Iyer, A. R., Swain, M. R., Zellem, R. T., Line, M. R., Roudier, G., Rocha, G., & Livingston, J. H. 2016, ApJ, 823, 109

Jackson, R. B. et al. 2020, Environmental Research Letters, 15, 071002

Johnstone, C. P. 2020, ApJ, 890, 79

Johnstone, C. P., Bartel, M., & Güdel, M. 2021a, A&A, 649, A96

Johnstone, C. P., Khodachenko, M. L., Lüftinger, T., Kislyakova, K. G., Lammer, H., & Güdel, M. 2019, A&A, 624, L10

Johnstone, C. P., Lammer, H., Kislyakova, K. G., Scherf, M., & Güdel, M. 2021b, EPSL, 576, 117197

Joshi, J. B., Mahajani, V. V., & Juvekar, V. A. 1985, Chemical Engineering Communications, 33, 1

Kasting, J., Whitmire, D., & Reynolds, R. 1993, Icarus, 101, 108

Kasting, J. F. 1993, Science, 259, 920 LP

Kasting, J. F., & Walker, J. C. G. 1981, J. Geophys. Res., 86, 1147

Kavanagh, R. D. et al. 2019, MNRAS, 485, 4529

Kay, C., Opher, M., & Kornbleuth, M. 2016, ApJ, 826, 195

Kendall, C., & Caldwell, E. A. 1998, in Isotope Tracers in Catchment Hydrology, ed. C. Kendall & J. J. McDonnell (Amsterdam: Elsevier Science B.V.), 51–86

Kharecha, P., Kasting, J., & Siefert, J. 2005, Geobiology, 3, 53

Kieu, N., Gordillo-Vázquez, F. J., Passas, M., Sánchez, J., Pérez-Invernón, F. J., Luque, A., Montanyá, J., & Christian, H. 2020, Geophys. Res. Lett., 47, e2020GL088755

Kirk, J., Wheatley, P. J., Louden, T., Doyle, A. P., Skillen, I., McCormac, J., Irwin, P. G. J., & Karjalainen, R. 2017, MNRAS, 468, 3907

Kite, E. S., Gaidos, E., & Manga, M. 2011, ApJ, 743, 41

Kolmašová, I., Santolík, O., Imai, M., Kurth, W. S., Hospodarsky, G. B., Connerney, J. E. P., Bolton, S. J., & Lán, R. 2023, Nature Communications, 14, 2707

Konhauser, K. O. et al. 2009, Nature, 458, 750

Konhauser, K. O., Robbins, L. J., Pecoits, E., Peacock, C., Kappler, A., & Lalonde, S. V. 2015, Astrobiology, 15, 804

Kooij, D. M. 1893, Zeitschrift für Physikalische Chemie, 12U, 155

Kopparapu, R. K. et al. 2013, ApJ, 765, 131

Kopparapu, R. K., Ramirez, R. M., Schottelkotte, J., Kasting, J. F., Domagal-Goldman, S., & Eymet, V. 2014, ApJL, 787, 0

Kotaki, M., & Katoh, C. 1983, J. Atmos. Terr. Phys., 45, 833

Kowalczyk, M., & Bauer, E. 1981, Lightning as a source of NOx in the troposphere, Tech. Rep. Tech. Rep. FAA-EE-82-4, Inst. for Def. Anal., Alexandria, Virginia

Kozakis, T., Mendonça, J. M., & Buchhave, L. A. 2022, A&A, 665, A156

Krenn, A. F. et al. 2023, A&A, 672, A24

Krider, E. P., Dawson, G. A., & Uman, M. A. 1968, J. Geophys. Res. (1896-1977), 73, 3335

Krissansen-Totton, J. 2023, ApJL, in press

Krissansen-totton, J. et al. 2019, BAAS, 51, 158

Krissansen-Totton, J., Garland, R., Irwin, P., & Catling, D. C. 2018a, AJ, 156, 114

Krissansen-Totton, J., Olson, S., & Catling, D. C. 2018b, Science Advances, 4, eaao5747

Kuga, M., Carrasco, N., Marty, B., Marrocchi, Y., Bernard, S., Rigaudier, T., Fleury, B., & Tissandier, L. 2014, EPSL, 393, 2

Kulikov, Y. N., Lammer, H., Lichtenegger, H. I. M., Penz, T., Breuer, D., Spohn, T., Lundin, R., & Biernat, H. K. 2007, Space Sci. Rev., 129, 207

Kuramoto, K., Umemoto, T., & Ishiwatari, M. 2013, EPSL, 375, 312

Köhn, C., Dujko, S., Chanrion, O., & Neubert, T. 2019, Icarus, 333, 294

Köhn, C., & Ebert, U. 2015, J. Geophys. Res. Atmospheres, 120, 1620

Lacy, B. I., & Burrows, A. 2020, ApJ, 905, 131

Lammer, H., Kasting, J. F., Chassefière, E., Johnson, R. E., Kulikov, Y. N., & Tian, F. 2008, Space Sci. Rev., 139, 399

Lammer, H., Lichtenegger, H. I. M., Khodachenko, M. L., Kulikov, Y. N., & Griessmeier, J. 2011, in Astronomical Society of the Pacific Conference Series, Vol. 450, Molecules in the Atmospheres of Extrasolar Planets, ed. J. P. Beaulieu, S. Dieters, & G. Tinetti, 139

Lammer, H., Sproß, L., Grenfell, J. L., Scherf, M., Fossati, L., Lendl, M., & Cubillos, P. E. 2019, Astrobiology, 19, 927

Lammer, H. et al. 2018, A&ARv, 26, 2

Lane, S. J., & Gilbert, J. S. 1992, Bulletin of Volcanology, 54, 590

Lecavelier des Etangs, A. et al. 2012, A&A, 543, L4

Lee, E., Dobbs-Dixon, I., Helling, C., Bognar, K., & Woitke, P. 2016, A&A, 594, A48

Lee, E., Taylor, J., Grimm, S. L., Baudino, J.-L., Garland, R., Irwin, P. G. J., & Wood, K. 2019, MNRAS, 487, 2082

Lee, J.-M., Fletcher, L. N., & Irwin, P. G. J. 2012, MNRAS, 420, 170

Levine, J. S., Gregory, G. L., Harvey, G. A., Howell, W. E., Borucki, W. J., & Orville, R. E. 1982, Geophys. Res. Lett., 9, 893

Levine, J. S., Hughes, R. E., Chameides, W. L., & Howell, W. E. 1979, Geophys. Res. Lett., 6, 557

Levine, J. S., Rogowski, R. S., Gregory, G. L., Howell, W. E., & Fishman, J. 1981, Geophys. Res. Lett., 8, 357

Li, J., Zhang, X., Orlando, J., Tyndall, G., & Michalski, G. 2020, Atmospheric Chemistry and Physics, 20, 9805

Li, L., Lollar, B. S., Li, H., Wortmann, U. G., & Lacrampe-Couloume, G. 2012, Geochim. Cosmochim. Acta, 84, 280

Lichtenberg, T. 2021, ApJL, 914, L4

Lichtenberg, T., Schaefer, L. K., Nakajima, M., & Fischer, R. A. 2022, arXiv preprint 2203.10023

Lichtenegger, H., Lammer, H., Grießmeier, J.-M., Kulikov, Y., von Paris, P., Hausleitner, W., Krauss, S., & Rauer, H. 2010, Icarus, 210, 1

Lincowski, A. P., Meadows, V. S., Crisp, D., Robinson, T. D., Luger, R., Lustig-Yaeger, J., & Arney, G. N. 2018, ApJ, 867, 76

Lindemann, F. A., Arrhenius, S., Langmuir, I., Dhar, N. R., Perrin, J., & McC. Lewis, W. C. 1922, Transactions of the Faraday Society, 17, 598

Lines, S. et al. 2018, A&A, 615, A97

Loison, J.-C. et al. 2017, MNRAS, 470, 4075

Loison, J.-C., Wakelam, V., & Hickson, K. M. 2014, MNRAS, 443, 398

Lorenz, R., Takahashi, Y., Imai, M., & SATO, M. 2022, BAAS, 54

Louden, T., Wheatley, P. J., & Briggs, K. 2017, MNRAS, 464, 2396

Lovelock, J. E., Kaplan, I. R., & Pirie, N. W. 1975, Proc. Royal Soc. B, 189, 167

Luger, R., & Barnes, R. 2015, Astrobiology, 15, 119

Luger, R., Barnes, R., Lopez, E., Fortney, J., Jackson, B., & Meadows, V. 2015, Astrobiology, 15, 57

Luger, R., Lustig-Yaeger, J., Fleming, D., Tilley, M., Agol, E., Meadows, V., Deitrick, R., & Barnes, R. 2017, ApJ, 837, 63

Lustig-Yaeger, J., Meadows, V. S., & Lincowski, A. P. 2019, AJ, 158, 27

Ma, J., Dasgupta, P. K., Blackledge, W., & Boss, G. R. 2010, Environmental Science & Technology, 44, 3028

MacGorman, D., & Rust, W. 1998, The Electrical Nature of Storms (Oxford University Press)

Mackerras, D., Darveniza, M., Orville, R. E., Williams, E. R., & Goodman, S. J. 1998, J. Geophys. Res., 37, 19791

Madhusudhan, N. 2012, ApJ, 758, 36

Madhusudhan, N., & Seager, S. 2009, ApJ, 707, 24

Mant, B. P., Yachmenev, A., Tennyson, J., & Yurchenko, S. N. 2018, MNRAS, 478, 3220

Marty, B., Zimmermann, L., Pujol, M., Burgess, R., & Philippot, P. 2013, Science, 342, 101 LP

Mayor, M., & Queloz, D. 1995, Nature, 378, 355

McCullough, P. R., Crouzet, N., Deming, D., & Madhusudhan, N. 2014, ApJ, 791, 55

McIlvin, M. R., & Casciotti, K. L. 2006, Analytical Chemistry, 78, 2377

Meadows, V. 2017, Astrobiology, 17, 1022

Meadows, V. S., & Crisp, D. 1996, J. Geophys. Res. Planets, 101, 4595

Meadows, V. S. et al. 2018, Astrobiology, 18, 630

Melnik, O., & Parrot, M. 1998, J. Geophys. Res. Space Physics, 103, 29107

Mesquita, A. L., Rodgers-Lee, D., & Vidotto, A. A. 2021, MNRAS, 505, 1817

Mewaldt, R. A. et al. 2005, J. Geophys. Res. Space Physics, 110, A09S18

Miller, D. N. 1987, AIChE Journal, 33, 1351

Miller, S. L. 1953, Science, 117, 528

——. 1957, Annals of the New York Academy of Sciences, 69, 260

Miller, S. L., & Schlesinger, G. 1983, Adv. Space Res., 3, 47

Misra, A., Meadows, V., Claire, M., & Crisp, D. 2014, Astrobiology, 14, 67

Miyakawa, S., Yamanashi, H., Kobayashi, K., Cleaves, H. J., & Miller, S. L. 2002, Proc. Natl. Acad. Sci. U.S.A., 99, 14628

Mojzsis, S. J., Harrison, T. M., & Pidgeon, R. T. 2001, Nature, 409, 178

Moncrieff, M. W., & Miller, M. J. 1976, Quarterly Journal of the Royal Meteorological Society, 102, 373

Moore, C. M. et al. 2013, Nature Geoscience, 6, 701

Moore, H. 1977, Atmospheric Environment (1967), 11, 1239

Mordasini, C., van Boekel, R., Mollière, P., Henning, T., & Benneke, B. 2016, ApJ, 832, 41

Morse, J. W., & Mackenzie, F. T. 1998, Aquatic Geochemistry, 4, 301

Moses, J. I., Fouchet, T., Bézard, B., Gladstone, G. R., Lellouch, E., & Feuchtgruber, H. 2005, J. Geophys. Res. E: Planets, 110, 1

Moses, J. I. et al. 2011, ApJ, 737, 15

National Academies of Sciences, E., & Medicine. 2021, Pathways to Discovery in Astronomy and Astrophysics for the 2020s, Tech. rep., National Academies Press, Washington, D.C.

Navarro-González, R., McKay, C. P., & Mvondo, D. N. 2001, Nature, 412, 61

Navarro-González, R. et al. 2019, J. Geophys. Res. Planets, 124, 94

Newman, B. L., & Carta, G. 1988, AIChE Journal, 34, 1190

Nguyen, T. G., Cowan, N. B., Banerjee, A., & Moores, J. E. 2020, MNRAS, 499, 4605

Nicoll, K. A. 2014, Weather, 69, 238

Niemann, H. B. et al. 2010, J. Geophys. Res. Planets, 115, E12006

Nijdam, S., Teunissen, J., & Ebert, U. 2020, Plasma Sources Science and Technology, 29, 103001

NIST Mass Spectrometry Data Center, William E. Wallace, D., in NIST Chemistry WebBook, NIST Standard Reference Database Number 69, ed. P. Linstrom & W. Mallard (National Institute of Standards and Technology, Gaithersburg MD, 20899)

Nna Mvondo, D., Navarro-González, R., McKay, C. P., Coll, P., & Raulin, F. 2001, Adv. Space Res., 27, 217

Odert, P. et al. 2020, A&A, 638

Öberg, K. I., Guzmán, V. V., Furuya, K., Qi, C., Aikawa, Y., Andrews, S. M., Loomis, R., & Wilner, D. J. 2015, Nature, 520, 198

Ohtomo, Y., Kakegawa, T., Ishida, A., Nagase, T., & Rosing, M. T. 2014, Nature Geoscience, 7, 25

Oparin, A. I. 1938, Origin of Life (New York: Macmillan)

Ortenzi, G. et al. 2020, Scientific Reports, 10, 10907

Orville, R. E., Huffines, G. R., Burrows, W. R., Holle, R. L., & Cummins, K. L. 2002, Monthly Weather Review, 130, 2098

Orville, R. E., & Spencer, D. W. 1979, Monthly Weather Review, 107, 934

Parker, E. T., Cleaves, H. J., Dworkin, J. P., Glavin, D. P., Callahan, M., Aubrey, A., Lazcano, A., & Bada, J. L. 2011, Proc. Natl. Acad. Sci. U.S.A., 108, 5526

Parker, E. T., Cleaves, J. H., Burton, A. S., Glavin, D. P., Dworkin, J. P., Zhou, M., Bada, J. L., & Fernández, F. M. 2014, Journal of Visualized Experiments, e51039

Parmentier, V. et al. 2018, A&A, 617

Pass, E. K., Winters, J. G., Charbonneau, D., Irwin, J. M., & Medina, A. A. 2023, AJ, 166, 16

Patel, B. H., Percivalle, C., Ritson, D. J., Duffy, C. D., & Sutherland, J. D. 2015, Nature Chemistry, 7, 301

Peacock, S., Barman, T., Shkolnik, E. L., Hauschildt, P. H., & Baron, E. 2019, ApJ, 871, 235

Pearce, B. K. D., He, C., & Hörst, S. M. 2022, ACS Earth and Space Chemistry, 6, 2385

Pearce, B. K. D., Pudritz, R. E., Semenov, D. A., & Henning, T. K. 2017, Proc. Natl. Acad. Sci. U.S.A., 114, 11327 LP

Piaulet, C. et al. 2023, Nature Astronomy, 7, 206

Picone, J. M., Boris, J. P., Greig, J. R., Raleigh, M., & Fernsler, R. F. 1981, J. Atmos. Sci., 38, 2056

Pillitteri, I., Wolk, S. J., Cohen, O., Kashyap, V., Knutson, H., Lisse, C. M., & Henry, G. W. 2010, ApJ, 722, 1216

Pont, F., Sing, D. K., Gibson, N. P., Aigrain, S., Henry, G., & Husnoo, N. 2013, MNRAS, 432, 2917

Postgate, J. R. 1998, Nitrogen fixation (Cambridge, U.K.: Cambridge University Press)

Price, C., Pechony, O., & Greenberg, E. 2007, J. Lightning Res., 1, 1

Price, C., Penner, J., & Prather, M. 1997a, J. Geophys. Res. Atmospheres, 102, 5929

——. 1997b, J. Geophys. Res. Atmospheres, 102, 5943

Quanz, S. P. et al. 2022, A&A, 664, A21

Rab, C., Güdel, M., Padovani, M., Kamp, I., Thi, W.-F., Woitke, P., & Aresu, G. 2017, A&A, 603, A96

Ragsdale, S. W. 2004, Critical Reviews in Biochemistry and Molecular Biology, 39, 165

Rahman, M., & Cooray, V. 2003, Optics & Laser Technology, 35, 543

Rakov, V. A., & Uman, M. A. 2003, Lightning: Physics and Effects (Cambridge: Cambridge University Press)

Ranjan, S., Schwieterman, E. W., Harman, C., Fateev, A., Sousa-Silva, C., Seager, S., & Hu, R. 2020, ApJ, 896, 148

Ranjan, S., Seager, S., Zhan, Z., Koll, D. D. B., Bains, W., Petkowski, J. J., Huang, J., & Lin, Z. 2022, ApJ, 930, 131

Ranjan, S., Todd, Z. R., Rimmer, P. B., Sasselov, D. D., & Babbin, A. R. 2019, Geochemistry, Geophysics, Geosystems, 20, 2021

Rauer, H. et al. 2011, A&A, 529, A8

Rehbein, N., & Cooray, V. 2001, Electrostatics 2001: 9th International Conference on Electrostatics, 51-52, 333

Reid, N., & Hawley, S. 2006, New Light on Dark Stars: Red Dwarfs, Low-Mass Stars, Brown Stars, Springer Praxis Books (Springer Berlin Heidelberg)

Renno, N. O., Wong, A.-S., Atreya, S. K., de Pater, I., & Roos-Serote, M. 2003, Geophys. Res. Lett., 30, 2140

Ribas, I., Guinan, E. F., Gudel, M., & Audard, M. 2005, ApJ, 622, 680

Ricker, G. R. et al. 2014, Journal of Astronomical Telescopes, Instruments, and Systems, 1, 014003

Rimmer, P. B., & Helling, C. 2013, ApJ, 774, 108

——. 2016, ApJS, 224, 9

——. 2019, ApJS, 245, 20

Rimmer, P. B., Herbst, E., Morata, O., & Roueff, E. 2012, A&A, 537

Rimmer, P. B., & Rugheimer, S. 2019, Icarus, 329, 124

Robinson, T. D. 2017, ApJ, 836, 236

Robinson, T. D. et al. 2011, Astrobiology, 11, 393

Roble, R. G., & Tzur, I. 1986, in The Earth's Electrical Environment, ed. E. P. Krider & R. G. Roble (Washington, DC: The National Academies Press), 206–231

Rodgers-Lee, D. et al. 2023, MNRAS, 521, 5880

Rodgers-Lee, D., Taylor, A. M., Vidotto, A. A., & Downes, T. P. 2021, MNRAS, 504, 1519

Rodler, F., Kürster, M., & Barnes, J. R. 2013, MNRAS, 432, 1980

Rodríguez-Barrera, M. I., Helling, C., Stark, C. R., & Rice, A. M. 2015, MNRAS, 454, 3977

Romani, P. N., Jennings, D. E., Bjoraker, G. L., Sada, P. V., McCabe, G. H., & Boyle, R. J. 2008, Icarus, 198, 420

Romps, D. M., Seeley, J. T., Vollaro, D., & Molinari, J. 2014, Science, 346, 851

Rosing, M. T. 1999, Science, 283, 674

Roussel-Dupré, R., Colman, J. J., Symbalisty, E., Sentman, D., & Pasko, V. P. 2008, Space Sci. Rev., 137, 51

Russell, C. T., Zhang, T. L., Delva, M., Magnes, W., Strangeway, R. J., & Wei, H. Y. 2007, Nature, 450, 661

Sagan, C., Thompson, W. R., Carlson, R., Gurnett, D., & Hord, C. 1993, Nature, 365, 715

Samara, E., Patsourakos, S., & Georgoulis, M. K. 2021, ApJL, 909, L12

Saunders, C. P. R. 1993, J. Appl. Meteorol. Climatol., 32, 642

Saxena, P., Villanueva, G. L., Zimmerman, N. T., Mandell, A. M., & Smith, A. J. R. W. 2021, AJ, 162, 30

Scheu, B., Dingwell, D. B., Cimarelli, C., Bada, J., Chalmers, J. H., & Burton, A. S. 2017, in AGU Fall Meeting Abstracts, Vol. 2017, B53A–1946

Scheucher, M. et al. 2020, ApJ, 893, 12

Schlesinger, G., & Miller, S. L. 1983, Journal of Molecular Evolution, 19, 376

Schopf, J. W., Kudryavtsev, A. B., Czaja, A. D., & Tripathi, A. B. 2007, Precambrian Research, 158, 141

Schumann, U., & Huntrieser, H. 2007, Atmospheric Chemistry and Physics, 7, 3823

Schwieterman, E. W. et al. 2016, ApJL, 819, L13

——. 2022, ApJ, 937, 109

Schwieterman, E. W., Reinhard, C. T., Olson, S. L., Ozaki, K., Harman, C. E., Hong, P. K., & Lyons, T. W. 2019, ApJ, 874, 9

Seager, S. 2010, Exoplanet Atmospheres (Princeton University Press)

Seager, S., Bains, W., & Hu, R. 2013a, ApJ, 775, 104

——. 2013b, ApJ, 777, 95

Segura, A., Kasting, J. F., Meadows, V., Cohen, M., Scalo, J., Crisp, D., Butler, R. A., & Tinetti, G. 2005, Astrobiology, 5, 706

Segura, A., Krelove, K., Kasting, J. F., Sommerlatt, D., Meadows, V., Crisp, D., Cohen, M., & Mlawer, E. 2003, Astrobiology, 3, 689

Segura, A., Meadows, V. S., Kasting, J. F., Crisp, D., & Cohen, M. 2007, A&A, 472, 665

Segura, A., Walkowicz, L. M., Meadows, V., Kasting, J., & Hawley, S. 2010, Astrobiology, 10, 751

Selverstone, J., & Fyfe, W. S. 2023, "metamorphic rock", Encyclopedia Britannica, 2023, 8 June 2023.

Sergeev, D. E., Lambert, F. H., Mayne, N. J., Boutle, I. A., Manners, J., & Kohary, K. 2020, ApJ, 894, 84

Shapiro, A. V. et al. 2023, Nature Communications, 14, 1893

Shi, G. et al. 2021, EPSL, 564, 116914

Sigman, D. M., Casciotti, K. L., Andreani, M., Barford, C., Galanter, M., & Böhlke, J. K. 2001, Analytical Chemistry, 73, 4145

Smith, E. M., Shirey, S. B., Nestola, F., Bullock, E. S., Wang, J., Richardson, S. H., & Wang, W. 2016, Science, 354, 1403

Solórzano, L. 1969, Limnology and Oceanography, 14, 799

Som, S. M., Buick, R., Hagadorn, J. W., Blake, T. S., Perreault, J. M., Harnmeijer, J. P., & Catling, D. C. 2016, Nature Geoscience, 9, 448

Som, S. M., Catling, D. C., Harnmeijer, J. P., Polivka, P. M., & Buick, R. 2012, Nature, 484, 359

Southworth, J. 2010, MNRAS, 408, 1689

Sproß, L., Scherf, M., Shematovich, V. I., Bisikalo, D. V., & Lammer, H. 2021, Astronomy Reports, 65, 275

Stamnes, K., Tsay, S.-C., Wiscombe, W., & Jayaweera, K. 1988, Applied Optics, 27, 2502

Stark, M. S., Harrison, J. T. H., & Anastasi, C. 1996, J. Geophys. Res. Atmospheres, 101, 6963

Stern, J. C., Sutter, B., Freissinet, C., Navarro-González, R., McKay, C. P., & Al., E. 2015, Proc. Natl. Acad. Sci. U.S.A., 112, 4245

Stozhkov, Y. I. 2003, Journal of Physics G: Nuclear and Particle Physics, 29, 913

Stüeken, E., Kipp, M., Koehler, M., Schwieterman, E., Johnson, B., & Buick, R. 2016a, Astrobiology, 16, 949

Stüeken, E. E., Boocock, T., Szilas, K., Mikhail, S., & Gardiner, N. J. 2021, Frontiers in Earth Science, 9, 286

Stüeken, E. E., Kipp, M. A., Koehler, M. C., & Buick, R. 2016b, Earth-Science Reviews, 160, 220

Summers, D. P. 1999, Orig. Life Evol. Biosph., 29, 33

Summers, D. P., Basa, R. C. B., Khare, B., & Rodoni, D. 2012, Astrobiology, 12, 107

Summers, D. P., & Chang, S. 1993, Nature, 365, 630

Summers, D. P., & Khare, B. 2007, Astrobiology, 7, 333

Sutter, B. et al. 2017, J. Geophys. Res. Planets, 122, 2574

Swain, M. R., Line, M. R., & Deroo, P. 2014, ApJ, 784, 133

Taubner, R.-S. et al. 2023, mSystems, 8, e01159

Taylor, J., Parmentier, V., Irwin, P. G. J., Aigrain, S., Lee, E., & Krissansen-Totton, J. 2020, MNRAS, 493, 4342

The LUVOIR Team. 2019, arXiv preprint 1912.06219

Thomas, R. J., Krehbiel, P. R., Rison, W., Hamlin, T., Boccippio, D. J., Goodman, S. J., & Christian, H. J. 2000, Geophys. Res. Lett., 27, 1703

Thomazo, C., & Papineau, D. 2013, Elements, 9, 345

Thompson, M. A., Krissansen-Totton, J., Wogan, N., Telus, M., & Fortney, J. J. 2022, Proc. Natl. Acad. Sci. U.S.A., 119, e2117933119

Thuillier, G., Floyd, L., Woods, T., Cebula, R., Hilsenrath, E., Hersé, M., & Labs, D. 2004, Solar Variability and Climate Change, 34, 256

Tian, F. 2009, ApJ, 703, 905

Tian, F., France, K., Linsky, J. L., Mauas, P. J., & Vieytes, M. C. 2014, EPSL, 385, 22

Tian, F., Kasting, J. F., Liu, H.-L., & Roble, R. G. 2008, J. Geophys. Res. Planets, 113, E05008

Tian, F., Kasting, J. F., & Solomon, S. C. 2009, Geophys. Res. Lett., 36, L02205

Tian, F., Kasting, J. F., & Zahnle, K. 2011, EPSL, 308, 417

Tian, H. et al. 2020, Nature, 586, 248

Tinetti, G., Meadows, V. S., Crisp, D., Fong, W., Velusamy, T., & Snively, H. 2005, Astrobiology, 5, 461

Todorov, K. O., Deming, D., Burrows, A., & Grillmair, C. J. 2014, ApJ, 796, 100

Tosca, N. J., Jiang, C. Z., Rasmussen, B., & Muhling, J. 2019, Free Radical Biology and Medicine, 140, 138

Troe, J. 1983, Berichte der Bunsengesellschaft für physikalische Chemie, 87, 161

Tsai, S.-M., Lyons, J. R., Grosheintz, L., Rimmer, P. B., Kitzmann, D., & Heng, K. 2017, ApJS, 228, 20

Uman, M. A. 1987, The Lightning Discharge, Vol. 39 (Orlando: Academic Press)

Uman, M. A., & Rakov, V. A. 2003, in Lightning: Physics and Effects, ed. M. A. Uman & V. A. Rakov (Cambridge: Cambridge University Press), 507–527

Uman, M. A., & Voshall, R. E. 1968, J. Geophys. Res. (1896-1977), 73, 497

Ushikubo, T., Kita, N. T., Cavosie, A. J., Wilde, S. A., Rudnick, R. L., & Valley, J. W. 2008, EPSL, 272, 666

Vasavada, A., & Showman, A. 2005, Reports on Progress in Physics, 68, 1935

Vedantham, H. K. et al. 2020, Nature Astronomy, 4, 577

Venot, O., Bounaceur, R., Dobrijevic, M., Hébrard, E., Cavalié, T., Tremblin, P., Drummond, B., & Charnay, B. 2019, A&A, 624, A58

Venot, O., Cavalié, T., Bounaceur, R., Tremblin, P., Brouillard, L., & Lhoussaine Ben Brahim, R. 2020, A&A, 634, A78

Venot, O., Hébrard, E., Agúndez, M., Dobrijevic, M., Selsis, F., Hersant, F., Iro, N., & Bounaceur, R. 2012, A&A, 546, A43

Venot, O., Rocchetto, M., Carl, S., Hashim, A. R., & Decin, L. 2016, ApJ, 830, 77

Vinatier, S., Bézard, B., & Nixon, C. A. 2007, Icarus, 191, 712

Vonnegut, B. 1963, in Severe Local Storms, ed. D. Atlas, D. R. Booker, H. Byers, R. H. Douglas, T. Fujita, D. C. House, F. H. Ludlum, J. S. Malkus, C. W. Newton, Y. Ogura, R. A. Schleusener, B. Vonnegut, & R. T. Williams (Boston, MA: American Meteorological Society), 224–241

Wakelam, V. et al. 2012, ApJS, 199, 21

Walters, W. W., & Michalski, G. 2015, Geochim. Cosmochim. Acta, 164, 284

Walters, W. W., Simonini, D. S., & Michalski, G. 2016, Geophys. Res. Lett., 43, 440

Wang, A., Jackson, A. W., Sturchio, N. C., Houghton, J., Yan, C. Y. C., Olsen, K. S., & Qu, Q. H. K. 2023, Geophys. Res. Lett., 50, e2022GL102127

Wang, Y., DeSilva, A. W., Goldenbaum, G. C., & Dickerson, R. R. 1998, J. Geophys. Res. Atmospheres, 103, 19149

Wang, Y., Tian, F., Li, T., & Hu, Y. 2016, Icarus, 266, 15

Weiss, M. C., Sousa, F. L., Mrnjavac, N., Neukirchen, S., Roettger, M., Nelson-Sathi, S., & Martin, W. F. 2016, Nature Microbiology, 1, 16116

Wilde, S. A., Valley, J. W., Peck, W. H., & Graham, C. M. 2001, Nature, 409, 175

Williams, E. 2005, Atmospheric Electricity, 76, 272

Wilson, C. 1929, Journal of the Franklin Institute, 208, 1

Wilson, C. T. R. 1921, Philos. Trans. Royal Soc. A, 221, 73

Wogan, N. F., & Catling, D. C. 2020, ApJ, 892, 127

Woitke, P., & Helling, C. 2003, A&A, 399, 297

——. 2004, A&A, 414, 335

Woitke, P., Helling, C., Hunter, G. H., Millard, J. D., Turner, G. E., Worters, M., Blecic, J., & Stock, J. W. 2018, A&A, 614, A1

Woitke, P., Herbort, O., Helling, C., Stüeken, E., Dominik, M., Barth, P., & Samra, D. 2021, A&A, 646, A43

Wong, M. L., Charnay, B. D., Gao, P., Yung, Y. L., & Russell, M. J. 2017, Astrobiology, 17, 975

Wood, B. E., Müller, H.-R., Zank, G. P., & Linsky, J. L. 2002, ApJ, 574, 412

Yair, Y., Fischer, G., Simões, F., Renno, N., & Zarka, P. 2008, Space Sci. Rev., 137, 29

Yang, J., Junium, C. K., Grassineau, N. V., Nisbet, E. G., Izon, G., Mettam, C., Martin, A., & Zerkle, A. L. 2019, Nature Geoscience, 12, 553

Ye, B., Del Genio, A. D., & Lo, K. K.-W. 1998, Journal of Climate, 11, 1997

Yung, Y. L., & McElroy, M. B. 1979, Science, 203, 1002 LP

Zahnle, K., Marley, M. S., Morley, C. V., & Moses, J. I. 2016, ApJ, 824, 137

Zahnle, K. J. 2006, Elements, 2, 217

Zahnle, K. J., Lupu, R., Catling, D. C., & Wogan, N. 2020, PSJ, 1, 11

Zarka, P., & Pedersen, B. M. 1986, Nature, 323, 605

Zel'dovich, Y. B., & Raizer, Y. P. 1966, Physics of shock waves and high-temperature hydrodynamic phenomena, ed. W. D. Hayes & R. F. Probstein (New York, NY: Academic Press)

Zellner, N. E., McCaffrey, V. P., & Butler, J. H. 2020, Astrobiology, 20, 1377

Zerkle, A. L., & Mikhail, S. 2017, Geobiology, 15, 343

Zerkle, A. L., Poulton, S. W., Newton, R. J., Mettam, C., Claire, M. W., Bekker, A., & Junium, C. K. 2017, Nature, 542, 465

Zhang, X., Sigman, D. M., Morel, F. M. M., & Kraepiel, A. M. L. 2014, Proc. Natl. Acad. Sci. U.S.A., 111, 4782

Zhang, X. et al. 2023, Environmental Science & Technology, 57, 2322

Zheng, X.-J. 2013, The European Physical Journal E, 36, 138

Zhong, Q., Huang, Y., Shen, H., Chen, Y., Chen, H., Huang, T., Zeng, E. Y., & Tao, S. 2017, Environmental Science and Pollution Research, 24, 864

Zieba, S. et al. 2023, Nature

Zuo, Y., & Deng, Y. 1999, Geochim. Cosmochim. Acta, 63, 3451